Title
Atomic Layer Deposition of Thin Films for 3D Lithium-Ion Microbatteries

Permalink
https://escholarship.org/uc/item/97g4t32w

Author
Sheil, Ryan Thomas

Publication Date
2020

Peer reviewed|Thesis/dissertation

UNIVERSITY OF CALIFORNIA

Los Angeles

Atomic Layer Deposition of Thin Films for 3D Lithium-Ion Microbatteries

A dissertation in partial satisfaction of the requirements for the degree

of Doctor of Philosophy in Chemical Engineering

by

Ryan Sheil

2020

ABSTRACT OF THE DISSERTATION

Atomic Layer Deposition of Thin Films for 3D Lithium-Ion Microbatteries

by

Ryan Sheil

Doctor of Philosophy in Chemical Engineering

University of California, Los Angeles, 2020

Professor Jane Pei-Chen Chang, Chair

This work demonstrates the synthesis and characterization of several material systems that meet the required functional properties for direct integration in 3D lithium-ion microbatteries—conformal thin film solid-state electrolytes with adequate ionic conductivity and cathodes exhibiting high volumetric capacity, excellent rate capability, and cycle life. The atomic layer deposition (ALD) process optimization allowed for the control of the structural, chemical, and electrochemical properties of $Li_{1+x}Mn_{2-x}O_4$, $Li_xAl_ySi_zO$, as well as their interfacial properties that ultimately dictate electrochemical performance.

The synthesis of $Li_{1+x}Mn_{2-x}O_4$ combined a plasma enhanced ALD process for MnO_2 and a thermal process for ALD LiOH. The PEALD MnO_2 showed self-limiting growth, stable composition (within 5% relative composition), and well-controlled growth rate over a temperature range of 205-265°C. As synthesized and amorphous ALD $Li_{1+x}Mn_{2-x}O_4$ films were crystallized into the electrochemically active spinel phase. Tuning of the ALD cycle ratio led to controlled Li content in $Li_{1+x}Mn_{2-x}O_4$ (x = 0-0.33), exhibiting electrochemical activity in both the 3.0V and 4.0V

region depending on the stoichiometry. The $Li_{1+x}Mn_{2-x}O_4$ thin films exhibited great rate capability and capacity retention—maintaining 66% of the areal capacity upon increasing the rate by a factor of a 100 as well as 97% capacity retention over 100 cycles at 35.9 $\mu A\ cm^{-2}$ (~5C). The measured volumetric capacity was 52 $\mu Ah\ cm^{-2}\ \mu m^{-1}$ at ~C/2 and 45 $\mu Ah\ cm^{-2}\ \mu m^{-1}$ after 100 cycles at ~5C, offering the potential for superior areal energy densities.

Amorphous $Li_xAl_ySi_zO$ thin films were synthesized and integrated on SiGe alloying anodes. Using *in-situ* transmission electron microscopy, the electrolyte layer was remained intact during the lithiation induced volume expansion of the nanowire for two different electrolyte thicknesses (8 and 20 nm). A novel hybrid solid-state electrolyte consisting of sequential deposition of ALD $Li_xAl_ySi_zO$ and iCVD PV4D4 was synthesized to improve upon the mechanical properties of $Li_xAl_ySi_zO$ for direct integration with high capacity anodes. Integration on Co_3O_4 thin films resulted in increased capacity-retention with continuous cycling with a discharge capacity 8.4% higher as compared to the uncoated Co_3O_4 anode after 100 cycles at ~2C.

The stoichiometry of ALD $Li_xAl_ySi_zO$ was controlled to allow for crystallization in the β-eucryptite phase for improved ionic conductivities. The crystallized $LiAlSiO_4$ exhibited a well-defined epitaxial relationship of β-$LiAlSiO_4$ ($1\bar{2}10$) $\parallel$ Si (100) and β-$LiAlSiO_4$ ($10\bar{1}0$) $\parallel$ Si(001). The ionic conductivity of the crystallized thin film was around two orders higher than the amorphous as-deposited films (10^{-7} vs. 10^{-9} S/cm) at room temperature. Due to the unique 1-D channel along the c-axis of β-$LiAlSiO_4$, the epitaxial thin film has the potential to facilitate ionic transport if oriented with the c-axis normal to the electrode surface making it a promising electrolyte material for 3D lithium-ion Microbatteries, where a properly oriented film offers the opportunity to achieve higher ionic conductivities.

The dissertation of Ryan Sheil is approved.

Bruce Dunn

Dante A. Simonetti

Philippe Sautet

Jane Pei-Chen Chang, Committee Chair

University of California, Los Angeles

2020

Dedicated to the loving memory of my mom

Jill Sheil

.

TABLE OF CONTENTS

LIST OF TABLES

LIST OF FIGURES

Assuming the average area to be 0.0442 cm^2, then the resulting ionic conductivities would have an average ionic conductivity $8.6 \pm 6 \times 10^{-7}$ S/cm. 160

ACKNOWLEDGEMENT

Firstly, I would like to thank Professor Chang for her mentorship over the past 5 years. I truly would not be where I am today without her guidance as a scientific researcher as well as a person—in critical thinking, work-ethic, and communication. Thank you for providing me the space to grow as a scientist and always supporting the pursuit of new ideas. I would like to thank Professor Dunn for always making himself available to me and providing guidance on my research projects. I would like to thank Professor Sautet and Professor Simonetti for making themselves available to advise my thesis research. It was really enjoyable working and learning from you both in my first time being a teacher's assistant and my first class in graduate school.

Next, I would like to thank all of my collaborators. Dr. Katie Jungjohann, thank you so much for all of your guidance on TEM and helping with all of the in-situ lithiation experiments, every visit to CINT was very enjoyable. I would like to thank Dr. Jinkyoung Yoo for providing all of the nanowire samples. I would also like to thank Dr. Priya Moni for all of the pV4D4 depositions and insight into iCVD reactor design. Lastly, I would like to thank Dr. Jon Lau, Danielle Butts, and Chris Choi for all of their electrochemistry insight as well as their endless willingness to help characterize materials and try new ideas.

I have been extremely lucky to have been able to work in the Chang lab with not only insightful and helpful people but also some of my best friends. First, I would like to thank Dr. Cyrus Cheung for being an incredibly understanding and helpful mentor on the vacuum systems in our lab. I would like to thank Dr. Colin Rementer for his guidance and friendship. Dr. Jeffery Chang, thanks for being a great friend, always being there to discuss all-things ALD, as well as always being down to go to Monkish can releases. Dr. Nick Altieri, I cannot thank you enough for always being the go-to person for any issue in lab and being a great friend. Gary and Adrian, I

have truly enjoyed all of our research discussions and I wish you both the best with your projects. Lastly, I would like to thank Ernest for always being there to talk over any issue or lend a helping hand. It truly has been great to have gone through my doctoral program with you and to have made such a great friend.

I would not be able to have done any of this without the love and support of my family. I would like to thank all of my aunt's and uncle's for continually supporting and encouraging me. I would like to thank Sasha for being like a sister to me as well as a great friend. I would like to thank Vladamir for on top of the countless things you have done for Nani and me, thank you for endlessly supporting me. I have always enjoyed talking science and research with you. I would like to thank Gordana for being truly my biggest supporter and always making me feel loved. I would like to thank Bubba for all of your support and friendship. I look up to you in many ways from the kindness you show others to your creative thinking. I want to thank my Grandma, Grandpa, Nana, and Papa for always supporting me, loving me, and teaching me. You have all been loving parent figures in my life and for that I will always be grateful. I would like to thank my Dad; without you I would not be the person I am today. I don't think there could be a more loving and supportive Dad. You inspire me to be the best person I can be. Lastly, I owe everything to my wife, my soulmate, and my best friend. I truly would not be where I am today without you. You inspire me every day with your kindness, compassion, intelligence, and passion. You have been my rock throughout my whole Ph.D. providing me endless support, love, laughs when I needed it most. I am so incredibly grateful to be able to spend the rest of my life with you.

VITA

2014	B.S., Chemistry
	University of California, Santa Barbara
	Santa Barbara, California
2015-2020	Ph.D. Candidate
	Graduate Student Researcher
	Department of Chemical and Biomolecular Engineering
	University of California, Los Angeles
	Los Angeles, CA

AWARDS

2014	Distinction in Major
	Chemistry and Biochemistry Department
	University of California, Santa Barbara
	Santa Barbara, CA
2018	Center for Clean Technology Fellowship
	Department of Chemical and Biomolecular Engineering
	University of California, Los Angeles,
	Los Angeles, CA
2019	James Harper Award Finalist
	Thin Films Division Graduate Student Award
	AVS 64th International Symposium and Exhibition
	Columbus, Ohio

PUBLICATIONS AND PRESENTATIONS

R. Sheil, J.P. Chang. Synthesis and Integration of Thin Film Solid State Electrolytes for 3D Li-ion Microbatteries. JVST A 38:3 2020

A. Acosta, K. Fitzell, J.D. Schneider, C. Dong, Z. Yao, **R.Sheil**, Y. E. Wang, G. Carman, N.X. Sun, J.P. Chang. Underlayer Effect on the Soft Magnetic, High Frequency, and Magnetostrictive Properties of FeGa Thin Films. Journal of Applied Physics 128 013903, 2020.

A. M. Schrader, J. I. Monroe, **R. Sheil**, H. A. Dobbs, T. J. Keller, Y. Li, S. Jain, M. S. Shell, J. N. Israelchvili, S. Han. Surface chemical heterogeneity modulates silica surface hydration. Proceedings of the National Academy of Sciences 115 (12) 2890-2895, 2018.

K. Huang*, C. N. Kingsley*, **R. Sheil***, C. Cheng, J. C. Bierma, K. W. Roskamp, D. Khago, R. W. Martin, S. Han. Stability of Protein-Specific Hydration Shell on Crowding. Journal of American Chemical Society. 138 (16), 2016.

R. Sheil, J. Lau, K. Jungjohann, J. Yoo, B. Dunn, J.P. Chang. Organic/Inorganic Solid Electrolytes for 3D Lithium-ion Batteries. American Vacuum Society 66th International Symposium and Exhibition. Columbus, Ohio. October 2019 (Oral)

R. Sheil and J.P. Chang. The Miniaturization of the Lithium-ion Battery. American Vacuum Society 66th International Symposium and Exhibition. Columbus, Ohio. October 2019 (Oral) (Competition Talk for Thin Films James Harper Award)

R. Sheil, J. Lau, B. Dunn, J.P. Chang. Radical Enhanced Atomic Layer Deposition of Cobalt Oxide Based Electrodes for 3D Lithium-ion Battery Applications. American Vacuum Society 65th International Symposium and Exhibition. Long Beach, CA. October 2018 (Oral)

R. Sheil, P. Moni, J. Lau, C. Choi, K. Jungjohann, J. Yoo, B. Dunn, K. Gleason, J.P. Chang*. Engineering Hybrid Thin Film Electrolytes for 3D Lithium-ion Micro-battery Applications. European Materials Research Society Spring Meeting and Exhibit. Strasbourg, Fr. June 2018. (Oral)

R. Sheil, J. Lau, P. Moni, C. Choi, K. Jungjohann, J. Yoo, K. Gleason, B. Dunn, J.P. Chang. Engineering Hybrid Thin Film Electrolytes for 3D Lithium-ion Battery Applications. American Vacuum Society 64th International Symposium and Exhibition. Tampa Bay, FL. October 2017 (Oral)

CHAPTER 1:   INTRODUCTION

The advent of the lithium-ion battery has been a truly transformative technology on society—recognized in 2019 with the Nobel Prize in Chemistry awarded to three scientists, M. Stanley Whittingham, John B. Goodenough, and Akira Yoshino for its development. First commercialized by Sony in the 1990's, the lithium-ion battery has been a key factor to the success of the mobile electronics industry since due to its superior energy and power density as compared to other battery chemistries—revolutionizing the way we communicate and interact with information. Beyond mobile electronics, the demand for lithium-ion batteries for use in electric vehicles is expected to increase as steady improvements have made electric vehicles more competitive with their combustion engine counterparts coupled with the increased awareness of climate impacts further solidifying electric vehicles hold in the automotive market. Enabled, in large part, by the electronics' industry's continual advancement in integrated circuits, fast paced development of new technologies in the space of wearable electronics, autonomous sensors, and biomedical devices has increased the demand for a miniaturized and integrated power source. In the era of internet of things (IoT), a projected trillion sensors are to be needed each year to support autonomous operation in sensing, actuation, and communication, where a wide range of physical, chemical, and biological stimuli need to be collected, processed, and disseminated in real time (Shit 2018). The lithium-ion battery is an ideal candidate for powering these novel devices, but fundamental limitations in the miniaturization of energy storage medium has prevented optimal device integration, where generally the device size is dictated by the size of the battery (Arthur 2011, Khan 2016, Moitzheim 2019).

The thin film battery consisting of all-solid-state components is the current state-of-the-art for powering these small-scale devices but suffers poor areal energy density (large footprint)

due to limitations in the electrode thicknesses. This has prompted the development of three-dimensional thin film batteries that take advantage of high surface area structures to promote high areal energy densities. Due to the inherent complexity and difficulty in fabrication, development of 3D lithium-ion batteries has been significantly challenging, where one of the biggest hurdles is deposition of conformal battery-relevant materials on the characteristic high aspect ratio structures. The scope of this thesis is in the development of several atomic layer deposition processes to synthesize novel thin films that meet the requirements for 3D device integration—not only in state-of-the-art electrochemical performance, but crucially the conformality needed for application on the high aspect-ratio structures utilizing in 3D lithium-ion microbatteries.

1.1   Lithium-Ion Battery Basics

The lithium-ion battery is composed of two electrochemically active materials the cathode (positive electrode) and the anode (negative electrode) separated by an ion-conducting, but electrically resistive electrolyte layer as shown in Figure 1-1. Li-ions are transported between electrodes during charge and discharge where the ions undergo a reversible reaction on the electrode surface within the cell, but electrons are limited to flow through an external circuit. During the charge process, lithium ions are intercalated into the anode through applying a current creating an increasing voltage difference between the electrodes corresponding to the chemical potential changes associated with the lithiation/delithiation reactions at each respective electrode. The total energy stored is a product of the current applied, the duration of charge, and the potential difference between electrodes. The stored chemical energy can then be released in the reverse process—decreasing the potential difference between the electrodes and supplying a current for a given amount of time. The rate at which this reversible process can take place can be dictated by

the kinetics of the lithium ion reaction at each electrode, the ion transport within the electrode and electrolyte, and the electrical conductivity of the electrodes.
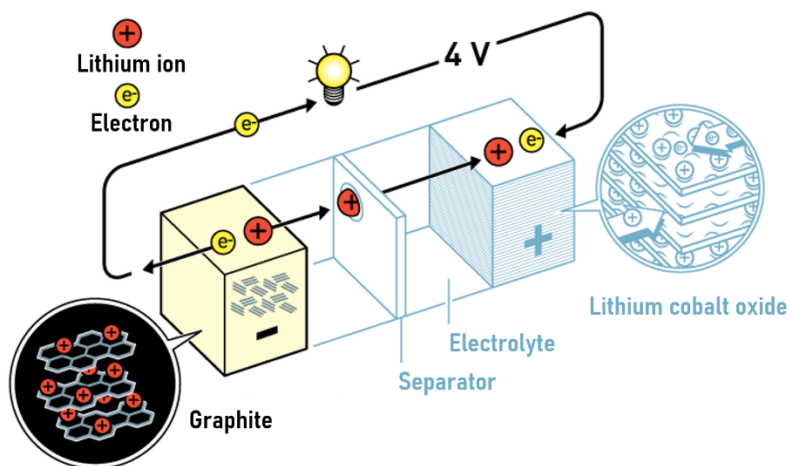
Figure 1-1. Schematic of the basic components of a lithium-ion battery consisting a cathode, anode and an electrolyte that separates them. Adapted from (Jarnestad 2019).

Some of the first lithium-based batteries were developed by M. Stanley Whittingham based on Li/TiS_2 electrode couple, operating at 2V, but suffered from instability and safety issues. John B. Goodenough improved the design by utilizing the metal oxide: lithium cobalt oxide as the cathode material improving the cell voltage to 4V, but still suffered similar issues due to the lithium metal component. Akira Yoshino developed an alternative to the lithium anode by replacing it with carbon based one (petroleum coke), which although has a much lower energy density than lithium metal allowed for increased safety and reversibility—which led to its first commercialization for use in mobile electronics. The battery design is relatively unchanged to date, but significant research has been performed over the last ~30 years in improvement of the battery mostly through development of new materials—to increase the energy density (device usage time, range of electric vehicles), power density (quick charging times), the cycle-life (battery performance over time), and safety (prevention of battery combustion).

The electrochemical reactions associated with lithiation and delithiation of the most common anode and cathode materials are shown in Eq. (1-1) and Eq. (1-2), respectively. Eq. (1-1) shows complete intercalation of graphite. Eq. (1-2) shows the delithiation reaction of $LiCoO_2$, where x is limited to ~0.5, as the crystal structure undergoes irreversible changes upon further delithiation.

$$C_6 + Li^+ + e^- \leftrightarrow LiC_6 \tag{1-1}$$

$$LiCoO_2 \leftrightarrow xLi^+ + xe^- + Li_{1-x}CoO_2 \tag{1-2}$$

To calculate the energy storage metrics for lithium ion batteries, first staring with the free energy associated with the chemical reaction, ΔG°, which is equal to the maximum amount of electrical work able to be performed via the chemical reaction as shown in Eq. (1-3), where n is the number of electrons transferred per mole of reactants, F is Faraday's constant and E° is the electromotive force (emf).

$$\Delta G^\circ = -nFE^\circ \tag{1-3}$$

Therefore, as spontaneous processes have negative free energy values, their corresponding E° values are positive. Moving beyond standard state conditions, the electromotive force for a given reaction can be described by the Nernst Equation (Eq. (1-4)), where Q is the reaction quotient for the overall reaction defined as the ratio between the activity of the products over the activity of the reactants.

$$E = E^\circ + \frac{RT}{nF} \ln Q \tag{1-4}$$

In the case of a battery, with two half-reactions as shown in Eq. (1-5) and Eq. (1-6) (oxidation and reduction) occurring at opposite terminals, the overall cell voltage is the difference between the

emf voltages of each half reaction (written as reduction reactions) Eq. (1-7), with the corresponding Nernst equation for the overall cell reaction given by Eq. (1-8).

$$aA + ne^- \leftrightarrow bB \qquad (1\text{-}5)$$

$$cC \leftrightarrow dD + ne^- \qquad (1\text{-}6)$$

$$E = E_+ - E_- \qquad (1\text{-}7)$$

$$E = E^\circ + \frac{RT}{nF} \ln \frac{\alpha_B^b \alpha_C^c}{\alpha_A^a \alpha_D^d} \qquad (1\text{-}8)$$

Eq. (1-9) directly rates the chemical reaction and current flow, where I is the current, t is the time of current flow, n_e is number of electrons transferred in the reaction, and N_i is the number of moles transformed in the reaction. Using Eq. (1-9), specific capacities of electrode materials can be calculated based on their redox reactions, for instance in the case of graphite with the lithiation reaction shown in Eq. (1-1), has a specific capacity of 371.9 mAh/g.

$$It = n_e F N_i \qquad (1\text{-}9)$$

Beyond the thermodynamic considerations there are also kinetic factors associated with the electrochemical reactions undergone in the battery system. There is an activation polarization or the associated kinetics of the redox reaction occurring at the electrode/electrolyte interface, an ohmic polarization associated with the resistances across the various device components along with the electrical contact to the battery terminals, and a concentration polarization associated with mass transfer limitations in the electrolyte and electrodes respectively that all effect the cell voltage during operation as can be seen in Figure 1-2 (Winter 2004).
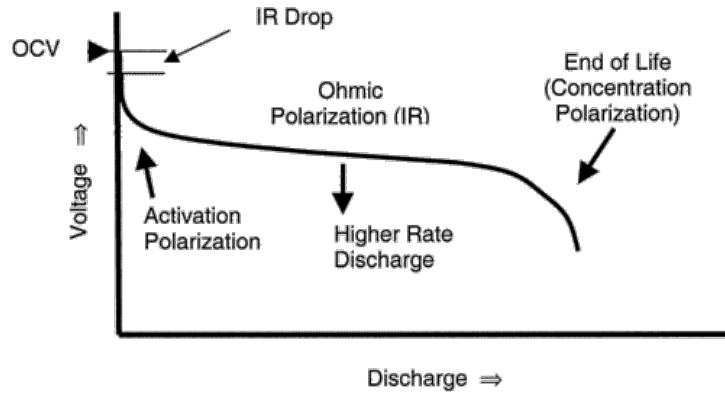
Figure 1-2. Discharge profile illustrating various polarizations in lithium-ion batteries (Winter 2004)

The energy and power density expressions are given in Eq. (1-10) and Eq. (1-11) , where i is the current density, A is the area of the electrode, and $t_{c/d}$ is the time of charge and discharge.

$$E_{Density} = \frac{\int_0^{t_{C/D}} V(t)iAdt}{Volume} \tag{1-10}$$

$$P_{Density} = \frac{E_{Density}}{t_{c/d}} = \frac{\int_0^{t_{c/d}} V(t)iAdt}{t_{c/d}Volume} \tag{1-11}$$

1.2 Thin Film Lithium-ion Batteries

Lithium-ion batteries have found success in powering devices with a remarkably wide range of size with electric cars being on the larger end and personal mobile electronics, such as smart phones, smart watches, and wireless headphones being significantly smaller. Although gradual advancements improvements in lithium-ion batteries (energy density, cycle stability, safety) has been made over the course of the last 30 years, technological advancement has been arguably very limited in comparison to portable electronics they power. Considering Moore's law—the observation that the number of transistors in integrated circuits doubles every two years has held relatively true for the past 50 years, where even now advancement to features on the scale

of 7 nm have been achieved. Considering the size of computing systems over the last 50 years, evokes Bell's law—that a new "form" of a computer is developed roughly every decade resulting in novel usage. This trend as shown in Figure 1-3 generally results in a new class of smaller computing systems, in which increasing quantities are manufactured. The idea of ubiquitous computing, first coined by Mark D. Weiser, is the delocalization of computing across a wide range of devices that vary greatly in size and functionality. This next evolution of the integrated circuit industry is captured by the Internet of things (IoT) paradigm, in which millimeter sized devices are deployed on a massive scale (Fojtik 2013). An example microsensor is shown in Figure 1-3 where the main components are a thin film battery for energy storage, a silicon based solar cell for energy harvesting, and microcontroller.
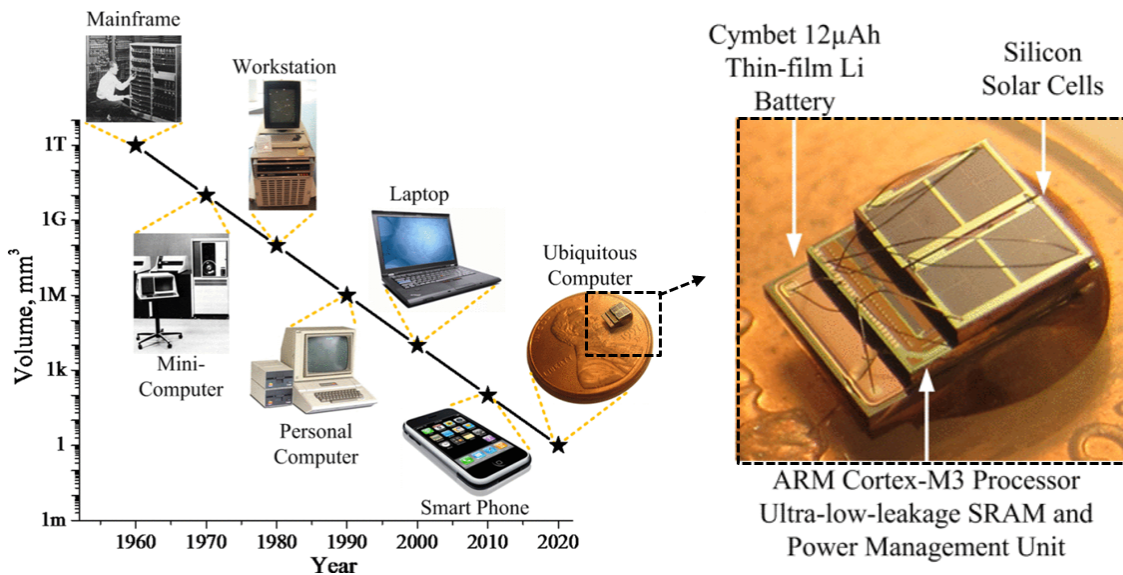
Figure 1-3. Bell's law predicts that that a new "form" of a computer is developed roughly every decade resulting in novel usage. New computer classes are generally cheaper, smaller, and are manufactured in increasing quantities. Ubiquitous computing is correlated to the IoT paradigm in which processing of information happens delocalized on a wide array of devices. One potential way the ubiquitous computing idea could come to fruition is through the deployment of a vast array of microsensors. An 8.75 mm^2 temperature microsensor is shown consisting of a thin film battery, silicon based solar cell, and microcontroller. Adapted from (Fojtik 2013).

The leading candidate to power these mm^3 microsensors are thin film lithium-ion batteries. Thin film lithium-ion batteries leverage synthesis techniques developed in the IC industry to fabricate an all-solid-state planar stack of materials consisting of sequential deposition steps. A typical process flow would start with a silicon wafer substrate, thermal oxidation, followed by sequential deposition of a current collector (Ti/Pt/Ti), cathode ($LiCoO_2$), electrolyte (LIPON), anode (Al), current collector, and insulation layer as shown in Figure 1-4 (a) (Moitzheim 2019). Thin film lithium-ion batteries offer many advantages to traditional lithium-ion batteries such as increased safety due to all-solid-state components, fast charging (thin electrodes), and long-term cycle life (solid state electrolyte), but suffer from poor areal energy density. Low areal density is rooted in restrictions on the cathode thickness, which is generally less than a few microns, due to limited Li-ion diffusion as well mechanical integrity issues (Dudney 2008). Conventional lithium-ion batteries mitigate these issues through utilizing electrode particles (on the order of microns), suspended in a conductive matrix that is soaked in liquid electrolyte allowing for adequate electrical conductivity and lithium-ion transport to the active material, where an example cross-section image is shown in Figure 1-4 (b). In contrast, thin film batteries must utilize solid-state electrolytes and electrodes due to size restraints, where a matrix-like electrode structure to mitigate transport issues is not feasible with gas-phase processing techniques.
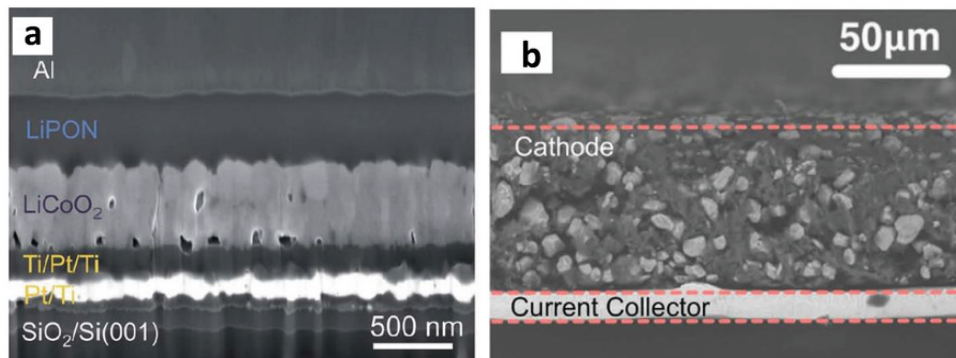
Figure 1-4. (a) Cross-section of a thin film lithium-ion battery and (b) a traditional slurry-based lithium-ion battery (Leite 2014, Ostfeld 2016)

The limitation in cathode thicknesses is related to limitations in the solid-state Li-ion diffusion, where the characteristic diffusion time for a lithium-ion to diffuse across an electrode layer is given in Eq. (1-12) which scales with the square of the electrode thickness (l). This relation gives an estimate to lithium-ion transport within the electrode (not considering migration component), where small l provides fast charging, but the maximum thickness of the electrode layer is dependent on the solid-state diffusion coefficient.

$$\tau = \frac{l^2}{D} \tag{1-12}$$

The characteristic diffusion time vs. the electrode thickness for several solid-state diffusion coefficients is plotted in Figure 1-5, where for instance the solid-state diffusion coefficient for $LiMn_2O_4$ a lithium-ion battery cathode material has been reported in the range of 10^{-11}-10^{-12} cm^2/s (Julien 2000, Tang 2007, Kuwata 2018). For example, the electrode material would be limited to a thickness of ~ 2 microns for a charge time of 1 hour assuming the solid-state lithium-ion diffusion coefficient was 10^{-12} cm^2 s^{-1}. C-rate terminology is often utilized to relate the specific current utilized to discharge a battery and the theoretical capacity. A C-rate of 1C refers to the current, that when applied would discharge the electrode(s) within one hour, as in a 1 mA/cm^2 specific current to discharge a thin film with a theoretical capacity of 1 mAh/cm^2. Eq. (1-13) gives the relation between the charge/discharge time, $t_{c/d}$, to the C-rate.

$$t_{c/d} = 1 \text{ hour/C-rate} \tag{1-13}$$

Higher C-rates correspond to faster discharge due to increased current density. C-rates are defined as nC, where n is an integer multiple of the 1C current. For instance, if 1C corresponded to a specific current of 1mA/cm^2, 2C would correspond to a specific current of 2mA/cm^2, and C/2 would correspond to a specific current of 0.5 mA/cm^2. Each of C-rates would results in the theoretical discharge of 1 hour, 30 minutes, and 2 hours, for the 1C, 2C, and C/2 rates, respectively.
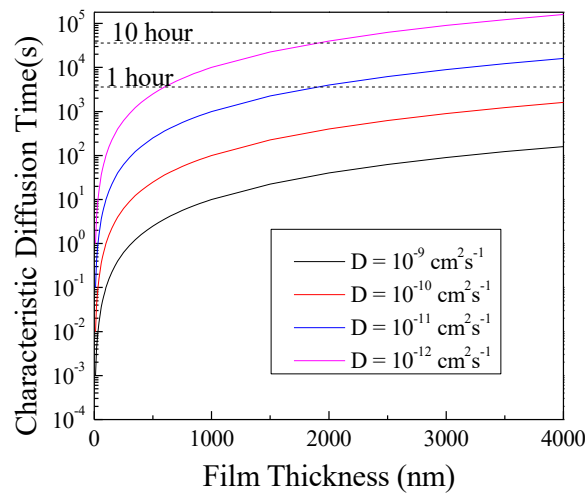
Figure 1-5. Characteristic diffusion time vs. electrode film thickness solid-state lithium ion diffusion coefficients ranging from D = 10^{-12}-10^{-9} cm^2 s^{-1}. The 10 hour and 1 hour are marked in reference to C-rate of 1C and C/10.

Limitations in the planar configuration has led to the development of more advanced three-dimensional (3D) electrode architectures, in which the kinetic issues associated with electrode thickness can be mitigated to produce batteries with improved areal energy density (Long 2004, Arthur 2011, Ferrari 2015). 3D battery architectures can be characterized by the utilization of high-aspect ratio structures that allow for the higher areal loading (thicker battery) but maintain the surface area to volume of the electrodes allowing for decoupling of the areal energy and power density. Many different 3D designs have been proposed such as nanowire or micropillar electrode

arrays, etched Si structures, porous electrode materials, and interdigitated trench electrodes (Chamran 2007, Cheng 2008, Arthur 2011, Wang 2011, Pearse 2018, Moitzheim 2019). Several theoretical designs are presented below where areal capacities are compared between 3D and 2D architectures.

1.3   3D Battery Designs

For lithium-ion batteries the total stored energy is equal to the product of the lithiation capacity, the cell voltage, and the volume of the active materials. The benefits of utilizing 3D structures is illustrated below in a significantly simplified example. As shown in Figure 1-6, for a square 2D battery arrangement (planar stack) with dimensions (width: l, length: l, height: h) the total capacity is given by Eq. (1-14) and the areal capacity is provided in Eq. (1-15), where C_i^* is the theoretical volumetric capacity of the electrodes. In this simplified case we assume that the capacities of the electrodes are equal, and h corresponds to the total thickness of both electrode layers, in addition we are not considering the electrolyte, current collector, packaging layers, etc.
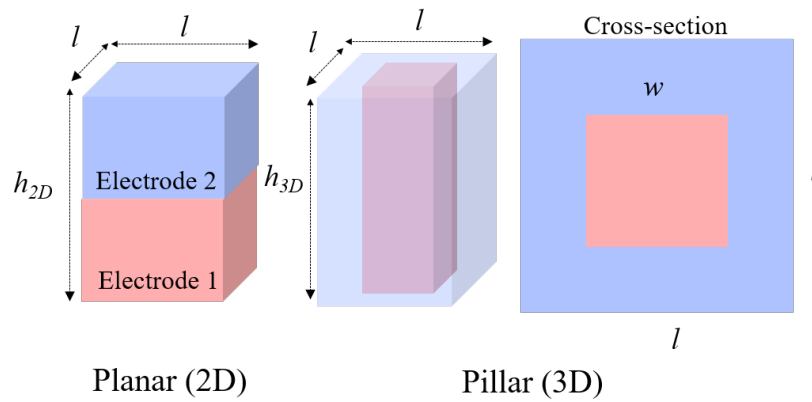
Figure 1-6. A comparison of between 2D and 3D battery architectures, considering the same footprint. The calculations assume the capacity of electrodes 1 and 2 are equal. The surface area refers to the interfacial contact between electrode 1 and electrode 2. For simplicity sake, the electrolyte, current collectors, and packaging are not shown.

A more relevant parameter to mm^3 sensor applications is the areal capacity, where the areal capacity scales with the electrode thicknesses, h. The areal energy density (E_{areal}) can be approximated as the product of the areal capacity (C_{areal}) with the average voltage (V_{avg}) during discharge.

$$C_{tot} = C_i^*(l^2h) \tag{1-14}$$

$$C_{areal} = C/l^2 = C_i^*(h) \tag{1-15}$$

Up until this point in discussion, no mention has been made in regard to the kinetics of the discharge/charge processes. The areal power density can be approximated by Eq. (1-16), where t is the time associated with the charge/discharge rate and E_{Areal} is the rate dependent energy density.

$$P_{areal} = E_{areal}/t_{discharge} \tag{1-16}$$

Higher rates (faster charge/discharge times) are associated with lower achievable energy densities due to kinetic limitations. This rate dependence is a complex function associated with the geometry of the device and the materials properties of its components (electrical conductivity, lithium-ion diffusivity, surface reaction rates, etc.). An alternative measure is the interfacial surface area to volume ratio, where increasing values ensures shorter Li-ion diffusion distances and lower interfacial kinetic overpotential allowing for higher achievable power densities (Long 2004). For the 2D device arrangement the interfacial surface area to volume ratio (an indirect measure of the areal power density) scales with h^{-1} as shown in Eq. (1-17), where in contrast the areal capacity scales with h.

$$SA_{2D}/V_{2D} = l^2(hl^2)^{-1} = h^{-1} \tag{1-17}$$

A direct consequence of this is an effective inverse coupling between the areal energy and areal power densities limiting thin film battery performance. The effect of this inverse relationship can be observed in thin film lithium ion batteries, where electrode thicknesses are limited to several

microns in thickness to maintain the minimal power requirements of the device severely limiting the areal energy densities of these devices. For instance, Li^+ diffusion was shown to be the limiting step in achieving high power density as the film thickness was increased above 1 μm for $LiCoO_2$ thin film cathodes (Dudney 2003).

The inherent limitations associated with the traditional planar 2D structure have culminated in increased interest in "3D" structuring of electrodes for enhanced areal energy and power densities through maximization of interfacial surface area. For example, in the simplest case consider a 3D battery consisting of an array of a single pillar where the inner electrode has a width, w, and the outer electrode has a width, l. For direct comparison to the 2D model, we simplify the structure by only considering the two electrodes, where the capacity of the outer and inner electrodes is equal. By setting the volume of the inner and outer electrode equal you can come to relation shown in Eq.(1-18). The interfacial surface area of the one pillar is given by Eq. (1-19), within the area footprint, l^2. The surface area enhancement over an equivalent 2D structure is given by Eq. (1-20), where it becomes clear the surface area enhancement increases with increasing aspect-ratio (h/l), where conditions for the $SA_{enhancement}$ to be greater than 1 are given in Eq.(1-21)

$$w = l(\sqrt{2})(2)^{-1} \tag{1-18}$$

$$SA_{3D} = 4(w)(h) = 2(\sqrt{2})l(h) \tag{1-19}$$

$$SA_{enhancement} = SA_{3D}/SA_{2D} = 2(\sqrt{2})(h)(l)^{-1} \tag{1-20}$$

$$SA_{enhancement} > 1, \text{ when } h > l(2\sqrt{2})^{-1} \tag{1-21}$$

The volume of the 3D structured electrode is given by Eq. (1-22), which is equivalent to the volume for the 2D structure, where the areal capacity is shown in Eq. (1-23). Crucially, if the height of the electrode cylinder is increased (corresponding to higher areal energy density) the

interfacial surface area to volume ratio of the electrode cylinder is unchanged, where the relation is given via Eq. (1-24).

$$V_{3D} = l^2h \tag{1-22}$$

$$C_{areal}{}^{3D} = C_i{}^*(V_{3D})(l^{-2}) \tag{1-23}$$

$$SA_{3D}/V_{3D} = 2(\sqrt{2})(l^{-2}) \tag{1-24}$$

A comparison of the 2D (planar) structure vs. the 3D (pillar) structure for various heights is shown in Figure 1-7, where for both cases the areal energy density increases with h. The Surface area to volume ratio for the 2D structure continually diminishes with h, where for the 3D structure the value (2) $(\sqrt{2})l^{-1}$ is independent of h. In summary, increasing the height in the 3D structure leads to higher values for the areal capacity at no cost to the surface area to volume ratio. The surface area to volume ratio—a stand in for the rate-capability and power density—can be improved in the 3D structure by increasing the aspect-ratio. It should be noted that in this simplistic design the aspect-ratio cannot be increased indefinitely as there is a trade-off in inhomogeneous current distribution due to ohmic resistance along the heigh of the pillar. A more complex and detailed design of a 3D lithium-ion battery is discussed below.
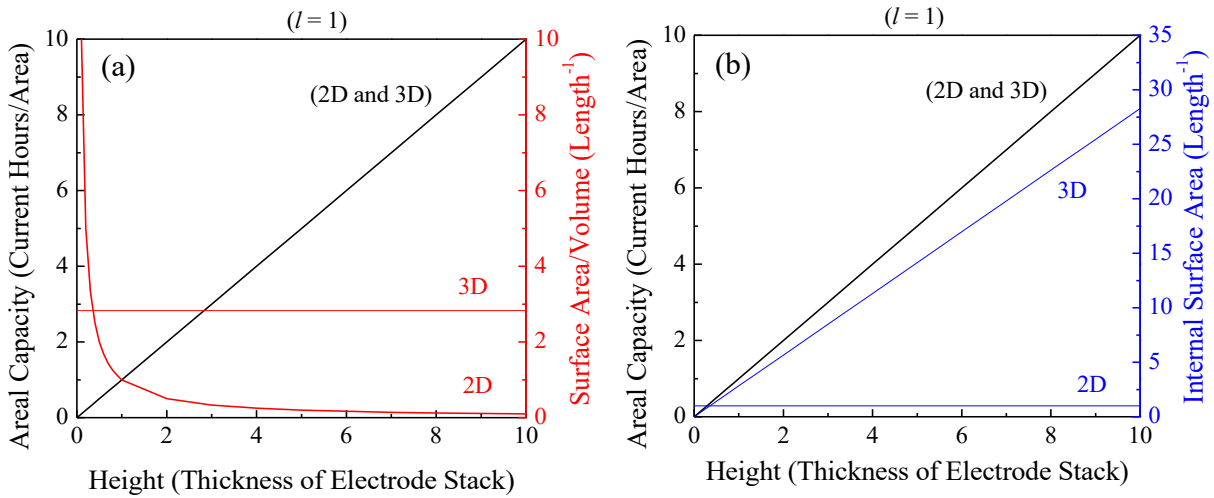
Figure 1-7. (a) The comparison of areal capacity and surface area to volume ratio for 2D and 3D battery designs. The benefit of the 3D-structure is clear when comparing the Surface Area/Volume with increasing h (thickness of electrode stack). For a given footprint, l^2, the areal capacity can be maximized through increasing h for both the 2D and 3D structure. In the 2D design, the surface area/volume ratio of the electrodes approaches zero as the areal capacity is maximized (trade-off between areal energy and power density). Crucially in the 3D design, if the height of the electrode cylinder is increased (corresponding to higher areal energy density) the interfacial surface area to volume ratio of the electrode cylinder is unchanged. (b.) The total internal surface area versus the height of the electrode stack (h), where for the 2D structure it is unchanged and the 3D structure it increases.

A more optimized 3D battery design is presented below based on the theoretical calculation and work by Moitzheim et al. (Moitzheim 2019, Moitzheim 2019) as well as the experimental work by Pearse et al. (Pearse 2018) to include all the necessary layers for battery operation (current collectors, anode, electrolyte, and cathode). The physical rational for the design is based off utilizing Si as a substrate, in which high aspect-ratio structures can be fabricated through a reactive ion etch process. A schematic of the 3D battery utilized for calculations is shown of Figure 1-8, that consists of initial Si pillars as the substrate, a current collector layer, anode layer, electrolyte

15

layer, cathode layer, and additional current collector. A square pillar was chosen for ease of calculations, but a close-packed cylindrical design is also feasible.
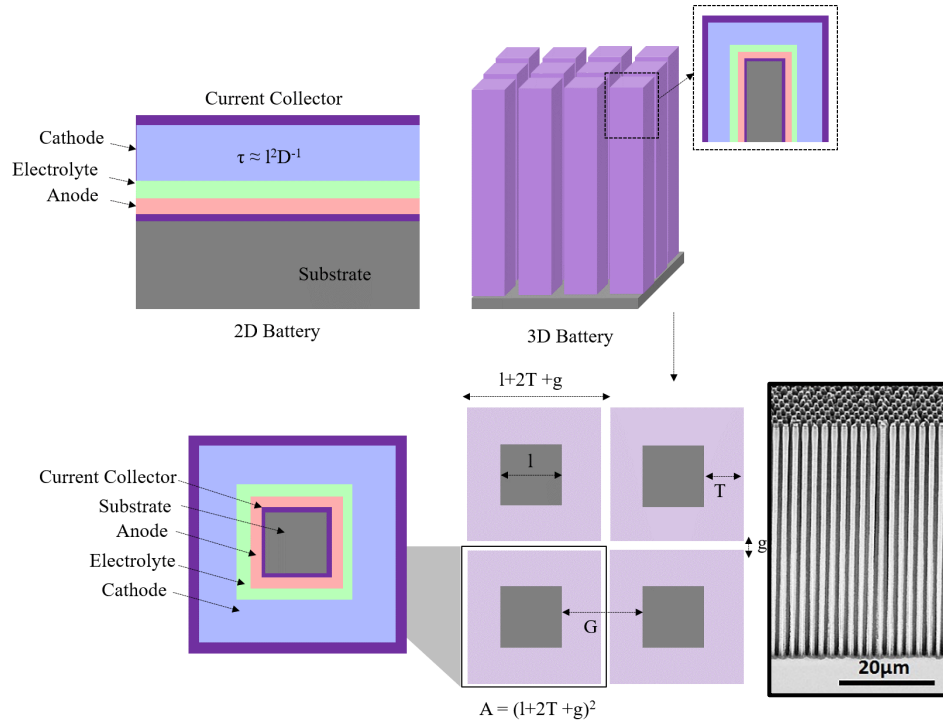
Figure 1-8. Schematics of 3D battery design where all battery material layers are deposited sequentially on a high-aspect ratio 3D structure, with an example 3D substrate fabricated with a modified BOSCH process demonstrating AR~50 Si micropillars (Chang 2018). Each pillar contains the following layers: substrate, current collector 1, anode, electrolyte, cathode, current collector 2. The anode is chosen for the inner electrode as it generally has a higher capacity than the cathode. The pillar width is given by l, T is the total thickness of all deposited layers, g is the final gap between the pillars post deposition, G is the gap before deposition, and A is the area of one repeating 3D pillar.

Two cases were considered: one in which the anode and cathode had equal volumetric capacities and the other, in which the anode volumetric capacity was 10 times higher than the cathode. A ten times higher volumetric capacity for the anode and cathode is not unreasonable when comparing the capacities of silicon (9,786 mAh/cm^3) vs. lithium cobalt oxide (~682

16

mAh/cm^3). Due to generally lowered capacities as compared the anodes, the cathode was chosen to be deposited as the second electrode so that more volume of material would be deposited for a given thickness. The thickness of both current collectors (t_{cc1}, t_{cc2}) were both set to be 15 nm and the solid electrolyte layer ($t_{electrolyte}$) 50 nm, to prevent discharge between the electrodes. 50 nm of lithium phosphazene film has previously been determined experimentally viable as a solid-electrolyte (Pearse 2018). The thickness of the cathode ($t_{cathode}$) was left as a variable, where the thickness of the anode (t_{anode}) was calculated to capacity match the cathode as shown in Figure 1-9 (d), where for a given cathode thickness, the deposited volume is dependent on the thickness of the underlying anode layer. The width of the pillars (l), the gap between pillars after deposition (g), and the height of the pillars (h) were left as variables. The total thickness (T) of the deposited layers is given in Eq. (1-25), in units of nanometers. The total area of one pillar is given by Eq. (1-26). The areal capacity solely based on the volume of the cathode ($V_{cathode}$) and the total area of one pillar is given in Eq. (1-27) with units mAh cm^{-2}. The focus on cathode thickness versus volume directly correlates to limitations in power density, but more crucially is the time limiting step during vapor phase deposition.

$$T = (t_{anode} + t_{cathode} + t_{electrolyte} + t_{cc1} + t_{cc2}) \qquad \text{(1-25)}$$

$$A = (l + 2T + g)^2 \qquad \text{(1-26)}$$

$$C_{areal} = (10^{-7})^2 \, (C_{cathode})(V_{cathode})(A_{pillar})^{-1} \qquad \text{(1-27)}$$

A volumetric capacity of 682 mAh cm^{-3}, was utilized based on 50% of the theoretical volumetric capacity of LiCoO$_2$. Instead of optimizing the 3D structure for the highest areal energy density which could potentially lead to structures not physically feasible—the effects of several variables

were explored, where values for other parameters were chosen for potential feasibility. Figure 1-9 (a) shows the areal capacity (mAh cm^{-2}) vs. cathode thickness for a 3D structure with $l = 1000$ nm and $g = 250$ nm—equating to a starting structure consisting of an array of 1 micron wide square pillars with a interpillar spacing that depend on thicknesses of the deposited layers, but at least 250 nm in width. The trends are plotted for two aspect ratios (10 and 100) and for two cathode/anode volume ratio's (C/A:1 and C/A:10), where the 3D structures outperform the 2D equivalent with higher achievable capacities associated with higher aspect-ratios. One potentially counterintuitive relation is the improved areal capacity with the lower C/A ratio. This is a direct result of an increased amount of cathode (total volume) deposited for a given cathode thickness, due to increased surface area of the 3D structure resulting from the thicker needed anode layer. Obviously, higher capacity anodes would produce higher overall areal capacities in a completely optimized structure, but this specific example illustrates the importance of these considerations when there exist limitations to the physical fabrications of these 3D devices. If the most time extensive step is the deposition of the two active materials, it is important to calculate the optimized structure based on both materials capacities. Figure 1-9 (b) is a plot of the areal capacity vs. the gap between the pillars post deposition (g) of all of the layers with a specified cathode thickness of 200 nm and a pillar width of 1 micron. As would be expected the areal capacity increased as g was decreased towards zero resulting in decreased void space in the 3D structure.
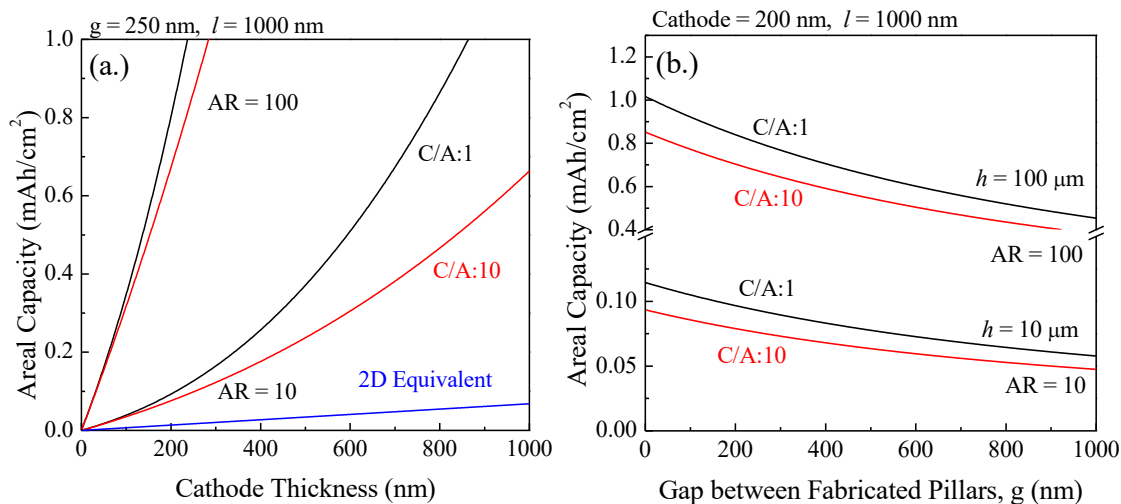
Figure 1-9. Analysis of 3D battery design parameters to achieve desired areal capacity: (a) The areal capacity vs. the cathode thickness for a 3D structure with l = 1000 nm and g = 250 nm. Since the kinetics are generally limited by the cathode thickness it was chosen as a variable to determine the effect on the areal capacity. The 3D structure quickly outperforms the 2D equivalent with increasing cathode thicknesses, where the effect is enhanced with increasing aspect-ratio of the 3D structures. (b) The effect of the gap between the pillar structures (post deposition of active materials) on the areal capacity for a cathode thickness of 200 nm and a pillar width of 1000 nm. As the gap between pillars decreases towards zero the areal capacity increases as expected with less unused void space.

Translating geometric calculations to actual fabrication is a significant challenge, but optimization of a pillar-type 3D structure is going to be highly dependent on host structure fabrication and feasibility (aspect ratio, pitch between pillars, width of pillars), the ability to uniformly coat the high aspect ratio structures, as well as material choice, where high capacity cathode materials are crucial.

1.4   3D Battery Demonstrations

The advantageous nature of 3D structured batteries has been demonstrated in many half-cell systems where thin film electrodes deposited across 3D structures exhibit significant improvements in areal capacity as compared to their 2D counterparts (Liu 2014, Dobbelaere 2016, Mattelaer 2017). More difficult, is successful full cell integration, where 3D structuring is required

of the anode, electrolyte, cathode, in addition to the electrical contact layers. A milestone for 3D

lithium-ion thin film batteries would be achieving an areal capacity of 1 mAh/cm^2 (Pearse 2018,

Moitzheim 2019) about an order of magnitude higher than current state-of-the-art thin film

batteries as shown in Table 1-1 (Ferrari 2015).

Table 1-1. Dimensions and areal capacity of commercialized thin film Li-
ion batteries. (Ferrari 2015)

Company	Anode/Cathode	Dimensions (cm) $t :w :l$	Areal Capacity (mAh/cm^2)
EnFilm	Li/LiCoO$_2$	0.02 : 2.54 : 2.54	0.109
IPS	Li/not specified	0.02 : 1.3 : 1.3	0.077
Exxallatron	Li/Si$_3$N$_4$/LiCoO$_2$	0.037 : 5 : 3.8	0.005 – 0.526

One of the first 3D thin film lithium-ion batteries was fabricated through physical vapor

deposition of the battery components on silicon trenches as the substrates. To fabricate the battery

structure, the following materials were deposited with: LiCoO$_2$ (cathode, 300 nm), LiPON

(electrolyte, 150-300 nm), and Si (anode 100 nm), where the device cross section is shown in

Figure 1-10 (a) (Talin 2016). The 3D structure outperformed the 2D counterpart at slow rates

(0.16C) but suffered a 90% capacity loss upon a modest increase in the rate (1.2C). Simulated Li-

ion concentration profiles are shown in Figure 1-10 (c), utilizing potential-dependent Butler-

Volmer kinetic models. Initially, due to the nonuniform thickness of the electrolyte, the

concentration of Li-ions increases in the electrolyte, then decrease in the cathode near the

electrolyte surface at the top of the microcolumns, where the distance between the anode and the

cathode is the shortest. As the charge process proceeds, this effect causes a reduction in the local

Li$^+$ flux into the cathode at the top of the pillar forcing Li-ions further toward the base of the

structure—producing a large potential drop across the electrolyte. It was concluded that the non-

uniform thicknesses of the deposited layers and the varying distances between the anode/cathode

led to its poorer electrochemical performance over an 2D equivalent structure (Talin, Ruzmetov et al. 2016).

Taking this same approach, Oleshko et al. synthesized a 3D solid state lithium-ion battery with subsequent sputter depositions of a TiN/Pt current collector, $LiCoO_2$ (cathode), LiPON (solid electrolyte), and amorphous silicon (anode) on a Si nanowire 3D host structure, where the full cell battery was on the order of 0.5 microns in diameter and 7 microns in length (Oleshko 2014). The directional nature of the deposition process coupled with a unique platelet-like microstructure formed upon annealing of $LiCoO_2$ (as shown in Figure 1-10) produced void formation within the battery significantly reducing the electrochemical performance (Oleshko 2014), illustrating the vital importance of the electrode/electrolyte interface especially in regard to development of 3D structures.
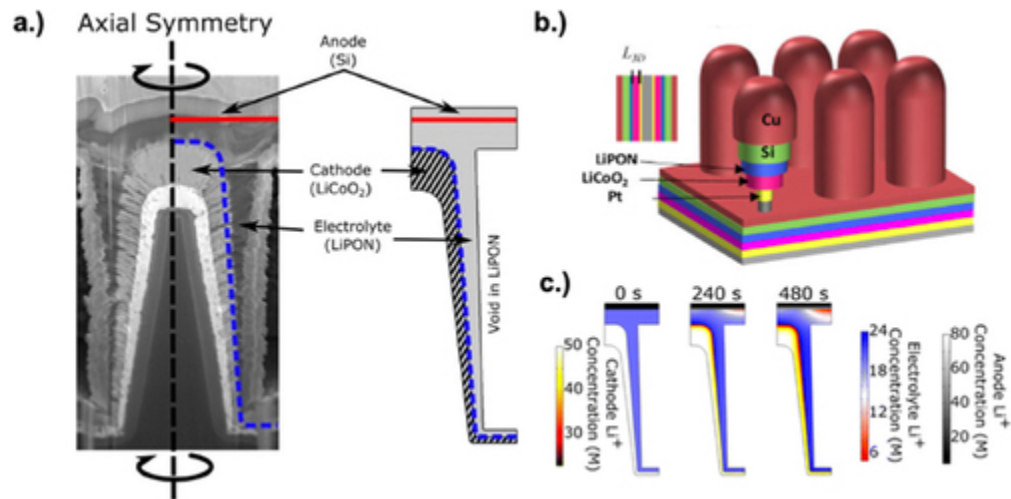
Figure 1-10.   (a) An SEM cross-section of an all-solid-state thin film battery fabricated via physical vapor deposition on a 3D Si trench structure. (b) Schematic of the various components that make of the solid-state thin film battery. (c) Simulation of the Li-ion concentration profiles as in the electrolyte, cathode, and anode, as a function of time of charge. (Talin 2016)

To combat the issue of non-conformal contact between all battery materials, Pearse et al. developed an all ALD 3D solid state microbattery consisting of an SnN_x cathode, a lithium

phosphazene solid electrolyte, aV_2O_5 cathode, and TiN/Ru current collectors (Pearse 2018), where the process flow is shown in Figure 1-11. Although they showed significant improvements in the 3D thin film battery over the corresponding 2D thin film system of the same material components, they were unable to surpass the areal energy density of commercial 2D thin film batteries synthesized via physical vapor deposition. The limited areal energy density performance was partially due to material selection along with the large void space in the 3D pore structure. V_2O_5 is a less energy dense (lower capacity and nominal voltage) cathode as compared to other more traditional cathode materials and must be lithiated electrochemically (solution phase) causing an interruption in the otherwise all vapor phase (without vacuum break) deposition process.
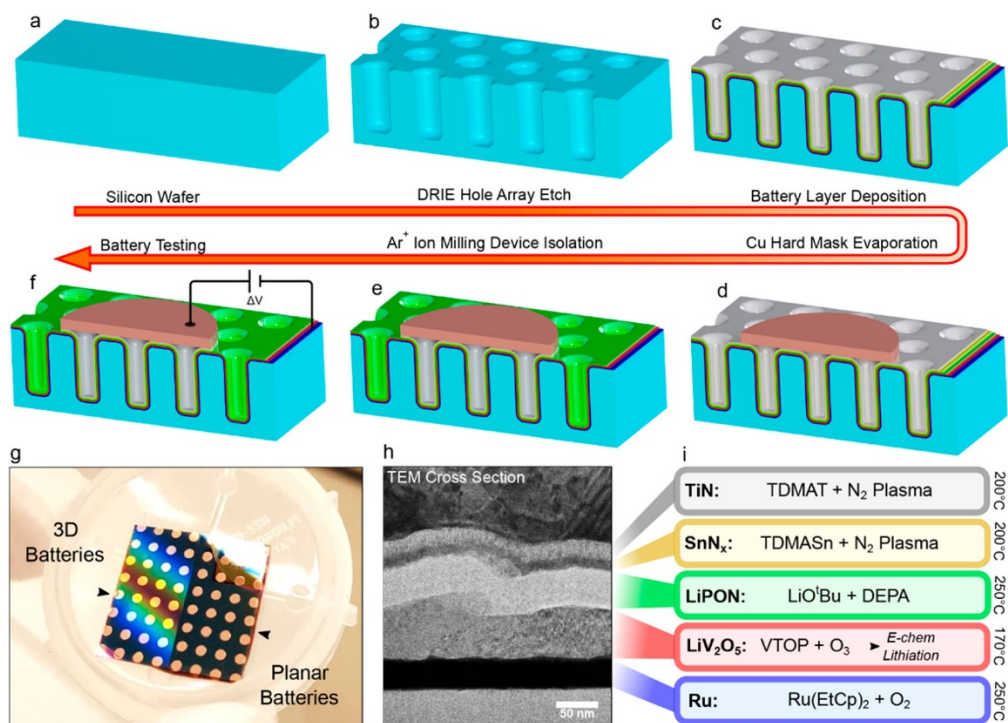
Figure 1-11. Fabrication Scheme utilized to synthesize 3D solid-state thin film batteries via atomic layer deposition (a-f). The 3D host structure was fabricated via a combination of photolithography and reactive ion etch to form the pored structure with various aspect-ratios. Atomic layer deposition was then utilized to deposit the subsequent materials (Ru: current collector, V_2O_5: cathode, LIPON: electrolyte, SnN_x: anode, and TiN: current collector). The ALD V_2O_5 layer was lithiathed electrochemically in solution phase prior to deposition of the other material layers. (g) shows the finished 3D battery "chip", where (h) shows a cross-sectional TEM image of the ALD layers with chemical description presented in (i). (Pearse 2018)

The device fabricated by Pearse et al., is an impressive starting point for further 3D thin film lithium-ion battery development based on a 3D host structure and conformal deposition of the battery relevant material layers. The next section discusses a conformal deposition technique, atomic layer deposition, as a means for development of highly functional materials that can be directly integrated into 3D structures.

1.5   Atomic Layer Deposition for Realizing 3D Thin Film Lithium-ion Microbatteries

Atomic layer deposition (ALD) offers compositional and angstrom level thickness control of a wide variety of metals, oxides, iodides, phosphides, carbide, selenides, fluorides, phosphates, sulfides, and nitrides finding wide applicability in the fields of energy storage, CMOS devices, optoelectronics, non-volatile memory, and photovoltaics. (Lim 2003, Kim 2009, Klug 2011, Delft 2012, Marichy 2012, Johnson 2014, Mattelaer 2017, Yang 2017, Zardetto 2017, Mallick 2019, Popov 2019). Atomic layer deposition offers significant advantages over other traditional vapor phase deposition techniques such as physical and chemical vapor deposition, due to its ability to form continuous and conformal pinhole free films on high aspect ratio structures, often at significantly lower substrate temperatures. There exist several types of atomic layer deposition processes, with the most common being thermal ALD, in which the substrate is heated to promote the self-limiting reaction. Alternatively, plasma enhanced atomic layer deposition (PEALD) employs plasma species as one of the reagents. Due to highly energetic species generated in the plasma (ions, neutrals, metastables, and electrons), ALD at lower temperatures with a wider processing window can often be realized. (Chang 2017)

Atomic layer deposition is characterized by a process of alternating self-limiting half reactions (Figure 1-12). An ideal ALD process consists of: (1) vapor phase introduction of the first reactant to the reactor allowing for all available surface sites to undergo a self-limiting reaction, (2) removal of all unreacted precursor vapor in the reactor via a purge step generally with an inert gas, (3) the second reactant is introduced to the reactor and allowed to react with all available surface sites to undergo a self-limiting reaction, and (4) the second reactant is then pumped out of the reactor and cycle can then be repeated to grow the desire film thickness. This process is

demonstrated in Figure 1-12 for the ALD growth of LiOH, in which lithium tert-butoxide and water are used as the two coreactants.
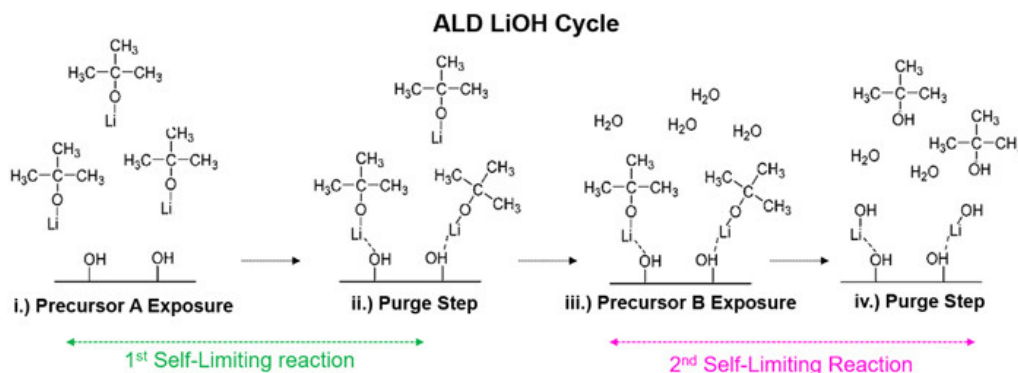
Figure 1-12. Atomic layer deposition process and reaction schemaitc for LiOH. (i.) lithium tert-butoxide (LiO^{t}Bu) is delivered to the system and undergoes a self-limiting half-reaction with surface hydroxyl groups. (ii.) unreacted LiO^{t}Bu as well as volatile reaction products are removed from the system and purged with a nonreactive gas. (iii.) H_2O is delivered and undergoes a self-limiting surface reaction. (iv.) Unreacted H_2O as well as volatile reaction produces are purges from the system. Steps 1 through 4 can be repeated until the desired film thickness is deposited. Adapted from (Cho 2016).

A characteristic ALD process demonstrates self-limiting growth across a range of temperatures deemed the "ALD temperature window". Changes to growth behavior outside of this processing window can be due to issues such as precursor condensation, limited reaction kinetics, precursor decomposition, or increased substrate desorption. Non-idealities can also occur for a given ALD process when the decomposition temperature is close to the temperature needed for the surface reaction to proceed, in addition to incomplete reaction of the chemical precursor leaving behind unwanted contaminations (Elam 2003, Zaera 2012). Processes for individual ALD grown materials can be combined to deposit more complex materials systems, if the temperatures windows for each individual process overlap. Altering the ratio of ALD cycles of each respective process allows for fine tuning of the overall composition in the deposited film. The self-limiting nature of the chemical reaction during each half cycle allows for conformal deposition on complex

3D hierarchal structures, where aspect-ratios as high as 5000:1 have been demonstrated (Elam 2006, Cremers 2019), but it should be noted that large quantities of precursor and excess process times are generally needed to conformally coat these high aspect-ratio structures.

In rechargeable lithium-ion batteries, atomic layer deposition has been applied to the synthesis of wide range of battery materials—electrolyte, active material, and current collectors, along with engineering interfacial surface coatings, which is discussed further in the next subsections, where a summary of various materials is presented in Figure 1-13. Although clearly a wide range of Li-containing materials has been demonstrated via ALD, various nonidealities in processing have made synthesis of complex materials with multiple atomic constituents not as straight forward. Some of these issues stem from non-surface-limited reactivity of specific precursors, high mobility of Li-ions, the hygroscopic nature of LiOH, the monovalency of lithium, and ambient reactivity making the growth process difficult to characterize without *in situ* techniques and difficult to control the properties of the thin films.(Nilsen 2014, Ruud 2017).
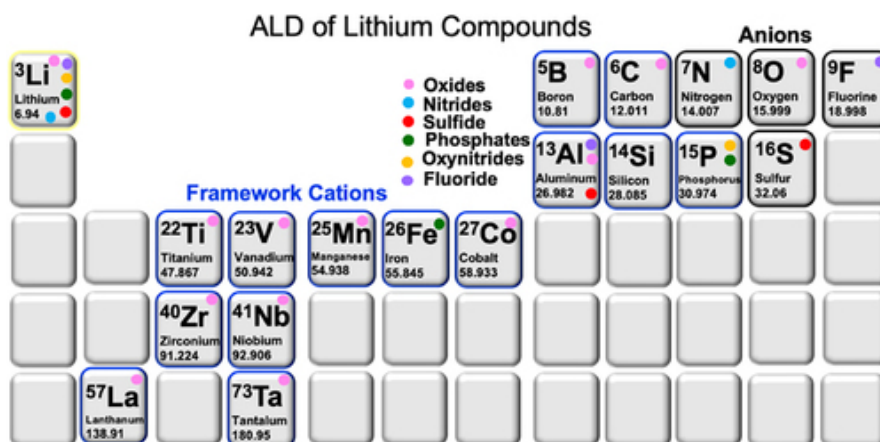
Figure 1-13. Periodic table highlighting lithium containing materials synthesized via atomic layer deposition. The materials can be characterized by various anions: oxides, nitrides, sulfides, phosphates, oxynitrides, and fluorides, listed with corresponding framework cations.(Sheil 2020)

Another limitation of ALD as compared to other vapor deposition techniques is the inherently slower growth rate, especially crucial for thin film batteries, where the areal energy density is related to the electrode thicknesses. This can be somewhat mitigated through transition to a spatial atomic layer deposition (sALD) process, in which chemical precursors are separated via an inert gas curtain and the sample is rapidly translated between the two precursor regions significantly speeding up deposition times. Spatial-ALD for 3D battery applications was recently explored for the optimization of precursor dose to assess conformality of Cl-doped TiO_2 on high aspect ratio structures (Moitzheim 2019). The high surface area/ large aspect ratio structures required of 3D thin film microbatteries (3D TFMB's) produces a trade-off in that high surface area is advantageous in that it corresponds to larger deposits of active material per ALD cycle, but a large aspect ratio also has a deleterious effect in that it may require much large precursor exposure times to ensure complete surface reaction. In the subsequent sections a review of materials (cathodes, anodes, and electrolytes) is given with specific focus on the state-of-the-art materials synthesized via atomic layer deposition for lithium-ion batteries

1.6   Cathode Materials for Li-ion Batteries

Since the inception of the solid-state 3D battery, the necessity to develop an ultra-thin solid electrolyte layer was clear, which has led to significant research effort over the last decade. Beyond the electrolyte layer equally crucial is the ability to deposit electrode materials (either the anode or cathode) with optimal interfacial properties to ensure homogeneous active material utilization, adequate cycle-life, and high rate performance. Furthermore, utilization of 3D battery architectures with high surface area allows for much thinner active materials layers for a given areal energy density allowing for high rate ability due to short Li-ion diffusion distances. This improvement is critical for the cathode material which generally needs to be much thicker than the anode to

27

compensate for the capacity discrepancy between the materials. Reduction in film thickness has shown to dramatically increase the rate-ability in thin film $LiMn_2O_4$, where similar effects have been also observed in other nanostructures such as nanoparticles and nanowires (Put 2015). The development and characterization of thin film electrode and electrolyte materials as well as their integration in 3D solid state batteries offers a unique opportunity to better understand materials specific properties applicable to batteries of all scales as well as study the unique phenomena that may arise during utilization in a complex geometry.

Lithium Cobalt Oxide ($LiCoO_2$) first demonstrated by Goodenough (Mizushima 1980) was one of the enabling materials for the mobilization of hand held electronics and has remained the most commonly used cathode materials today, due to its high theoretical gravimetric capacities and inherent cycling stability. The main drawbacks of $LiCoO_2$ are its low thermal stability and the high cost of cobalt, where nickel and manganese-based oxides have been studied as alternative materials. Substitution of Co with other transition metals in the layered $LiCoO_2$ structure such as $LiNi_{0.8}Co_{0.15}Al_{0.05}O_2$ (NCA) and $LiMn_{1/3}Ni_{1/3}Co_{1/3}O_2$ (NCM) help to stabilize the overall structure during continual charge and discharge allowing for higher achievable experimental capacities. $LiMn_2O_4$ is cheaper and less toxic alternative to cobalt containing oxides, but Mn^{2+} dissolution in the liquid electrolyte causes short cycle life, an issue that can be potentially mitigated in solid-state batteries (Nitta 2015). Stoichiometric lithium-rich manganese oxide spinels, $Li_{1+x}Mn_{2-x}O_4$, where $x \leq 0.33$ exhibit improved performance as compared to $LiMn_2O_4$, where lithium substitution in the octahedral Mn sites promote increased cycling stability due to suppression of both the Jahn-Teller distortion upon deep discharge as well as the Mn^{3+} disproportionation reaction. This improvement in cycling stability must be weighed against the decrease in theoretical capacity in the 4.0V region as the manganese ions become tetravalent to maintain charge neutrality (theoretical capacity of

154 mAh/g, where x=0)(Gummow 1994). Substituted spinel structures such as $LiMn_{2-x}M_xO_4$ (M= Co, Ni) are materials of interest due to their high discharge voltage (~5V), where the specific stoichiometry of $LiMn_{1.5}Co_{0.5}O_4$ has been shown to exhibit improved energy density.(Mukai 2017) One of the biggest limitations in the commercial utilization of these 5V cathodes is electrolyte instability (Thackeray 2018), while this presents a challenge in liquid based systems, thin film solid state electrolytes have been shown to be stable at these higher voltages (Kazyak 2018). Another group of materials termed: *layered-layered* $(xLi_2MnO_3(1-x)LiMO_2$, (M=Mn, Co, Ni)) are of particular interest to stabilize the layered structure upon lithium extraction, where for instance $Li_{1-x}CoO_2$ is stable up to x=0.5 (capacity ~140 mAh/g) before damaging structural changes start to occur reducing cycle stability.(Thackeray 2018)

Lithium metal phosphates, such as $LiFePO_4$, have been also widely used as lithium-ion batteries due to their excellent cycling stability, but are limited in capacity. Due to the increased electronegativity of the PO_4 group they generally exhibit higher operating voltages as compared to their oxide counterparts (Liu 2016). The biggest drawback to these materials is there lower electrical and ionic conductivities that severely limit their rate ability (Nitta 2015). V_2O_5 cathode materials are of interest for lithium-ion batteries due their ability to uptake more than one lithium ion. The associated structural changes associated with three separate lithium-ion insertions lowers the cycling stability, where if more stable conditions are used lower operating voltage limits their achievable energy density (Whittingham 2004). Conversion type cathodes such as Li_2S, S, and O_2, have been proposed as next generation lithium-ion battery cathodes offering significant capacity improvements, but there are many engineering obstacles (irreversibility, Li_2S shuttling etc.) to overcome to realize such materials (Xu 2013). A brief summary of reported lithium-ion battery

cathodes is shown in Table 1-2, which presents theoretical and experimentally-achieved capacities

(Nitta 2015).

Table 1-2. Electrochemical properties of common cathode materials, adapted from (Nitta 2015)

Structure	Material	Theoretical Volumetric Capacity (mAh/cm^3)	Theoretical Gravimetric (Experimental) Capacity (mAh/g)
Hexagonal (Layered)	$LiCoO_2$	1363	274 (148)
	$LiNiO_2$	1280	275(150)
	$LiMnO_2$	1148	285(140)
	$LiMn_{1/3}Ni_{1/3}Co_{1/3}O$	1333	280(160)
	$LiNi_{0.8}Co_{0.15}Al_{0.05}O$	1284	279(199)
	Li_2MnO_3-$LiMnO_2$	1428	382(>250)
	Li_2MnO_3	1708	458(180)
Spinel	$LiMn_2O_4$	596	148(120)
	$LiMn_{1.5}Ni_{0.5}O_4$	669	147(130)
Olivine	$LiFePO_4$	589	170(165)
	$LiMnPO_4$	567	171(168)
	$LiCoPO_4$	510	167(125)

Several thin film cathode materials have been synthesized via ALD including: $LiCoO_2$, $LiMn_2O_4$, VO_2, V_2O_5, $LiFePO_4$, each with their unique benefits as well as inherent material limitation and processing challenges (Miikkulainen 2014) (Chen 2012, Donders 2013, Liu 2014, Østreng 2014, Mattelaer 2016, Mattelaer 2017, Pearse 2018) summarized in Table 1-3. Crystalline and amorphous vanadium oxides ($Li_xV_2O_5$ and Li_xVO_2) are promising due to their potential to undergo multiple lithiation steps, but generally suffer from cycle instability at higher amounts of lithium intercalation and possess lower capacities than the other metal oxide cathodes. $LiFePO_4$ is another promising cathode material synthesized via atomic layer deposition due to its long-term cycling stability and lox toxicity but has a lower average operating voltage as well as capacity as compared to layer oxide and spinel cathodes. $LiCoO_2$ thin films have been synthesized through

plasma enhanced atomic layer deposition (PEALD), but the deposited materials demonstrated limited capacity, most likely due inability to control the stoichiometry (Donders 2013). $FePO_4$ has also been synthesized via PEALD, where once deposited was electrochemically lithiathed to form the electrochemically active $LiFePO_4$ and demonstrated on a 3D structure. (Dobbelaere 2016). $LiMn_2O_4$ was demonstrated, in which ALD MnO_2 was surface treated with a lithium precursor to form the spinel $LiMn_2O_4$ films (Miikkulainen 2014). ALD deposited Li_2S demonstrated a high lithiation capacity of 500 mAh/g over 500 cycles at 0.72C (Meng 2014). Sulfur based materials although demonstrate high capacities have long term stability issues in full cell set-ups. In addition, sulfides present difficulties in processing, due to their chemical sensitivity in ambient atmosphere along the dangers associated with utilizing H_2S as chemical precursor in their synthesis via ALD.

Table 1-3. Literature reported thin film cathodes deposited via ALD.

Material	Structure	Number of Cycles	C-Rate	Capacity (μAh cm^{-2} μm^{-2})	Reference
$LiCoO_2$	Polycrystalline	13	0.35C	25	(Donders 2013)
$LiMn_2O_4$	Polycrystalline	10	3C	57[a]	(Miikkulainen 2014)
Li_2S	Amorphous	500	0.72C	83[b]	(Meng 2014)
VO_2	Amorphous	50	1C	140	(Mattelaer 2017)
V_2O_5	Amorphous	50	1C	49	
$LiFePO_4$	Polycrystalline	200	1C	21	(Dobbelaere 2016)

[a]Only considering 4V region, [b]Average voltage ~2.2V vs. Li/Li^+

Due to the inherent control over composition, atomic layer deposition is a unique tool to explore various compositions of lithium manganese oxides as well as lithium cobalt oxides and their corresponding structural and electrochemical properties for the development of high-performance thin film cathodes. A specific focus is the controlling of the stoichiometry of $Li_{1+x}Mn_{2-x}O_4$ for improved cycle life as well as capacity in the 4.0V region. In this work, a generalized approach was taken via incorporation of a PEALD process for MnO_2 and Co_3O_4 with the thermal ALD process for LiOH to form complex metal oxides applicable to incorporation of other transition row metal oxides. Due to the high reactivity of plasma species, plasma-enhanced

atomic layer deposition offers generally a wider processing window making the process more compatible with other ALD processes that may have varying temperature windows as well induce crystallization in some cases (Schindler 2016).

1.7   Anode Materials for Lithium-ion Batteries

Significant development has been performed in the discovery and optimization of new anode materials with high energy density. Li metal serves as the upper limit in capacity and lower limit in operating voltage and therefore acts as the standard of comparison in comparing next generation anodes. Lithium metal presents many difficulties in integration for liquid based Li-ion batteries due to safety concerns but has been deemed as an ideal candidate for solid state batteries. Beyond Li metal, the wide range of anode materials can be classified by their lithiation mechanism (shown in Table 1-4) where example lithiation reactions are presented in Eq. (1-28), Eq. (1-29), and Eq. (1-30).

Intercalation anodes are the most commonly used materials due their excellent cycling stability and negligible volumetric changes during the lithiation and delithiation reactions. Graphitic based anodes have been most commonly utilized in conventional lithium-ion batteries, where the intercalation reaction for graphite is shown in Eq. (1-28).

$$C_6 + Li^+ + e^- \leftrightarrow LiC_6 \qquad \text{(Intercalation)} \qquad (1\text{-}28)$$

Intercalation of ions into the graphite is generally categorized by "stages", in which intercalation between every layer is termed 1st stage, where the n stage terminology is used where n is the number of graphite layers between intercalant layers. The bond in lithiated graphite is ionic in nature, further supported by the low volume expansion associated with intercalation, the higher electrical conductivity of lithiated graphite, as well as the in-plane ordering of lithium atoms suggesting some coulombic interaction between neighbors (Gholam-Abbas and Gianfranco 2009).

Graphite's 2s and 2p orbitals make up its valence band, consisting of pi bonds coming from $2p_z$ orbtials along the c-axis giving rise to delocalized pi electrons. Upon intercalation of lithium-ions into graphite, graphite acts as an electron acceptor, where some of the Li 2s electron density is delocalized, the antibonding pi orbital's of graphite can accept an electron (conduction band), in which the Fermi level is raised accordingly. The interaction generates ionic bonding between layers and produces high mobility of charged carriers in LiC_6 (Kganyago 2003). Carbon based electrodes can be generally characterized as soft carbons (graphitic) with an ordered layer structure and hard carbons that exhibit a more disordered structure. Hard carbons generally offer higher capacity (~500 mAh/g), but poor rate ability due to the disordered structure, which has solidified graphite as the most commonly used carbon based anode (Goriparti 2014, Yao 2015). Nansotructured carbons have also gained much interest such as carbon nanotubes. The theoretical capacity of single walled carbon nanotubes is ~1000 mAh/g corresponding to a Li_2C stoichiometry, coupled with their high electrical conductivity making them ideal candidates for 3D structure batteries. Other intercalation anodes of interest are $Li_4Ti_5O_{12}$ and TiO_2, which exhibit moderate lithiation capacities and exhibit low volume expansion upon intercalation of lithium. Their slightly higher operating potential gives them the added safety and cycling stability (1.5V vs. Li/L^+) through reducing SEI formation, but at the cost of decreased energy density. Furthermore, Li diffusivity and electrical conductivity (10^{-13} S/cm) severely limit their rate ability (Zhu 2013, Goriparti 2014).

Alloying type electrodes such as silicon, germanium, aluminum and tin have been deemed next generation electrodes exhibiting the highest theoretical lithiation capacities as much as 10 times larger than traditional intercalation anodes. This class of materials is characterized by the alloying

reaction that occurs upon lithiation where the crystalline anode forms an amorphous lithium alloy phase as shown in Eq. (1-29).

$$4Si + 15Li^+ + 15e^- \leftrightarrow Li_{15}Si_4 \qquad \text{(Alloying)} \qquad (1\text{-}29)$$
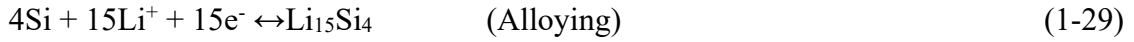
The largest obstacle to their commercialization is the large volume expansion/contraction that occurs during the charge/discharge cycling leading the mechanical fracture, loss of current collector contact, and capacity fade (Ashuri 2016) as shown in Figure 1-14. This large volume expansion also leads to SEI instability issues that cause capacity fade through mechanical cracking of the SEI layer in addition to the increased exposed electrode surface areas during expansion events leading to additional electrolyte degradation. These engineering obstacles have been tackled in a variety of ways including nano-structuring (Cho 2013), porous structuring (Ikonen 2017), and synthesis of composite structures (Kim 2016), where the sources listed are only one example from the vast amount of scientific throughput dedicated to optimizing these materials.
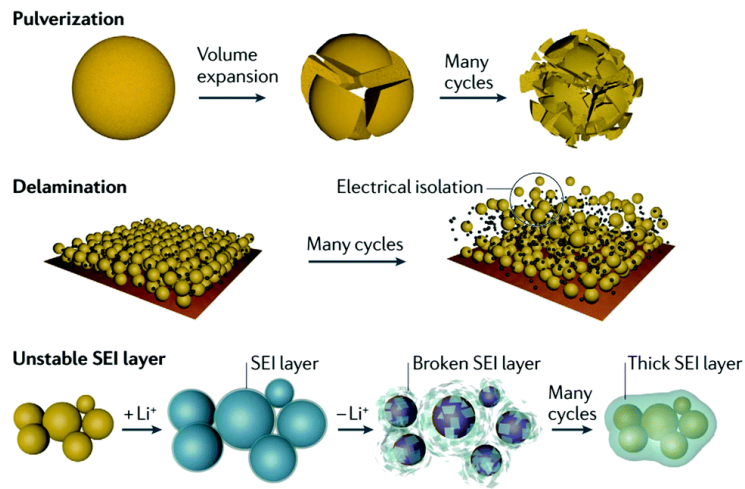
Figure 1-14. Illutration of issues in alloying anodes associated with volume expansion on contraction during the lithiation and delithiation. Some of the issues include pulverization of the material resulting in electrical isolation, delamination from curret collectors, as well as continaully broken and reformed solid-electrolyte interphase formation (SEI) resulting in low coulombic efficiencies. (Choi 2016)

Out of all of the alloying type anodes, silicon has garnered the most significant research effort in its development as it exhibits the highest gravimetric and volumetric lithiation capacity along with its natural abundance. In bulk silicon, lithium diffusion limits the homogeneity of the lithiation reaction causing the outermost regions to readily uptake lithium, where the large volume expansion localized to the surface region of the electrode causes fracture of the bulk structure (Soni 2012, Mcdowell 2013). Using In-situ TEM techniques where lithiation and delithiation can be directly observed in real time gives a unique perspective to understand the dynamic changes undergone in nanostructure electrodes, as illustrate in Figure 1-15, where large volume expansion is observed during the potentiostatic lithiation of a Si nanowire (Liu 2012). Despite the inherent difficulties associated with Silicon based electrodes various nanostructure and composites have exhibited >1000 mAh/g over a significant number of charge/discharge cycles (Zuo 2017).
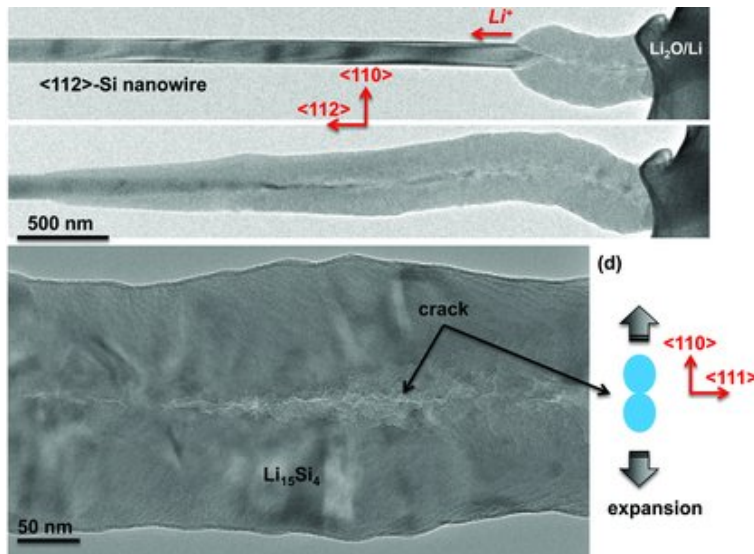
Figure 1-15. In-situ TEM characterization of Si Nanowire during potentiostatic lithiation, where the large volume expansion can be observed as the lithiation front proceeds, leading to cracking due to hoop stress (Liu 2012)

Germanium is another interesting material exhibiting higher Li^+ diffusivity and electrical conductivity than silicon, in addition to undergoing an isotropic lithiation process in nanowire form (Lee 2015), but is significantly more expensive limiting its use in large scale applications (Tian 2015). Regardless, it offers a higher Li-ion diffusivity as compared Si (~400 times) (Fuller 1954, Chockla 2012, Li 2012) Lastly, Sn is another alloying material that has gained significant research with its large theoretical lithiation capacity (960 mAh/g), but the >300% volume expansion has significantly limited its use, where even in nanoparticle form mechanical pulverization upon cycling has been observed (Wang 2014).

Conversion anodes are of have gained research interest due to their increased lithiation capacity as compared to intercalation compounds generally exhibiting >2x that of graphitic electrodes (See Table 1-4), in addition to providing increased safety due to their slightly elevated operation voltage (~0.5-1.0V). Upon lithiation the metal oxide is reduced leaving the metal in a matrix of Li_2O according to Eq. (1-30). Their low electrical conductivity and large volume expansion upon lithiation has limited their use on the bulk scale, but promising results have been demonstrated for various nanostructures.

$$Co_3O_4 + 4Li^+ + 4e^- \leftrightarrow 3Co + 4Li_2O \qquad \text{(Conversion)} \qquad (1\text{-}30)$$

FeO, Fe_2O_3, and Fe_3O_4 are promising conversion anodes with high capactites (745, 1007, 924 mAh/g, respectively), high natural abundance, low cost, and low toxicity (Xu 2012, Goriparti 2014). They suffer from poor electrical conductivity, low lithium diffusivity, volume expansion, and Fe particle aggregation during charge, where most research has been to improve these properties through nanostructuring or engineering composite materials (Goriparti 2014). For example, coating iron oxide nanostructures with a CVD graphitic carbon coating showed promising improvements in capacity fade demonstrating >500mAh/g capacities over 300 cycles

(Chunyan 2017). Another noteworthy material is SnO_2, which uniquely undergoes a two-step mechanism. Upon the initial lithiation cycle the material undergoes the conversion reaction to form Li_2O and Sn, but on subsequent cycles the Sn is lithiated in an alloying reaction to form $Li_{4.4}Sn$ (Cao 2017). Due to this two-step reaction process, large irreversible capacity loss accompanies the Li_2O formation, where reversibility is only regained on the second charge cycle.

CoO and Co_3O_4 nanostructures have also spurred much research interest due to their higher capacity (716, 891 mAh/g, respectively) as compared to traditional intercalation anodes. Using in situ TEM it was observed that Co_3O_4 nanoparticles upon discharge show preferred oxidation to CoO rather than Co_3O_4, where 2 Li^+ per Co_3O_4 are irreversibly lost on the first cycle in the form of Li_2O (Su 2014), potentially making CoO a more ideal anode candidate. Recently, CoO nanofibers demonstrated capacities ~800 mAh/g over 125 cycles at 1C (Liu 2017). One of the biggest drawbacks to conversion type anodes is the voltage hysteresis (charge and discharge profiles dissimilar), where the discharge profile is shifted to a higher potential leading to limited energy efficiency. Moving to nanoscale structured anodes with increased surface sites (higher reactivity) in addition to shorter Li-ion diffusion distances may help partially mitigate the voltage hysteresis on discharge due to the improved kinetics (Cao 2017). A summary of various anode materials and their properties are given in Table 1-4.

Table 1-4. Electrochemical properties of common anode materials.

Class	Anode	Theoretical Capacity (mAh/g)	Volume Expansion	Ref
Alloying	Si	3579	300%	(Zhang 2011)
	Ge	1384	270%	(Zhang 2011)
	Al	993	100%	(Zhang 2011)
	Sn	960	360%	(Zhang 2011)
	Sb	660	135%	(Zhang 2011)
Intercalation	Graphite	372	12%	(Zhang 2011)
	[1]TiO_2	335	3%	(Zhang 2017)
	$Li_4Ti_5O_{12}$	175	1%	(Zhang 2011)
Conversion	Fe_3O_4	928	-	-
	Co_3O_4	891	-	-
	CoO	716	-	-
	[2]SnO_2	711	360%	(Cao 2017)
	[3]ZnO	987	228%	(Cao 2019)

The atomic layer deposition of anode materials has been primarily focused on metal-oxides. The first ALD anode materials were TiO_2 and SnO_2. Amorphous TiO_2 deposited on a 3D network of carbon nanowires demonstrated a capacity of 309 mAh/g at 0.2C over 213 charge/discharge cycles and maintained a 214 mAh/g capacity over 2000 cycles at 10C (Wang 2015). Amorphous ultra-thin ALD SnO_2 showed improved electrochemical behavior over its bulk counterpart most likely due to increase structural stability. ALD SnO_2 deposited on a 3D Nickel foam current collector, reduced graphene oxide (r-GO), and MXlene substrates demonstrated >500 mAh/g (Haag 2013, Xie 2015, Ahmed 2017). The molecular layer deposition of litium terephtalate thin film anodes was demonstrated showing a lithiation capacity of roughly 350 mAh/g. Coupled with the ALD solid electrolyte thin-film, LiPON, the electrode maintained 97% capacity retention at 3.2C over 200 cycles (Nisula 2016). Additionally, the atomic layer deposition of $Li_4Ti_5O_{12}$ was also demonstrated showing very high rate ability (100C) and a lithiation capacity

of ~120 mAh/g (Wang 2017). More recently, Cl-doped TiO_2 was deposited on a high aspect ratio scaffold via sALD exhibiting areal capacities > 225 µAh cm^{-2} (Moitzheim 2019). Lastly a ZnO/TiO_2 nanolaminate anode was fabricated via atomic layer deposition that showed improved cycle life and capacity then a uniform ZnO film, exhibiting a capacity of 667 mAh/g (Cao 2019).

One of the largest bottlenecks in the development of all solid-state batteries is in limited ion transport across the electrolyte/electrode interface. The interface quality, highly dependent on material choice and the synthetic route can be a determining performance factor, where non-ideal contact between the solid electrolyte and electrode layers can lead to high interfacial resistance significantly decreasing electrochemical performance (Santhanagopalan 2014, Yu 2017). In the context of 3D solid state batteries, the increased interfacial area makes the solid electrolyte/electrode interface even more crucial. (Ruzmetov 2012). Furthermore, as can be seen in Table 1-4, critical for solid state systems is the accommodation of stresses induced through expansion and contraction of both electrodes during operation with generally higher energy density materials exhibiting larger expansions (Si: ~300%, Ge: 270% Sn: 360%). For example, implementation of a thin ALD solid electrolyte layer was shown to pulverize upon the large volume expansion of a SnO_2 nanowire (Zhang 2012). The next section's focus is on state-of-the-art solid-state electrolytes and some of the challenges associated with their integration with 3D solid-state lithium-ion batteries.

1.8   Electrolyte Materials for Li-ion Batteries

An ideal solid electrolyte material for thin film lithium-ion batteries exhibits high ionic conductivity, a wide electrochemical stability window, be pinhole free and prevent leakage current between the anode and cathode, possess suitable mechanical properties for integration with high volume expansion anodes, and lastly be able to be conformally coated on high aspect-ratio

structures. The ionic conductivity is the key metric in electrolyte performance, where higher values lead to improved power densities allowing for quicker charge and discharge. For thin film batteries an ionic conductivity of 10^{-6} S/cm is the state-of-the-art and adequate at thin electrolyte thicknesses, but continued improvement is key to improve device performance.(Bates 1992, Bates 1993, Talin 2016) Due to the large volume expansion and contraction during lithiation and delithiation of high capacity anodes, in addition to dendrite formation in lithium metal anodes, the mechanical properties such as elastic modulus, shear modulus, and the critical tensile strain of the electrolyte should be considered in material design. Delineating thickness effects on specific material properties, especially when scaling down the electrolyte thickness should be considered as significant effects have been observed in ALD thin films (Jen 2011). Specific target metrics should be determined based on materials integration with other battery components, where for instance a low value for the elastic modulus may be preferred for integration with alloy-based anodes, but high values for the shear modulus may be desired when integrating with lithium metal to prevent lithium dendrite penetration.

1.8.1   Electrochemical Stability Window and the Solid Electrolyte Interphase (SEI)

The ideal electrolyte candidate is chemically stable over the voltage range during charge and discharge of the device. When the lowest unoccupied molecular orbital (LUMO) of the electrolyte falls below the chemical potential of the anode during charging, the electrolyte is reduced at the anode surface. Furthermore, if the highest occupied molecular orbital (HOMO) falls above the chemical potential of the cathode during charge, the electrolyte is oxidized at the cathode surface. For the most commonly used liquid electrolytes consisting of lithium salts (ex. $LiPF_6$) in organic solvent electrolyte breakdown does occur particularly on the anode surface. The breakdown of the electrolyte at the electrode surface is termed the solid electrolyte Interphase

(SEI) layer and is common place in the majority of lithium-ion batteries playing a significant role in their safety, power density, and cycle life (Peled 2017). The SEI layer consists of inorganic compounds such as Li_2O, LiF, $LiCl$ and organics originating from the breakdown of salt anions, solvent, and from any additional impurities within the electrolyte (Peled 2017). SEI formation generally occurs upon the first cycle and leads to an overall reduction in capacity correlated with the electrode surface area. A stable SEI layer must have the following properties: (1.) low electrical conductivity, (2.) resistive to electrolyte diffusion (3.) selectively conductive to Li-ions. Once the SEI fully covers the anode surface, ideally its growth should be self-limiting. In an ideal case where electrons cannot penetrate the SEI layer to further degrade the electrolyte, the resulting surface potential of the electrolyte is shifted within that stability window of the electrolyte (An 2016). No SEI layer completely possesses these ideal properties leading to continual (although slower) growth with continuous charging/discharging leading to a capacity fade over time. Furthermore, expansion and contraction of the electrode during charge/discharge can cause breaking in the SEI layer exposing more anode surface to electrolyte breakdown. The associated issues with SEI formation have driven research towards the use of solid electrolytes with potentially improved electrochemical stability to improve the overall cycling stability of the electrodes.
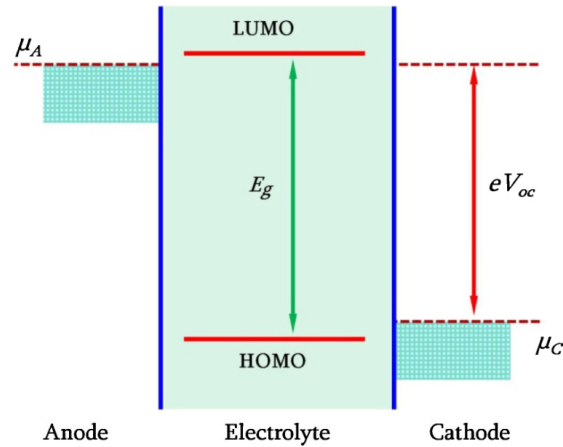
Figure 1-16. Illustration of an electrochemical stability window of an electrolyte. When the lowest unoccupied molecular orbital (LUMO) of the electrolyte falls below the chemical potential of the anode during battery usage, the electrolyte is reduced at the anode surface. Furthermore, if the highest occupied molecular orbital (HOMO) falls above the chemical potential of the cathode during battery usage, the electrolyte is oxidized at the cathode surface.

1.8.2 Ionic Transport in Solids

Before discussing ionic transport in crystalline and amorphous solids, various solid diffusion mechanisms are discussed below. If the solute atom is much smaller than the host atom then diffusion can occur between interstitial sites in the host lattice. For example, in the cubic BCC and FCC crystal structures octahedral and tetrahedral interstitial sites are available to accommodate solute atoms, where direct interstitial to interstitial diffusion does not require the presence of defects within the crystal structure. For atoms of similar size to the host atom usually substitute for host atoms in the lattice, where the corresponding diffusion through the lattice can be characterized by vacancy mediated motion. The exchange jump rate, Γ, can be characterized by Eq. (1-31) below, where υ_0 is the jump frequency, S^F and S^M are the vacancy formation and entropy of vacancy migration respectively, and H^F and H^M are the vacancy formation and migration enthalpies (Mehrer 2007).

$$\Gamma = \upsilon_0 e^{\frac{S^F + S^M}{k_B}} e^{\frac{-H^F - H^M}{k_B T}} \tag{1-31}$$

Furthermore, a solute atom can also undergo diffusion via an interstialcy mechanism (indirect interstitial mechanism) where a solute and host atoms motion is coupled in that the solute atom moves into a host lattice position pushing out a host atom into an interstitial site. This exchange between lattice site and interstitial can occur in non-linear fashion as the solute atom diffuses through the host lattice (Mehrer 2007)

Ionic conduction in crystalline materials is characterized by periodic energy barriers associated with given lattice sites giving rise to favorable diffusion pathways—making ionic conductivity potentially an anisotropic property depending on the material structure. The ion motion is characterized by an activated jump process where the diffusion coefficient can be described by Eq. (1-32) (Tuller 2007), where a is the jump distance, υ_0 is the jump frequency, Z is the number nearest neighbors, c is the fraction occupation, γ includes the geometric and correlation factors, and E_m is the migration energy. Using Eq. (1-33) the mobility can be obtained, where Z_i is the number of charges per carrier. From the ion mobility expression using equation (1-33, the ionic conductivity can be calculation using Eq. (1-34) resulting in Eq. (1-35), where N is the density of ion sites in the sublattice (Tuller 2007).

$$D = \gamma(1-c)Za^2\upsilon_0 e^{\frac{\Delta S}{k_B}} e^{\frac{-E_M}{k_B}} \tag{1-32}$$

$$\mu = \frac{Z_i q D_i}{k_B T} \tag{1-33}$$

$$\sigma_{ionic} = NcZ_i q \mu \tag{1-34}$$

$$\sigma_{ionic} = N\frac{(Z_i q)^2}{k_B T}\gamma c(1-c)Za^2\upsilon_0 e^{\frac{\Delta S}{k_B}} e^{\frac{-E_M}{k_B}} \tag{1-35}$$

Additionally, considering that the mobility of the ions within the lattice are dictated by both the migration energy along with the number of available sites (interstitial and vacancies) for ion occupation, the overall activation energy of for lithium conduction is a product of the defect formation energy and the migration energy. If we assume the ion concentration of carriers to be independent to temperature then the ionic conductivity can be modeled using the Arrhenius relationship as shown in Eq. (1-36) (Bachman 2016, Chen 2016).

$$\sigma_{ionic} = \sigma_0 e^{\frac{-E_A}{k_B T}} \tag{1-36}$$

In contrast to crystalline solids, amorphous glasses are characterized by ions that conduct through disorder in the lattice, where one cation species ensures rigidity and another more mobile species can conduct via site hopping to equivalent sites marked by weak potential barriers to migration (Souquet 1981). For example, in amorphous oxide glasses, oxygen atoms are covalently bonded to cations to form elementary units such as SiO_4^{4-}, where one or more oxygen atoms are bridged and shared between the tetrahedral units. A mobile cation species can then act as network modifier bonding to non-bridged oxygen species. These mobile cations hop along anion sites along the covalently bonded macromolecular chain, where their conduction is partially coupled to the overall temperature dependent collective movement of the chains (Souquet 1981). In contrast, amorphous polymers are characterized by a backbone polymer chain and a dissolved ionic salt, where the positive cation is complexed through a coulombic interaction with an electronegative atom covalently bonded to the polymer chain. Similarly, the ionic conductivity of amorphous polymers is also correlated with chain motion as shown in Eq. (1-37), where T_0 is the glass transition temperature (Tuller 2007).

$$\sigma_{ionic} = \sigma_0 e^{\frac{-B}{T-T_0}} \tag{1-37}$$

1.8.3   Inorganic Solid Electrolytes

Inorganic solid electrolytes for lithium-ion batteries fall within a few material classes such as oxides, phosphates, sulfides, and nitrides where they can be both crystalline and amorphous in structure. For crystalline electrolytes, lithium ion conduction is often a dimensional dependent property if one or more directions within the crystal lattice offers a lower energy barrier to ion conduction.   Common solid lithium-ion conductors and their respective room temperature ionic conductivities are shown in Table 1-5. $Li_{14}Zn(GeO_4)_4$ was one of the first compounds to exhibit high lithium-ion conductivity, where within the crystal structure the oxygen atoms covalently bonded to cation network weakens their interaction with Li atoms providing a lower migration energy for lithium transport (Chen 2016). Unfortunately, the compound is unstable against lithium metal and is highly reactive with CO_2 (Thangadurai 2006). Another structural class of solid electrolytes is the NASICON group (sodium super ion conductors) which consist of corner-sharing PO_4 tetrahedra and MO_6 octahedra assembled to form a 3D network structure, where the metal atoms are generally titanium and germanium. The compounds abbreviated as LAGP and LATP or lithium aluminum germanium/titanium phosphates exhibit high ionic conductivities on the order of 10^{-4} S/cm along the c-axis of the structure. They are generally stable in ambient conditions, but their biggest limiting factor is the reduction of Ti^{4+} at the anode (Thangadurai 2006, Bachman 2016, Chen 2016). $LiLa(TiO_3)_2$ is another candidate for solid state electrolytes, where lanthanum large radius and high valence cause increased interstitial vacancies creating additional sites for Li^+ diffusion. Like the LATP solid electrolyte, the titanium can be reduced at the anode, in which the $LiLa(TiO_3)_2$ uptakes lithium and becomes more electronically conductive (Ren 2015, Chen 2016). The Li_3N solid electrolyte demonstrates a high room temperature conductivity, but possesses a poor thermal and electrochemical stability (Thangadurai 2006).

Sulfide based electrolytes have garnered much attention due to their markedly higher ionic conductivities (10^{-2} S/cm) that can even surpass those of liquid electrolytes. Fundamentally, higher ionic conductivities in analogue sulfides over oxides can be attributed to the lowered electronegativity of sulfur (S^{2-}) as compared to oxygen (O^{2-}) producing weaker interaction with Li-ions allowing for a lower energy barrier for ion conduction.(Lian 2019)   Amorphous sulfides composed of $x(Li_2S)$-$y(SiS_2)$, $x(Li_2S)$-$y(SiS_2)$-$z(Li_3PO_4)$, and $x(Li_2S)$-$y(P_2S_5)$ have demonstrated ionic conductivities on the order of 10^{-4}-10^{-5} S/cm, where a small incorporation (<5%) of metal oxides such as Li_xMO_y, where M= (Si, P, Ge, B, Al, Ga, In) has shown to improve the ionic conductivities to 10^{-3}-10^{-4} S/cm at room temperature. (Aotani 1994, Morimoto 1999, Minami 2006, Tatsumisago 2012, Sakuda 2013) One of the most notable crystalline solid electrolytes is $Li_{10}GeP_2S_{12}$ (LGPS) boasting a room temperature ionic conductivity of 1.2×10^{-2} S/cm,(Kamaya 2011). Despite the high ionic conductivity, the major limitation to this materials widespread implementation is instability at low potential due to oxidation of the Ge^{4+} sites-limiting its integration with lithium metal.(Lian 2019) Also, another practical limitation is the generally more air-reactive nature and smaller electrochemical stability windows as compared to oxides.(Lau 2018)

Table 1-5. Ionic conductivity range of various Li-ion solid-state Electrolytes

Material Class	Common Compositions	σ_{ion} Range	Challenges	Ref.
NASICON	$Li_{1+x}M_{2-x}M`_x(PO_4)_3$ (M: Ti, Ge, Hf; M`: In, Sc, Ga, Cr, Al, Fe)	10^{-3} -10^{-5} S/cm	Anode interface	1
Garnet	$Li_{7-x}M_xLa_3Zr_2O_{12}$ (M: Al, Ga,Ta, Nb, Ti, W)	10^{-3}-10^{-4} S/cm	Air Stability, Difficult synthesis, interfacial resistance	2
Perovskite	$Li_{3x}La_{2/3-x}TiO_3$, $Li_{2x-y}Sr_{1-x}Ta_yZr_{1-y}O_3$,	10^{-4}-10^{-5} S/cm	Anode interface, lower ionic conductivity	3
LISICON	$Li_{4-x}M_{1-x}M'_xO_4$ (M: Si, Ge, M': Al, P, V)	10^{-5}-10^{-6} S/cm	Lower ionic conductivity	4
Sulfides	$Li_{4-x}M_{1-x}M'_xS_4$ (M: Si, Ge, Zr, M': P, Al, Zn, Ga)Li_4GeS_4, $Li_{10}GeP_2S_{12}$, $Li_2SP_2S_5$	10^{-2}-10^{-5} S/cm	Air stability, cathode interface	5
Argyrodite	Li_6PS_5Cl, Li_6PS_5Br, Li_6PS_5I	10^{-3}-10^{-7} S/cm	Air stability, cathode interface	6
Anti-perovskite	$Li_3OM_xM_{1-x}$ (M: Cl, M':Br)	10^{-2}-10^{-7}	Air stability, cathode interface	7

[1](Arbi 2015, Jian 2017, Gao 2018) (Xu 2007) (Aono 1990, Thokchom 2008, Kahlaoui 2017)
[2](Ohta 2011, Allen 2012, Dhivya 2013, Wagner 2016, Shao 2017, Liu 2018, Zheng 2018)
[3](Thangadurai, Shukla et al. 1999; Huang, Xu et al. 2016; Kimura, Wagatsuma et al. 2016; Li, Xu et al. 2018; Zheng, Kotobuki et al. 2018; Le, Ngo et al. 2019)
[4](Hu 1977, Kuwano 1980, Song 2015, Deng 2017, Zheng 2018)
[5](Murayama 2002, Mizuno 2005, Liu 2008, Kamaya 2011, Tatsumisago 2012, Chu 2016, Lau 2018)
[6](Rao 2011, Boulineau 2012, Yu 2016, Zheng 2018, Lian 2019),
[7](Zhao 2012, Zheng 2018, Yin 2020)

1.8.4 ALD Electrolytes and Electrode Coatings

Beyond the scope of thin film batteries, conformal thin film solid electrolytes have been utilized in a range of lithium-ion battery applications. Significant research has been performed on the engineering of the electrode-liquid electrolyte interface, where a wide range of ALD metal oxides as well as solid electrolytes have been found to stabilize the solid electrolyte interphase (SEI)—the outcome of electrolyte and solvent oxidation/breakdown on the anode surface—improving coulombic efficiency and capacity retention. Beyond SEI stabilization, thin ALD coatings have also been shown to improve metal dissolution in cathode materials (Lu 2014,

Miikkulainen 2014), crucial for Mn and S based cathodes, as well as removal of surface carbonate surface species on LiMn$_2$O$_4$ cathodes.(Young 2019) Furthermore, ALD thin films have been utilized to coat Li metal to help improve efficiency and reduction of dendrite formation during lithium plating and stripping—potentially unlocking a large improvement in capacity for solid-state batteries.(Kazyak 2015, Zhao 2019) ALD thin films have also been utilized to improve the interfacial resistance between lithium metal and a bulk crystalline solid electrolytes—which has been a major roadblock to development of solid-state lithium metal batteries.(Han 2017, Liu 2018) Lastly, another potential application is in the development of Electro-Chemical Random-Access Memory (ECRAM).(Fuller 2017, Tang 2018)

A wide range of solid-state electrolytes have been synthesized via atomic layer deposition as shown in Table 1-6. One of the first thin film solid electrolytes developed was lithium phosphorus oxynitride (LiPON) first developed in Oak Ridge National Laboratory in the early 1990's.(Bates 1992, Bates 1993, Wang 1995) Its moderate ionic conductivity (~10^{-6} S/cm) is much lower than traditional crystalline bulk solid electrolytes, but its electrochemical stability (~0-5V vs. Li/Li$^+$)(Yu 1997) makes it an ideal solid electrolyte material for thin film batteries. As such, there has been a concerted research effort in developing an ALD process for conformal synthesis of LiPON.(Kozen 2015, Nisula 2015, Shibata 2016, Pearse 2017, Put 2019) First reported synthesis of ALD LiPON was in 2015 (Kozen 2015) exhibiting an ionic conductivity of 1.45 ± 3×10^{-7} S/cm. The process was further optimized through tuning the plasma power to modulate nitrogen incorporation (Put 2019). Beyond the plasma enhanced process for the synthesis of ALD LiPON, a binary thermal ALD process utilizing a novel precursor, diethyl phosphoramidate (DEPA), in which the desired nitrogen and phosphorus binding is already incorporated in the chemical precursor was shown to be a viable synthetic approach demonstrating films with ionic

conductivities ranging from 9.3×10^{-8} to 6.6×10^{-7} S/cm, depending on the deposition temperature (Nisula 2015). More recently, a binary thermal process has been developed utilizing the more well studied lithium precursor source, LiO^{t}Bu, combined with DEPA which led to synthesis of materials with stoichiometry close to Li_2PO_2N with an ionic conductivity of $6.51 \pm 0.36 \times 10^{-7}$ S/cm at 35°C.(Pearse 2017) Beyond LiPON, there have several studies on the ALD synthesis of Li_3PO_4. One specific work demonstrated ionic conductivities as high as 6.2×10^{-7} S/cm depending on film thickness and deposition temperature, a 4.2V electrochemical stability window, conformal coating over high aspect-ratio (AR:50) $TiO_2/Pt/Al_2O_3$-Si microstructures (Létiche 2017). Currently, LiPON and Li_3PO_4 based materials have demonstrated some of the best characteristics of thin film solid-state electrolytes synthesized via atomic layer deposition but may possess a lower ceiling to potential improvements in ionic conductivity and electrochemical stability window as compared to other classes of materials. One potential material that could provide improvements to the ionic conductivity is LiSiPON, where ionic conductivities as high as 10^{-5} S/cm have been achieved through co-sputtering multiple targets such as Li_3PO_4-Li_2SiO_3 and Li_3PO_4-Si_3N_4. (Famprikis 2019) (Lee 2003, Su 2017) Ionic conductivities were found to increase with an increasing ratio of Si/P from 0 to 0.45. (Lee 2003)

Table 1-6. Reported thin film solid-state electrolytes synthesized via ALD
and their corresponding ionic conductivity. Adapted from (Sheil 2020)

Material	σ_{ion} (S/cm) 25°C	ALD Precursors	Ref.
Li_xTa_yO	2×10^{-8}	LiOtBu/H_2O, Ta(OEt)$_5$/H_2O	(Liu 2013)
$Li_xLa_yTa_zO$	Not reported	LiOtBu/H_2O, TiCl$_4$/H_2O, La(thd)$_3$/O_3	(Aaltonen 2010)
Li_xNb_yO	6.39×10^{-8}	LiOtBu/H_2O, Nb(OEt)$_5$/H_2O	(Wang 2018)
Li_xSi_yO	5.72×10^{-9} Not reported Not reported	LiOtBu/H_2O, TEOS/H_2O Li(N(SiME$_3$)$_2$)/O_3 LiTMSO/O_3/H_2O	(Kazyak 2017) (Hämäläinen 2011) (Ruud 2017)
Li_xAl_yO	Not reported Not reported 5×10^{-9}–10^{-10} *5.6×10^{-8} Not Reported Not Reported Not Reported	TMA/H_2O, LiOtBu/H_2O TMA/H_2O, LiOtBu/H_2O TMA/O_3, LiTMSO/H_2O TMA/H_2O, LiOtBu/H_2O TMA/H_2O, LiOtBu/H_2O TMA/O_3, LiOtBu/H_2O TMA/O_3, LiTMSO/H_2O	(Perng 2014) (Comstock 2013) (Hu 2016, Ruud 2017) (Park 2014) (Aaltonen 2011) (Miikkulainen 2014) (Ruud 2017)
$Li_xAl_ySi_zO$	10^{-7}-10^{-9}	LiOtBu/H_2O, TEOS/H_2O, TMA/H_2O	(Zhang 2012, Perng 2014, Cho 2016)
$Li_{6.28}La_3Zr_2O_{12}$	*1×10^{-8}	LaFAMD/O_3, LiOtBu/O_3, TDMAZ/O_3, TMA/O_3	(Kazyak 2017)
Li_2CO_3	Not reported Not reported NotReported - 10^{-10} 10^{-10}	Li(thd)/O_3 LiOtBu/H_2O LiN(SiMe$_3$)$_2$/H_2O/CO_2 LiTMSO/H_2O/CO_2 LiOtBu/O_2 LiOtBu/H_2O/CO_2	(Putkonen 2009) (Putkonen 2009) (Østreng 2012) (Ruud 2017) (Hornsveld 2017) (Hornsveld 2017)
Li_3BO_3-Li_2CO_3	2.2×10^{-6}	[(CH$_3$)$_2$CHO]$_3$B/O_3, LiOtBu/O_3	(Kazyak 2018)
Li_3N	Not reported	LiN(SiMe$_3$)$_2$/NH$_3$	(Østreng 2012)
$LiPO_3$	Not reported Not reported *3.3×10^{-8} 6.2×10^{-7}	LiOtBu/TMPO LiHMDS/TMPO LiOtBu/TMPO LiOtBu/TMPO	(Hämäläinen 2012) (Hämäläinen 2012) (Wang 2014) (Létiche 2017)
$Li_xP_yO_zN$	3.2×10^{-7} $1.45\pm3\times10^{-7}$ 5×10^{-7} 6.6×10^{-7} $6.51\pm0.4\times10^{-7}$	TDMAP/O_2, LiOtBu/NH$_3$ LiOtBu/H_2O, TMPO/N_2 LiOtBu/H_2O, TMPO/N_2 LiHMDS/DEPA LiOtBu/DEPA	(Shibata 2016) (Kozen 2015) (Put 2019) (Nisula 2015) (Pearse 2017)
Li_xAl_yS	2.5×10^{-7}	TMDA-Al/H_2S, LiOtBu/H_2S	(Cao 2016)
LiF	Not reported Not Reported 10^{-14} S/cm	Li(thd)/Mg(thd)$_2$/TiF$_4$ LiOtBu/TiF$_4$ LiOtBu/HF/pyridine	(Mäntymäki 2013) (Xie 2017) (Chen 2018)
Li_xAl_yF	$3.5\pm0.5\times10^{-8}$	LiOtBu/TiF$_4$, AlCl$_3$/TiF$_4$	(Xie 2017)

Various crystalline oxide materials have exhibited ionic conductivities as high as 10^{-3} S/cm at room temperature, possess excellent electrical insulation properties, mechanical robustness, but depending on the metal constituents can exhibit a limited electrochemical stability window.(Zheng

2018) The specific crystal lattice of these groups of compounds allow for pathways for quick Li-ion conduction, making some exhibiting anisotropic ion conduction. Deposition of epitaxial and or highly oriented polycrystalline metal oxides has been established via atomic layer deposition, but significant challenges remain. Obtainment of a specific desired stoichiometry of a multi-component oxide is generally more challenging as it requires more extensive process optimization—such as characterization of individual incubation times, due the potential chemical interactions between constituents. Next, generally substrate choice with good lattice match as well as similar thermal expansion coefficients are needed along with thermal treatment to crystallize in the necessary structure, which is limited in choice to suitable anode or cathode materials for lithium-ion batteries. This is compounded by the high mobility of lithium that can diffuse into the substrate in addition to evaporate during annealing generally requiring the use of specific substrates and excess Li sources during the annealing or very short rapid thermal annealing processes.(Kazyak 2017, Loho 2017) Furthermore, orientation of grains, grain boundary composition and corresponding resistance, as well interfacial structure may likely play a significant role in the solid electrolyte's functional properties. ALD $Li_xLa_yZr_zO$ doped with ALD Al_2O_3 has been demonstrated with fine tuning of the ALD cycle sequence producing thin films with very close to stoichiometric $Li_7La_3Zr_2O_{12}$, but the film was amorphous as-deposited and crystallization into the ion conducting phase was unfruitful.(Kazyak 2017) Regardless, a wide range of amorphous lithium metal oxides has been synthesized via ALD, where lithium aluminum oxide was one of the first Li-ion conducting oxides reported to be synthesized via ALD, where room temperature ionic conductivities have been measured between 5×10^{-8}-10^{-10} S/cm depending on composition and precursor chemistry. (Comstock 2013, Park 2014, Perng 2014, Hu 2016) Building off previous work of Li_xAl_yO ALD, a process for synthesis of $Li_xAl_ySi_zO$ was developed

through the addition of a low temperature ALD SiO_2 process, utilizing tetraethyl orthosilicate (TEOS) and H_2O, where SiO_2 deposition is catalyzed by the presence of Al-OH groups which help promote the disproportionation reaction of the TEOS ligands in the presence of water.(Perng 2014, Cho 2015, Cho 2016) ALD $Li_xAl_ySi_zO$ exhibited ionic conductivities in the range of 10^{-7}-10^{-9} S/cm, where increased lithium content as well as decreased film thickness was observed to increase the ionic conductivity, where further optimization of composition may prove to produce increased ionic conductivities.(Shin-Ichi 2004, Perng 2014) Li_xTa_yO(Liu 2013), Li_xNb_yO(Wang 2018), and $Li_xLa_yZr_zO$ have been synthesized as solid electrolytes demonstrating room temperature ionic conductivities of $2×10^{-8}$, $6.39×10^{-8}$ S/cm, and $1×10^{-8}$ S/cm, respectively. Lastly, the highest ionic conductivity of any material deposited via ALD reported to date is a solid-solution of Li_3BO_3 and Li_2CO_3 (termed LBCO) exhibiting room temperature ionic conductivities as high as $2.2×10^{-6}$ S/cm.(Kazyak 2018).

Beyond oxides, lithium metal fluorides and sulfides have also been synthesized via ALD. ALD of thin film Li_xAl_yF exhibited moderate ionic conductivities of $3.5 ± 0.8×10^{-8}$ S/cm at room temperature, about an order of magnitude less than ALD LiPON. Further improvement might be gained through further optimization of the of the Li/F ratio as well as potential crystallization into the $β$-Li_3AlF_6 phase that upon mechanical milling into nano-sized particles exhibited ionic conductivities as high as $1×10^{-7}$ S/cm.(Miyazaki 2012). Atomic layer deposition of metal sulfides presents a specific challenge in that H_2S is generally deployed as a precursor, which due to its reactivity, toxicity, and reaction with water to form sulfuric acid require specific reactor material and safety precaution designs.(Dasgupta 2010, Dasgupta 2015) Li_xAl_yS demonstrated via ALD exhibited a room temperature ionic conductivity of $2.5×10^{-7}$ S/cm.

1.8.5 Unique 1D Channel LiAlSiO$_4$ Solid Electrolyte

Another crystalline oxide material of interest is β-LiAlSiO$_4$ that although exhibits a moderate room temperature ionic conductivity has unique 1D channels that exhibit fast anisotropic Li-ion conduction along the c-axis, that can be up to three orders in magnitude higher in ionic conductivity as compared to transport in alternate directions.(Nagel 1982) β-LiAlSiO$_4$ thin films have been previously synthesized via Pulsed laser deposited, where increased ionic conductivity was observed with decreasing film thickness making it an ideal candidate for an ALD solid electrolyte (Shin-Ichi 2004). The β-eucryptite structure has a framework of β-quartz (pure SiO$_2$) formed by building blocks of SiO$_4$ tetrahedra with each corner O atom bonded to two tetrahedra, also referred to as bridging oxygens (BO's). In the β-eucryptite, lithium is incorporated in interstitial sites, where Al directly substitute silicon in SiO$_4$ tetrahedra. LiAlSiO$_4$ exhibits moderate ionic conductivities in the crystalline, glass, and glass ceramic phases at room temperature(Alpen 1977, Nagel 1982, Thangadurai 2002, Furusawa 2007),is electronically insulating, and has an activation energy for ion motion in the range of 0.77~0.95 eV.(Shin-Ichi 2004). If the 1-D channels can be aligned in the direction normal to the two electrode surfaces in a thin film battery structure, enhanced ion transport is expected. Beyond the scope of microbatteries, a electrochemically stable thin film electrolyte may be viable to improve interfacial properties in solid-state batteries (Vinado 2018, Zhao 2018).

1.8.6 Inorganic/Polymeric Composite Electrolytes

Beyond the ionic conductivity, the mechanical properties such as the elastic modulus and critical tensile strain of the solid electrolyte become increasingly important when integrating with next generation high capacity alloying and conversion anodes (Si, Sn, SnO$_2$, and Ge) as well as lithium metal. Alloying type anodes offer large increases in the theoretical capacity for instance

from 372 mAh/g (graphite) to 3579 mAh/g (Si), but with increased capacity comes much more lithium incorporation in the host structure causing large expansions/contractions during charge and discharge. Li metal presents a different challenge in that during plating and stripping, lithium dendrite formation can penetrate electrolytes separator and short-circuit the device. Beyond inorganic solid electrolytes, polymer materials are also promising candidates for rechargeable LIB,(Grünebaum 2014) possessing good chemical and electrochemical stabilities which support the operation of LIB as well as superior mechanical stability and elasticity, which better accommodates the electrode volumetric expansion.(Grünebaum 2014).

Most of the polymer electrolytes studied are based on polyethylene oxide (PEO)(Armand 1994) for its high solubility for lithium salts.(Christie 2005) Strong coupling effects between the Li^+ ion and the oxygen atoms in the PEO chains may be the source of increased ionic conductivity(Wright 2002) and mechanical and safety properties.(Diddens 2010, Hallinan 2013) There are also reports of hybrid electrolytes consisting of solid polymer electrolytes coupled with inorganic fillers, such as SiO_2 and Al_2O_3 nanoparticles,(Fu 2016) showing improved transference number,(Pitawala 2008, Zewde 2013) increased ionic conductivity,(Dissanayake 2013, Masoud 2013) and improved mechanical properties.(Zewde 2013)

One promising thin film option is group of polycyclosiloxanes polymers that can be synthesized via initiated chemical vapor deposition (iCVD). Solid electrolytes derived via initiated chemical vapor deposition have many benefits such as room temperature deposition, high growth rate, as well as opening the door to a wide range of chemistries and functionality not accessible via ALD. Although iCVD does not have the same robustness as ALD for the deposition of conformal thin films on high-aspect ratio structures, fine tuning of process parameters such as the partial pressure of precursors can help promote conformality.(Moni 2017) Poly(1,3,5,7-tetravinyl-

1,3,5,7-tetramethylcyclotetrasiloxane (PV4D4) is a promising material that when soaked in liquid electrolyte can exhibit ionic conductivities $>10^{-8}$ S/cm(Chen 2015) and has been recently shown to improve the cycling performance of thin film silicon anodes. (Shen 2019). Further improvement to the ionic conductivities may be possible through optimization of lithium incorporation, whether it be through optimization of the liquid electrolyte solution (solvent, salt, additives) or new precursor functionalities. One of the greatest challenges to address for polymer based electrolytes for 3D LIB is that these materials typically require soaking in a liquid electrolyte for an extended time for lithium incorporation.(Reeja-Jayan 2015) The prolonged soaking is impractical and the surface tension effect could result in the collapse of the nanostructured anodes during the drying process.

As discussed previously, an ideal solid electrolyte for 3D battery applications has the following properties: high ionic conductivity, highly conformality, high electrical resistivity and breakdown field, large electrochemical stability, and lastly resistance to mechanical fracture due to stresses produced at the electrolyte/electrode interface during device operation. Across the range of various classes of solid electrolyte materials (polymers, metal oxides, sulfides, and nitrides) the unique chemistries and microstructures possessed by these different classes of materials allows for some, but not all of these criteria for an ideal solid electrolyte to be met. Although individual materials may fall short of meeting all of the criteria, composite structuring of different classes of materials may provide the opportunity to produce highly functional electrolyte materials. For example, combination of a polymer and metal oxide material such as pV4D4 and $Li_xAl_ySi_zO$ may provide a wider range of functional properties making their composite structure an ideal candidate for direct integration with solid state 3D batteries.

The electrical and mechanical properties of the two solid lithium-ion electrolytes, pV4D4 and $Li_xAl_ySi_zO$ are summarized in Table 1-7, where properties of similar materials were utilized for unknown property values. The metal oxide, $Li_xAl_ySi_zO$ can offer high resistivity and breakdown field crucial for scaling down electrolyte film thicknesses on the order of tens of nanometers for improved ion transport. The pV4D4 polymer materials offers the potential for unique mechanical properties, specifically lower elastic moduli and higher critical tensile strains, which may prove effective in accommodating electrode volume expansions during the lithiation process. Direct combination of these materials does not guarantee that the resulting hybrid structures exhibits the properties of their individual components, where the synthesis conditions would most likely play a large role in the overall properties of the hybrid structures. Ultimately, this combinatorial approach to synthesize composite hybrid materials may offer improved solid electrolyte properties for realization of 3D lithium-ion microbatteries.

Table 1-7. Ionic Conductivity, Electrical, and Mechanical Properties of ALD metal oxide and iCVD polymer materials.

Deposition Technique	Breakdown Field (MV/cm^2)	Ionic Conductivity at 25°C (S/cm)	Elastic Modulus (GPa)	Critical Tensile Strain (%)
ALD	7 Al_2O_3 (Seong 2017)	1.5×10^{-8} $Li_xAl_ySi_zO$ (reported here)	170 Al_2O_3 (Ylivaara, Liu et al., 2014)	0.52% -2.4% Al_2O_3 (Moon, Seong et al., 2015)
iCVD	5 PV3D3 (Seong 2017)	7.5×10^{-8} PV4D4 (Chen 2015)	4.5 PDVB (Zhao 2017)	~ 4 % PV3D3 (Jen, Bertrand et al., 2011)

1.9   Scope of Thesis

This work aims to develop novel thin film electrode and electrolyte materials that can be readily integrated in 3D thin-film lithium-ion batteries. Beyond specific material criteria for the individual battery components, crucial for integration into 3D solid-state lithium-ion microbatteries is conformality/uniformity of the deposited layers on high aspect ratio structures to ensure uniform kinetics across the 3D structures—making atomic layer deposition an ideal process for synthesizing these materials. Key material properties required for direct integration with 3D lithium-ion microbatteries is (1.) conformality of all layers, (2.) electrolytes: adequate ionic conductivity, adequate electrical resistivity and breakdown strength, and (3.) cathodes: high volumetric capacity, good rate capability, good capacity retention.

Chapter 3 discusses the development and optimization of thin film cathodes with specific focus on $Li_{1+x}Mn_{2-x}O_4$. For the $Li_{1+x}Mn_{2-x}O_4$ stoichiometry, fine tuning of the lithium content alters the electrochemical properties (redox potential, cycle stability). As the lithium content is increased ($x \leq 0.33$) Li cations can directly substitute Mn cations in the octahedral sites of the spinel structure causing neighboring Mn cations to become tetravalent to maintain charge neutrality. With increased substitution come structural stability during lithiation/delithiation, but decreased capacity in the 4.0 V region—where a balance must be struck to optimize for cycle stability/cycle life and capacity. The work presented here utilizes an iterative approach to map processing conditions to thin film composition as well as determine the interplay between composition, crystal structure, and the electrochemical properties. The optimized $Li_{1+x}Mn_{2-x}O_4$ thin films exhibited excellent cycle stability and rate capability.

Chapter 4 and Chapter 5 discusses the development of various conformal solid-state electrolytes as well as their integration with nanostructured anodes. ALD lithium aluminum silicate

thin films were developed and shown to be functional in the as-deposited state and found to be mechanically intact and functional upon the expansion/contraction of the underlying SiGe nanowire during lithiation/delithiation. Amorphous lithium aluminum silicate was also integrated with polymer Poly(1,3,5,7-tetravinyl-1,3,5,7-tetramethylcyclotetrasiloxane (PV4D4) thin film to form novel hybrid solid-state electrolytes with wider ranging physiochemical properties. Integration of the hybrid thin film solid state electrolytes improved capacity retention of thin film conversion anodes with the potential to offer further improvements to alloying anodes that undergo larger volumetric changes during operation. To improve on the ionic conductivity, amorphous $Li_xAl_ySi_zO$ thin films were crystallized in to the β-Eucryptite phase exhibiting improved ionic conductivities (10^{-7} S/cm) at room temperature meeting the requirement for integration with 3D thin film lithium-ion microbatteries.

.

CHAPTER 2:   EXPERIMENTAL SETUP

To synthesize thin film materials for both electrolyte and electrode applications in 3D batteries, two atomic layer deposition (ALD) processes were developed and an initiated chemical vapor deposition (iCVD) was used. This chapter discusses the custom-built reactors used for material synthesis as well as the relevant characterization techniques to assess the functional properties of the synthesized thin films. First, the relevant deposition parameters are discussed for thermal ALD of $Li_xAl_ySi_zO$ and LiSiPON, the plasma enhanced ALD processes for Co_3O_4 and MnO_2, as well as the iCVD process for PV4D4 deposition. Next, relevant material characterization techniques are discussed with a specific focus on theory and analysis of experimental data. These techniques include spectroscopic ellipsometry (SE) for film thickness measurements, x-ray photoemission spectroscopy (XPS) for composition characterization, x-ray diffraction (XRD) for structural analysis, and scanning electron microscopy (SEM) and atomic force microscopy (AFM) for characterizing film thickness and morphology. Next, the experimental conditions utilized to perform in-situ TEM experiments is discussed, including sample preparation and analysis. Lastly, electrochemical characterization of both the electrolyte and electrode materials is discussed, in which key functional parameters for lithium ion batteries are characterized such as ionic conductivity (electrochemical impedance spectroscopy), redox potential (cyclic voltammetry), as well as capacity retention and rate capability (galvanostatic cycling).

2.1   Thin Film Deposition Systems

Two custom-built hot wall ALD reactors were used for deposition with one equipped with a coaxial microwave cavity radical beam source. The main component of the thermal based ALD system utilized for deposition of lithium aluminum consisted of a CF 6-way cross with OD 2.75" (MDC, 407002). Similar in design, the PEALD system's main component was made up a CF 6-

way cross with OD 4 5/8". The temperature of both reactors was controlled via heating wire (Ari Industries, BXX09B88-4T) monitored with type-k thermocouples controlled by an Omega CN1500 multi-zone with seven independent PID temperature controllers. Both reactors were maintained at 30 mTorr through use of a mechanical pump. Sample temperature was maintained through a custom stainless-steel dish spot-welded to nickel-chromium wire (Omega Engineering, N180-040-50) for resistive heating, where the temperature was monitored via a type-K thermocouple. Complex metal oxide films were synthesized via a solid solution of constituent binary oxides. The term ALD super-cycle and sub-cycle are used throughout this work to describe various thin films. A super cycle is a repeating sequence of individual ALD sub-cycles. For instance to deposit $Li_xAl_ySi_zO$ thin films a super cycle sequence consists of $n[a(Al_2O_3)$-$b(LiOH)$-$c(SiO_2)]$, where the a,b,c refer to number of sub-cycles in the repeatable super cycle sequence, where n is the number of super cycles. The stoichiometry of the resulting $Li_xAl_ySi_zO$ thin films can be modulated through tuning of the a,b,c parameters, where films deposited with $10(Al_2O_3)$-$6(LiOH)$-$4(SiO_2)$ would be expected to have a different composition then films deposited with the sequence: $9(Al_2O_3)$-$5(LiOH)$-$6(SiO_2)$. The sub-cycle ratio of each constituent oxide can be calculated and related to the deposited composition, where for instance the aluminum oxide sub-cycle percentage of a super-cycle consisting of $9(Al_2O_3)$-$5(LiOH)$-$6(SiO_2)$ would be 45% (9 of the total 20 sub-cycles).

2.1.1 ALD of $Li_xAl_ySi_zO$ (Al_2O_3, SiO_2, $LiOH/Li_2O$) and LiSiPON

The chemical precursors: trimethyl aluminum (TMA), tris-tertbutoxy silianol (TTBS), lithium tert-butoxide (LiO^{t}Bu), diethyl phosphoramidate (DEPA), tetraethylorthoxy silane (TEOS), and H_2O were utilized in the thermal ALD system as shown in Figure 2-1, where relevant properties are shown in Table 2-1.
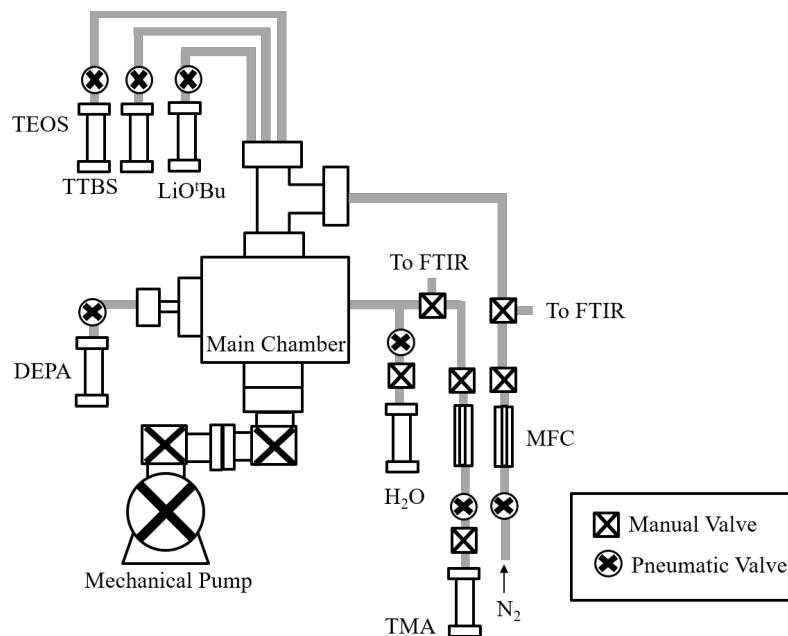
Figure 2-1 Thermal ALD reactor for deposition of $Li_xAl_ySi_zO$ and LiSiPON. The main component of the reactor consisted of a CF 6-way cross with OD 2.75", where the walls were heated to 150°C to prevent precursor adsorption. The pressure was maintained in the mTorr regime through use of a mechanical pump. Precursors were stored in 1.33" conflat housings, heated to provide adequate vapor flux to the sample surface.

Heated precursors were stored in a 1.33" OD stainless steel housing with conflat flange attached at one end and the other to a SS-HB series Swagelok pneumatic valve via VCR fittings. The precursor vapor was delivered to the main chamber without use of carrier gas, where adequate precursor vapor was produced through heating of the precursor housing. Lithium-tert butoxide was heated to 140°C and delivered to main reactor component via a ¼" stainless steel doser heated to 160°C to ensure proper precursor flux to the sample surface, where the doser was heated with flexible Kapton heaters. Tris-tertbutoxy silanol, a solid at room temperature, was heated to 45°C and its corresponding gas-line to 75°C. Trimethyl aluminum (TMA) and tetraethylorthosilicate (TEOS) was not heated as it was found to have adequate volatility at room temperature. The TMA precursor was delivered to the main reactor component using a mass flow controller. The oxidant

source, H_2O, was not heated and delivered through the use of a needle valve with its corresponding gas-line heated to 60°C. The reactor wall was maintained at a temperature of 150°C to inhibit unwanted precursor condensation. Finally, the deposition temperature (sample temperature) was heated in the range of 225°C-290°C to ensure reactivity of all chemical precursors. N_2 was delivered to the reactor via ¼" stainless steel tubing where the flow rate was controlled via a mass flow rate controller.

Table 2-1 Properties of precursors utilzied in the thermal ALD system for synthesis of $Li_xAl_ySi_zO$ and LiSiPO(N)

Precursor	Lithium tert-butoxide (LTB)	Trimethyla luminum (TMA)	Tris(*tert*butoxy) silanol (TTBS)	Tetraethyl orthosilicat e (TEOS)	Diethyl phosphoramid ate (DEPA)	H_2O
Purity	>98%	97%	>99%	99.5%	98%	D.I.
Vendor	Strem	Sigma-Aldrich	Strem	Sigma-Aldrich	Strem	-
Precursor Temp. (ºC)	140 -160	25	45	25	120	25
Gas-line Temp. (ºC)	160	75	75	75	150	75

The pulse times for the respective ALD processes (Al_2O_3, Li_2O, SiO_2, LIPON) are shown in Table 2-2. Depositions were either performed under constant N_2 flow (~1 sccm) or in a purge/pump process where N_2 was delivered to chamber (~15 sccm) and then the system pumped out before the next precursor exposure. The pneumatic valves were controlled through a custom LABVIEW program interfaced utilizing a NI USB-9481 DAQ controller. $Li_xAl_ySi_zO$ thin films were deposited as a solid solution of the constituent oxides via a *super cycle* consisting of of a(TMA/H_2O)-b(LiO^{t}Bu/H_2O)-c(TEOS/H_2O), where a, b, c is the number of each *sub cycle* that can be modulated to tune the composition. LiSiPON thin films were deposited with global cycle sequence: $n[a$(LiO^{t}Bu/DEPA)-b(TEOS/H_2O)].

Table 2-2. Precursor dosing conditions for the individual oxides utilized in the thermal based ALD system

ALD Process	Metalorganic Precursor Pulse(s)	Pumpdown Time (s)	Coreactant Pulse Time (s)	Pumpdown Time (s)
Al_2O_3	5 (TMA)	90	5 (H_2O)	90
Li_2O	5 (LiO^tBu)	90	5 (H_2O)	90
SiO_2	2 (TEOS)	90	5 (H_2O)	90
r-SiO_2	200(TTBS)	90	5 (H_2O)	90
LiPON	5(LiO^tBu)	120	2(DEPA)	120

2.1.2 PEALD of $Li_{1+x}Mn_{2-x}O_4$, $Li_xCo_yO_z$

The plasma enhanced atomic layer deposition system was equipped with two oxidant sources: the coaxial microwave cavity radical sources as well as H_2O.
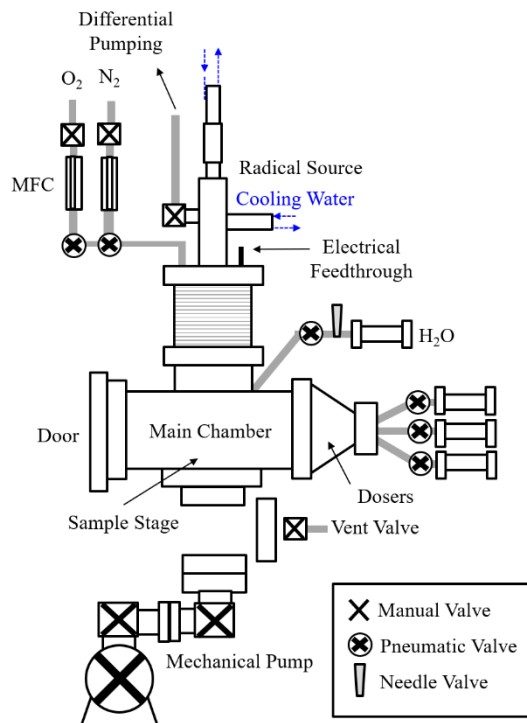
Figure 2-2-2. PEALD reactor for deposition of $Li_{1+x}Mn_{2-x}O_4$ and $LiCoO_2$. The main component of the reactor consisted of a CF 6-way cross with OD 4 5/8", where the walls were heated to 150°C to prevent precursor adsorption. The pressure was maintained in the mTorr regime through use of a mechanical pump. Precursors were stored in 1.33" conflat housings, heated to provide adequate vapor flux to the sample surface. A water-cooled coaxial microwave cavity radical beam was utilized as the O_2 plasma source

The β-diketonate based metalorganic precursors, Bis(2,2,6,6-tetramethyl-3,5-heptanedionato)cobalt(II) and tris(2,2,6,6-tetramethyl-3,5-heptanedionato)manganese(III) were utilized with O_2 plasma to deposit cobalt and manganese oxide. LiOH incorporation to form $Li_{1+x}Mn_{2-x}O_4$ and $Li_xCo_yO_z$ was performed via a thermal ALD process as described above utilizing the metalorganic precursor lithium tert-butoxide and utilizing H_2O as the oxidant source. The family of β-diketonate metalorganic precursors is a common choice for CVD and ALD processes, characterized by relatively bulky ligands making growth rates relatively lower than other precursors due to steric hindrance. One benefit of utilizing β-diketonate based precursors is being solid at room temperature as well as low reactivity in ambient conditions allowing for ease of

processing as compared to other more reactive precursors. All metalorganic precursors were delivered within a few inches of the sample surface via ¼" stainless steel tubing with flexible Kapton heaters to prevent precursor condensation. LiO^{t}Bu, Co(thd)$_2$, and Mn(thd)$_3$ were heated to 140°C, 135°C, and 125°C, respectively, where all three dosers were heated to 155°C. The relevant physical properties of the chemical precursors utilized in this system are presented below in Table 2-3.

Table 2-3. Precursors utilized in PEALD system and their physical properties

Precursor	(LiO^{t}Bu); Lithium tert-butoxide	(Co(thd)$_2$); Bis(2,2,6,6-tetramethyl-3,5-heptanedionato)cobalt(II)	(Mn(thd)$_3$); tris(2,2,6,6-tetra-methyl-3,5-heptanedionato) manganese(III)	O$_2$
Purity	>98%	99.9%	97%	UHP
Vendor	Strem	Alfa-Aesar	Sigma-Aldrich	-
Precursor Temp. (ºC)	140 -160	120	135	25
Gas-line Temp. (ºC)	160	155	155	-

Depositions were performed in the following sequence: precursor pulse, pump down to base-pressure, oxidant exposure, followed by another pump down to base-pressure. Precursor pulse and purge times for the individual oxides are shown in Table 2-4. Li$_{1+x}$Mn$_{2-x}$O$_4$ thin films were deposited with the cycle sequence: $n[a$(Mn(thd)$_3$:O)-b(LiO^{t}Bu/H$_2$O)], where the a,b parameters could be modulated to control the stoichiometry of the deposited films. Li$_x$Co$_y$O$_z$ and Li$_{1+x}$Mn$_{2-x-y}$Co$_y$O$_4$ thin films were deposited with a cycle sequence of $n[a$(Co(thd)$_2$:O)-b(Mn(thd)$_3$:O)-c(LiO^{t}Bu/H$_2$O)], where b = 0 for deposition of lithium cobalt oxide.

Table 2-4. Precursor dosing conditions for the individual oxides utilized in the plasma enhanced based ALD system.

ALD Process	Metalorganic Precursor Pulse(s)	Pumpdown Time (s)	Oxidant Pulse Time (s)	Pump-down Time (s)
MnO_2	30 ($Mn(thd)_3$)	30	15 (O)	30
Co_3O_4	30 ($Co(thd)_2$)	30	15 (O)	30
LiOH	5 (LiO^tBu)	75	5 (H_2O)	75

2.1.3 Coaxial Microwave Cavity Radical Beam Source

A schematic of the coaxial microwave cavity radical beam source is shown in the appendix. The coaxial radical source was originally designed by Chang et al. (Chang 1997) in order to improve the radical flux of traditional microwave plasma sources. The cavity consisted of two coaxial conductors; one hollow 0.25" center conductor and one 0.625" outer conductor, which were fixed in series by a metal clamp which surrounded a quartz ampoule at the end. The quartz ampoule was held in place through clamping with a stainless-steel fitting against a hollowed block of stainless steel that was water-cooled. To facilitate conductive heat transfer, the quartz ampoule was wrapped with a thin layer (~0.25 mm thick) of 99.9975% purity indium foil. As significant heat was produced during plasma generation cooling water was connected to the center conductor consisting of a hollow 0.25" stainless steel tube coated with gold through which an additional 0.125" inner tube sat inside.

The cavity was vacuum sealed by two Teflon bushings which sealed up to ~10^{-8} Torr, although the chamber was operated in the mTorr range. The two Teflon bushings formed a small volume which was differentially pumped via mechanical pump in order to reduce the leak rate of the radical source. Gas was fed from the air side through a vacuum feed through and connected via PTFE heat-shrink tubing to the arm of quartz ampoule. Molecular oxygen, at 99.999% purity, was fed to the quartz ampoule at a rate between 0.5 and 0.75 sccm, in which the rate was controlled by an MKS instruments mass flow controller. Microwave power was supplied by a 2.45 GHz,

Sairem microwave power supply using an N-type connector which was attached in series to the center conductor. During depositions, the radical beam source was operated at 25 W with ~4-5 W reflected power, where the reflected power was dependent on the resonance condition of the microwave cavity. The resonance condition can be determined by Eq. (2-1), where Z_0 is the cavity impedance, ω is the microwave frequency, C_0 is the cavity capacitance, and λ is the microwave wavelength. When the gap between the center conductor and the end of the metal clamp is smaller than λ and $Z_0 \omega C_0 \ll 1$, the resonance cavity length can be estimated via Eq. (2-2).

$$\frac{2\pi L}{\lambda} = \tan^{-1} \frac{1}{Z_0 C_0 \omega} \tag{2-1}$$

$$L_{res} = (\frac{n}{2} + \frac{1}{4})\lambda, \text{ where n} = 0,1,2,3\ldots \tag{2-2}$$

The resonance condition could be achieved by adjusting the cavity length to an integral number of half-wavelengths which could be adjusted via the tuning slug as well as movable collar where the N-type connector was fixed, both located on the air-side of the system. Additionally, the radical beam source had an ignition wire that was wrapped around the channel of the quartz ampoule, where the O_2 gas was fed. The plasma could be ignited manually by touching the feed through with a Tesla coil while applying microwave power. During normal operation, the microwave power source and tesla coil were controlled remotely by LABVIEW software and NI DAQ USB-9481 interface which allowed for automated depositions.

2.1.4   Initiated Chemical Vapor Deposition (iCVD)

Initiated chemical vapor deposition (iCVD), is a low temperature process that allows for the deposition of polymer materials through polymerization of vinyl bonds, with the benefit of maintaining the structure of all non-vinyl bonds present in the monomer (Coclite 2013). The process consists of combining a monomer of interest along with a thermally labile initiator

molecule in the vapor phase. When the initiator molecule impedes upon a heated filament a bond is broken and a radical species is formed. The gas phase species are condensed on the sample surface, where the radical species can react with the monomer to form the polymer film (Lau 2006). Separation of the heated filaments (260°C) and the sample surface is particularly advantageous, in that the sample can be maintained at much lower temperatures (25-35°C) allowing for deposition on heat-sensitive materials. The process is performed either in a closed-batch configuration where a specific quantity of chemical precursor is pulsed into a closed chamber for reaction or a continuous process configuration where the chemical precursors are continually flowed into the reactor, while the reactor is maintained at constant pressure through the use of a butterfly valve. A key parameter in the iCVD process is the ratio of the partial pressure of the monomer species to the saturation vapor pressure of the monomer at the temperature of the sample surface, $P_{monomer}/P_{sat}$. Where the $P_{monomer}/P_{sat}$ ratio can be qualitatively used as a measure of the amount of monomer condensed on the surface, which can be assumed to have a linear relationship at low $P_{monomer}/P_{sat}$ values (<x) due to reaching the limit of Henry's law (Lau 2006). To explore the effect of the $P_{monomer}/P_{sat}$ on the iCVD growth properties, several acrylate monomers were compared with increasing carbon chain lengths corresponding to decreases in their respective saturated vapor pressures (Lau 2006). By holding the partial pressure of the monomer and initiator species constant, it was observed that monomers with decreased P_{sat} (i.e. larger $P_{monomer}/P_{sat}$ values) showed increased deposition rates and average molecular weight of the deposited polymers. The effect of substrate temperature was also explored to determine the kinetic limiting step of the iCVD process, where higher temperatures would favor increased reaction rates for the initiation, propagation, and termination steps of the polymerization, while lower temperature favor increased condensation of the vapor-phase monomer species. Interestingly, increasing deposition rates were observed for

decreasing substrate temperatures suggesting monomer condensation is limiting step in the iCVD polymerization process (Lau 2006).

iCVD synthesis was performed by the Gleason Group at MIT in a custom-built iCVD vacuum reactor. The monomer tetravinyltetramethylcyclotetrasiloxane, V4D4 (Gelest, Inc.), and the initiator molecule tertbutylperoxide (TBPO, Sigma Aldrich) were heated to 75ºC and 25ºC respectively, and delivered to the main reactor at a flow rate of 0.15 and 0.85 sccm (Chen 2015). The reactor pressure was maintained constant at 200 mTorr through use of a butterfly valve. The filament temperature was maintained at 300ºC and the sample temperature was maintained at 35ºC. The thickness of the pV4D4 films was monitored using an *in-situ* laser interferometer system. For iCVD deposition, monomer and initiator vapor is flowed into the reactor. The initiator vapor is thermally activated by heated filaments to form radical species (200-400°C). Both the initiator and radical species are adsorbed on a temperature-controlled surface, where polymerization (initiation, propagation, termination) takes place (Lau 2006). A typical iCVD reactor schematic is shown in Figure 2-2-3 (Lau 2006)
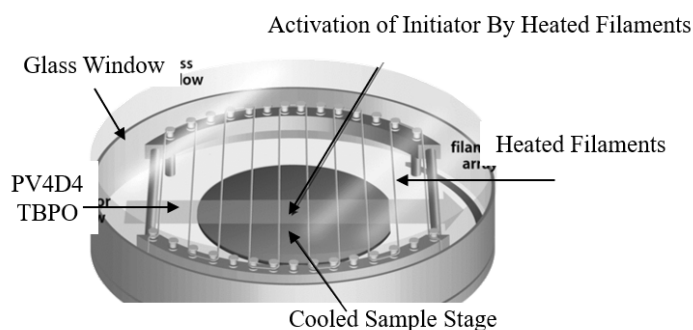
Figure 2-2-3. Schematic of an iCVD Reactor. Initiator vapor is thermally activated by heated wire filaments producing primary radical species. Both the radical species and monomer vapor are adsorbed onto a cooled substrate surface, where polymerization takes place. A glass window is utilized for in-situ optical monitoring of film thickness. Adapted from (Lau 2006)

2.2   Material Characterization

In this section the materials characterization techniques used in this work are discussed along with the operating principles of each characterization technique.

2.2.1   Spectroscopic Ellipsometry (SE)

Spectroscopic Ellipsometry is a non-destructive optical technique that can be used to measure the optical properties and film thickness of thin-film materials. Spectroscopic ellipsometry works by monitoring changes to linearly polarized light with components s- and p- (parallel and perpendicular to the incident plane) as it is reflected off a sample surface becoming elliptically polarized (Figure 2-4).
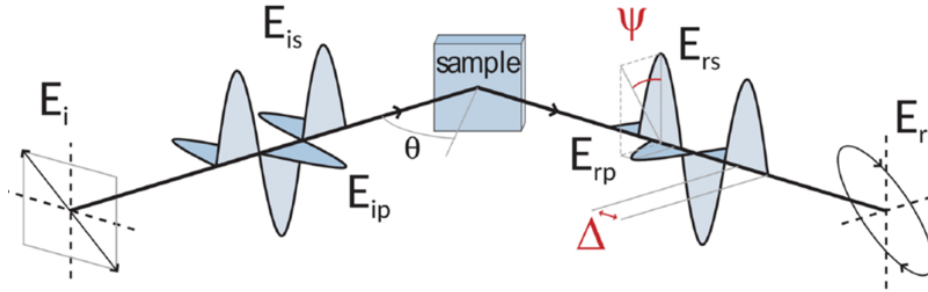
Figure 2-4. Schematic of spectroscopic ellipsometry measurement (Leick 2016)

As the incident light reflects off the sample surface the amplitude and phase of the reflected waves are different for the p- and s- components producing an elliptically polarized wave. SE works through monitoring changes to both the phase difference, Δ, and the amplitude ratio, $\tan(\Psi)$, of the s- and p- components of the polarized light. The expression for the complex reflectance ratio, ρ, is given in Eq. (2-3), where r_s and r_p are the amplitude reflectivities for the s- and p- components respectively. This ratio is in general a complex number, due to the relative phase shift between the s and p reflected waves (Durgapal 1998). For samples of known thickness, measured Δ and Ψ

can be used to determine the wavelength dependent extinction coefficient, k, and index of refraction, n. the real index of refraction, $\tilde{n}(\lambda)$ relation is given by Eq. (2-4).

$$\rho = \frac{r_p}{r_s} = \tan(\Psi)e^{i\Delta} \tag{2-3}$$

$$\tilde{n}(\lambda) = n(\lambda) + ik(\lambda) \tag{2-4}$$

Spectroscopic ellipsometry is an indirect method of measuring film thickness as the proper optical model for the materials of interest must be known to determine accurate film thicknesses. Various models are used to model the optical properties dependent on the materials. For transparent materials, Cauchy Eq. (2-5) and Sellmeier Eq. (2-6) dispersion models can be used to fit the wavelength dependent index of refraction.

$$\tilde{n}(\lambda) = A + \frac{B}{\lambda^2} + \frac{C}{\lambda^4} \tag{2-5}$$

$$\frac{1}{\tilde{n}^2(\lambda) - 1} = \frac{-A}{\lambda^2} + B \tag{2-6}$$

Additionally anomalous dispersion models can be used to fit the real dielectric constant as a function of wavelength, where the dielectric function can be modeled as a sum or ensemble of various oscillators, where the expression for the Lorentz oscillator is shown in Eq. (2-7), where E_c is the center energy of the incident photons, ε_1 is the dielectric offset in the measurement, E is the energy of the incident photon, and A/B are material specific constants.

$$\tilde{\varepsilon} = \tilde{n}^2 = \varepsilon_1 + \frac{AE_C}{E_C - E^2 - iBE} \tag{2-7}$$

Spectroscopic ellipsometry measurements were performed using a J.A. Woollam M-88 system with a wavelength range of 280-760 nm. The experimental data was then fit using a Cauchy (Al_2O_3, SiO_2, $LiOH/Li_2O$), Lorentz (Co_3O_4), or Tauc-Lorentz (MnO_2/M_2O_3) dispersion model

71

depending on the material being analyzed. SEM cross-sectional imaging was utilized as a secondary measure of film thickness to further verify the film thickness.

Table 2-5. Models and corresponding fitting parameters for ellipsometric data

Material	Model Type	Parameters
Al_2O_3	Cauchy	A: 1.62, B_n:2.6 × 10^{-3} µm, C_n:2.0 × 10^{-6} µm^4
SiO_2	Cauchy	A: 1.46, B_n:2.38 × 10^{-3} µm, C_n:9.75 × 10^{-5} µm^4
LiOH	Sellmeier	A: 1.10 × 10^{-6} µm^2, B: 0.96
CoO/Co_3O_4	Lorentz Model	ε_{offset}:1.04, A:2.96, B:0.52, Ec:0.51
MnO_2/Mn_2O_3	Tauc-Lorentz, Gaussian	A: 8.0293, En: 3.8125, C: 1.8735, Eg: 0.8213 A:5.332, En:5.3115, Br: 2.0201

Example data and fitting are shown in Figure 2-5 for ALD of LiOH/Li$_2$O and MnO$_2$. Utilizing a Sellmeier model to fit LiOH/Li$_2$O (D. Shannon 2002) the estimated thickness was 49.7 Å for a film deposited with 50 cycles of (LiO^{t}Bu/H$_2$O) at 225°C, resulting in a growth rate of 1.0 Å/cycle. As comparison, the SEM X-section of a film deposited with 150 cycles of (LiO^{t}Bu/H$_2$O) was measured to be 14.6-18.0 nm, whereas the expected thickness according to the SE determined growth rate would be 15.0 nm as shown in part (c) of Figure 2-5. The value is fairly good agreement with the value estimated from ellipsometry considering the error associated with measuring film thickness via SEM. LiOH films are also air-reactive, which could have a surface roughness effect. Part (b.) of Figure 2-5 shows experimentally measured data for a MnO$_2$ film consisting of 315 (Mn(thd)$_3$/O$_2$ Plasma) cycles resulting in an estimate thickness of 76.1 Å. Part (d.) shows an SEM image of 1000 cycles of (Mn(thd)$_3$/O$_2$ Plasma), where the measured thickness ranged from 18.9 to 21.4 nm—in line with the estimate growth rate of 0.2 Å/cycle for the PEALD MnO$_2$.
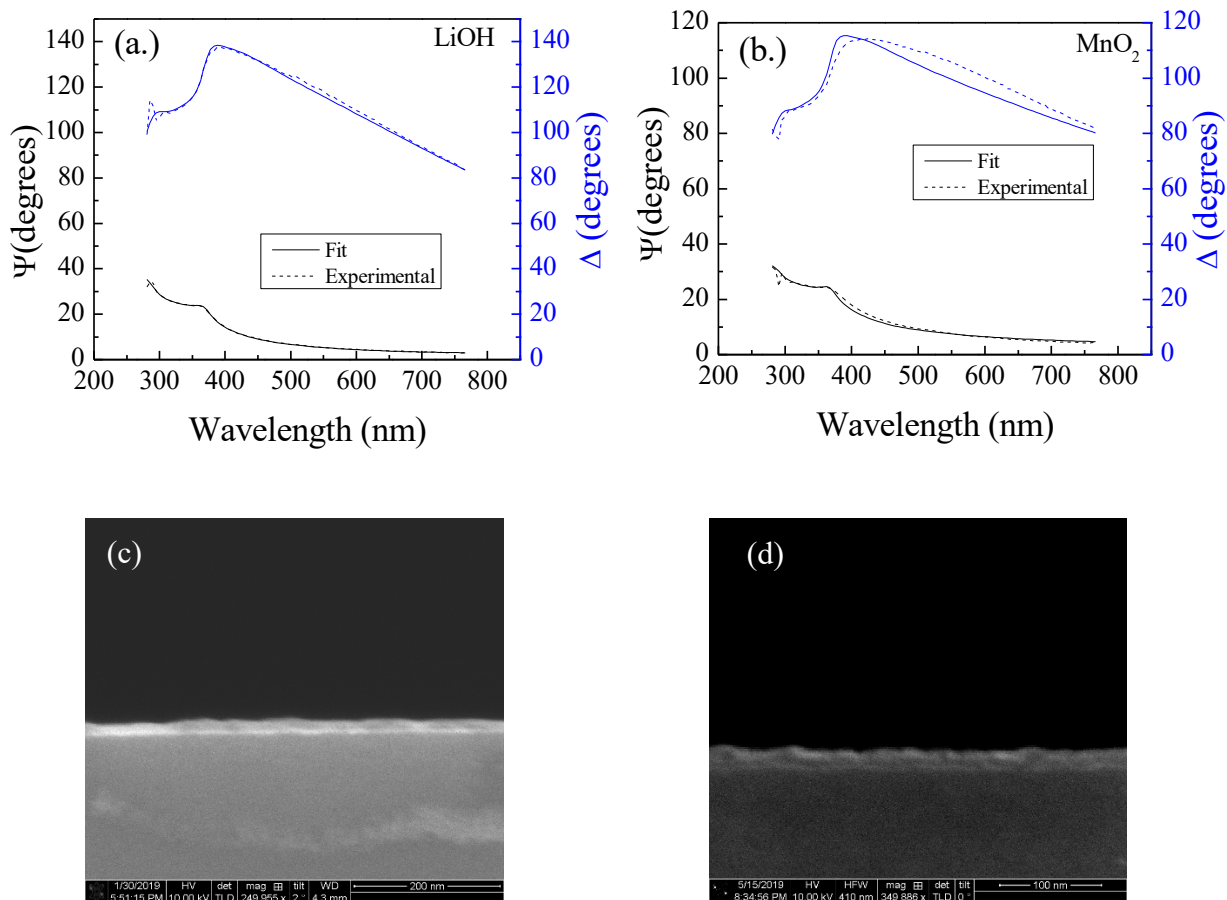
Figure 2-5. Ellipsometric Ψ (polarization) and Δ (intensity) fitting of (a) LiOH/Li$_2$O thin film deposited with 50 cycles at 225°C with an estimated thickness of 49.7 Å utilizing a Sellmeier model (D. Shannon 2002) and (b) MnO$_2$ utilizing a TaucLorentz model consisting of 300 cycles at 225°C with an estimated thickness of 76.1 Å. (c.) SEM x-section image of 150 cycles of LiOH deposited at 225°C , measured to vary between 14.6-18.0 nm (d.) SEM X-section image of 1000 cycles of MnO$_2$ at 225°C, measured to vary between 18.9 to 21.4 nm via ImageJ.

2.2.2   X-ray Photoelectron Spectroscopy (XPS)

X-ray Photoelectron Spectroscopy was utilized to monitor the composition of the ALD thin films. XPS takes advantage of the photoelectron effect, where core electrons can be ejected upon collision with an incident photon of higher energy than the binding energy of the core electron. The kinetic energy of the ejected photoelectron is measured, which can be then related back to its

original binding energy equation via Eq. (2-8), where hv is the energy of the incident photon and ϕ is the work function of the spectrometer.

$$KE = h\nu - BE - \phi \tag{2-8}$$

The probability that a photoelectron is emitted is deemed the photoelectron cross section and is element and orbital dependent, but independent of the chemical state of the element. X-ray photoelectron microscopy is a surface sensitive technique (<10 nm) where the sampling depth is dependent on the inelastic mean free path of the ejected photoelectrons within the sample as shown in Eq. (2-9) , where λ_{IMFP} is the inelastic mean free path of the ejected photoelectron within the sample, and θ is the angle relative to the surface in which the photoelectrons are analyzed (Van Der Heide 2011).

$$D = 3\lambda_{IMFP} \cos\theta \tag{2-9}$$

The relative composition of elements present in the sample can be quantified by analyzing the integrated intensities of the element signal, normalized to its corresponding atomic sensitivity factor (ASF) as shown in Eq. (2-10).

$$C_i = \frac{I_i / ASF_i}{\sum_{i=1}^{n} I_i / ASF_i} \tag{2-10}$$

The atomic sensitivity factors associated with the elements: Li, Al, Si, O, C, Mn and Co are listed in Table 2-6 below. The raw spectra obtained via XPS is generally aligned in binding energy to the C1s peak at 284.8 eV, where especially if the sample is insulating positive charge can build up near the sample surface shifting the obtained spectra to having higher apparent binding energies (Van Der Heide 2011). A survey spectrum as well as detailed scans of the Li 1s, Al 2p, Si 2p regions for a 21 nm LiAlSiO$_4$ sample is shown in Figure 2-6. The Al 2p and Si 2p regions were fit with a single peak, since the splitting between 2p$_{3/2}$ and 2p$_{1/2}$ could not be resolved.

Table 2-6. The atomic sensitivity factors (ASF), spin orbital split and the spin orbit split ratio for elements studied in this work. The ASF values correlate to the fitting of just the $2p_{3/2}$ and $3p_{3/2}$ peaks, in which the $2p_{1/2}$ and $3p_{1/2}$ area is accounted for.(Lebugle 1981) (Chuang 1976, Hagström 1977, Briggs 1981, Fives 1989)

Element	ASF	SOS	SOR
Li 1s	0.025	N/A	N/A
Al 2p	0.193	0.4	2:1
Si 2p	0.328	0.6	2:1
O 1s	0.780	N/A	N/A
C 1s	2.780	N/A	N/A
N 1s	0.477	N/A	N/A
P 2p	0.486	0.86	2:1
Co 2p	3.590	14.9-15.6	2:1
Co 3p	0.447	1.10	2:1
Mn 2p	2.660	11-11.9	2:1
Mn 3p	0.280	*	2:1
Mn 3s	0.165	**	N/A

**Not reported in NIST XPS database *See Table 2-9 below for values for Mn 3s exchange splitting
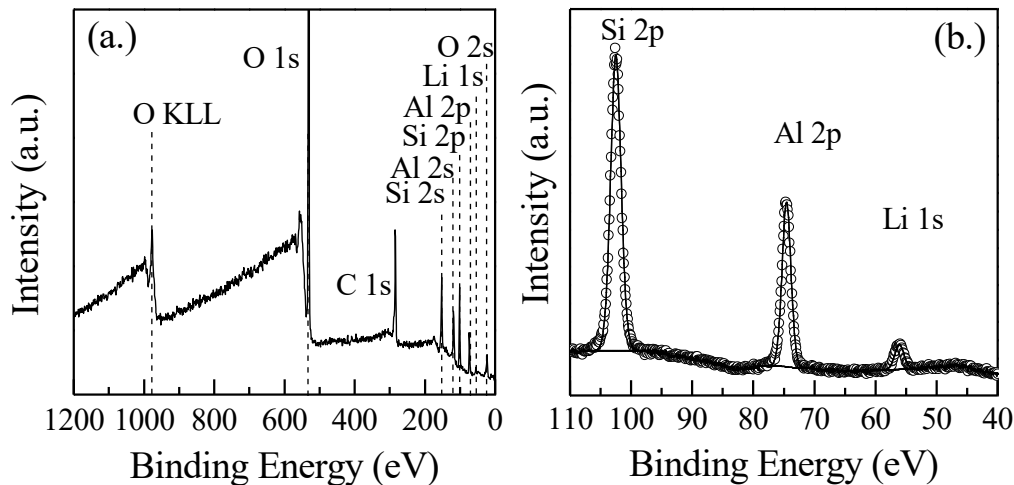
Figure 2-6 (a) XPS survey spectra scan of a 21 nm $LiAlSiO_4$ thin film deposited on Si(001) at a pass energy of 160eV. (b) XPS spectra taken at 40eV pass energy in the region of 110-40 eV, with fitting for the Si 2p, Al 2p, and Li 1s peaks. Since the $2p_{3/2}$ and $2p_{1/2}$ could not be resolved for the Si 2p and Al 2p orbitals a single peak was fit.

Nominally, for films less than three times its photoelectron escape depth (~8-10 nm), XPS allows for estimation of the film thickness through quantification of the attenuation of the substrate signal as shown in Eq. (2-11), where λ is the inelastic mean free path of the electron, I_{sub} and I_o are the photoelectron intensities of the substrate and the overlayer (Hill 1976).

$$t = \lambda \sin \theta \ln \left(1 + \frac{I_0/ASF}{I_{sub}/ASF}\right) \tag{2-11}$$

Angle resolved XPS was performed through tilting the sample towards the x-ray source modulation the alignment of the sample and detector making the information depth decrease and the technique more surface sensitive. As the normal information depth is approximately 10 nm determined by the inelastic mean path of the ejected electron through the analyte, reducing the take-off angle below 90° makes it so only ejected electrons at a shallower depth (<10 nm) able to reach the detector as the path within the analyte to the detector becomes greater. Specific quantification of the measured depth is a complex function of the inelastic mean free path of electrons ejected from orbitals interest as well as the material composition. The approximate depth sampled (d) is given by Eq. (2-12), where λ is the inelastic mean free path of the ejected electron. (Schneider 2005)

$$D = 3\lambda \sin\theta \tag{2-12}$$

Here, a qualitative trend is analyzed as decreasing the take-off angle corresponds to more surface-sensitive compositions (<10 nm). Beyond the take-off angle, the sample position was modulated to account for changes in the *x,y,z* direction during tilting, utilizing an algorithm calibrated for the Kratos XPS instrument.
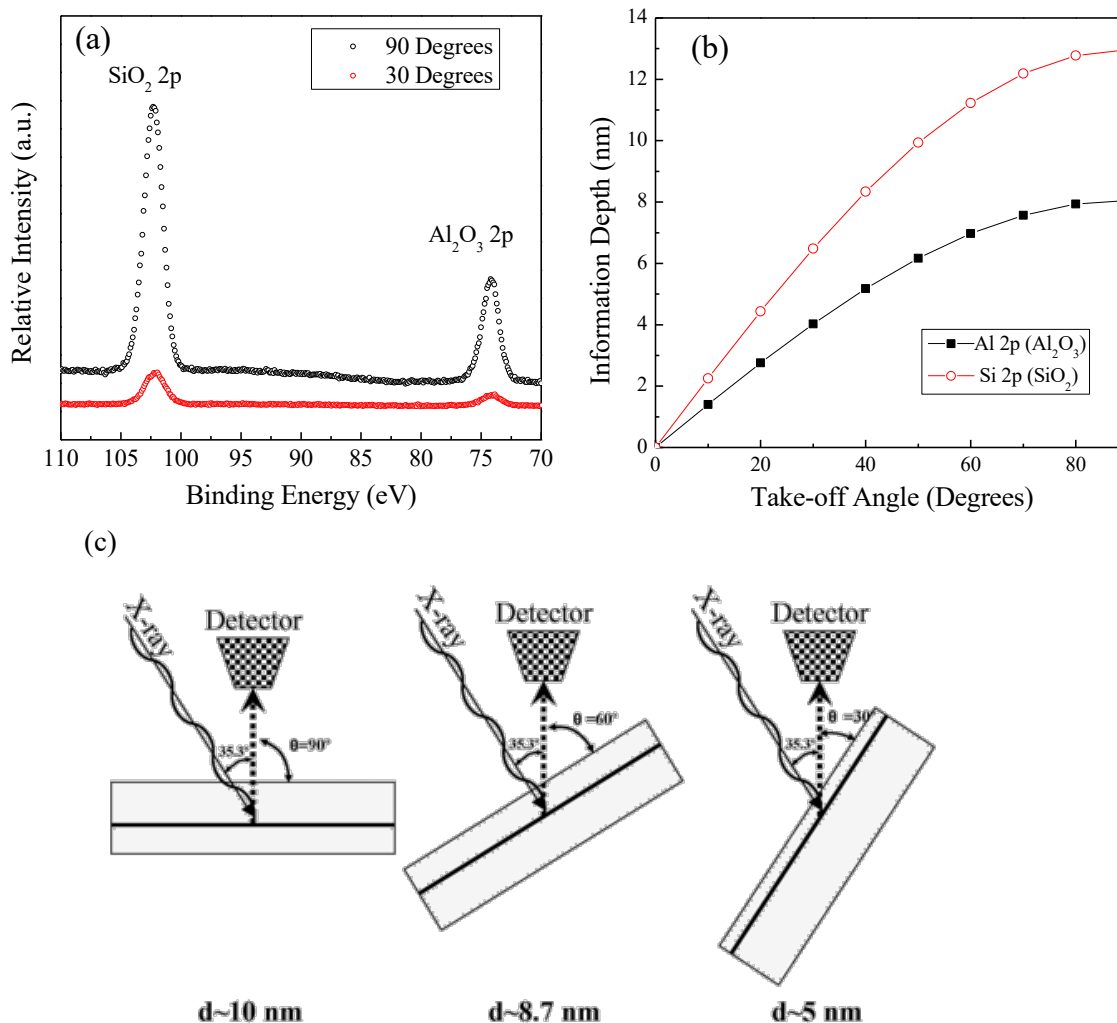
Figure 2-7. (a.) XPS detailed scans of the Si 2p and Al 2p regions of a LiAlSiO$_4$ thin film at various take-off angles (90 and 30 degrees). (b.) Calculated information depth vs. take-off angle for Al 2p and Si 2p electrons utilizing inelastic mean free paths associated with each respective oxide (Akkerman 1996). (c.) Sample-setup in angle-resolved XPS. The sample is tilted with away from the detector decreasing the take-off angle, effectively reducing the sample depth. (Schneider 2005)

Fitting of Co 2p spectra were performed by fixing the *fwhm* for peaks of the same orbital, fixing the area relation between 2p$_{3/2}$ and 2p$_{1/2}$ peaks, as well as the splitting as reported in Table 2-7. Cobalt oxide is one of the few materials, in which the Co^{3+} peak lies to lower binding energy as compared to the Co^{2+} oxidation state (Chuang 1976).

Table 2-7. Binding Energies for Cobalt Oxides, values obtained from (Chuang 1976)

Material	Co2p$_{3/2}$ (eV)	Co 2p$_{1/2}$ (eV)	Co 2p splitting (eV)	2p$_{3/2}$ satellite (eV)	2p$_{3/2}$ satellite splitting (eV)
CoO	780.5	796.3	15.8	786.4	5.9
Co$_3$O$_4$	779.6: Co^{3+}(oct), 780.7 Co^{2+} (tetra)	794.5 Co^{3+} (oct), 796: Co^{2+} (tetra)	14.9	789.5	9.9

XPS detailed scans are shown in Figure 2-8 of a cobalt oxide film deposited at 205°C utilizing Co(thd)$_2$ and O$_2$ plasma. The film is most likely majority Co$_3$O$_4$ due to the weak satellite feature, the 2p splitting of 14.7 eV.
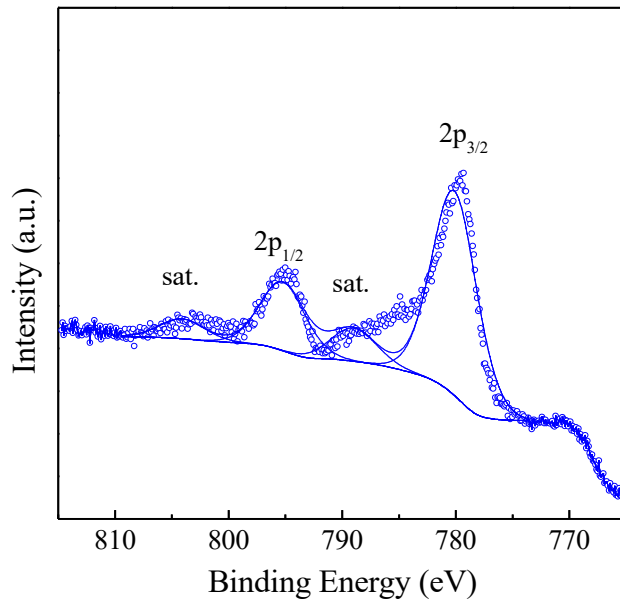
Figure 2-8. XPS detailed scans of plasma enhanced ALD of Co$_3$O$_4$ at a deposition temperature of 205°C.

Binding energies for various manganese oxides are shown in Table 2-9. Fitting of the Mn 2p spectra also followed the same fixing of the *fwhm*, splitting, and area parameters for peak fitting of the same orbital, but is more complicated due to the larger number of Mn oxidation states and

very small changes to binding energy associated with them. The binding energy of associated with Mn $2p_{3/2}$ orbital for various manganese oxides is shown in Table 2-8.

Table 2-8. Mn $2p_{3/2}$ binding energies for various Mn oxides.

Compound	Mn $2p_{3/2}$ Binding Energy (eV)	Ref.
Mn	638.8-639 eV	(Hsin-Kuei 1981, Chourasia 1994)
MnO	640.8 eV	(Di Castro 1989)
Mn_3O_4	641.6 eV	(Tan 1991)
Mn_2O_3	641.7 eV	(Di Castro 1989)
MnO_2	642.2 eV	(Tan 1991)

XPS detailed scans are shown in Figure 2-9 of manganese oxides deposited at substrate temperatures ranging from 205°C to 265°C. Across the deposition temperature range, the Mn 2p binding energy mostly correlated to that measured for MnO_2, but all samples exhibited a shoulder to lower binding energy associated with a lower oxidation state.
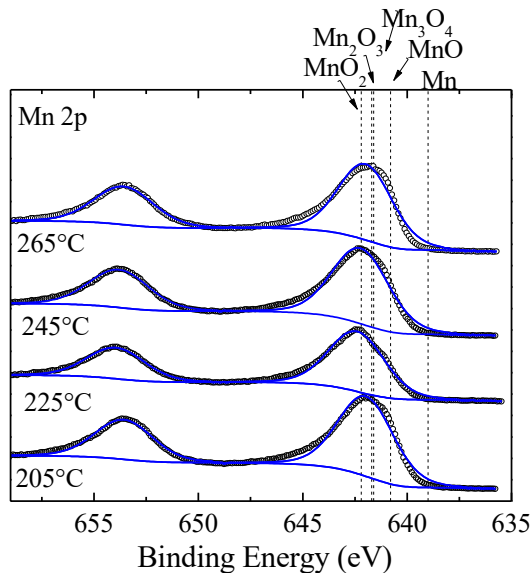
Figure 2-9. XPS detailed spectra of Mn 2p regions for films deposited utilizing (Mn(thd)$_3$ and O$_2$ plasma) at deposition temperatures ranging from 205°C to 265°C. Binding energies of various manganese oxides Mn $2p_{3/2}$ peaks are shown as dashed lines.

Photoelectron transitions for the Mn 3s valence state have two possible final states $(3s^13p^63d^x)$ from an initial state $(3s^23p^63d^x)$, where $x = 3,4,5$ for the oxidation states of Mn^{4+}, Mn^{3+}, Mn^{2+}, respectively, where in one final state the 3s electron is correlated with the 3d electrons of parallel spin and the other antiparallel (Nelson 2000). From this quantification of the splitting of the Mn 3s through exchange interaction with the 3d orbitals can be a measure of the oxidation state of Mn.

Table 2-9. Binding Energies for Manganese Oxides, values obtained from (Ilton 2016) (Di Castro 1989) (Tan 1991)

Oxidation State	Mn 3s Exchange Splitting (eV)	Mn 3s Peak Position (eV)	Mn $2p_{3/2}$ Peak Position (eV)
Mn(IV) (MnO_2, Pyrolusite)	4.4	85.3	642.2
Mn(III) (Mn_2O_3, Manganite)	5.4	83.9	641.7
Mn(II) (MnO)	6.1	82.2	640.8

2.2.3 X-ray Diffraction (XRD)

X-ray diffraction (XRD) was utilized to assess the structural properties of the ALD thin films. In a polycrystalline or crystalline sample, one can determine the crystal structure based on Bragg's law of diffraction given in Eq. (2-13), where d is the distance between lattice planes, θ is the Bragg diffraction angle, λ is the incident x-ray wavelength, and n is the order of reflection.

$$2d \sin \theta = n\lambda \qquad (2-13)$$

When Bragg's law is fulfilled for a given angle constructive interference of the x-rays gives rise to characteristic peaks, which then can be indexed to determine structural information of the material of interest. Intensity of the diffraction peaks can be determined by the structure factor, which is dependent on the symmetry of the crystal structure. Beyond calculation of the lattice constant, the mean crystallite size can be estimated using the Scherer Equation presented in

Eq.(2-14), where L is the mean grain size, λ is the x-ray wavelength, η is the *fwhm* of the diffraction

peak, and θ is the Bragg angle, and K is the shape factor that range associated with the geometry

of the crystallite.

$$L = \frac{K\lambda}{\eta \cos \theta} \tag{2-14}$$

In this study, the materials were characterized by synchrotron X-ray diffraction (XRD)

analysis using a photon energy of 13.5 keV at SSRL beamline 10-2 with a four-circle

diffractometer and a Pilatus 300K-W silicon hybrid pixel detector (pixel size 172 μm x 172 μm,

sample detector distance 1.1 m) as well as a laboratory scale Panalytical X'Pert Pro X-ray powder

diffractometer (40 keV) with a Cu Kα source producing a wavelength of 1.54 Å.

The four-circle diffractometer (SSRL) was used to define the scattering vector q with

respect to the thin-film surface normal with four motors, θ, 2θ, φ and χ, as shown in Figure 2-10.

When the sample was oriented horizontally, specular θ-2θ scans were performed to detect peaks

corresponding to planes oriented parallel to the sample surface. Peak positions along the 2θ axis

were directly correlated to the interplane spacing by Bragg's law. When the sample was oriented

vertically, in-plane θ-2θ scans resolve peaks related to planes perpendicular to the surface. In-plane

scans with θ and 2θ fixed for particular peaks and varying φ axis allowed the study on symmetry

of the peak and the capability of determining an epitaxial relationship between the film and the

substrate. Diffraction peaks were then identified by referencing the Joint Committee on Powder

Diffraction Standards (JCPDS) database.
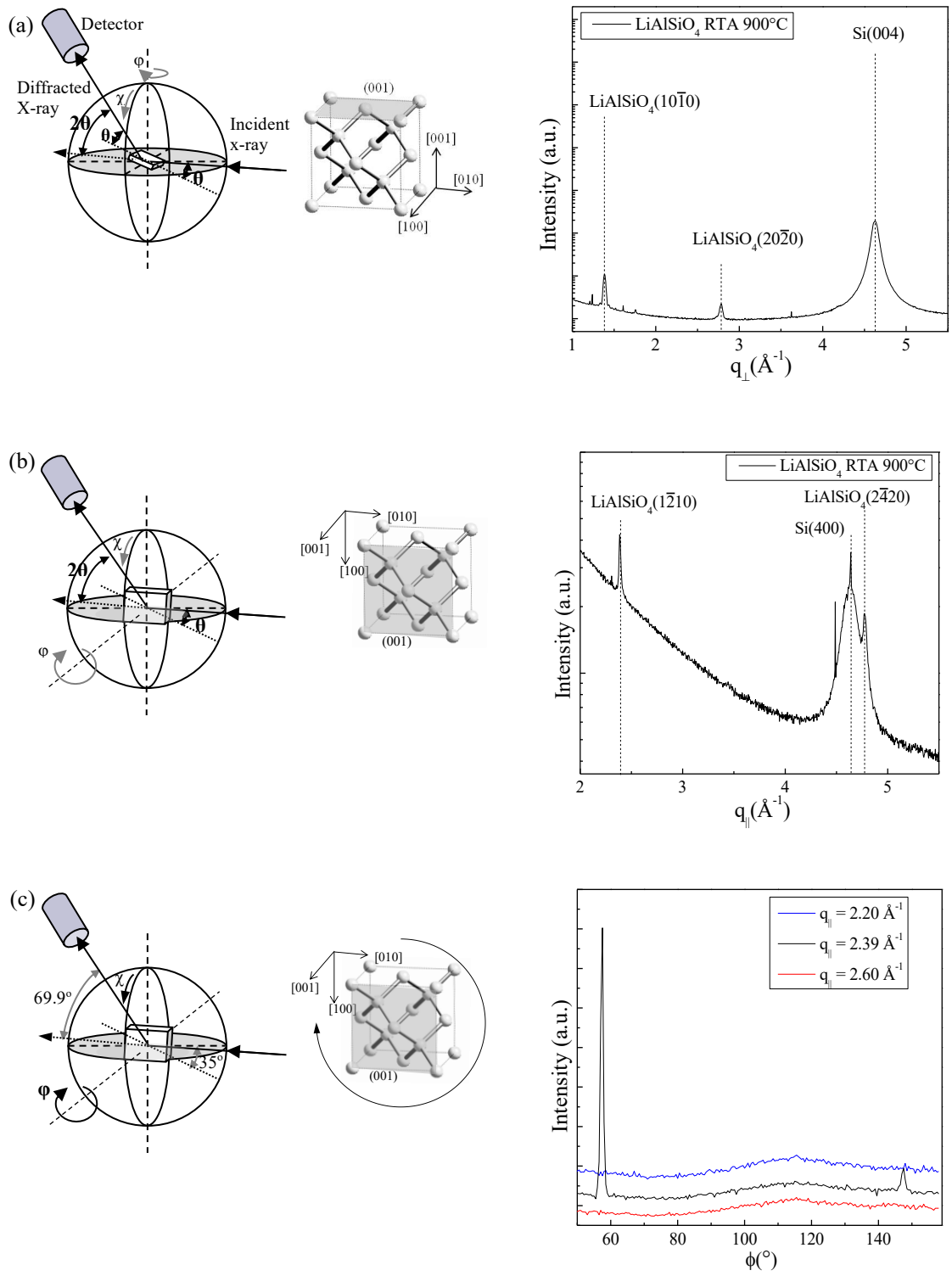
Figure 2-10. XRD geometries utilized on the four-circle diffractometer (SSRL) to analyze LiAlSiO$_4$ thin films and the resulting spectra (a) out-of-plane scans, (b) in plane scans, and (c) phi scans, where the shaded region is the (001) plane of Si.

A list of JCPDS references for a range of materials analyzed are listed in Table 2-10 as well as the various substrates utilized in this work.

Table 2-10. List of JCPDS references utilized in this work

Material	JCPDS Reference Code
Si	00-027-1402
Co_3O_4, CoO	00-042-1467, 00-042-1300
$LiAlSiO_4$	01-077-0158
MnO_2, MnO, M_2O_3	00-024-0735, 00-004-0326, 00-004-0732
$LiCoO_2$	00-044-0145, 00-050-0653, 00-037-1162
$LiMn_2O_4$	00-035-0782
$LiMnO_2$, Li_2MnO_3	00-009-0109, 00-027-1252
$Li_{22}Si_5$	01-073-2049
Pt	00-004-0802

An example XRD spectra is shown in Figure 2-11 for a $Li_{1+x}Mn_{2-x}O_4$ thin film deposited with cycle sequence 50(MnO_2)-1(LiOH) on a substrate consisting of 100 nm Pt/20 nm TiO_2/300 nm SiO_2/Si. X-rays of the wavelength associate with kβ of Al were not completely filtered out giving rise to a second smaller intensity peak associated with Pt(111) reflection on the Panalytical X'Pert Pro X-ray powder diffractometer. The (111) and (222) reflections of the $LiMn_2O_4$ spinel phase were observed indicating crystallization into the electrochemically active phase.
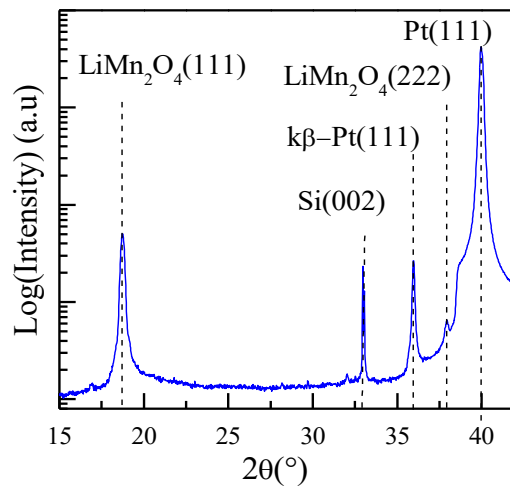
Figure 2-11. XRD scan of $Li_{1+x}Mn_{2-x}O_4$ thin film deposited on a Pt(111)-Si substrates, where the (111) and (222) reflection was observed of the spinel phase utilizing the Panalytical X'Pert Pro X-ray powder diffractometer.

2.2.4 Atomic Force Microscopy (AFM)

Atomic Force Microscopy was utilized to measure the surface morphology of the hybrid solid electrolyte thin films. AFM measurements are performed by monitoring the deflections in a Si cantilever with a 10-25 nm (nominal radius) sharp tip coated with an optically reflective PtIr coating connected to a piezoelectric actuator that maintains either a constant force or height above the sample. Deflections of the cantilever as it is moved across the sample surface are measured using a photodetector to monitor changes to an incident diode laser on the backside of the cantilever (Jalili 2004). AFM measurements can be performed in three modes: (1) contact mode, (2) non-contact mode, and (3) tapping mode (combination of contact and non-contact modes). Contact mode is generally used for harder samples, where the AFM probe tip is held with a constant force in contact with the surface and dragged across the surface measuring surface interactions. In non-contact mode, the cantilever tip is maintained at a set distance from the surface and the piezoelectric actuator is oscillated at or near its natural resonance frequency, where shifts

in its oscillation frequency are measured corresponding to interaction with the sample surface. Tapping mode is utilized for softer samples and to minimize stresses to the AFM probe tip from contact with the sample (Jalili 2004). In this work, surface morphology measurements were performed utilizing Bruker Scan Assyst probes on a Bruker Dimension FastScan Scanning Probe Microscope. The surface root mean square (RMS) roughness of a sample can be calculated using the equation below:

$$RMS = \sqrt{\frac{\sum(z_i - z_{avg})^2}{N}}$$

(2-15)

An example AFM scan is shown in Figure 2-12 of a 35 nm PV4D4 film deposited on a Si(001) substrate. All surface roughness analysis was performed utilizing the NanoScope Analysis Software, where AFM spectra were first plane-fit and flattened.
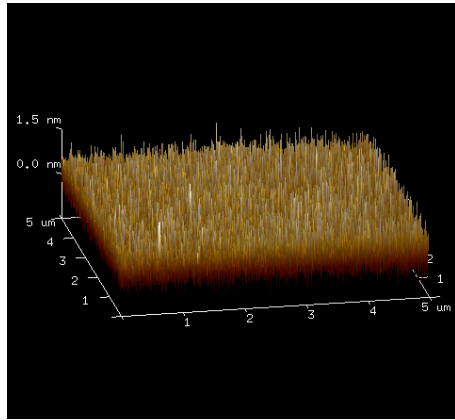
Figure 2-12. 3D AFM image of a 35 nm Poly(1,3,5,7-tetravinyl-1,3,5,7-tetramethylcyclotetrasiloxane (PV4D4) thin film deposited on Si(001). The surface roughness (RMS) was calculated to be 0.344 nm utilizing the NanoScope Analysis software.

2.2.5   Electron Microscopy

Electron Microscopy utilizes an accelerated electron beam to produce images with much higher resolution than traditional optical microscopy due to significantly reduced wavelength of the electrons. Transmission Electron Microscopy (TEM) requires thin samples generally below

<100 nm in thickness (depending on the acceleration voltage) to allow for the electron beam to pass through the sample. In bright field (BF) mode only the transmitted electrons are collected (not diffracted) making crystalline regions oriented in a way for strong diffraction to appear dark along with heavier atoms as they scatter a larger portion of the electron beam. In dark field (DF) mode the electron beam is tilted slightly from the optical axis and the diffracted beam is measured giving insight into the structure and morphology of the sample analyzed (Alford 2007). The capability of TEM to obtain high resolution imaging is owed to small wavelength of the accelerated electrodes, where the wavelength of the incident electron beam can be given by the de Broglie equation as shown in Eq.

(2-16), where λ_e is the wavelength of the electron, h is Plank's constant, m_0 is the mass of the electron, c is the speed of light, and E is the energy of the accelerated electron.

$$\lambda_e = \frac{h}{\sqrt{2m_0E(1 + \frac{E}{2m_0c^2})}}$$

(2-16)

Selected Area Electron Diffraction (SAED) can be utilized to gain site specific structural information, in which the incident electron beam makes the appropriate angle with a specific set of crystal planes such that Bragg's Law is satisfied (Eq. (2-14)). Due to the small wavelength of the electron beam in addition to the small Bragg Angles, the relation in Eq. (2-17) can be approximated, where R is the distance measured on the diffraction pattern, $L\lambda$, is the camera constant (product of the electron wavelength and cameral length) (Alford 2007).

$$Rd_{hkl} = L\lambda$$

(2-17)

The diffraction patterns of polycrystalline materials are marked by ring patterns consisting of the superposition of many differently oriented single crystals. Amorphous materials without the presence of long-range order produce diffraction patterns that appear as diffuse rings. CrysTBox

software was utilized for initial analysis utilizing the *diffract*Gui and *ring*Gui as shown in Figure 2-13 (Klinger 2015). First, the scale was calibrated for the diffraction pattern for nm^{-1} per pixel in the image. From the main beam (blanked by the beam blanker) the radius of the of each ring (1/nm) could then be related to the lattice plane from taking the inverse (nm) and indexed based on the Joint Committee on Powder Diffraction Standards (JCPDS) database. Several measured lattice spacing once indexed were then utilized to calculate the lattice constant.
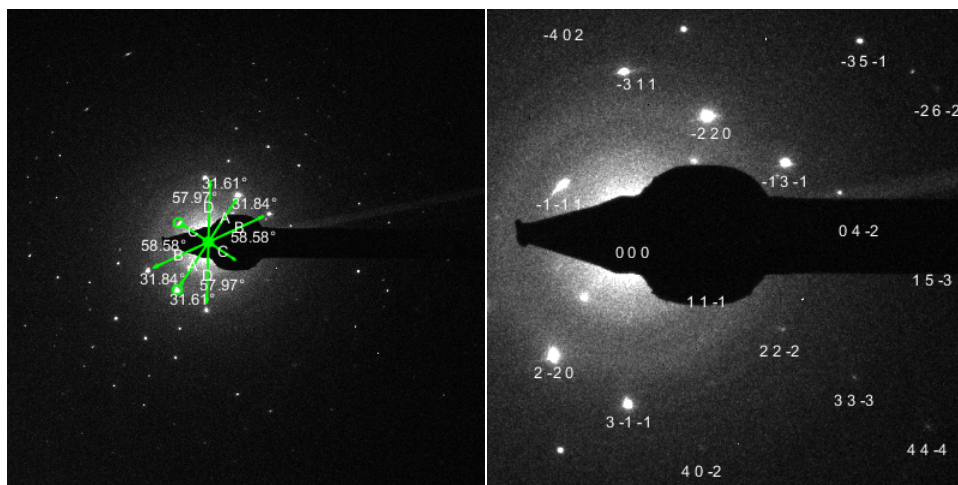
Figure 2-13. SAED analysis of a $Li_xAl_ySi_zO$ coated SiGe nanowire post lithiation utilizing the *diffract*Gui CrysTBox software. (Klinger 2015)

2.2.6 SiGe Nanowires for In-situ TEM Lithiation

SiGe nanowires with [112] axial growth direction were grown on various substrates Si(001) wafer and PVD TiN coated Si wedge substrates (Hysitron 5-0923) as shown in Figure 2-14. The Au nanoparticles were dispersed onto the Si wedge substrate and then heated up to 470°C under 3 Torr under H_2 flow. SiGe NWs were then synthesized through exposure to the silicon and germanium precursors (SiH_4 and GeH_4) diluted in 50% and 30% H_2, respectively. Post SiGe synthesis, the samples were deposited on via ALD $Li_xAl_ySi_zO$ as described above. For fabrication of a full cell, ALD $Li_{1+x}Mn_{2-x}O_4$ was deposited after ALD $Li_xAl_ySi_zO$ deposition and

the whole structure was annealed at 750°C. The wedge samples were adhered to Si(001) coupons

via high temperature carbon paste (Ted Pella 16057) for ease of handling.
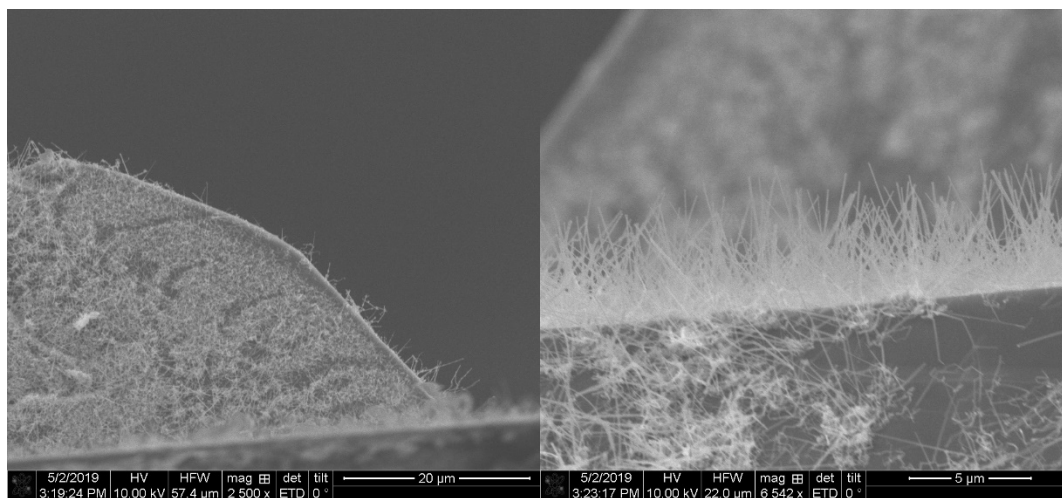
Figure 2-14. SEM images of SiGe nanowires before ALD deposition grown on PVD TiN coated Si wedge substrates (Hysitron 5-0923).

TEM sample preparation consisted of flattening the tip of Al-wire with a drill press

followed by cutting of flattened Al-tip with a razorblade to make a narrow plateau at the tip. The

silicon wedge substrates were then attached on the end of the Al wire utilizing conductive epoxy

(Chemtronics CW2400). When utilizing the silicon substrate, a small piece of the surface was

chipped under an optical microscope and attached to Al-wire via a conductive epoxy coated eye-

lash paint brush. The Al-wire was then fastened in the STM-TEM nanofactory sample holder

equipped with a piezoelectric manipulator. The counter electrode was made by scraping lithium

metal in an Ar glovebox with tungsten wire and attaching it to an Au "hat" that could be fastened

to the piezoelectric manipulator as shown in Figure 2-15. Samples were exposed to ambient for a

few seconds prior to loading the nanofactory holder into the TEM.
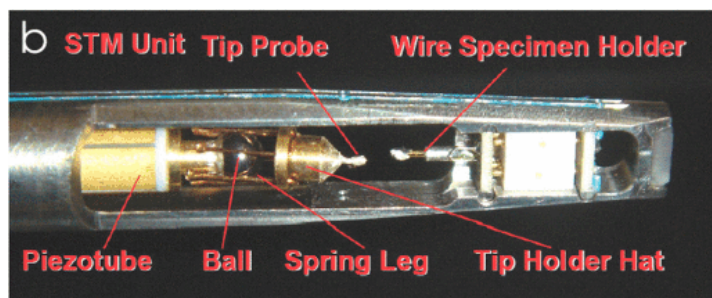
Figure 2-15. Example of STM-TEM Nanofactory holder that allows for electrical contact *in-situ* (Dong 2008). The SiGe nanowire sample was held on the fixed end at the tip of the holder, while the Li metal/Tungsten wire was fastened into the Au tip holder hat as shown above.

TEM Characterization was performed on FEI Technai F30 TEM operating at 300 kV. Electrical contact in-situ was made utilizing a piezoelectric manipulator with nanometric control. A Solartron Analytics Modulab equipped with a femptoammeter was used to perform galvanostatic and potentiostatic experiments. Image analysis was performed via imageJ, where threshold area mapping was performed to quantify the areal change in the nanowire post-lithiation as shown below in Figure 2-16.
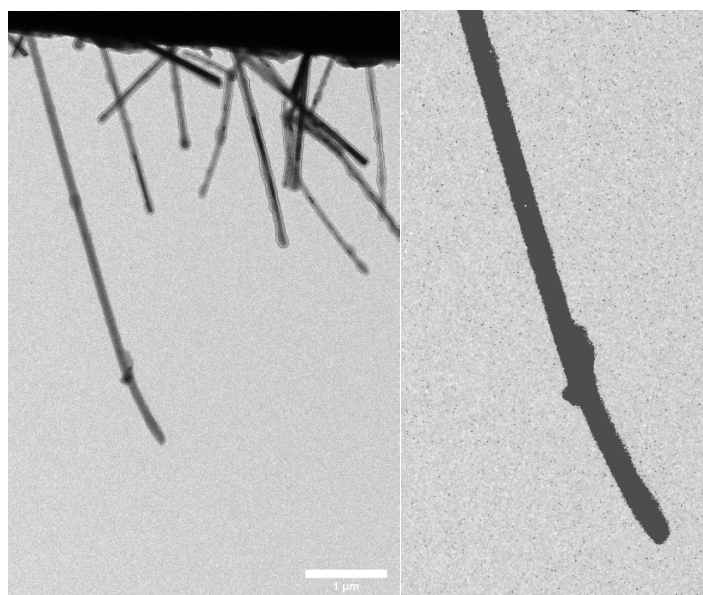
Figure 2-16. TEM image of SiGe nanowire post lithiation (left), and threshold adjustment processing (right) of single nanowire via ImageJ software for area analysis.

2.2.7 Electrochemical Impedance Spectroscopy (EIS)

Impedance is a circuit parameter that is the more general analogue of resistance defined for an ideal resistor. Spectroscopic Impedance measurements are generally performed by applying an AC sinusoidal potential (Eq. (2-18)) to an electrochemical cell and then measuring the resulting current response through the cell with a corresponding phase shift (Eq.(2-19)). Through using Euler's relationship, the expression for the impedance is given in Eq. (2-20).

$$E_t = E_0 \exp(j\omega t) \qquad (2\text{-}18)$$

$$I_t = I_0 \exp(j\omega t + \phi) \qquad (2\text{-}19)$$

$$Z = \frac{E_T}{I_T} = Z_0 e^{j\phi} = Z_0 (cos\phi + jsin\phi) \qquad (2\text{-}20)$$

The expression for the impedance is composed of a real and imaginary part. A Nyquist plot is generated by plotting the real component on the x-axis and the imaginary component on the y-axis with each point on the graph corresponding to a single frequency. EIS data is commonly analyzed by fitting the data to an equivalent electrical circuit consisting of the passive circuit elements: inductors, resistors, and capacitors. There are many possible circuit configurations for a given data set, making it crucial to only pick components that have physical analogue in the sample cell to be measured.

Table 2-11. Passive circuit elements and their corresponding impedance expressions

Component	Impedance
Resistor	$Z = R$
Inductor	$Z = j\omega L$
Capacitor	$Z = 1/j\omega C$
Constant Phase Element (CPE)	$Z = 1/(j\omega)^n C$

A simple model useful for modeling the ionic conductivity of a thin film between two metal electrodes is a resistor and capacitor in parallel. The simulated impedance response of a resistor in parallel with a capacitor and resistor in series with two sets of a resistor and capacitor in parallel, for several circuit parameter values are shown in Figure 2-17. The second circuit was chosen, in which R_1 might correlate to the contact resistance, and the two resistor and capacitor in parallel is associated with the ionic conductivity of two phases.
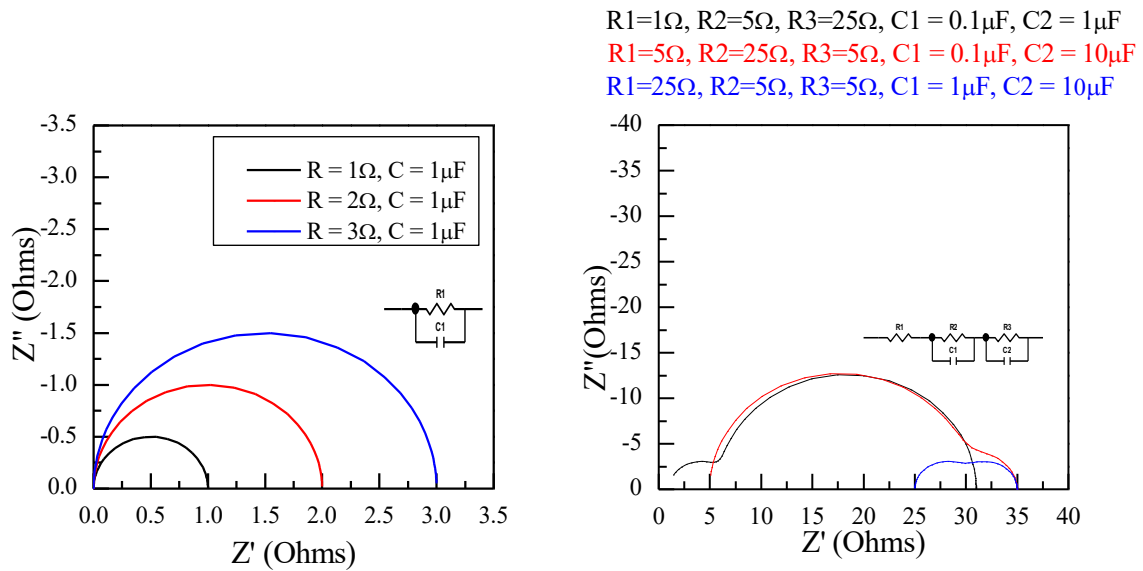
Figure 2-17. A Nyquist plot showing the simulated impedance response of (a) a resistor in parallel with a capacitor and (b) resistor in series with two sets of a resistor and capacitor in parallel, for several circuit parameter values.

For an ion conducting thin film the extrapolated DC resistance given by the diameter of the semi-circle (fitted resistor value) can be used to calculated the ionic conductivity of the sample as shown in Eq. (2-21), where t_{film} is the thickness of the thin film, A is the area of the electrode, and R_{Bulk} is the extrapolated DC resistance.

$$\sigma_{ionic} = \frac{t_{film}}{R_{Bulk} A}$$

(2-21)

91

Electrochemical Impedance Spectroscopy (EIS) was performed with a HP4284A LCR meter over a frequency range of 1MHz to 20Hz with an input signal of 13 mV. The thin films were characterized on a heated sample stage (Cascade Microtech), where temperatures were monitored by a type-k thermocouple. ALD $Li_xAl_ySi_zO$ films were deposited on conductive Si substrates with resistivity 0.003-.005 Ohms-cm. 500 μm diameter circular electrodes were sputtered through use of a shadow mask consisting of 10 nm Ti and 200 nm of Cu. A portion of the Si coupon was scribed with a diamond scribe then a tungsten probe was contacted within the scribe mark to make contact to the substrate. Tungsten probes were also utilized to make top contact to the circular Cu pads under light pressure.

The EIS spectra were fit utilizing an equivalent circuit model consisting of a resistor in series with a resistor and constant phase element in parallel, where the impedance as a function of frequency is given in Eq. (2-22).

$$Z(\omega) = R_1 + (R_2 + [(j\,\omega)^n C_1]^{-1})^{-1} \tag{2-22}$$

R_2 represents the extrapolated dc resistance utilized in the ionic conductivity calculation, where R_1 refers to a contact resistance and the constant phase element C_2 is utilized in place of a capacitor due to surface non-idealities behavior of the thin film system, where when $n = 1$ the constant phase element becomes an ideal capacitor (Sharon 2018)

2.2.8 Galvanostatic Charge/Discharge Cycling

All electrochemical measurements were performed in a flooded three electrode cell in an Ar-filled glove box (less than 1 ppm O_2/H_2O), where lithium metal foil was utilized as the counter and reference electrode. 1M $LiClO_4$ in a 1:1 by volume solution of ethylene carbonate and dimethyl carbonate was utilized as the liquid electrolyte. Thin film electrodes were deposited on Pt(100 nm)/TiO_2(20 nm)SiO_2(300 nm)/Si substrates to allow for electrical contact. Although the Si wafer

was thermally oxidized, Si surface was exposed upon cleaving of the wafer, so all measurements were performed with at least a 0.2V cut-off to prevent lithiation of the silicon substrate The $LiMn_{2-x}Co_xO_4$ thin films deposited on Pt-Si wafers was clipped via an alligator clip for electrical connection, where the active area was calculated for only the area exposed to liquid electrolyte. The defined area for liquid electrolyte contact was optically imaged and the area calculated from a custom MATLAB script. Volumetric capacities for 2D samples were calculated based on SE/SEM determine thicknesses and the active area exposed to liquid electrolyte, where gravimetric capacities were estimated based on the bulk density of Co_3O_4, and $LiMn_2O_4$. All electrochemical measurements were performed via a Bio-Logic VMP-3 potentiostat.

Galvanostatic cycling is a measure of the potential vs. time, while applying a constant current allowing one to determine the discharge/charge capacity of an electrode of interest. The term, C-rate, is utilized to provide relation of the applied current to the theoretical capacity. For example, if a specific current of 1 mA/cm^2 was applied to a thin film electrode with an areal capacity of 1 mAh/cm^2, it would be expected to charge/discharge in 1 hour and the associated C-rate would be 1C. Doubling the specific current to 2 mA/cm^2 would result in the electrode charging/discharging of the electrode in 0.5 hours and the applied current would be classified as a C-rate of 2C, etc.

In this work several thin film electrodes (both anodes and cathodes) were characterized utilizing Li metal for both the counter and reference electrodes. The upper and lower voltage limit was set based on the material of interest (4.5 – 3.5 V vs. Li/Li$^+$ for $Li_{1+x}Mn_{2-x}O_4$) in which the direction of the applied current was changed once the voltage cut-off had been reached. The charge/discharge curves allow for calculation of the lithiation capacity of a given electrode through Eq. (2-23), where I is the applied current, t is charge/discharge time before reaching the voltage

cut-off and V_{active} is the volume of electrochemically active material used in the working electrode. Specific capacities (mAh/g) can also be calculated through substitution of V_{active} with the mass of active materials used for the working electrode.

$$C_V = \frac{It}{V_{active}}$$ (2-23)

C-rates were determined utilizing the theoretical density of materials as well as volumetric estimates of the thin films. Rate capability of an electrode can be assessed by determining the capacity reduction of the electrode as a function of higher and higher rates due to increases in ohmic as well as charge transfer resistance. Furthermore, the coulombic efficiency can be determined through the ratio of the discharge/charge capacity, where low coulombic efficiencies are usually characteristic of unstable SEI formation. Galvanostatic cycling is a useful technique to assess an electrode's performance for continual use through monitoring the capacity retention as a function of continuous charge/discharge cycling. Charge/Discharge curves of a $Li_{1+x}Mn_{2-x}O_4$ thin film cathode is shown in Figure 2-18 at a specific current of 359.1 μA cm^{-2} with increasing upper voltage cut-off from 4.3-4.5 V vs. Li/Li^+. For example, the coulombic efficiency of the charge/discharge cycle with the 4.5V cut-off shown in Figure 2-18, would be (3.47 μAh cm^{-2}/3.51 μAh cm^{-2}) x100 = 98.8%.
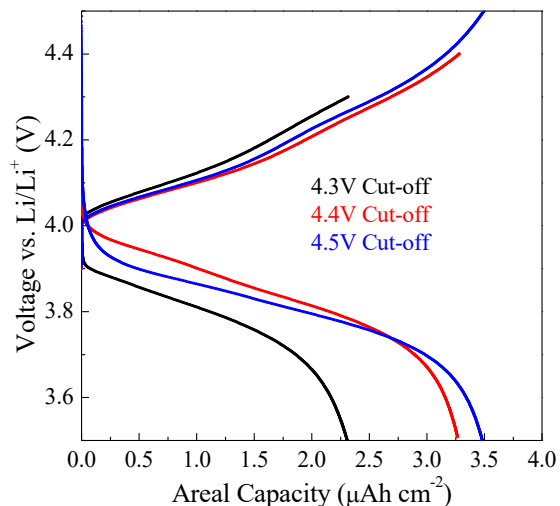
Figure 2-18. Galvanostatic charge/discharge curves for $Li_{1+x}Mn_{2-x}O_4$ sample deposited with sequence 250(MnO_2)-1(LiOH) with various higher voltage cut-offs at a specific current of 359.1 μA cm^{-2} corresponding to an estimated 50C.

In summary, this chapter discussed the custom-built reactors utilized to synthesize the thin films in this thesis as well as well as relevant material characterization techniques associated with assessing their structural, chemical, and electrochemical properties. For each characterization technique, a brief summary of the theory associated with each technique as well as example data and analysis were presented and are the basis for analysis for the subsequent chapters. Crucial for the development of thin films for integration into 3D lithium-ion microbatteries is first the interplay between processing conditions, precursor chemistries, and quantifying the resulting thin films chemical composition. As discussed previously, XPS is a excellent tool to determine surface composition, as well as provide additional information via depth profiling XPS (information about the bulk of the film(>10 nm)) and angle resolved XPS (information about the uppermost surface (<10 nm)). Next techniques such as TEM, SEM, AFM provide insight into the structural and morphological properties—especially important when interfacing multiple solid-state components as is the case in 3D lithium-ion microbatteries. Next, XRD plays the crucial role of determining

95

crystal structure, which then can provide insight into the interplay between thin film composition and the resulting crystallinity. Lastly, electrochemical characterization (EIS for solid-state electrolytes and CV/GV for thin film cathodes) is the most crucial technique to determine the ultimate performance of the synthesized thin films and to give comparison to other state-of-the-art materials in the literature. Utilizing a wide range of characterization techniques in this way helps to efficiently iterate on synthesis conditions to develop thin films with the desired properties and highest functionality.

CHAPTER 3:   ALD THIN FILM CATHODES

The ALD processes for the synthesis of two thin film cathodes ($Li_xCo_yO_z$ and $Li_{1+x}Mn_{2-x}O_4$) was developed through combination of a solid solution of constituent oxides (Co_3O_4, MnO_2, and LiOH) for direct integration in 3D Lithium-ion microbatteries. $Li_xCo_yO_z$ thin films were found to be air reactive and the crystallization of the layered $LiCoO_2$ phase proved difficult, so further focus was put into development of thin film $Li_{1+x}Mn_{2-x}O_4$. First, the PEALD process for MnO_2 was characterized demonstrating self-limiting growth, stable composition (within 5% relative composition), and well-controlled growth rate (MnO_2:0.2-0.3 Å/cycle) over various deposition temperatures. The stoichiometry of ALD $Li_{1+x}Mn_{2-x}O_4$ was effectively controlled to allow for crystallization into the electrochemically active $Li_{1+x}Mn_{2-x}O_4$ phase, but large lithium incorporation was observed at low ALD subcycle percentage potentially indicative a sub-surface reaction of LiO^tBu with MnO_2. Regardless, tuning of the ALD cycle ratio led to various degrees of Li content with a stoichiometry of $Li_{1+x}Mn_{2-x}O_4$, exhibiting electrochemical activity in both the 3.0V and 4.0V region depending on the lithium content. The $Li_{1+x}Mn_{2-x}O_4$ thin films exhibited great rate capability and capacity retention—maintaining 66% of the areal capacity upon increasing the rate by a factor of a 100 as well as 97% capacity retention over 100 cycles at 35.9 $\mu A \ cm^{-2}$ (~5C). In comparison, with micron-sized $LiMn_2O_4$ particles, the thin film $Li_{1+x}Mn_{2-x}O_4$ exhibited improved areal energy densities as well as superior rate-capability. The ALD $Li_{1+x}Mn_{2-x}O_4$ thin films exhibited a volumetric capacity of 52 $\mu Ah \ cm^{-2} \ \mu m^{-1}$ at a C-rate of ~0.5C, coupled with the high operating voltage (4.0V) offers some of best potential areal energy densities for ALD thin film cathodes, making it a viable material for integration with 3D lithium-ion microbatteries.

3.1   Atomic Layer Deposition of Cobalt Oxide

A thermal atomic layer deposition process for cobalt oxide using the chemical precursors cobalt bis(2,2,4,4-tetramethylheptanedioante) ($Co(tmhd)_2$) and H_2O was first explored. First the growth rate was characterized as a function of deposition temperature across a temperature range of 225-285°C. Film thicknesses were measured using spectroscopic ellipsometry on Si(001) substrates with a fitted SiO_2 native oxide layer between 1-2.5 nm, where relevant parameters and models are given in Table 2-5. Initially, the growth rate seemed to follow a similar trend as observed with the same precursor but with O radicals as the oxidant (Pham 2017), in that the apparent growth rate increased steadily with deposition temperature, without a true ALD temperature window, as shown in Figure 3-1 (a). At deposition temperatures of 265°C and above there existed a large variation in the apparent growth rate across depositions—which most likely could be due to a CVD-type reaction.
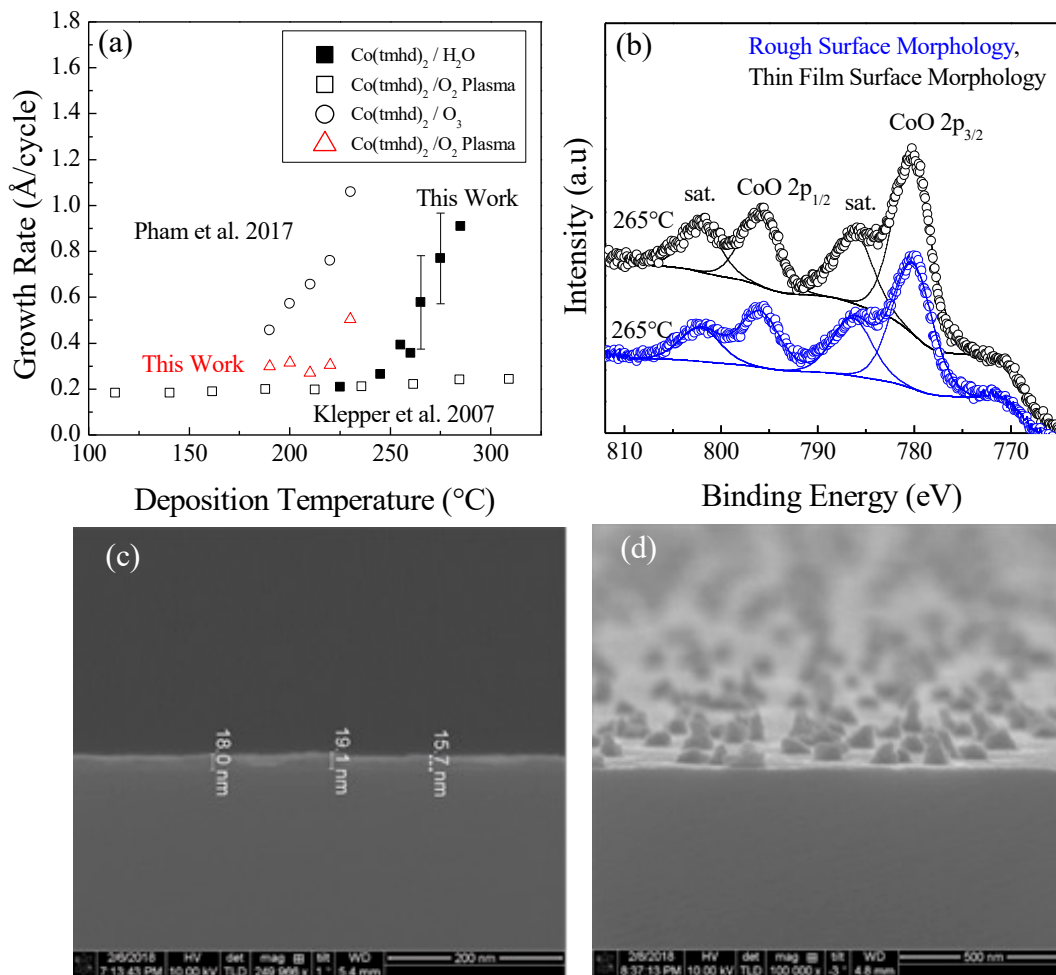
Figure 3-1. (a) Growth rate versus temperature for ALD of $Co(tmhd)_2$ with various oxidants (O radicals, O_3, and H_2O (this work)), showing ALD temperature window. All thicknesses were measured with spectroscopic ellipsometry, where factors such as material density and roughness can affect the fitted growth rates. Two distinct morphologies were observed during CoO_x deposition most likely due to precursor decomposition near the deposition temperature (b) the corresponding Co 2p XPS spectra for each morphology and (c-d) SEM images of the surfaces.

Upon inspection of the films via SEM, two distinct film morphologies were observed. For some of the samples a uniform film would be formed on the Si(001) surface, whereas for others a rough surface morphology would occur with a non-intact film visually similar to crystalline islands as shown in Figure 3-1 (c-d). The difference in surface roughness/morphology most likely was the

cause of the large variation of apparent growth rates at higher temperatures. Next the films were characterized by XPS to determine if there was chemical composition difference between the samples with the varied surface morphologies. Figure 3-1 (b) shows the XPS spectra for two samples exhibiting different surface morphologies, both deposited at 265°C. The survey spectra showed the presence of Co, O, C, and a week Si signal coming from the substrate, but no significant impurities were observed. Furthermore, the carbon content was similar between samples within the error of the measurement at 19-22%, where a significant portion can be attributed to adventitious carbon due to the ex-situ nature of the XPS measurement. The cobalt to oxygen ratio was calculated to be between 0.69 -0.73 for the two samples, which falls more closely in line with the Co_3O_4 (0.75) as compared to CoO (0.5), but at least some of the oxygen signal may be attributed to either organics on the surface and/or adsorbed CO_2. The Co 2p detailed scan is shown in where both samples have similar Co 2p binding energies as well as similar intensity of the shake-up satellite peaks. The spectra were aligned to sp^3 carbon at a binding energy of 284.8 eV. It is difficult to delineate the shift in binding energy when comparing the CoO $2p_{3/2}$ vs. Co_3O_4 $2p_{3/2}$, due to the resolution of the spectrometer, where the difference in binding energies is around 0.5 eV. The measured CoO_x $2p_{3/2}$ was at 780.2 eV and the CoO_x $2p_{3/2}$ satellite was measured to be 786.1 eV. The separation for the satellite peak is on the order of ~6 eV(Shen 1990), which is what has been observed for CoO versus 9 eV (Petitto 2004) for Co_3O_4. Furthermore, the ratio of the $2p_{3/2}$ and corresponding satellite peak is additionally indicative of CoO vs. Co_3O_4, where Co_3O_4 exhibits a much weaker as well as broader satellite peak. (Petitto 2004). From this it is concluded that the films are largely CoO. Due to the lack of true ALD temperature window—or near constant growth rate in some range of temperature a different process for CoO_x ALD was explored. Furthermore, the surface morphology and variation in growth rates at higher temperatures limits

the controllability desired for integration with other ALD processes, at least under the conditions tested here. A new process utilizing O_2 plasma as the oxidant is discussed below.

A plasma-based process consisting of the $Co(tmhd)_2$ and O_2 plasma was utilized to synthesize cobalt oxide thin films. In general, plasma based ALD processes generally exhibit larger processing windows that have the potential to allow a wider range of film properties. O_2 plasma was generated via a microwave power source remotely in a quartz ampoule as described in Chapter 2. All depositions were started with a 15s O_2 plasma exposure to both clean the substrate surface as well as confirm the stability of the O_2 plasma. First the growth rate was characterized at a deposition temperature of 200°C. A linear fit of the film thickness data with a y-intercept set to zero produced a fit growth rate of 0.3Å/cycle as shown in Figure 3-2. Film thicknesses of samples deposited with a lower number of cycles fell above the line indicative a slightly positive y-intercept. This could be due to error in accounting for the thickness of the native oxide layer, which also may be affected from O_2 plasma exposure during the pretreatment step as well as the initial ALD cycles. The saturation behavior for both the O_2 plasma and $Co(tmhd)_2$ exposure steps was characterized in which both showed self-limiting behavior in the 2D geometry tested. The growth rate was characterized for 50 ALD cycles with various pulse times (s), where the co-reactant was held at a constant pulse time. The O_2 plasma exposure was held constant at 10s, while the $Co(tmhd)_2$ pulse was increased from 5 to 20 seconds. For the O_2 plasma optimization the $Co(tmhd)_2$ pulse was held at 15s, while O_2 plasma exposure time was varied between 5 and 20 seconds. The self-limited growth rate was measured to be 0.4 Å /cycle, slightly higher than observed for depositions with a larger number of cycles. This again could be due to error in determination of the native oxide thickness as determination of thinner samples would be more prone to error.
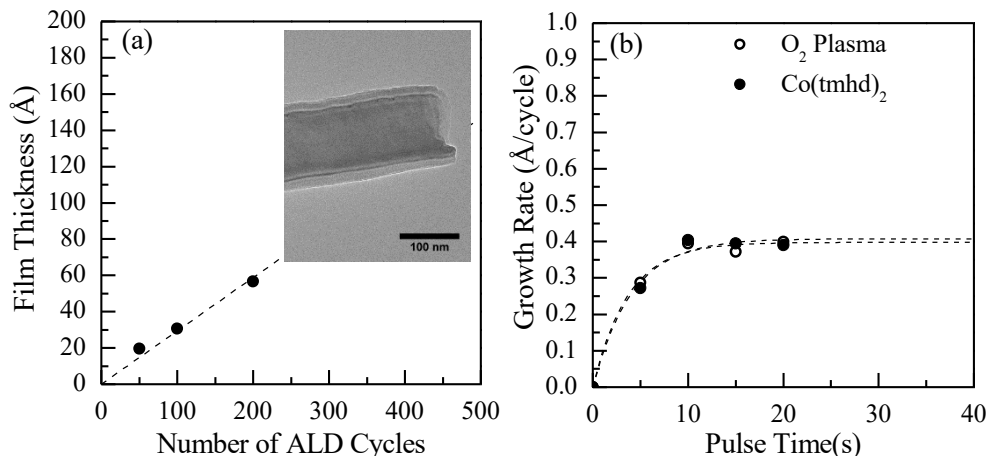
Figure 3-2. The growth rate and precursor saturation for PEALD of Co$_3$O$_4$. (a) Film thickness of Co$_3$O$_4$ measured via spectroscopic ellipsometry versus the corresponding number of ALD cycles. The growth rate was fit with a zero intercept at 0.3 Å/cycle all deposited on Si(001). A TEM image of a SiGe nanowire coated with PEALD Co$_3$O$_4$ is shown as the inset. (b) Precursor saturation of Co(tmhd)$_2$ and O$_2$ Plasma, where the growth rate was determined by dividing the number ellipsometry determined thickness vs. the number of cycles. 15s is adequate for the metal-organic precursor as well as the oxidation step.

Next, the growth rate and composition were characterized for Co$_3$O$_4$ films deposited with 500 ALD cycles at various substrate temperatures (190-230°C) to assess the ALD temperature window and establish a temperature region characterized by stable growth. The growth rate was relatively constant near 0.3 Å/cycle for temperatures between 190 and 220°C as can be seen in Figure 3-3. The growth rate increased to 0.5 Å/cycle at 230°C. XPS was utilized to determine the surface composition of the deposited films as shown in Figure 3-3, where a relatively constant composition was observed for deposition temperatures between 190 and 220°C with an oxygen content ranging from 51-55% and cobalt content ranging from 25-34% and carbon content ranging from 16-20%--resulting in a Co:O ratio between (0.45 -0.67). At a deposition temperature of 230°C, the carbon content was slightly increased (25%), while the oxygen content decreased

(45%)—potentially indicative of some precursor decomposition, where more detailed analysis of the XPS spectra is given below.
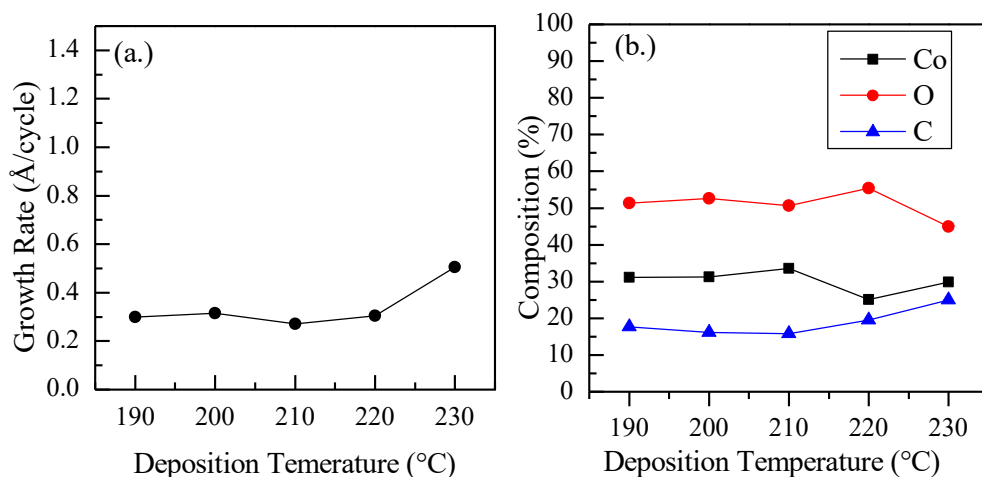
Figure 3-3. Growth rate and composition vs. deposition temperature for ALD Co_3O_4. (a) There exists a stable growth regime between 190 and 220°C, which is mirrored by a near constant composition (b) within the error of XPS measurements. An increase in growth rate is observed at 230°C along with a slight increase in carbon content potentially indicative of slight precursor decomposition or potential changes in film density.

XPS detailed scans of the Co 2p, O1s, and C1s are shown in Figure 3-4 for samples deposited at 200°C, 220°C and 230°C. The C 1s line-shape remains relatively unchanged across the samples deposited at different temperatures, in which a new peak corresponding to a different carbon bonding environment and/or a change in ratio between (C-O) and (C-C) would be expected from precursor decomposition at the higher deposition temperature. The Co 2p spectra of the samples deposited below 220°C are shifted around 0.5 eV in lower binding energy as compared to the sample deposited at 230°C, along with a smaller intensity satellite peak shifted to higher binding energy around 789 eV as compared to 786 eV. These observations coupled with the lower Co:O ratios are indicative of a majority of the Co_3O_4 phase at temperatures below 220°C and CoO phase at 230°C. It should be noted, that $Co(3^+)$ is one of the few cases, in which its binding energy

is shifted to lower binding energies as compared to its binding energy in the lower oxidation state of Co(2^+). Furthermore, the O1s peak for the samples grown below 220°C are consistent, whereas at 230°C although fit with 1 peak, the metal-oxygen peak becomes much broader indicative of changes that most likely are coming from a different oxygen binding environment.
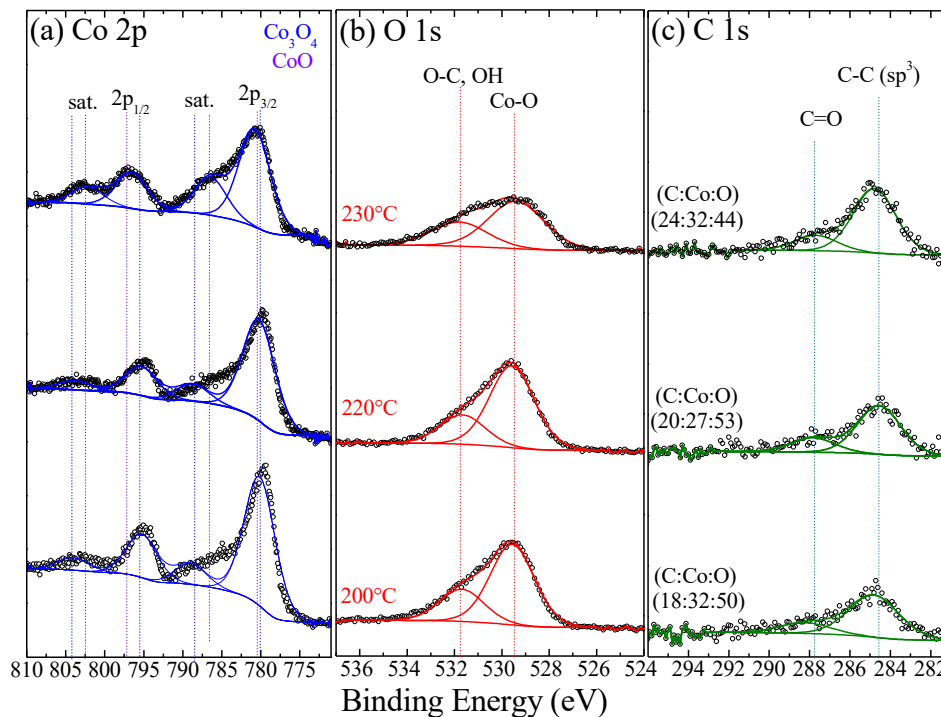
Figure 3-4. XPS detailed scans of ALD Co_3O_4 deposited at several substrate temperatures. Slight changes can be observed in both O 1s as well as Co 2p spectra at deposition temperatures above 220°C.

Clearer is the comparison of the Co 2p spectra of a plasma enhanced ALD Co_3O_4 sample deposited at 200°C as compared to the a CoO sample grown via thermal ALD deposited at 265°C as shown in Figure 3-5. The oxidation of cobalt in Co_3O_4 exists in a 2:1 ratio of Co^{3+} and Co^{2+}, where in the spinel structure, Co^{3+} sit in the octahedral sites, whereas Co^{2+} exist in the tetrahedral sites. The relevant binding energies and splitting values are given in Table 2-7 for both CoO and Co_3O_4. For the thermal ALD cobalt oxide sample the Co2p$_{3/2}$ peak lies at 780.3 eV, the Co2p$_{1/2}$ at

795.7 eV resulting in a splitting of 15.4 eV. The satellite peak lies at 786.1 eV resulting in a splitting of 5.8 eV from the corresponding Co 2p$_{3/2}$ peak. In comparison to the values obtained by (Chuang 1976) the satellite intensity and splitting are indicative of the CoO phase, but the 2p$_{3/2}$ and 2p$_{1/2}$ splitting falls between the Co$_3$O$_4$ and CoO phase. It has been observed that CoO oxidizes from prolonged atmospheric exposure—making the most likely scenario that the thermal ALD film is majority CoO with a surface Co$_3$O$_4$ layer. For the PEALD cobalt oxide sample the Co2p$_{3/2}$ peak lies at 779.5 eV, the Co2p$_{1/2}$ at 794.7 eV resulting in a splitting of 15.2 eV. The satellite peak lies at 788.7 eV resulting in a splitting of 9.2 eV from the corresponding Co 2p$_{3/2}$ peak. Therefore, it is concluded that majority phase is Co$_3$O$_4$ due to weak satellite feature at higher binding energies associated with Co^{3+} oxidation state, in addition to the 2p and satellite splitting.
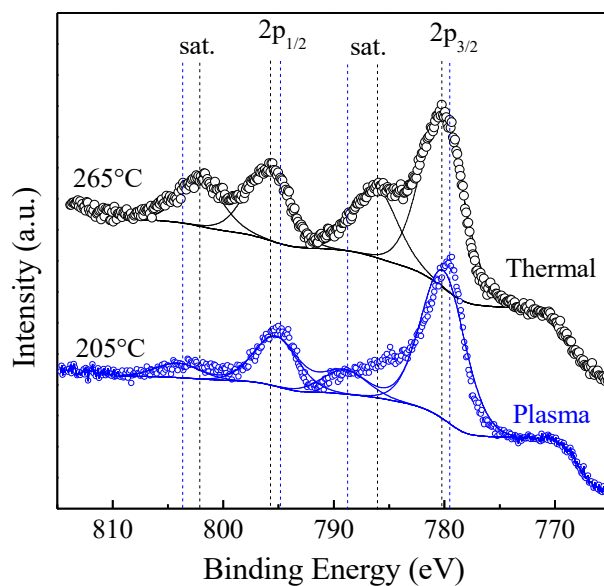
Figure 3-5. XPS detailed scans of thermal and plasma enhanced ALD of CoO$_x$. PEALD allowed for lower deposition temperatures as well as higher oxidation state of Cobalt.

The structural properties of the PEALD cobalt oxide thin films deposited on Pt(111) oriented-Si substrates were characterized via XRD as shown in Figure 3-6. In the as-deposited

state (shown in red) the films were polycrystalline with a broad $Co_3O_4(111)$ peak near 19.1° 2θ. The sample was rapid thermal annealed at 750°C for 1 min in O_2 at a ramp rate of 50°C/s and the XRD spectra measured. The *fwhm* of the $Co_3O_4(111)$ peak decreased significantly indicating larger grain size upon annealing. For electrochemical characterization the as-deposited Co_3O_4 was utilized for analysis allowing for integration with a wider range of battery relevant materials with a low thermal budget.
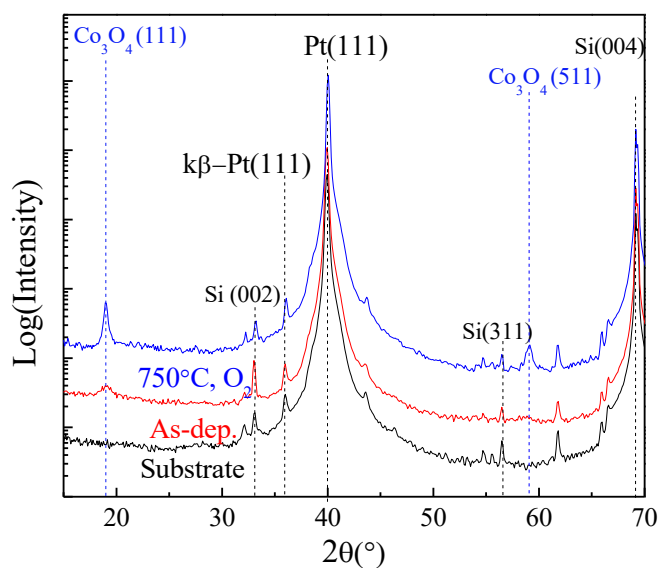
Figure 3-6. XRD spectra of PEALD Co_3O_4 deposited on Pt-Si substrates. The material was polycrystalline in the as-deposited state, where rapid thermal annealing in O_2 showed further crystallization and grain size growth.

3.2   Electrochemical Characterization of Co_3O_4 thin film Anodes

CoO and Co_3O_4 are conversion type anode materials exhibiting a high theoretical capacity (745 mAh/g), but their low electrical conductivity and mechanical stability severely limit their cycling and rate ability (Nitta 2015). To mitigate these structural issues, cobalt oxides have been synthesized as various nanostructures demonstrating improved electrochemical performance and

106

promise as a viable high capacity anode (Li 2011, Chen 2015, Jin 2015, Liu 2017). The proposed

overall conversion reaction mechanism for the lithiation of CoO and Co_3O_4 is shown below:

$$2Li^+ + 2e^- + CoO \rightarrow Li_2O + Co \qquad\qquad (3-1)$$

$$8Li^+ + 8e^- + Co_3O_4 \rightarrow 4Li_2O + 3Co \qquad\qquad (3-2)$$
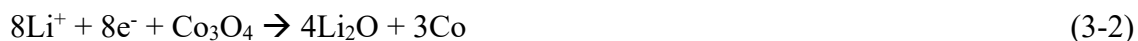
Cobalt oxide upon lithiation forms nanostructured cobalt metal clusters surrounded by a

Li_2O matrix. Complete elucidation of the delithiation mechanism has yet to be realized where

extraction of Li^+ from Li_2O is highly thermodynamically unfavored, but is thought to be catalyzed

via the cobalt metal nanoclusters, in addition to the increased reactivity due from the high surface

area nature of the Co and Li_2O domains (Poizot 2000, Wang 2002). Atomic layer deposition of

cobalt oxide films offers a unique opportunity to further explore the potential benefits of nano-

structuring the otherwise mechanically unstable anode and probe the electrochemical properties

(such as high rate ability) of the proposed thin films that may differ from those observed in bulk

or other nanostructures (Maier 2014, Put 2015).

To probe the electrochemical properties of the Co_3O_4 anodes, galvanostatic cycling was

utilized to assess the rate-ability and cycle-life as shown in Figure 3-7. Co_3O_4 films were

characterized (as-deposited) on Pt-Si in a 3-neck flask set-up with lithium metal as both the counter

and reference electrode submerged in 1M $LiClO_4$ in a 1:1 EC: DMC mixture. The submerged

substrate area was utilized to calculate the active area (cm^2) and the film thickness estimated via

spectroscopic ellipsometry. The higher voltage cut-off was set to 3V vs. Li/Li^+ and the lower

voltage was first set to 0.4V, to prevent unwanted lithiation of the Pt-Si substrate. The thin film

Co_3O_4 was cycled for 3 cycles at several rates ranging from C/10 to 5C corresponding to 2.3 μA

cm^{-2} to 114.7 μA cm^{-2}, where the rate was calculated based on theoretical capacity, the bulk density,

and the measured thin film volume. The 1st cycle had a rather lower coulombic efficiency (38.1%)

107

as observed previously with cobalt oxide-based anodes potentially due to irreversible Li_2O formation during the conversion reaction and solid electrolyte interphase (SEI) formation. With increasing charge/discharge the coulombic efficiency increased to >98%, with about a 1% drop on the first cycle when increasing the charge/discharge rate. At C/10 with a voltage cut-off at 0.4V the measured capacity was 3183 mAh/cm^3 and 3762 mAh/cm^3 with a 0.2V cut-off. Moving the theoretical charging time of C/10 to 5C (increasing the charge/discharge time from 10 hours to 0.2 hours), the capacity retention was 77%. The theoretical capacity for Co_3O_4 is 5444 mAh/cm^3 (891 mAh/g). The discrepancy in the results here can be due to several reasons most likely due to error in the thin film volume calculation as well as with the assumption that the as-deposited film density is the same as in the bulk. If the volume of the Co_3O_4 thin film was less than expected the measured capacity would be lowered, compounded by the fact that the theoretical rates would be higher further leading to reduced capacity. If the third cycle at C/10 0.2 V cut-off is to be taken and the non-rate limited capacity, then the corresponding rates would be rates would be increased by a factor of 1.4 Assessment of the effect of adding various solid electrolyte coating as well as the long-term cycling stability is discussed in Section 5.2. Specifically, addressment of the low coulombic efficiency is crucial for implementation of Co_3O_4 as a thin film anode in a solid-state device in which Li^+ is limited in the solid electrolyte layer.
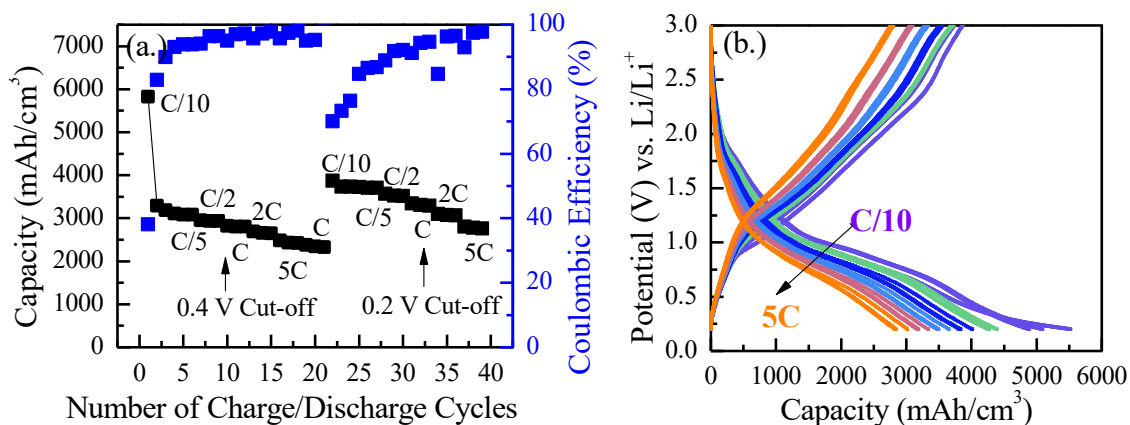
Figure 3-7. (a) Summary of the discharge capacity and Coulombic efficiency of a ~40 nm ALD Co_3O_4 film at various rates. Two lower voltage cut-offs were utilized (0.4V and 0.2V vs. Li/Li$^+$) to prevent lithiation of the underlying silicon substrate layer. The large first cycle capacity loss was most likely due the conversion reaction and the loss of Li to form Li_2O. The C-rates were calculated from the theoretical capacity and density of Co3O4 where C-Rates of C/10 to 5C corresponded to a specific current of (2.3 to 114.7 $\mu A/cm^2$) (b) Charge/discharge curves for a ~40nm ALD Co_3O_4 film at various rates (C/10 to 5C) where the C-rate was determined from the theoretical capacity and theoretical density of Co_3O_4.

3.3   Atomic Layer Deposition of $Li_xCo_yO_z$

ALD of $LiCoO_2$ has been previously demonstrated utilizing the precursors: $CoCp_2$, LiO^tBu, and O_2 plasma, but the 1:1 Li:Co stoichiometry was not able to be achieved as the films were cobalt rich even at higher CoO_x/LiOH ALD cycle ratios demonstrating a maximum capacity of around 90 mAh/g.(Donders 2013). A different approach was explored here, combining the thermal ALD process for LiOH with LiO^tBu and H_2O with the PEALD process of Co_3O_4. Utilization of H_2O as the oxidant over O_2 plasma was chosen as the LiO^tBu/O_2 process has been observed to grow Li_2CO_3 thin films (Kozen 2014, Hornsveld 2017). The growth rates for the individual oxides is shown in Figure 3-8 (a) corresponding to 1 Å/cycle for LiOH (225°C) and 0.3 Å/cycle for Co_3O_4 (200°C). Next the composition of was characterized for various ratios of ALD cycle ratios between the LiOH and Co_3O_4 process with the following super cycle $n[x(Co_3O_4)-y(LiOH)] +50(Co_3O_4)$ capping layer. A 50 cycle Co_3O_4 layer (approximately 1.5 nm) was chosen in order to prevent

LiOH surface reaction with CO_2 to form lithium carbonate. Initial characterization of ALD $Li_xCo_yO_z$ showed low growth rates most likely due to some incubation time in combining the two processes, so a "nanolaminate" approach was taken. The Li/(Li + Co) composition vs. Li/(Li+Co) Cycle percentage is shown in Figure 3-8 (b) for samples grown with the following supercycles: 25(Co_3O_4)-25(LiOH), 25(Co_3O_4)-50(LiOH), 25(Co_3O_4)-100(LiOH), 20(Co_3O_4)-100(LiOH), and 10(Co_3O_4)-90(LiOH), corresponding to ratios of 1:1, 1:2, 1:4, 1:5, and 1:9.
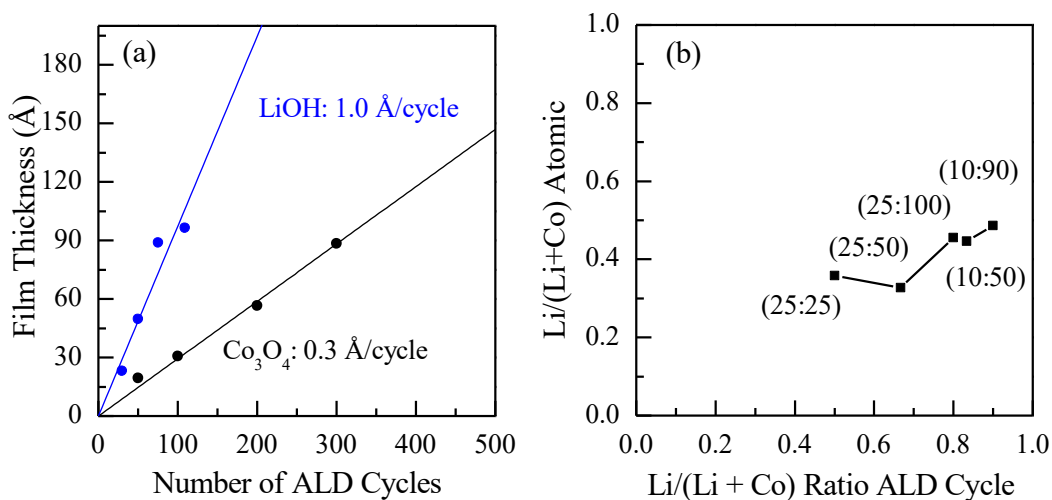
Figure 3-8. (a) The growth rate for individual oxides of LiOH/Li_2O and Co_3O_4 and (b) the composition vs. ALD cycle ratio for ALD $Li_xCo_yO_z$ with the ALD cycle sequence of a(Co_3O_4)-b(LiOH) with a 1.5 nm capping layer of Co_3O_4.

The Co 3p and Li 1s regions as well as XPS survey spectra are shown in Figure 3-9. Due to the low atomic sensitivity factor (ASF: 0.025), quantification of lithium concentration is difficult and prone to air due to low signal to noise. The $3p_{3/2}$ and $3p_{1/2}$ components cannot be resolved, where a single peak is observed near 61 eV, as expected for cobalt oxide, where delineation of the specific oxidation state is difficult to resolve at the resolution of the spectrometer. The Li 1s peak is found to be near 54.5 eV indicative of lithium oxide, which lends to idea of the absence of lithium carbonate.
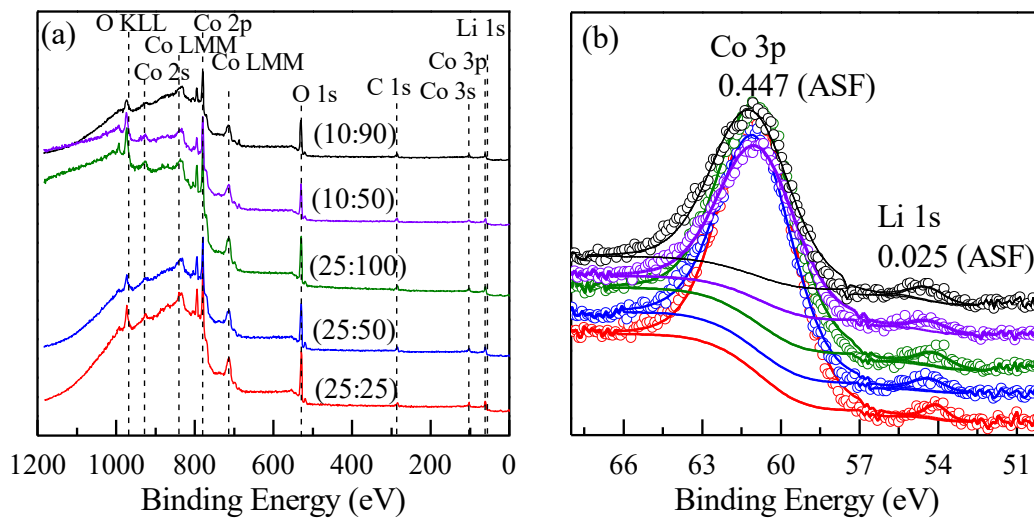
Figure 3-9. XPS (a) survey spectra and (b) detailed scans in the Co 3p and Li 1s region for ALD Li_xCo_yO samples deposited with various ALD cycle ratios consisting of a(Co_3O_4)-b(LiOH) all with a 1.5 nm Co_3O_4 capping layer

Increasing the number of LiOH cycles in the overall super led to an increase the lithium content as expected. Since all films were capped with 1.5 nm of Co_3O_4 (50 cycles) to protect from ambient reaction it is expected that a higher Co composition on the surface as compared to the bulk of the film. This trend contrasts to what was observed previously for ALD $LiCoO_2$ (Donders 2013), where increasing Li_2CO_3 ALD cycles did not lead to increase lithium content past a certain threshold, most likely due to the nanolaminate structure deployed here. Although similar cycle ratios were used in that study, the difference here is the use of greater number of cycles for each oxide component (i.e. 25(Co_3O_4)-100(LiOH) vs. 1(Co_3O_4)-4(LiOH)) which potentially can eliminate the effect of incubation times of each constituent oxide. These findings are in stark contrast to the results presented in the following sections, in which the growth behavior for similar process for synthesizing $Li_xMn_yO_z$ is dramatically different, reflecting some of the processing challenges in synthesizing lithium containing metal oxides.

A series of rapid thermal annealing treatments were assessed at 650ºC, 750ºC, and 850ºC for 1 minute. Upon visual inspection the films post rapid thermal annealing across all of the compositions became opaque with visual optical features upon annealing. This could be due to film delamination during the annealing step, where platinum as an order of magnitude lower thermal expansion coefficient (2.6×10^{-5} vs. 1.30×10^{-5} °C^{-1}), although the lattice mismatch between the $LiCoO_2(001)/Pt(111)$ is around 1.5%. X-ray diffraction is shown in Figure 3-10 of a thin film $Li_xCo_yO_z$ (25:25) sample in the as-deposited state, after rapid thermal annealing at 750°C, as well as the Pt-Si substrate and a ALD Co_3O_4 sample rapid thermal annealed at 750°C. In the as-deposited $Li_xCo_yO_z$ there is a very broad peak centered around 19°, which could be correlated to the $Co_3O_4(111)$ or $LiCoO_2(003)$ reflection. In the annealed $Li_xCo_yO_z$ sample two peaks appear one at 18.64° and 18.12° as compared to the single peak observed in the annealed Co_3O_4 sample at 18.72 corresponding to the (111) reflection. These peaks could be associated with the $Co_3O_4(111)$ or $LiCoO_2(003)$, with literature values of 19.001° (00-042-1467) and 18.959° (00-050-0653), respectively. The second peak shifted to lower 2 theta could be the result of a lithium-deficient $Li_{1-x}CoO_2$ consistent with the XPS results. Furthermore, there are weak peaks that could be associated with the $LiCoO_2(101)$ and $LiCoO_2(015)$ planes not observed in the Co_3O_4 sample, but shifted to lower 2 theta. Also, there was the absence of the $Co_3O_4(220)$ and $Co_3O_4(511)$ peaks observed in the Co_3O_4 sample.
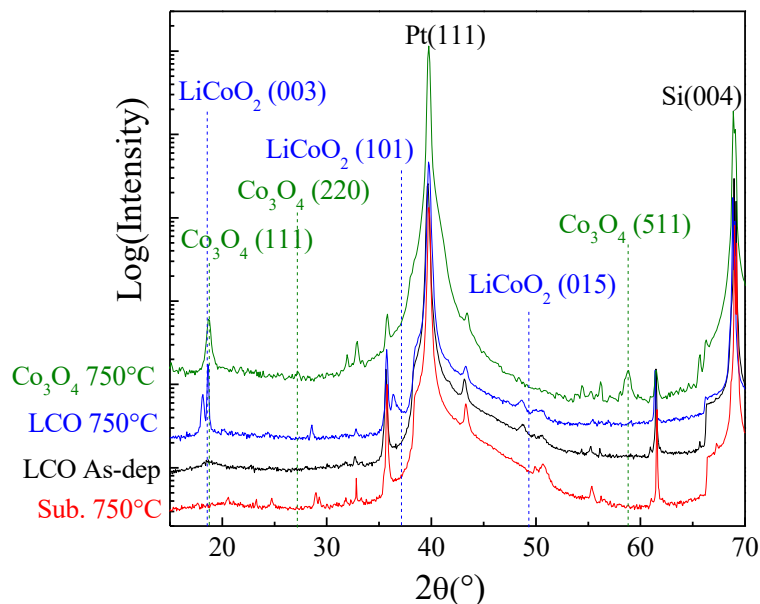
Figure 3-10. XRD spectra of 25(Co$_3$O$_4$)-25(LiOH) with measured as-deposited composition of Li$_{0.36}$Co$_{0.63}$O$_x$ in the as-deposited state and post rapid thermal annealing for 1 minute at 750°C (black, blue). As a comparison the XRD spectra of an ALD Co$_3$O$_4$ sample and the Pt-Si substrate both rapid thermal annealed for 1 minute at 750°C are shown.

Although the stoichiometry was able to be controlled through tuning of the ALD process, the LiCoO$_2$ thin films were found to be opaque upon annealing as well as sensitive to ambient exposure. In the next section, a similar process utilizing Mn(thd)$_3$ instead of Co(thd)$_2$ is discussed for synthesis of LiMn$_2$O$_4$ thin film cathodes.

3.4   Plasma Enhanced Atomic Layer Deposition of MnO$_2$

Like the PEALD process for Co$_3$O$_4$ as described above, a process was characterized for PEALD of MnO$_x$ with the metal-organic precursor tris-(2,2,6,6-tetramethylheptan-3,5-dione) manganese (III) and O$_2$ plasma. A PEALD process utilizing Mn(thd)$_3$ with several plasma co-reactants (H$_2$, NH$_3$, H$_2$O) has also been developed, where various oxidation states of Mn ranging from MnO to MnO$_2$ were obtained for the varying plasma species. (Mattelaer 2015). In the study

by Mattelaer et al., O_2 plasma was shown to produce manganese oxide thin films, but self-limiting behavior was not achieved in the conditions tested. This process for PEALD of MnO_x was further explored over a wider range of processing conditions as presented below. First the saturation conditions for each co-reactant was characterized at a deposition temperature of 225°C. Holding the O_2 plasma exposure to 10s, the growth rate of deposited MnO_x thin films was characterized as a function of $Mn(thd)_3$ pulse time—showing constant growth rates for $Mn(thd)_3$ pulses greater than 30s. The growth rate was then characterized for depositions carried out holding the $Mn(thd)_3$ pulse to 50s and varying the O_2 plasma exposure from 5-20s, where for all plasma exposures tested the growth rate was consistent around 0.2 Å/cycle—confirming saturation behavior for precursor couple as shown in Figure 3-11. These findings in comparison to the study by Mattelaer et al., could potentially due to the varying processing conditions: deposition temperatures (>205°C reported here vs. 180°C), as well as the plasma conditions (Microwave: 25W reported here vs. RF:300W). The varying plasma conditions could have wide range of effects of electron temperature, radical and ion density, etc. in the O_2 plasma. These saturation conditions (precursor pulse length) characterized here for this specific reactor set-up, shown adequate for planar deposition, most likely would also need to be optimized for high-aspect ratio structures. Next the growth rate of the as-deposited MnO_x thin films on Si(001) was characterized via spectroscopic ellipsometry. Initially at a low number of cycles (<100), the growth rate is linear, with a growth rate of 0.6 Å/cycle, while at increased number of cycles the growth rate decreases to 0.2 Å/cycle as shown in Figure 3-11. Due to the thickness of the films (<2 nm) at a low number of ALD cycles, cross-checking to cross-sectional SEM was not possible. The change in growth rate could be a nucleation effect, where there could be an increased growth rate on the Si(001) surface.
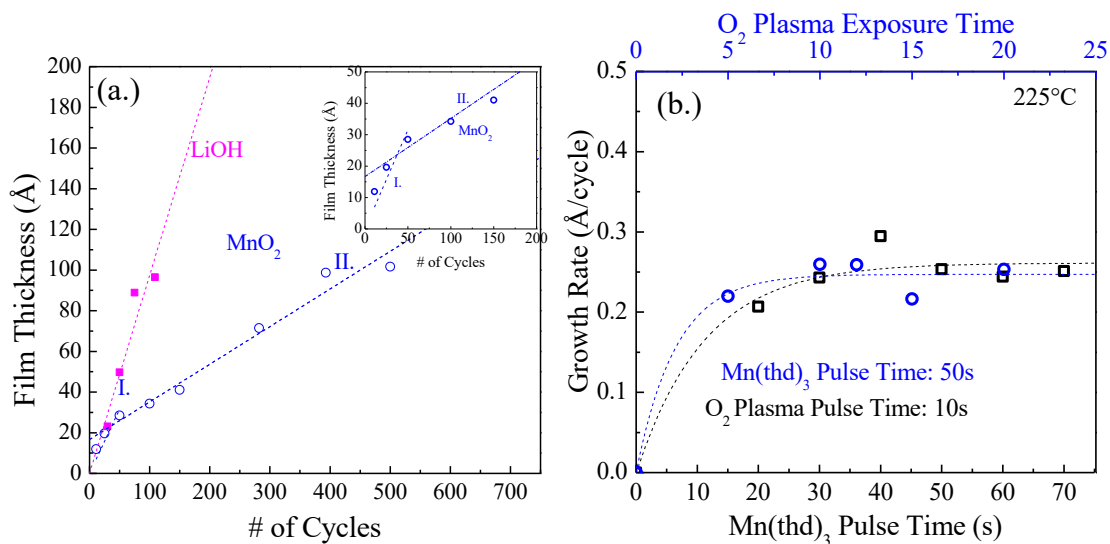
Figure 3-11. Growth characterization for PEALD of MnO$_x$ and ALD of LiOH: (a) Growth rates for LiOH(pink) and MnO$_x$(blue) measured via spectroscopic ellipsometry with a calculated growth rate of 1.0 Å/cycle and 0.3 Å/cycle, respectively. The growth rate appeared to follow two regimes changing near 100 ALD cycles for ALD MnO$_x$ more clearly seen in the zoomed-in inset. (b) The growth rate as function of precursor pulse time for Mn(thd)$_3$ and O$_2$ plasma demonstrating self-limiting behavior.

Next, the growth rate and composition of the as-deposited films were characterized as a function of the deposition temperature ranging from (205°C-265°C). The growth rate of MnO$_x$ thin films consisting of 500 cycles on Si(001) varied between 0.19-0.26 Å/cycle, increasing slightly with increasing deposition temperature as shown in Figure 3-12. The slight increase in observed growth rate could also be a function of changes in film density and film roughness, which can affect film thickness measurements utilizing spectroscopic ellipsometry. Lastly, the surface topology was characterized with atomic force microscopy for the samples deposited between 205°C - 265°C as shown in Figure 3-12. An increasing surface roughness was observed with increasing deposition temperatures from 0.44 -1.83 nm.
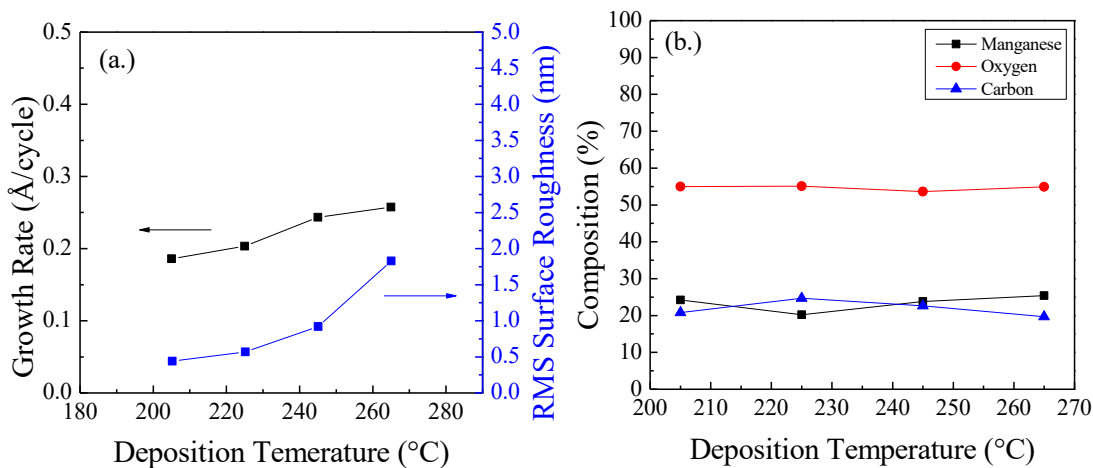
Figure 3-12. ALD temperature window of PEALD MnO_x. (a) The growth rate and surface roughness as a function of deposition temperature for MnO_2 films deposited on Si(001) and the corresponding surface composition (b) as quantified via XPS.

The composition was characterized via XPS spectroscopy, where the composition was relatively constant across the deposition temperatures varying within 5% as shown in Figure 3-12 (b). The Mn:O ratio ranged from 0.37 to 0.46 most indicative of the MnO_2 phase, although excess oxygen is expected on the surface due to the ex-situ nature of the measurements. For all samples, there was around 20-25% carbon content—where a large contribution is expected to be adventitious carbon species due to prolonged ambient exposure prior to XPS characterization. The XPS detailed scans were further analyzed to determine the oxidation state as manganese oxide exists is several different stoichiometries: MnO, Mn_3O_4, Mn_2O_3, and MnO_2. Figure 3-13 shows the detailed scans for Mn 2p, O1s, and C1s for the 4 samples deposited at temperatures ranging from 205°C-265°C. First, upon inspection of the C1s spectra there was large peak associated with sp^3 carbon species, which served as the binding energy alignment at 284.8 eV. For all the samples there was a peak to higher binding energy most-likely associated carbon-oxygen species at 288.5 eV—indicative of potential adsorbed CO_2, surface organic species from ambient exposure, or a degree of the thd

ligand incorporation. Upon inspection of the O1s spectra, there exists two peaks one at near 529.5 eV—attributed to the Mn-O bond, and another at 531.5 eV attributed to oxygen-carbon bonded containing species, where the O1s peak associated with Mn-O bonding has been observed to vary between 529.5 – 530.0 eV depending on the oxidation state (Nelson 2000).
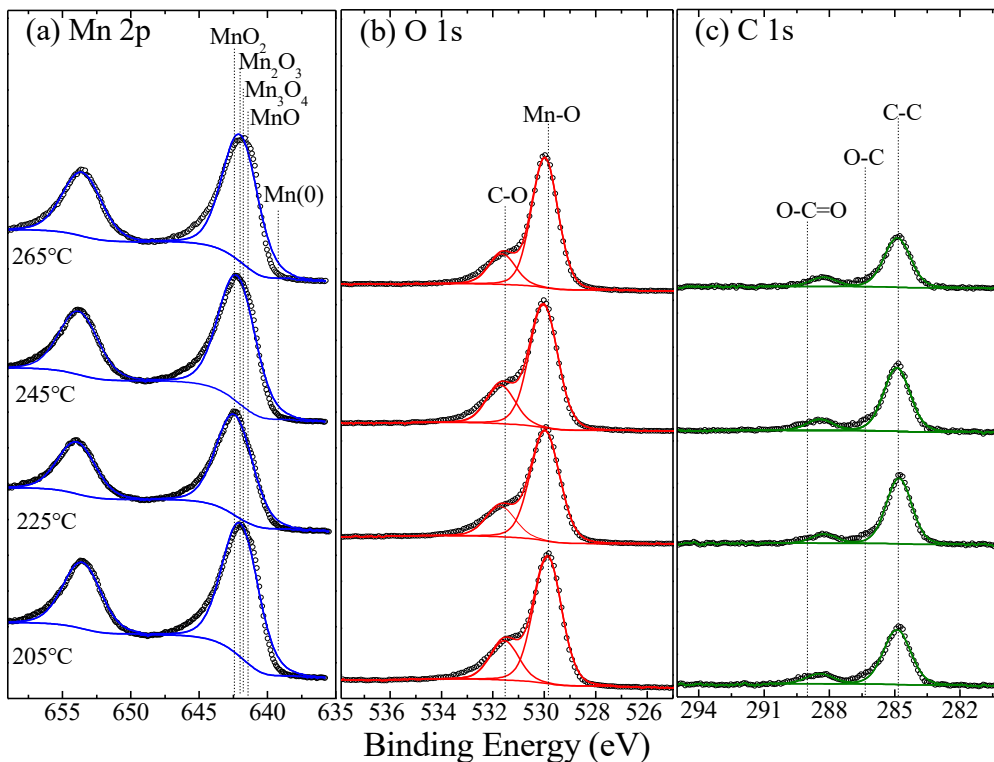
Figure 3-13. XPS Detailed Scans of the Mn 2p, O1s, C1s of the MnO$_x$ samples deposited with temperlatures ranging from 205 to 265°C.

Various fitted values of the Mn 2p spectra for samples deposited at the four deposition temperatures are tabulated in Table 3-1. The shift in binding energy for the various oxidation states of Mn are within 1-2 eV, making definitive assignment difficult at the resolution of the spectrometer. The Mn 2p$_{3/2}$ was fit to a single peak, which was 642.0-642.4 eV for all the samples. From the NIST XPS database marked reliable, with two-point correction of the energy scale, the following ranges for the Mn 2p$_{3/2}$ peaks were as follows: Mn (638.8-639 eV) (Hsin-Kuei 1981,

Chourasia 1994), MnO (640.8 eV) (Di Castro 1989), Mn_3O_4 (641.6 eV) (Tan 1991), Mn_2O_3 (641.7 eV) (Di Castro 1989), MnO_2 (642.2 eV) (Tan 1991). From the peak position fit here, MnO can be ruled out, with MnO_2 as the most likely oxidation state. This coupled with the measured composition ratio of Mn:O being less than 0.5 is further indicative of the MnO_2 phase.

Table 3-1. Fitted XPS parameters for Mn 2p and Mn 3s spectra.

Deposition Temperature (°C)	Mn $2p_{3/2}$ (eV)	Mn $2p_{1/2}$ (eV)	Mn 2p splitting (eV)	Mn3s ^7S (eV)	Mn 3s ^5S (eV)	Mn 3s exchange-splitting (eV)	Mn:O
205	642.0	653.6	11.6	83.7	89.0	5.3	0.44
225	642.4	653.9	11.5	84.0	89.0	5.0	0.37
245	642.2	653.8	11.6	83.7	89.0	5.3	0.44
265	642.0	653.6	11.6	83.6	89.0	5.4	0.46

XPS detailed scans of the Mn 3s spectra were also measured to further assess the oxidation state of the deposited MnO_x. Photoelectron transitions for the 3s valence state have two possible final states $(3s^13p^63d^x)$ from an initial state $(3s^23p^63d^x)$, where x = 3,4,5 for the oxidation states of Mn^{4+}, Mn^{3+}, Mn^{2+}, respectively, where in one final state the 3s electron is correlated with the 3d electrons of parallel spin and the other antiparallel (Nelson 2000). Across all samples the Mn 3s splitting was between 5.0-5.3 eV as compared to those measured for MnO_2 (4.5 eV) and Mn_2O_3 (5.4 eV), indicative of most likely a mixed phase of MnO_2 and Mn_2O_3 (Nelson 2000). Analysis of oxidation of metal oxides is often difficult to fully characterize due to surface sensitive nature of XPS as a technique coupled with the fact that the oxidation state may be a function of surface depth. After the characterization of the PEALD process for MnO_x, incorporation of the thermal ALD process for LiOH was carried out for deposition of $LiMn_2O_4$ thin films as discussed in the next section.

3.5   Growth Characterization of PEALD of $LiMn_2O_4$

Building off the PEALD process for MnO_2, a process for ALD of lithium manganese oxide was developed via incorporation of the thermal ALD process of LiOH. $LiMn_2O_4$ has been previously synthesized via atomic layer deposition process consisting of $Mn(thd)_3$, Li(thd), and O_3 where Li(thd) and LiO^tBu was found to directly react with MnO_2 to form the spinel $Li_{1+x}Mn_{2-x}O_4$ structure (Miikkulainen 2014). $Li_xMn_yO_z$ thin films were deposited utilizing a cycle sequence of $[x(MnO_2)$-$y(LiOH)]x$ n cycles deposited on Pt(111)-Si substrates for electrochemical characterization and Si(001) substrates for growth rate characterization via either spectroscopic ellipsometry or SEM. Before every deposition the substrate was exposed to a 15s O_2 plasma exposure prior to starting the deposition. First the composition was characterized as a function of deposition sequence, as shown in Figure 3-14, where various cycle ratios: $n[x(MnO_2)$-$y(LiOH)]$, where n was chosen to make the total number of cycles near 800. Samples referred to as (a:b) correspond to the MnO_2 to LiOH ALD cycle ratio; for instance (50:1) refers to a deposition sequence of $[50(Mn(thd)_3)$-$1(LiOtBu/H_2O)]$. Remarkably, lithium rich films were observed for samples deposited with ALD cycles ratios between: $[15(MnO_2)$-$1(LiOH)]$ to $[200(MnO_2)$-$1(LiOH)]$, corresponding to 6.25-0.5% LiOH ALD cycles of the total super cycle in the as-deposited state and as low as 1% after rapid thermal annealing treatment.
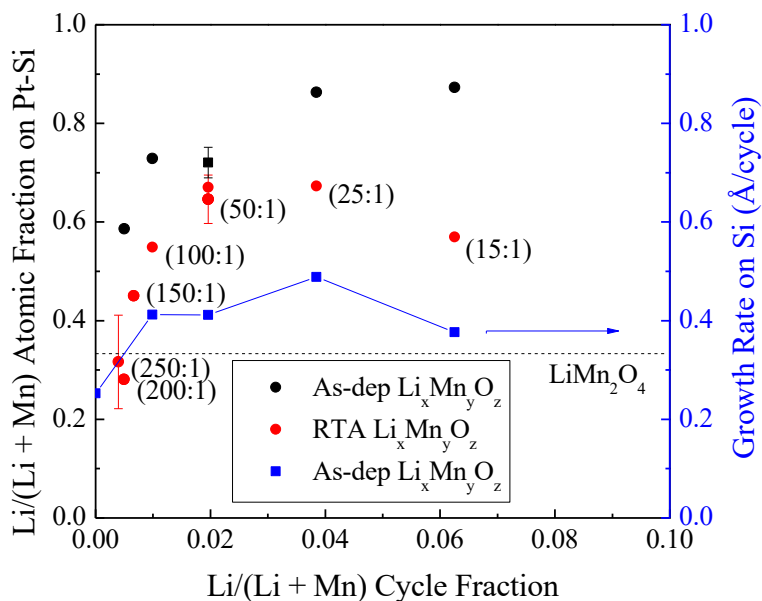
Figure 3-14. Growth Rate and Lithium Incorporation as a function of ALD cycle ratio. The Li/(Li + Mn) atomic fraction as determined via XPS as a function of the Li/(Li + Mn) ALD cycle fraction for as-deposited samples (black) and samples annealed at 750°C. Large lithium incorporation is observed for sample with very few LiOH ALD cycles in the overall super cycle. The growth rate as-determined via ellipsometry for samples deposited on Si(001) for various Li/(Li + Mn) ALD cycle fractions is shown in blue, where the growth rate was relatively constant near 0.4 Å/cycle.

Although films were lithium-rich, the growth rate did not increase significantly with an increasing fraction of LiOH sub-cycles, where a growth rate of ~0.4 Å/cycle was observed. An SEM X-section image of a $Li_{1+x}Mn_{2-x}O_4$ thin film consisting of 3 super-cycles of [250(MnO_2)-1(LiOH)] is shown in Figure 3-15. The growth rate agrees well with spectroscopic ellipsometry measured growth rates exhibiting a growth rate of 100 Å per super-cycle and 0.4 Å/cycle calculated dividing the thickness by total number of sub-cycles.
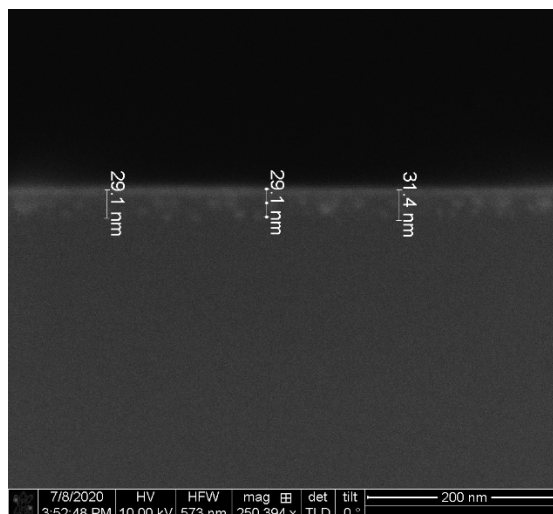
Figure 3-15. SEM x-section of $Li_{1+x}Mn_{2-x}O_4$ thin film deposited with 3 super cycles of the [250(MnO$_2$)-1(LiOH)] ALD sequence on Si(001). The growth rate calculated from the measured thickness would equate to a growth rate of 100 Å/super cycle

Due to the surface sensitive nature of XPS, there can always be added complexity due to different chemical states near the top-most surface, especially when samples are characterized ex-situ. For stoichiometric $LiMn_2O_4$, there should be an equal ratio of Mn^{4+} and Mn^{3+}. Li-substitution in the spinel structure ($Li_{1+x}Mn_{2-x}O_4$) is commonly observed, where for every substitution a Mn^{3+} is oxidized to maintain charge neutrality up to the extreme of $Li_{4/3}Mn_{5/3}O_4$ ($Li_4Mn_5O_{12}$) in which all Mn exist in the Mn^{4+} oxidation state. It follows that if the $Li_xMn_yO_z$ is in the spinel structure (which has been verified and is discussed below), then the ratio of the Mn^{4+} and Mn^{3+} oxidation state should be a measure to degree of lithium-substitution—highly relevant to the corresponding electrochemical properties. XPS Detailed Spectra (Mn 2p, O1s, C1s, and Li 1s/Mn3p) for several $Li_xMn_yO_z$ samples as well as ALD MnO_x as a comparison are shown in Figure 3-16, where emphasis on the samples post rapid thermal annealing are shown here due to their relevance to electrochemical testing. First in comparison of the (15:1) before and after rapid thermal annealing, the presence of C1s signal at high binding energy (>289 eV) attributed to lithium carbonate is observed in the as-deposited sample, but not after rapid thermal annealing. Changes are also

evident in the O 1s spectra, where the ratio of the two fit peaks is attributed to more metal bound oxygen post rapid thermal annealing. Furthermore, an increase in Mn 2p signal is observed, and the Li 1s shifts to lower binding energy most likely indicative of a majority lithium oxide versus that of lithium carbonate surface composition. Next, in comparison of the rapid thermal annealed samples deposited with various ALD sequences, in comparison of each C1s XPS spectra, the majority of the C 1s signal is attributed to sp^3 carbon with the large majority expected to be adventitious carbon from ambient exposure. In fitting the Mn 2p spectra, four peaks (2 for $2p_{3/2}$ and 2 for $2p_{1/2}$) with constrained fwhm, peak splitting, and peak area (2:1 for $2p_{3/2}$:$2p_{1/2}$) were utilized. Across the samples, there was not a significant change clearly evident in the Mn 2p, where the Mn $2p_{3/2}$ peak near 642.5 eV attributed to Mn(IV)-O, and a shoulder at 641.8 eV attributed Mn(III)-O. Slightly more clear is observed in changes to the Mn 3p spectra, where comparing the (15:1) to the (100:1 and 250:1) the ratio of the two fit peaks attributed to the Mn(IV) and Mn(III) oxidation states decreases with fewer LiOH ALD cycles. This could be indicative of a more lithium substituted spinel ($Li_{1+x}Mn_{2-x}O_4$), but due to the surface-sensitive nature of XPS cannot be fully confirmed.
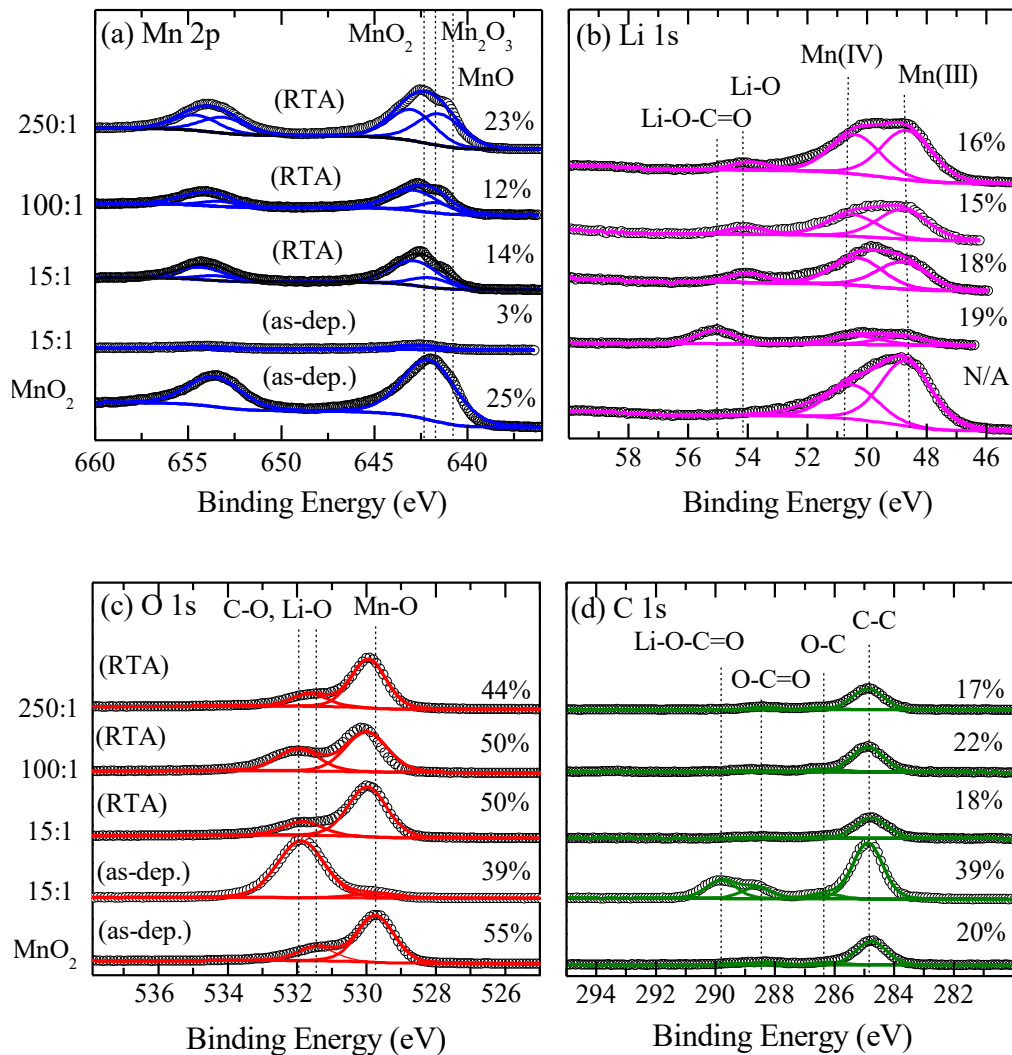
Figure 3-16. XPS Detailed Scans of 3 representative $Li_xMn_yO_z$ samples deposited with cycle sequences of $15(MnO_2)$-$1(LiOH)$ (as-dep, RTA), $100(MnO_2)$-$1(LiOH)(RTA)$, $250(MnO_2)$-$1(LiOH)(RTA)$, and MnO_2, where the XPS spectra for the Mn 2p (a), Li 1s(b), O 1s(c), and C1s(d), orbitals are shown, respectively. In the as-deposited state, the surface was carbon rich and manganese deficient as can be seen in comparing the $15(MnO_2)$-$1(LiOH)$ sample before and after rapid thermal annealing, where reduction of lithium carbonate signatures can be observed in the C 1s detailed scan shown in part (d.)

Table 3-2 summarizes the relative compositions determined via XPS for several sets of

$Li_xMn_yO_z$ samples. The carbon content was consistently lower after rapid thermal annealing as

compared to the as-deposited state consistent with reduction in surface lithium carbonate, in addition to increased Mn content—reflecting a more uniform surface composition.

Table 3-2. Relative Composition for $Li_xMn_yO_z$ samples determined via XPS

Annealing Treatment	Cycle Sequence (MnO_2:LiOH)	Li	Mn	O	C	Li/(Li+Mn)
As-dep	15:1	0.19	0.03	0.39	0.39	0.87
As-dep	25:1	0.17	0.03	0.45	0.35	0.86
As-dep	50:1	0.20	0.09	0.39	0.33	0.69
As-dep	100:1	0.24	0.09	0.39	0.28	0.73
As-dep	200:1	0.13	0.09	0.27	0.50	0.59
RTA 5 min, 750°C	15:1	0.18	0.14	0.50	0.18	0.57
RTA 5 min, 750°C	25:1	0.17	0.08	0.44	0.31	0.67
RTA 5 min, 750°C	50:1	0.15	0.07	0.39	0.39	0.67
RTA 5 min, 750°C	100:1	0.15	0.12	0.50	0.22	0.55
RTA 1 min, 750°C	150:1	0.12	0.15	0.38	0.35	0.45
RTA 1 min, 750°C	200:1	0.10	0.26	0.47	0.17	0.28
RTA 1 min, 750°C	250:1	0.16	0.23	0.44	0.17	0.41

In a previous ALD study by Nilsen et al. working to synthesize lithium titanate, a lithium and carbon rich-surface formed upon atmosphere exposure as lithium hydroxide can react to form lithium carbonate (Miikkulainen 2013), which could be potentially occurring in the $Li_xMn_yO_z$ thin films. To further assess the bulk composition vs. surface composition, in-situ Ar ion beam sputtering was performed in conjunction with XPS. Ar^+ sputtering is a physical process that can alter the surface especially due to varying sputtering rates due atomic weights as well as chemical bonding. Figure 3-17 (a) shows the survey spectra after during Ar^+ etch times, where substrate

signal is observed after 540s (Ar^+ 4keV), indicating less than 10 nm of $LiMn_2O_4$ thickness remaining. Figure 3-17 (b) shows the relative compositions as function of etch time (depth within film). After the first etch step (180s) the carbon content decreased from ~25% to around 5%-- which potentially is the amount of carbon incorporated within the film due to precursor decomposition or incomplete ligand exchange. After the first etch step the lithium content decreases, while the manganese and oxygen content increased. Post 360s etch time, the film composition remained stable within (1-2%) with a relative composition of Li: 13%, Mn: 31%, O:51%, and C: 5%. Figure 3-17 (c) shows the Li/(Li + Mn) atomic fraction as well as Mn 3s splitting as a function of etch time. After 360s the Li/(Li +Mn) decreases to a constant value of about 0.3 slightly less than what would be expected for $LiMn_2O_4$. The Mn 3s splitting increases significantly after the first etch step (4.5 to 5.3 eV), then steadily increases to 5.6 eV, indicative of a lower Mn oxidation state. Taking the effect of Ar^+ etching aside, there is a significant variance in surface vs. bulk composition (more lithium and carbon rich). The relatively stable Li/(Li + Mn) ratio after the first etch step could be indicative a more uniform composition as well as a coupling of the two elements, where the individual oxides, respectively would be expected to have varying sputtering rates.
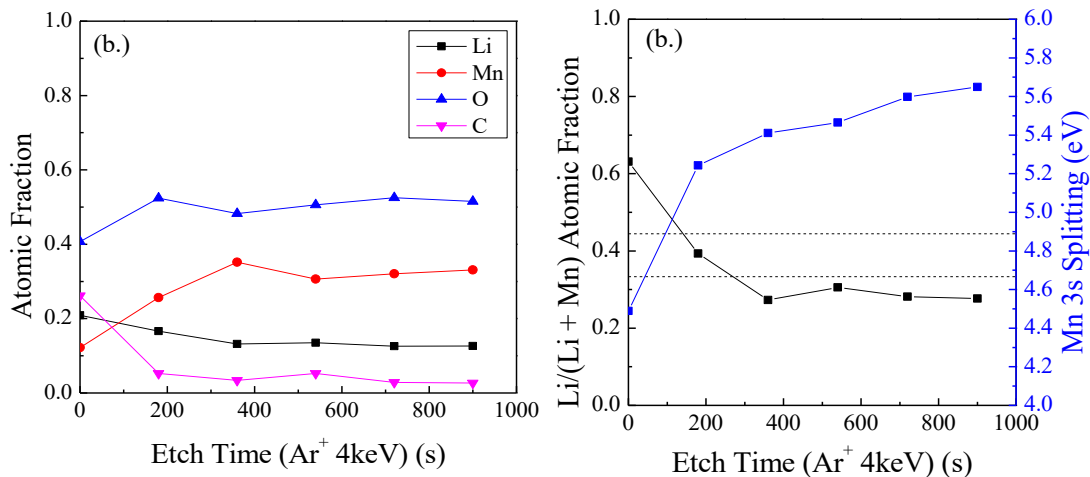
Figure 3-17. In-situ Depth Profile XPS Spectra of LixMnyO sample deposited with the 50(MnO$_2$)-1(LiOH) on Pt-Si, annealed at 750°C. (a) Relative composition of the Li$_x$Mn$_y$O$_z$ thin film vs. etch time as determined via XPS. (b) Li/(Li +Mn) atomic fraction vs. etch time, where a relatively constant ratio was observed after 360s etch near the LiMn$_2$O$_4$ stoichiometry.

The Li$_x$Mn$_y$O$_z$ thin films crystal structure was probed as a function of rapid thermal annealing treatment. Thin films with ALD cycle sequences ranging from (15:1) to (2501:1) were amorphous as-deposited, but crystallized post rapid thermal annealing into the spinel structure. Figure 3-18 (a) shows the XRD spectra of a Li$_x$Mn$_y$O$_z$ thin film annealed at various temperatures for 1 minute (550-750°C). Figure 3-18 (b) shows XRD spectra of two films with ALD deposition sequence [50(MnO$_2$)-1(LiOH)] and [250(MnO$_2$)-1(LiOH)] in both the as-deposited state as well as after rapid thermal annealing at 750°C. The measured lattice spacing for the (111) reflection was 4.72 Å and 4.75 Å for the 50:1 and 250:1, respectively as compared to 4.76 Å (JCPDS reference pattern 00-004-0802) reported in the literature. A shift to lower value of the (111) reflection is indicative of a compressed unit cell, where lithium substituted spinels (Li$_{1+x}$Mn$_{2-x}$O$_4$, x ≤ 0.33) have been observed to decreased lattice constant with increased lithium substitution.(Gummow 1994) In comparing the shift in the XRD spectra further suggests more

126

lithium-substituted $Li_{1+x}Mn_{2-x}O_4$ with a higher percentage of LiOH ALD subcycles, where the electrochemical properties is discussed below.
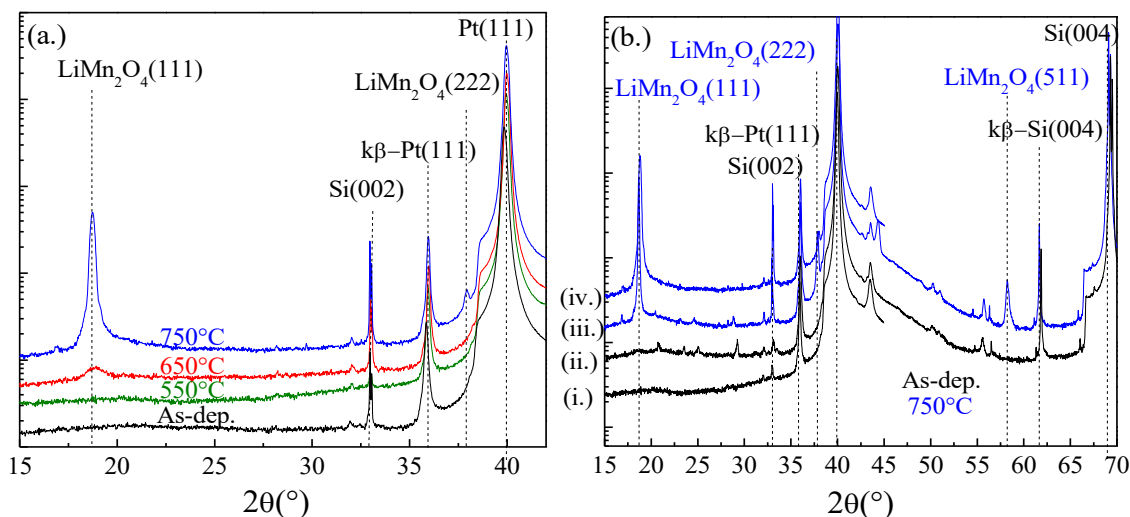
Figure 3-18. XRD spectra (a) of a $Li_xMn_yO_z$ thin film deposited with the cycle sequence 50(MnO2)-1(LiOH) for various rapid thermal annealing treatments (As-dep, 550°C, 650°C, 750°C). (b) XRD of a (50:1) denoted as (ii,iv) and (250:1) denoted as (i.,iii.) in the as-deposited state (black) and post rapid thermal annealing (blue).

Next the surface morphology was characterized via atomic force microscopy, where significant increase in surface roughness was observed in the $LiMn_2O_4$ thin films (RMS: ~3.0 nm) as shown in Figure 3-19 as compared to those measured for MnO_x as shown in Figure 3-12. Clear cubic crystallites can be observed in the samples annealing for 1 min at 750°C in an O_2 and N_2 environment with relatively large grains (AFM scan size 500x500 nm) approaching ~20 nm.

This coupled with Pt signal in the XPS spectra of some thinner (sub 20 nm) annealed $Li_xMn_yO_z$ samples could be indicative of island-like crystallization potentially due to lattice mismatch and as well as thermal expansion coefficient discrepancy. It remains unclear if this is an issue for utilization as a thin film cathode, where for instance as compared to the solid electrolyte layer in a solid-state battery needs to be uniform to prevent short-circuiting. This issue could also

be mitigated through utilization of another metallic substrate with better lattice match and thermal expansion coefficients, but none were explored here. The rather rough surface morphology was similarly observed in the thermal ALD process of $LiMn_2O_4$ developed by (Miikkulainen 2014), which further makes quantification of film thickness more difficult, which becomes crucial for exact quantification of volumetric lithiation capacities.
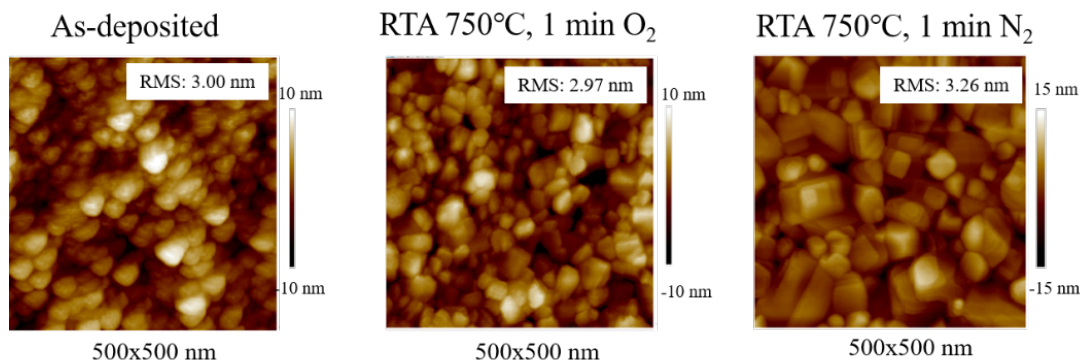
Figure 3-19. Surface Morphology of a $Li_xMn_yO_z$ film deposited with cycle sequence $200(MnO_2)-1(LiOH)$ in the as-deposited state, rapid thermal treatment at 750°C under O_2 flow and N_2 flow. The overall surface roughness does not change significantly upon rapid thermal annealing, but the local microstructure was affected, where cubic crystals were observed.

3.6   Electrochemical Characterization of PEALD $LiMn_2O_4$

Lithium-rich manganese oxide spinels ($Li_{1+x}Mn_{2-x}O_4$, $x \leq 0.33$) exhibit improved performance as compared to $LiMn_2O_4$, where lithium substitution in the octahedral Mn sites promote increased cycling stability due to suppression of both the Jahn-Teller distortion upon deep discharge as well as the Mn^{3+} disproportionation reaction. This improvement in cycling stability must be weighed against the decrease in theoretical capacity in the 4.0V region as the manganese ions become tetravalent to maintain charge neutrality (theoretical capacity of 154 mAh/g, where x=0) (Gummow 1994). For lithium manganese oxide spinels of stoichiometry $Li_4Mn_5O_{12}$ ($Li_{1.33}Mn_{1.67}O_4$), no lithium can be extracted at 4V since all Mn ion are tetravalent. $Li_4Mn_5O_{12}$ can

be lithiathed in a reversible two-phase reaction at 3V, up to $Li_{4+x}Mn_5O_{12}$, where $x \leq 2.5$ (Thackeray 1997). In this section, electrochemical characterization of $Li_xMn_yO_z$ thin films with various ALD cycle ratios was assessed and compared to compositional analysis of the previous section. First cyclic voltammetry was utilized to determine the redox activity of the rapid thermal annealed $Li_xMn_yO_z$ thin films. For samples deposited with cycle sequences with more than 0.66% LiOH subcycles (> 150(MnO_2)-1(LiOH)), the $Li_xMn_yO_z$ was not electrochemically active in the 4V region, but delithiation was observed in the 3.0V region—indicative of the $Li_4Mn_5O_{12}$ phase. Cyclic voltammograms of the $Li_xMn_yO_z$ deposited with fewer than 0.66% LiOH subcycles are shown in Figure 3-20, where the distinct duplet redox peak at 4.0 V associated with a two-step delithiation/lithiation process of $LiMn_2O_4$. The 4.0V region is associated with insertion or removal of Li-ion from 8a tetrahedral sites, where the ~150 mV splitting between peaks is due to the preferential ordering in one half of the available tetrahedral sites (Thackeray 1997).
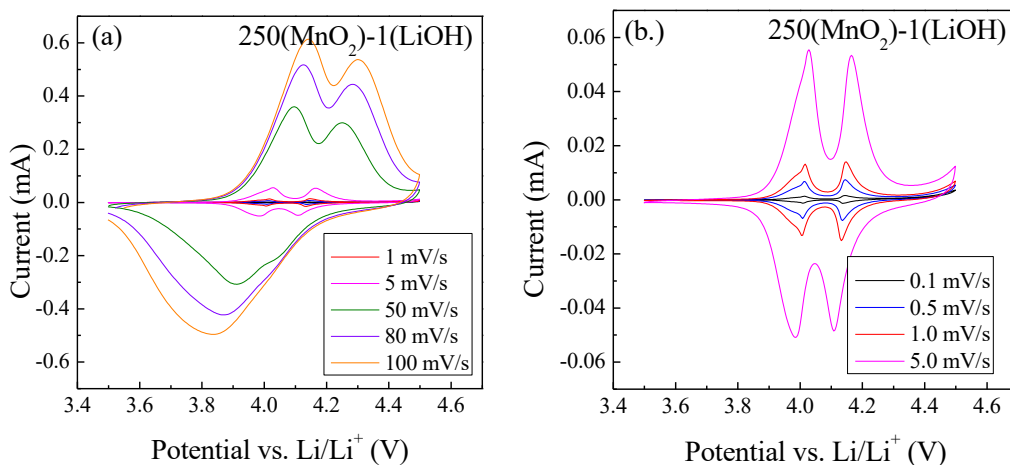
Figure 3-20. Cyclic Voltammetry of a $Li_{1+x}Mn_{2-x}O_4$ thin film deposited with ALD cycle sequence of 250(MnO_2)-1(LiOH) at various rates (0.1 -100 mV/s) with a voltage window of 3.5 to 4.0 V. All measurements were performed in a 3 neck flask set-up in 1M $LiClO_4$ in 1:1 EC:DMC. The C-V curves are shown at (a) sweep rates from 1-100 mV/s and (b) sweep rates from 0.1 – 5.0 mV/s

Galvanostatic cycling, or charge/discharge at constant applied current more akin to the actually battery operation, was performed on sample deposited with cycle sequence 12[50(MnO2)-1(LiOH)] to assess the rate-ability as well as cycle stability. Galvanostatic cycling was performed in a 3 neck flask set-up with lithium metal as the counter and reference electrode, in 1M LiClO$_4$ electrolyte in 1:1 EC:DMC. Rates were calculating assuming the theoretical density of LiMn$_2$O$_4$ and the estimated thickness as determined via SE. Due to the difficulty in assessing the exact film thickness all capacities are reported in areal capacities. First the rate-ability was assessed by measuring the capacity for 3 charge/discharge cycling at increasing currents (3.6 to 359.1 µA/cm^2) corresponding to approximate c-rates of C/2, C, 2.5C, 5C, 10C, 15C, 25C, 40C, 50C, and then returning back to lowest applied current, 3.6 µA/cm^2. Three sets of rate testing were performed with increasing upper voltage cut-off of 4.3, 4.4, 4.5 V to assess whether cycling degradation would occur at higher voltages from potential increase Mn ion dissolution and/or electrolyte breakdown as observed at the slower rates in the cyclic voltammetry characterization of the Li$_x$Mn$_y$O$_z$ samples. The charge/discharge curves for the set of data with the highest voltage cut-off (4.5V) are shown in Figure 3-21. At the lowest rate (3.6 µA/cm^2) the areal capacity was measured to be 5.24 µAh/cm^2. Increasing the current 20-fold (35.9 µA/cm^2) resulted in a capacity of 4.40 µAh/cm^2 and an increase 100 fold resulted in a capacity of 3.48 µAh/cm^2 corresponding to a 66% capacity retention at a specific current of 359.1 µA/cm^2 . Furthermore, after cycling at 359.1 µA/cm^2, the current was then reduced back to 3.6 µA cm^{-2} to assess any damage from high rate cycling, in which 98% of the initial capacity remained. Next the sample was cycled at a constant rate of 5C (35.9 µA/cm^{-2}) for 100 cycles (190 total cycles) to assess the cycling stability. The coulombic efficiency and discharge capacity started at 94.6 % and 4.73 µAh/cm^2, respectively and 98.7% and 4.57 µAh/cm^2 after the 100th cycle. A 96.6% capacity retention over 100 cycles

suggests some level of lithium substitution as the Mn^{3+} disproportionation reaction does not appear to be significantly contributing to capacity fading or poor coulombic efficiency. High coulombic efficiency becomes increasing important for integration in thin film batteries due to limited lithium reservoir due the ultra-thin nature of the electrolyte layer.
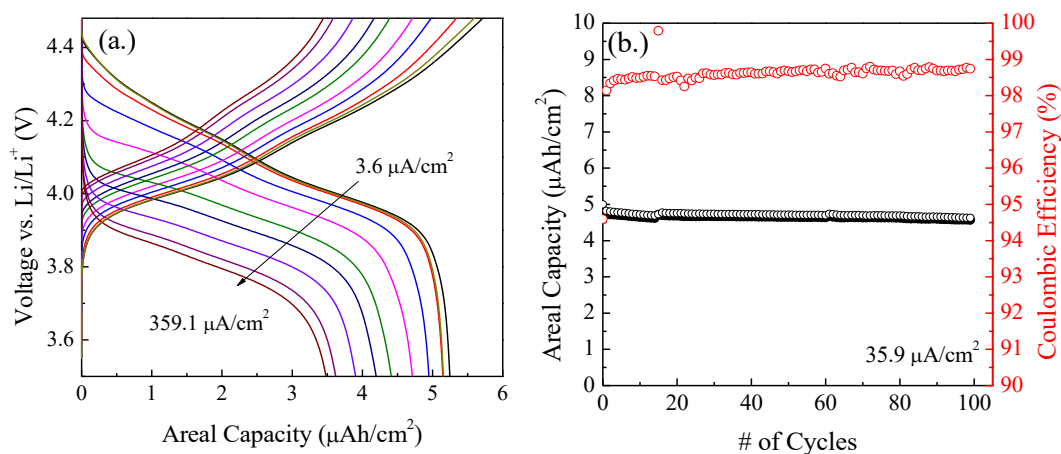
Figure 3-21. Galvanostatic cycling from 3.5 to 4.5 V vs Li/Li$^+$ of Li$_{1+x}$Mn$_{2-x}$O$_4$ thin film with ALD cycle sequence of 12[250(MnO$_2$)-1(LiOH)]. (a) Charge/Discharge curves of the 3rd cycle at each current density ranging from 3.6 µA cm^{-2} to 359.1 µA cm^{-2} roughly corresponding theoretically calculated rates of C/2, C, 2.5C, 5C, 10C, 15C, 25C, 40C, 50C based on the estimated thickness and bulk density (b) Charge/Discharge capacity and coulombic efficiency as a function of cycle number at a specific current of 35.9 µA cm^{-2}.

Based on the estimated thickness based on ellipsometry of amorphous Li$_x$Mn$_y$O$_z$ thin films grown on Si(001) and the bulk density of LiMn$_2$O$_4$ would result in a capacity of 109 mAh/g as compared to the theoretical capacity of 148 mAh/g. This could be due to being partially lithium-rich resulting in reduced activity in the 4.0V region, which could be improved via increasing the LiOH ALD cycle % even lower. Most likely it is a combination of being slightly lithium rich over the LiMn$_2$O$_4$ as well as error in the accuracy in both the film density and overall thickness. Regardless the thin film LiMn$_2$O$_4$ exhibited excellent rate-ability at high rates (50C, theoretical

charge/discharge in 1.2 minutes) as well as excellent cycling stability resulting in 96.6% capacity

retention after 100 cycles at 5C. A summary of various cathodes synthesized via atomic layer

deposition is shown in Table 3-3. As the various cathode materials operate at different voltages an

estimate of the maximum achievable energy density was calculated through the product of an

average discharge voltage and the capacity. It should be noted for all cases, that differences in

thicknesses, number of charge/discharge cycles, voltage window, measurement set-up (i.e. liquid

electrolyte etc.), and c-rates will have an effect on the measured capacities making direct

comparison of the materials more difficult. This compounded with the fact of needing precise area

and thickness measurements of the thin films when determining the rates and capacities adds a

degree of error to the reported values. Both ALD $LiMn_2O_4$ materials ((Miikkulainen 2014) and the

data reported here) present the best achievable energy densities due to the higher operating voltage

(4.0 V) and areal capacities. In the comparison of both of these materials only the capacity from

the 4.0V region was utilized due to ideality of a single voltage range upon integrating into an actual

solid-state battery.

Table 3-3. Literature reported thin film cathodes deposited via ALD.

Material	Average Voltage (V)	Number of Cycles	C-Rate	Capacity ($\mu Ah\ cm^{-2}\ \mu m^{-1}$)	Energy Density ($\mu Wh\ cm^{-2}\ \mu m^{-2}$)	Reference
$LiCoO_2$	3.9	13	0.35C	25	98	(Donders 2013)
$LiMn_2O_4$	4.0	10	3C	58[a]	232	(Miikkulainen 2014)
		550	12C	~51	204	
		1000	12C	32	128	
Li_2S	2.2	500	0.72C	83	183	(Meng 2014)
V_2O_5	3.25	50	1C	49	159	(Mattelaer 2018)
$LiFePO_4$	3.2	200	1C	21	67	(Dobbelaere 2016)
$LiMn_2O_4$	4.0	9	C/2	52	209	(This Work)
		9	10C	44	176	
		9	50C	35	140	
		190	5C	45	180	

The other reported ALD LiMn$_2$O$_4$ does exhibit higher areal capacities (with the caveat of differing measurement conditions) and was electrochemical active without an annealing step. This study looked at two different Li-based precursors, Li(thd) and LiO^{t}Bu, where the ALD LiOH cycles were performed post MnO$_2$ deposition (best electrochemical performance) as well as incorporated as a super-cycle, similar to the process reported here. The method of lithium-incorporation with a super-cycle approach taken here allows for better controllability of the Li-composition throughout the thickness of the thin film. Furthermore, more precise tuning of the ALD cycle sequence could lead to achievable capacities closer to that of the theoretical value as the ALD cycle sequence taken here (250(MnO$_2$):1(LiOH)) potentially still exhibits a degree of Li-substitution. In addition, alternative choice of substrate could allow for a different grain orientation of the thin film LiMn$_2$O$_4$, where PVD films with a (100) orientation where observed to have better rate-capability than those with (111) and (110) orientation (Hendriks 2018). Comparisons of the volumetric capacity of various reported LiMn$_2$O$_4$ thin films, nano and microstructures are presented in Figure 3-22. For the data shown, bulk density was assumed if reported data was presented in mAh/g and only the capacity associated with the 4.0V region was considered. In comparison to micron-size particles (orange), the ALD LiMn$_2$O$_4$ thin films significantly out-perform in both volumetric capacity and rate capability. From the data included only the electrochemical deposited (ECD) LiMn$_2$O$_4$ and the ALD LiMn$_2$O$_4$ can be coated conformally on 3D structures. Another interesting work of note is the nanostructured mesoporous LiMn$_2$O$_4$ reported from (Lesel 2016) that exhibited pseudocapacitive behavior demonstrating capacity at rates as high as 1000C.
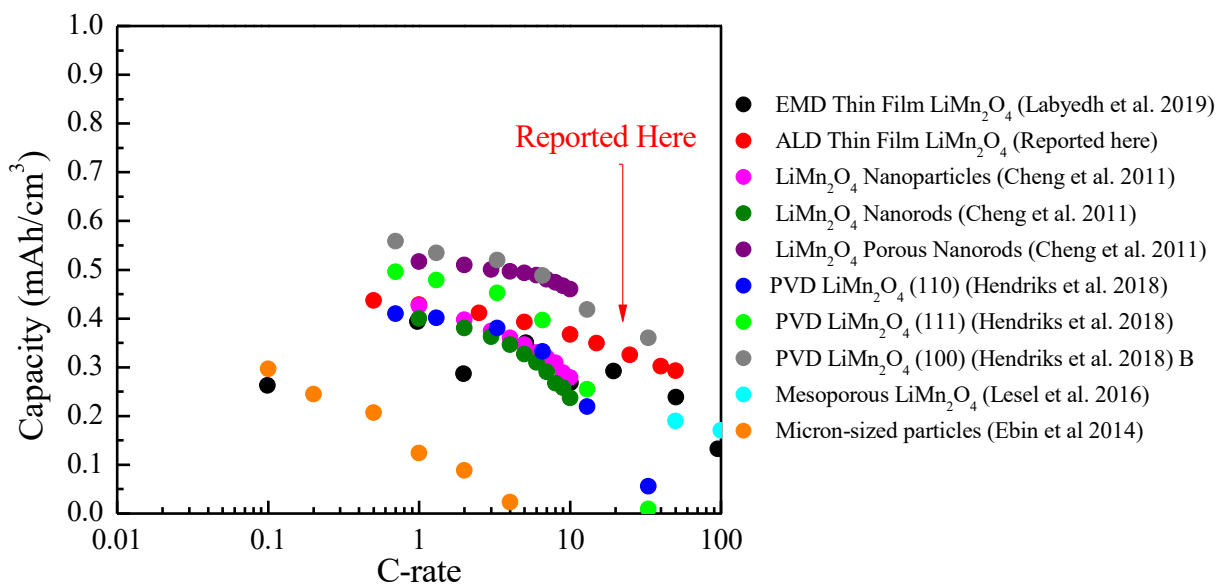
Figure 3-22. Volumetric Capacity vs. C-rate for various LiMn$_2$O$_4$ thin films, nanostructures, and bulk-like (micron-sized) materials. Bulk density was assumed if reported data was presented in mAh/g and only the capacity associated with the 4.0V region was considered. Of the various materials presented here only the EMD (shown in black), and the ALD LiMn$_2$O$_4$ thin films (reported here in red) can be coated conformally on 3D structures. (Cheng 2011, Ebin 2014, Lesel 2016, Hendriks 2018, Labyedh 2019)

Lastly, this work lays the groundwork for the synthesis of more complex metal oxide cathode structures such as LiMn$_{1.5}$Co$_{0.5}$O$_4$ and LiMn$_{1.5}$Ni$_{0.5}$O$_4$, which could be accomplished utilizing similar precursor chemistries to further increase the operating voltage. As an initial demonstration, Li$_{1+x}$Mn$_{2-x-y}$Co$_y$O$_4$ was synthesized and the composition compared in the as-deposited state as well as post thermal annealing (1 min, 750°C) as shown in Figure 3-23. The samples were deposited with an ALD cycles sequence of n[a(Co$_3$O$_4$)-b(MnO$_2$)-c(LiOH)]. The thin film deposited with a majority of Co$_3$O$_4$ cycles showed little lithium incorporation, where no Li 1s signal was observed post rapid thermal annealing, in line with the results on Li$_x$Co$_y$O$_z$ shown previously. The sample with the majority MnO$_2$ ALD cycles had a cation ratio of (Co 4%:Mn

54%:Li 42%) post annealing, with significantly more lithium incorporation most likely due to the interaction between ALD LiOH and the manganese oxide component. Although, detailed characterization of ALD $Li_{1+x}Mn_{2-x-y}Co_yO_4$ is beyond the scope of this work, initial characterization demonstrates the feasibility of utilizing similar ALD precursor chemistries for developing next generation high voltage thin film cathodes.
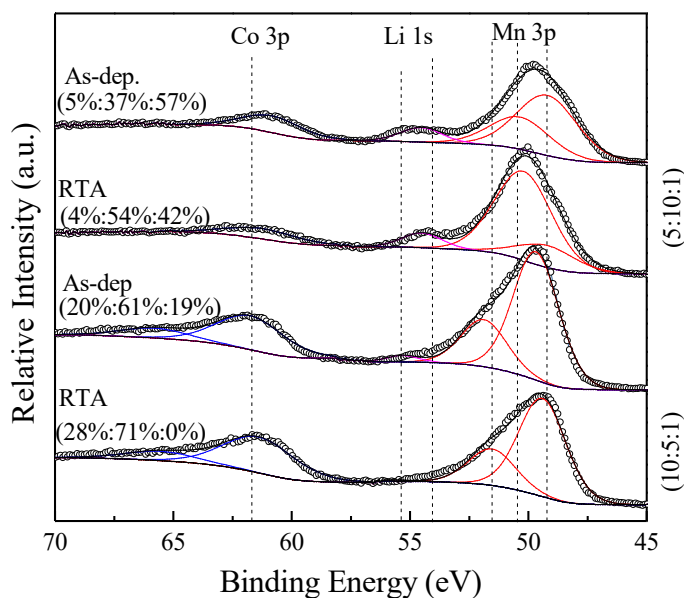
Figure 3-23. XPS detailed scans (Co 3p, Li 1s, Mn 3p) of $Li_{1+x}Mn_{2-x-y}Co_yO_4$ samples in the as-deposited state and post rapid thermal annealing, deposited with the cycle sequence of n[a(Co_3O_4)-b(MnO_2)-c(LiOH)]. The calculated relative compositions are given above the spectra in the format (Co%:Mn%:Li%). The thin film with larger amount of Co_3O_4 cycles showed very little lithium content before and after annealing, in-line with the $Li_xCo_yO_z$ results presented previously.

In summary, the stoichiometry of ALD thin film $Li_{1+x}Mn_{2-x}O_4$ could be controlled through tuning of the ALD sequence allowing for crystallization into the electrochemically active spinel phase. The ratio of Li/Mn content could be tuned from 2:1 to 0.4:1. The thin film cathodes exhibited excellent rate capability at high rates (66% capacity retention at 50C) as well as excellent

cycling stability resulting in 96.6% capacity retention after 100 cycles at 5C. Integration of thin film $Li_{1+x}Mn_{2-x}O_4$ as an cathode for 3D lithium-ion microbatteries should exhibit excellent rate capability (fast-charging) and improved cycle-life, especially when integrated with a solid-state electrolyte. $Li_{1+x}Mn_{2-x}O_4$ offers an energy density of 209 $\mu Wh\ cm^{-2}\ \mu m^{-2}$ competitive with literature reported ALD thin film cathodes as shown in Table 3-3. Further optimization of the lithium content when directly integrated with all solid-state lithium-ion batteries has the potential to further improve the capacity. Lastly, this work lays the groundwork for the synthesis of more complex metal oxide cathode structures such as $LiMn_{1.5}Co_{0.5}O_4$, which could be accomplished utilizing similar precursor chemistries to further increase the operating voltage.

CHAPTER 4:   ALD THIN FILM SOLID-STATE ELECTROLYTES

The synthesis of LiAlSiO$_4$ thin films via atomic layer deposition was performed via combination of the individual thermal ALD processes for Al$_2$O$_3$, LiOH/Li$_2$O, as well as catalyzed SiO$_2$ for development of a viable solid-state electrolyte for 3D lithium-ion microbatteries. Incorporation of SiO$_2$ into ALD Li$_x$Al$_y$Si$_z$O thin films was performed with two silicon metalorganic precursors, both catalyzed by the presence of the other constituent cations (Al, Li). The stoichiometry of the ALD Li$_x$Al$_y$Si$_z$O thin films was controlled through modulation of the ALD cycle sequence to achieve the LiAlSiO$_4$ stoichiometry. Thin film Li$_x$Al$_y$Si$_z$O was amorphous as deposited and exhibiting a room temperature ionic conductivity on the order of 10^{-9} S/cm. The as-deposited film can be crystallized into the β-Eucryptite LiAlSiO$_4$ structure via rapid thermal annealing, where a well-defined epitaxial relationship of β-LiAlSiO$_4$ $(1\bar{2}10)$ ‖ Si (100) and β-LiAlSiO$_4$ $(10\bar{1}0)$ ‖ Si(001) was observed. The ionic conductivity of the crystallized thin films was found to be on the order of 10^{-7} S/cm at room temperature, competitive with LiPON based solid electrolytes and demonstrating its viability as a thin film solid-state electrolyte for 3D lithium-ion microbatteries. Crystalline LiAlSiO$_4$ is one of the first crystalline metal oxide solid electrolytes reported to be synthesized via ALD with further improvements to the ionic conductivity possible through optimizing crystallization conditions. Although ALD of crystalline LiAlSiO$_4$ was demonstrated, further material development is required for enhanced ionic conductivities $>1\times10^{-7}$ S/cm. One potential promising material is LiSiPON, which offers better electrical properties and enhanced ionic conductivities than LIPON. ALD LiSiPON shows promise for as a solid electrolyte due to its high ionic conductivity ($8.6 \pm 6\times10^{-7}$ S/cm) in the as-deposited state, where further composition optimization could lead to further enhancement.

4.1   Atomic Layer Deposition of Lithium Aluminum Silicate

Atomic layer deposition of lithium aluminum silicate was achieved via combination of the individual oxides Al_2O_3, $LiOH/Li_2O$, as well as SiO_2, where the latter is catalyzed by the presence of electropositive cations (in this case Li and Al). The reactor schematic and components are detailed in Figure 2-1 and the properties of the various precursors utilized are given in Table 2-1. For the specific reactor set-up precursor pulse, purge, and pump-down times are given in Table 2-2. First Al_2O_3 and LiOH thin films were characterized at a deposition temperature of 225°C utilizing the metal-organic precursor trimethylaluminum and lithium tert-butoxide, with water as the co-reactant. The as-deposited thin films were characterized with spectroscopic ellipsometry to determine the film thickness, where model parameters are presented in Table 2-5. The growth rate for Al_2O_3 was determined to be 1.5Å/cycle and 1.0Å/cycle for a deposition temperature of 225°C as can be seen in Figure 4-1.
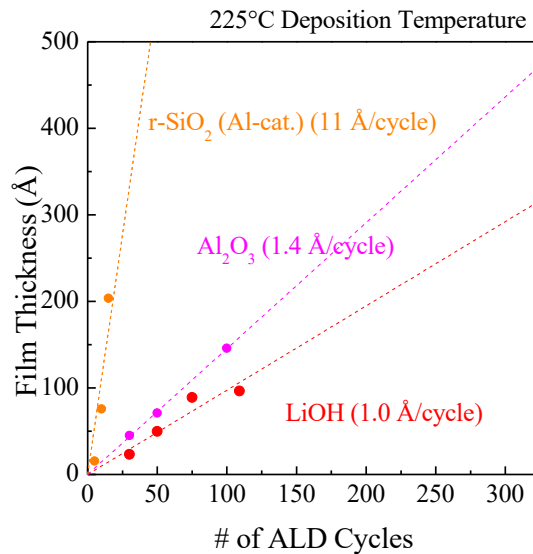
Figure 4-1. Growth rates of the individual oxides Al_2O_3, LiOH, and SiO_2 as determined via spectroscopic ellipsometry on Si(001), deposited at 225°C. Silicon incorporation was performed with two precursors both catalyzed in the presence of LiOH or Al_2O_3.

Tris-tertbutoxy silanol (TTBS) and tetraethylorthosilicate (TEOS) were utilized as silicon

which have different reaction mechanisms as well as significantly different growth

rates(Hausmann 2002, Cho 2015, Cho 2016). The reaction mechanism for $TEOS/H_2O$ acts similar

to most thermal metal oxide ALD processes, but ligand removal is catalyzed in the presence of

Al_2O_3 and or LiOH, where the process of $TEOS/H_2O$ does not deposit SiO_2 due to inability of H_2O

to hydrolyze the chemisorbed precursor at reasonable temperatures. This puts the upper limit of

silicon incorporation into tertiary metal oxides, as increasing the number of $TEOS/H_2O$ ALD

subcycle in the supercycle sequence only results in an increase in silicon content up to a certain

percentage. The TTBS precursor has a much different mechanisms and is termed a "Rapid ALD"

process, in which once catalyzed the TTBS precursor can undergo a polymerization reaction that

leads to around ~1.2 nm of SiO_2 per cycle. Utilizing this precursor for incorporation into multi-

cation metal oxides, then puts the limitation of a large amount of silicon incorporation per ALD

cycle, if saturation behavior is to be observed. Furthermore, long pulse times are required to ensure

saturation and conformality (Hausmann 2002). LiO^tBu/H_2O was also utilized to catalyze the r-

SiO_2 growth which exhibited similar growth behavior to the films grown with TMA. XPS Survey

spectra of 15 cycles of $LiO^tBu/H_2O/TTBS/H_2O$ and $TMA/H_2O/TTBS/H_2O$ are shown in Figure

4-2, where the composition of the thin films was determined to be $Si_{0.18}O_{0.5}C_{0.28}(Li_{0.03})$ and

$Si_{0.18}O_{0.55}C_{0.20}(Al_{0.06})$, respectively. The Si 2p peaks were centered near 103.1 eV, as expected for

SiO_2.
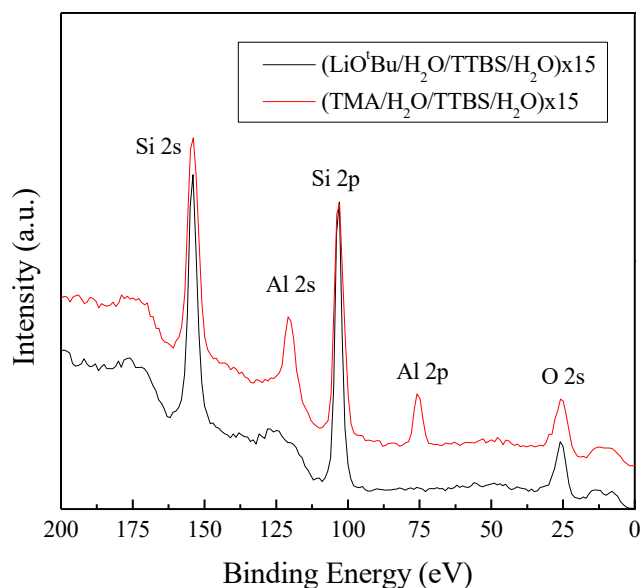
Figure 4-2. XPS Survey spectra of 15 cycles of r-SiO$_2$ ALD with both LiOH and Al$_2$O$_3$ as a catalyst utilizing the precursor tris-tertboxy silanol.

Next the deposition of Li$_x$Al$_y$Si$_z$O was demonstrated utilizing the TTBS silicon precursor. The growth rate of Li$_x$Al$_y$Si$_z$O grown with the deposition sequence of 10(TMA/H$_2$O)-3(LiO^{t}Bu/H$_2$O)-1(TTBS/H$_2$O)-3(LiO^{t}Bu/H$_2$O) utilizing the TTBS precursor is shown in Figure 4-3 (a) which was linearly fit to 4.1 nm/super cycle. XPS detailed spectra of a Li$_x$Al$_y$Si$_z$O thin film deposited with cycle sequence is shown in Figure 4-3 (b). The composition of the as-deposited Li$_x$Al$_y$Si$_z$O thin film was measured to be Li$_{0.1}$Al$_{0.11}$Si$_{0.9}$O$_{0.56}$(C$_{0.14}$). The 14% carbon signal is attributed to adventitious carbon on the sample surface as the XPS measurements were performed in-situ. Regardless, the Li:Al:Si was very close to the desired LiAlSiO$_4$ stoichiometry of the β-Eucryptite phase. The conformality of the as-deposited Li$_x$Al$_y$Si$_z$O thin films were assessed, where a SEM X-section of a Li$_x$Al$_y$Si$_z$O film deposited on a 2D silicon substrate is shown in Figure 4-3 (c) and HRTEM images of Li$_x$Al$_y$Si$_z$O coated SiGe nanowires run with the same ALD cycle sequence via TEM as shown in Figure 4-3 (d).

140
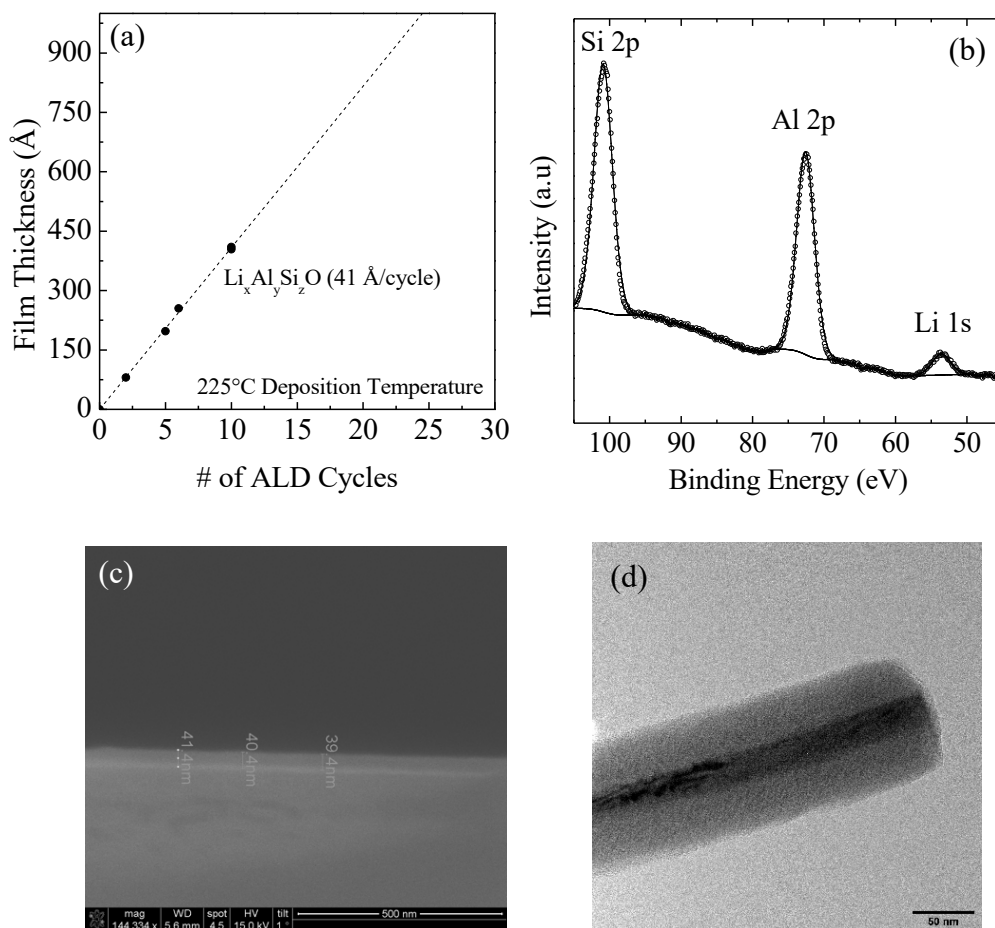
Figure 4-3. (a) Growth rate of $Li_xAl_ySi_zO$ deposited with ALD cycle sequence of $10(TMA/H_2O)$-$3(LiO^tBu/H_2O)$-$1(TTBS/H_2O)$-$3(LiO^tBu/H_2O)$ with a 1.5 nm Al_2O_3 capping layer (b) XPS spectra of $Li_xAl_ySi_zO$ deposited with the cycle sequence $10(TMA/H_2O)$-$3(LiO^tBu/H_2O)$-$1(TTBS/H_2O)$-$3(LiO^tBu/H_2O)$ with a 1.5 nm Al_2O_3 capping layer (c) SEM X-section of $10[10(TMA/H_2O)$-$3(LiO^tBu/H_2O)$-$1(TTBS/H_2O)$-$3(LiO^tBu/H_2O]$ on Si (d.) HRTEM of same ALD cycle sequence on a SiGe nanowire.

The ionic conductivity of a 15 nm amorphous $Li_xAl_ySi_zO$ thin film deposited on a ITO/glass substrate was determined via electrochemical impedance spectroscopy (EIS). The EIS spectra is shown in Figure 4-4 and was fit to an equivalent circuit consisting of a resistor in parallel with a constant phase element. An ionic conductivity of 1×10^{-8} S/cm was calculated based on the fitting resistance value.
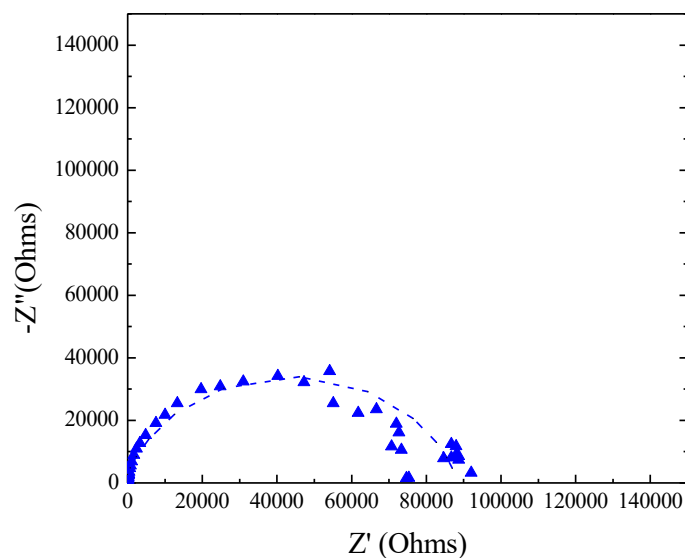
Figure 4-4. EIS spectra of 15 nm amorphous $Li_xAl_ySi_zO$ thin film at room temperature. The ionic conductivity was calculated to be 1.0 x 10^{-8} S/cm.

Although, synthesis of $Li_xAl_ySi_zO$ thin films utilizing TTBS for SiO_2 incorporation was viable, the TEOS precursor was chosen for further optimization of the functional and structural properties of $Li_xAl_ySi_zO$ due to increased controllability due the lower growth rate as well as the much shorter precursor dose times. Lithium aluminum silicate thin films were synthesized via combination of the individual ALD process for LiOH, Al_2O_3, and cat-SiO_2 utilizing TEOS. Each super cycle consisted of the following sequence: $n[a(Al_2O_3)-b(LiOH)-c(SiO_2)]$, in which the *a,b,c* parameters could be altered to tune the composition of the resulting $Li_xAl_ySi_zO$ thin films. The cycle sequence is chosen to start with Al_2O_3 in order to ensure optimal nucleation, due to high reactivity of the trimethyl aluminum precursor. The films were found to be sensitive to ambient exposure that could be somewhat mitigated (or delayed) generally with a capping layer of SiO_2 of Al_2O_3 (1-3 nm). Lithium aluminum silicate was able to be synthesized with two silicon precursors have significantly growth properties, where the process involving the precursor tetraethylorthosilicate (TEOS) is discussed here, in which the presence of an electropositive cation

(i.e. Al or Li) catalyzes the hydrolysis of the ethoxy ligand upon H_2O exposure allowing for growth of SiO_2. With the goal of obtaining a stoichiometry of $LiAlSiO_4$, lithium aluminum silicate thin films with various supercycles as shown in Figure 4-5 (all 20 -30 nm) were characterized via XPS to determine the effect of ALD cycle ratio on composition.

The composition of the 5 samples were characterized with ex-situ XPS in the as-deposited state as well as after rapid thermal annealing at 900°C (1 minute, N_2, ramp rate: 50°C/s). In the development of the multicomponent oxides via atomic layer deposition tuning of composition does not always follow that which is predicted from the growth properties of the individual components due to a wide range of potential chemical interactions and the evolving surface with chemically distinct reactive sites, which makes the surface different from those formed in the individual binary ALD processes. Figure 4-5 shows a tertiary diagram with the ALD cycle fractions for each supercycle and their corresponding composition determined via XPS in the as-deposited state as well as post rapid thermal annealing treatment.
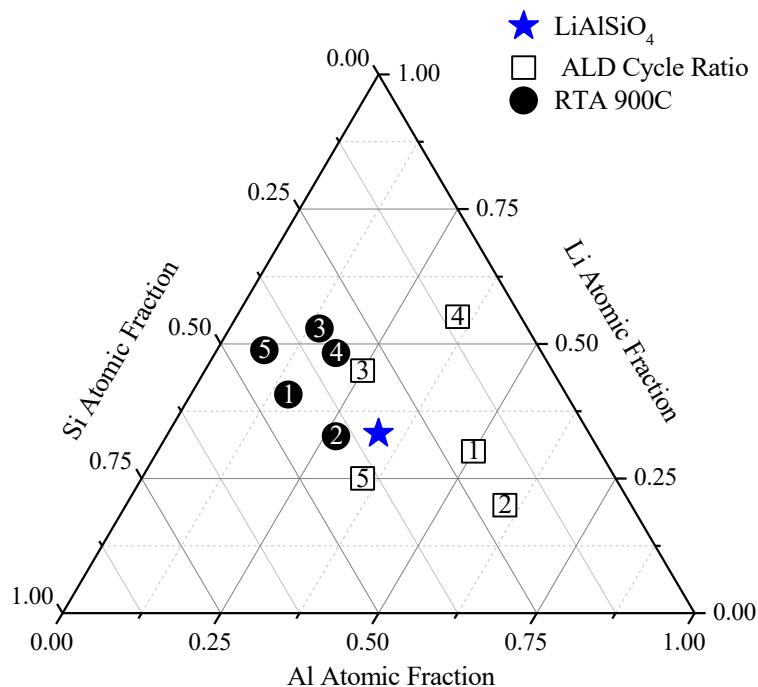
Figure 4-5. Composition of $Li_xAl_ySi_zO$ synthesized with various ALD supercycle sequences.

As can be seein in Figure 4-5, independent of the supercycle sequence the surface of the as-deposited samples were all extremely lithium rich, where a large presences of the carbon 1s signal shown in Figure 4-6 can be attributed to lithium carbonate. This is most likely the outcome of ambient exposure rather than from the deposition conditions, but in-situ XPS was not available for confirmation. As mentioned previously, lithium hydroxide as well as lithium oxide reacts readily with CO_2 (g) at room temperature and atmospheric pressure, where the Gibbs free energy of reaction for both reactions are negative as shown in Table 4-1. Upon annealing at 900°C for 1 minute, the lithium carbonate signal as shown in Figure 4-6 has been significantly reduced and the composition (Li, Al, Si) reflects closer to what would be expected from the ALD cycle ratio (Figure 4-5). Reduction of the lithium content in the surface region probed by XPS could be due to redistribution throughout the film (20-30 nm) and possible intercalation into the Si(001) substrate.

Furthermore, lithium carbonate in the presence of metal oxides has been observed to undergo reaction at elevated temperatures to release CO_2 to form lithium metal oxides. (Atosuo 2017, Mäntymäki 2019).

Table 4-1. Gibbs free energies of various lithium hydroxide and lithium oxide reactions at 1 atm.

Reactions	ΔG_{rxn} (kJ/mol)
$2LiOH(s) + CO_2(g) \rightarrow Li_2CO_3(s) + H_2O(g)$	-88.5 (25°C)
$Li_2O(s) + CO_2(g) \rightarrow Li_2CO_3(s)$	-177.2 (25°C)

The desired in stoichiometry ($LiAlSiO_4$) is shown via the blue star in Figure 4-5, where the cycle sequence with $12(Al_2O_3)$-$4(LiOH)$-$4(SiO_2)$ sequence demonstrated via XPS atomic fractions of 0.36, 0.28, and 0.36 for lithium, aluminum, and silicon, respectively. Across all the samples, the measured compositions proved to be aluminum deficient even with a larger portion of Al_2O_3 cycles as compared to the other metal constituents. Analysis of the XPS spectra were quantified utilizing a single peak ($2p_{3/2}$ and $2p_{1/2}$ cannot be resolved for Si 2p and Al 2p), where the atomic sensitivity factors (Li: 0.025, Al: 0.193, Si: 0.328) vary for each element orbital. In the annealed samples the Al 2p was found to be at 74.6 eV, Li 1s at 56.0 eV, and Si at 102.5, each corresponding to what would be expected for their respective oxides. It should be noted that for the samples measured, analysis of the trends on increasing the ALD cycle % on the corresponding cation content for each constituent oxide did not follow an ideal linear trend, which is expected due to potential chemical interaction at varying surface reactive sites depending on the ALD supercycle sequence. This being said, for LiOH there was observed lithium cation content with increasing ALD cycle percentage observed both in the as-deposited and rapid thermal anneal treated samples, but Al_2O_3 and SiO_2 were more complex.
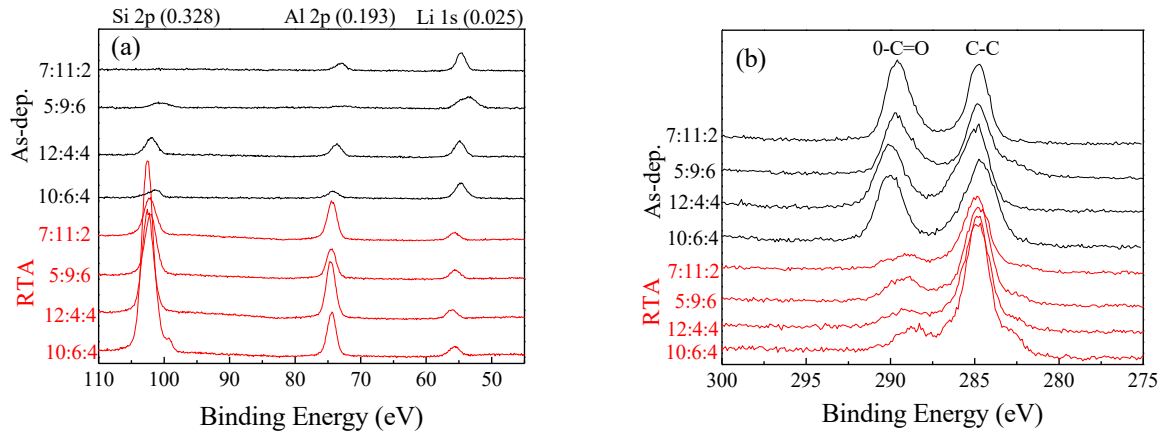
Figure 4-6. XPS spectra of various $Li_xAl_ySi_zO$ films ranging from 15-20 nm in the as deposited and post rapid thermal annealing at 900°C. The ALD super cycle is labeled on the right of both figures, in which (7:11:2) refers to a ALD super cycle consisting of $7(Al_2O_3)$-$11(LiOH)$-$2(SiO_2)$ (a) XPS detailed scans of the Si 2p, Al 2p, and L 1s regions and (b) the C 1s spectra. Reduction of the lithium carbonate signature in the C 1s spectra was observed post rapid thermal annealing.

Next to study the composition with regards to depth within the film, the $12(Al_2O_3)$-$4(LiOH)$-$4(SiO_2)$ the sample most consistent with the $LiAlSiO_4$ stoichiometry was characterized via angle resolved XPS. XPS is most commonly aligned that the electron energy analyzer is aligned so that the majority of signal is from electrons with a take-off angle of 90° (normal to surface) and the x-ray source is aligned at an incident angle of 60° from the sample surface. Utilizing angle resolved XPS, the sample is tilted towards the x-ray source modulating the alignment of the sample and detector making the information depth decrease and the technique more surface sensitive. As the normal information depth is approximately 10 nm determined by the inelastic mean path of the ejected electron through the analyte, reducing the take-off angle below 90° makes it so only ejected electrons at a shallower depth (<10 nm) able to reach the detector as the path within the analyte to the detector becomes greater. Specific quantification of the measured depth is a complex function of the inelastic mean free path of electrons ejected from orbitals interest as well as the material composition. Here, we analyze more qualitative trends as decreasing the take-off angle

146

corresponds to more surface-sensitive compositions (<10 nm). The relative composition determined via XPS are shown in Figure 4-7, where the most obvious trend is a decrease in oxygen content and increase in carbon content near the surface. The measurements were only quantified down to a take-off angle of 30° as the signal to noise made it difficult to quantify the composition. Upon inspection of specifically the relation of the metal cations (Li, Al, and Si) it was observed that the lithium content increased towards the samples surface, whereas the aluminum and silicon content decreased uniformly towards the surface. These observations could be potentially to the rapid thermal annealed samples not being completely immune to surface lithium carbonate formation or potentially represents excess surface lithium oxide/carbonate species from incomplete reaction during the annealing treatment.
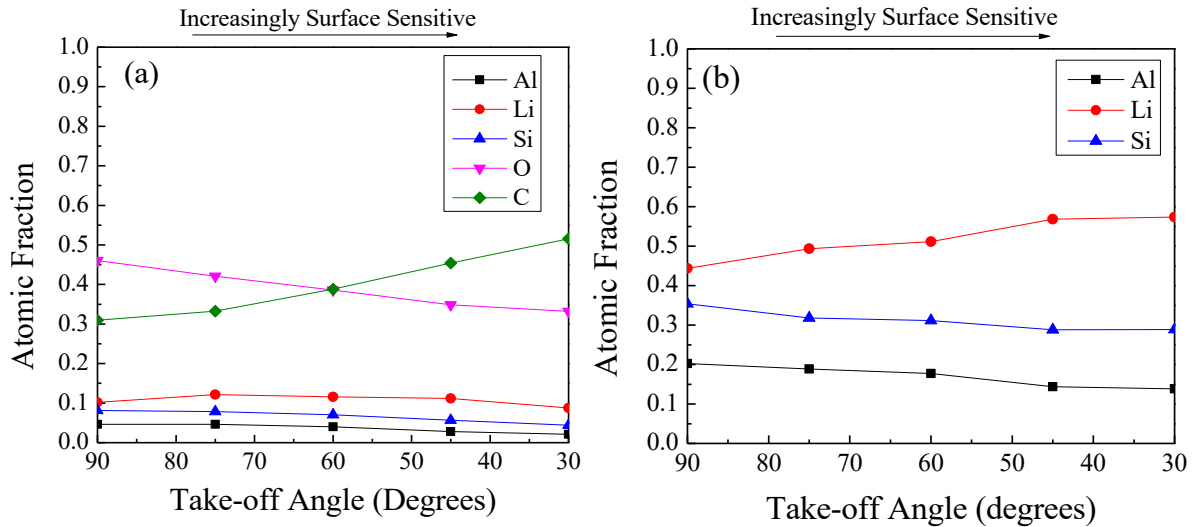
Figure 4-7. Angle resolved XPS of 20 nm $Li_xAl_ySi_zO$ thin film deposited with cycle sequence of 12(Al_2O_3)-4(LiOH)-4(SiO_2). (a) Relative compositions of Li, Al, Si, O, C as a function of the take-off angle and (b) relative composition of Li, Al, Si as a function of the take-off angle.

4.2   Structural Characterization of ALD LiAlSiO$_4$

Initial characterization of the annealed Li$_x$Al$_y$Si$_z$O thin films were performed utilizing XRD post annealing treatment. Of the various Li$_x$Al$_y$Si$_z$O samples deposited, the sample with closest composition to the LiAlSiO$_4$ stoichiometry deposited with a sequence of 12(Al$_2$O$_3$)-4(LiOH)-4(SiO$_2$) showed peaks associated with the β-Eucryptite phase of LiAlSiO$_4$ at 19.4° and 39.3° associated with reflections of the (10$\bar{1}$0) and (20$\bar{2}$0) planes as shown in Figure 4-8.
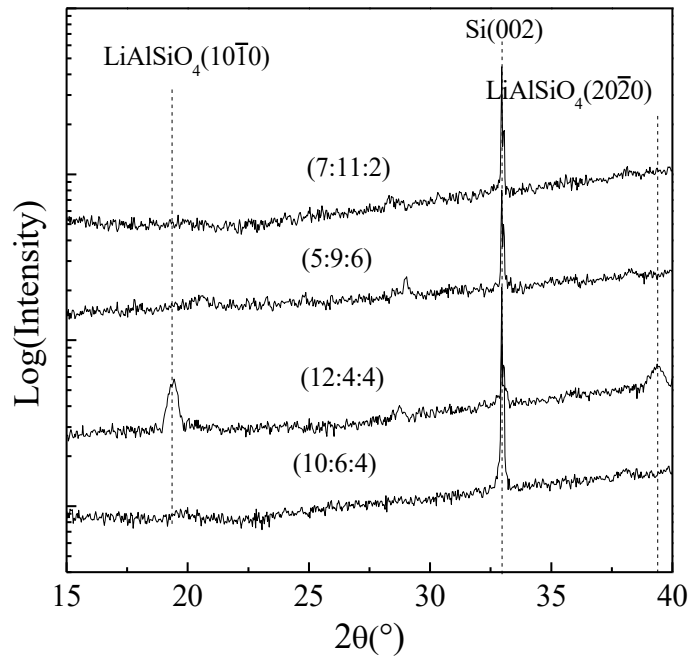
Figure 4-8 XRD Spectra of various Li$_x$Al$_y$Si$_z$O thin films annealed at 900°C for 1 minute on Si(001). The sample deposited with sequence: 12(Al$_2$O$_3$)-4(LiOH)-4(SiO$_2$) had observed reflections associated with the β-eucryptite LiAlSiO$_4$ phase.

To further assess the crystal structure, the 12(Al$_2$O$_3$)-4(LiOH)-4(SiO$_2$) sample was analyzed via XRD at the 7-2 Beamline at Stanford Linear Accelerator Center (SLAC) to assess the epitaxial relationship of the LiAlSiO$_4$ thin film with respect to the silicon substrate via specular

out-of-plane, radial in-plane, and in various phi XRD scans, where the experimental set-up is shown in Figure 2-10.

As can be seen in specular scans shown in Figure 4-9, for the as-deposited film the only reflections observed are from the Si(004) plane as well as one centered at 2.23Å^{-1}, not seen in the initial scans shown in Figure 4-8, but which is most likely the "forbidden" (002) reflection.. After rapid thermal annealing at 900°C, several peaks can be observed with the most prominent peaks at 1.39 Å^{-1} and 2.78 Å^{-1} corresponding to the reflections of the ($10\bar{1}0$) and ($20\bar{2}0$) planes. The corresponding d value for the ($10\bar{1}0$) plane was 4.52 Å, slightly less than the literature value of 4.55 Å (JCPDS 01-077-0158), indicating compression in normal to surface direction. There are also weaker intensity peaks observed at 1.24 Å^{-1}, 1.61 Å^{-1}, and 1.76 Å^{-1}, which were identified as the (110), (111), (020) of the α-$Li_{4-3x}Al_xSiO_4$ phase as reported by (Smith 1991), which can be described as an Al doped Li_4SiO_4 structure.
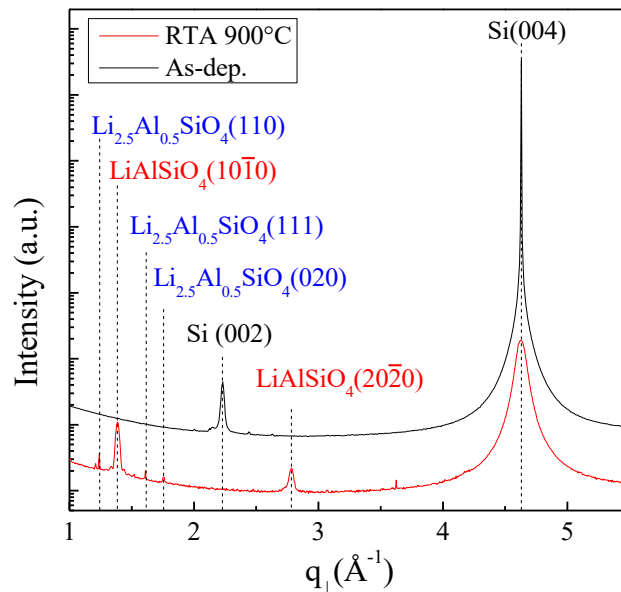
Figure 4-9. Out-of-plane XRD scans of 21 nm $Li_{0.36}Al_{0.28}Si_{0.36}O_{1.32}$ deposited by a 12(Al_2O_3)-4(LiOH)-4(SiO_2) sequence on Si(001).

In-plane scans were also taken of the rapid thermal annealed $12(Al_2O_3)$-$4(LiOH)$-$4(SiO_2)$ thin film to determine the orientation of the crystalline film with regard to the substrate. As can be seen in Figure 4-10, peaks were observed at q = 2.39 Å^{-1}, 4.64 Å^{-1}, and 4.78 Å^{-1} corresponding to the $LiAlSiO_4(1\bar{2}10)$, Si(400), and $LiAlSiO_4(2\bar{4}20)$. There was an additional sharp peak at q = 4.49 Å^{-1} that is most likely a signature of some unknown impurity. The corresponding d value for the $(1\bar{2}10)$, plane was 2.63 Å, slightly larger than the literature value of 2.62 Å (JCPDS 01-077-0158), indicating slight expansion of the unit cell.
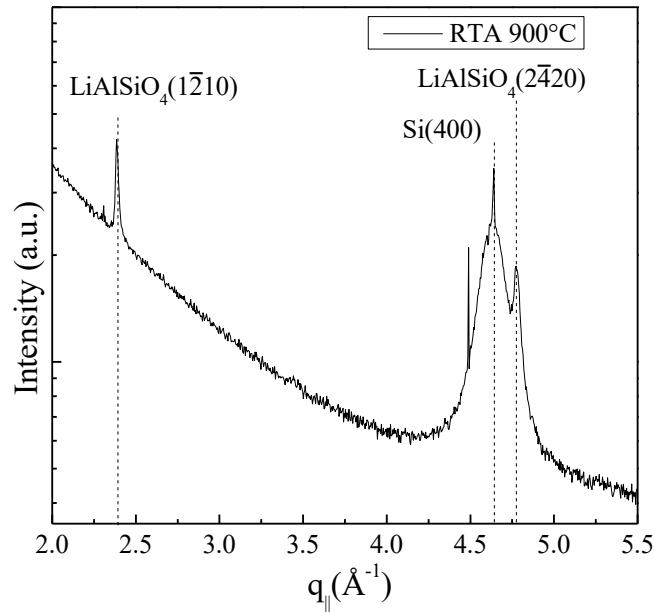
Figure 4-10. In-plane XRD scans of 21 nm $Li_{0.36}Al_{0.28}Si_{0.36}O_{1.32}$ $12(Al_2O_3)$-$4(LiOH)$-$4(SiO_2)$ sequence on Si(001) then annealed at 900°C.

An estimate of the grain size(D) was determined via the Scherer Equation presented in (2-14, where the full-width at half-max (fwhm), was determined utilizing a pure gaussian fit of both the $LiAlSiO_4(20\bar{2}0)$ and $LiAlSiO_4(1\bar{2}10)$, and the shape factor (b) was assumed to be 0.9 . For the out-of-plane peak the grain size estimate was calculated at 14.4 nm, whereas the in-plane

peak was found to correspond to a grain size estimate of 26.1 nm, for the 20-21 nm thin film. No peaks corresponding to the α-Li$_{4-3x}$Al$_x$SiO$_4$ were observed in the in-plane XRD measurements.

Further analysis was performed utilizing a phi scan around several of the observed reflections in the in-plane direction to assess the symmetry. First a phi scan from was measured at q = 2.39 Å^{-1} corresponding to the LiAlSiO$_4$($1\bar{2}10$) plane as well as at q values lower and higher in value (q = 2.20 Å^{-1} and, 2.60 Å^{-1}), where two peaks separated by 90° was only observed for the q = 2.39 Å^{-1} scan although a two-fold symmetry is expected for the ($1\bar{2}10$) plane as shown in Figure 4-11 (a). Furthermore, a phi scan was also taken at q = 4.64 Å^{-1}, 4.78 Å^{-1}, 5.00 Å^{-1}, where the symmetry of the Si(400) and β-LiAlSiO$_4$($2\bar{4}20$) could be assessed. Both the Si(400) and LiAlSiO$_4$($2\bar{4}20$) peaks demonstrated four-fold symmetry (90°) separation, whereas two-fold symmetry was expected for LiAlSiO$_4$($2\bar{4}20$) as shown in Figure 4-11 (b). The observed four-fold symmetry for both the LiAlSiO$_4$($1\bar{2}10$) and LiAlSiO$_4$($2\bar{4}20$) planes indicated the presence of twinned structures. Additionally, the peak intensity for the LiAlSiO$_4$($2\bar{4}20$) peak rotated by 90° was much weaker in intensity, which could be due to a slight miscut in the Si(001) substrate. . The epitaxial relationship of the crystalline β-LiAlSiO$_4$ to the silicon substrate was determined to be β-LiAlSiO$_4$ ($1\bar{2}10$) || Si (100) and β-LiAlSiO$_4$ ($10\bar{1}0$) || Si (001) as shown in Figure 4-11 (c-d). It would be ideal for the c-axis to be normal to the Si(001) for thin film battery applications—which would orient the ion-conduction pathways normal to electrode surface, but alternate substrate selection may produce the desired orientation.
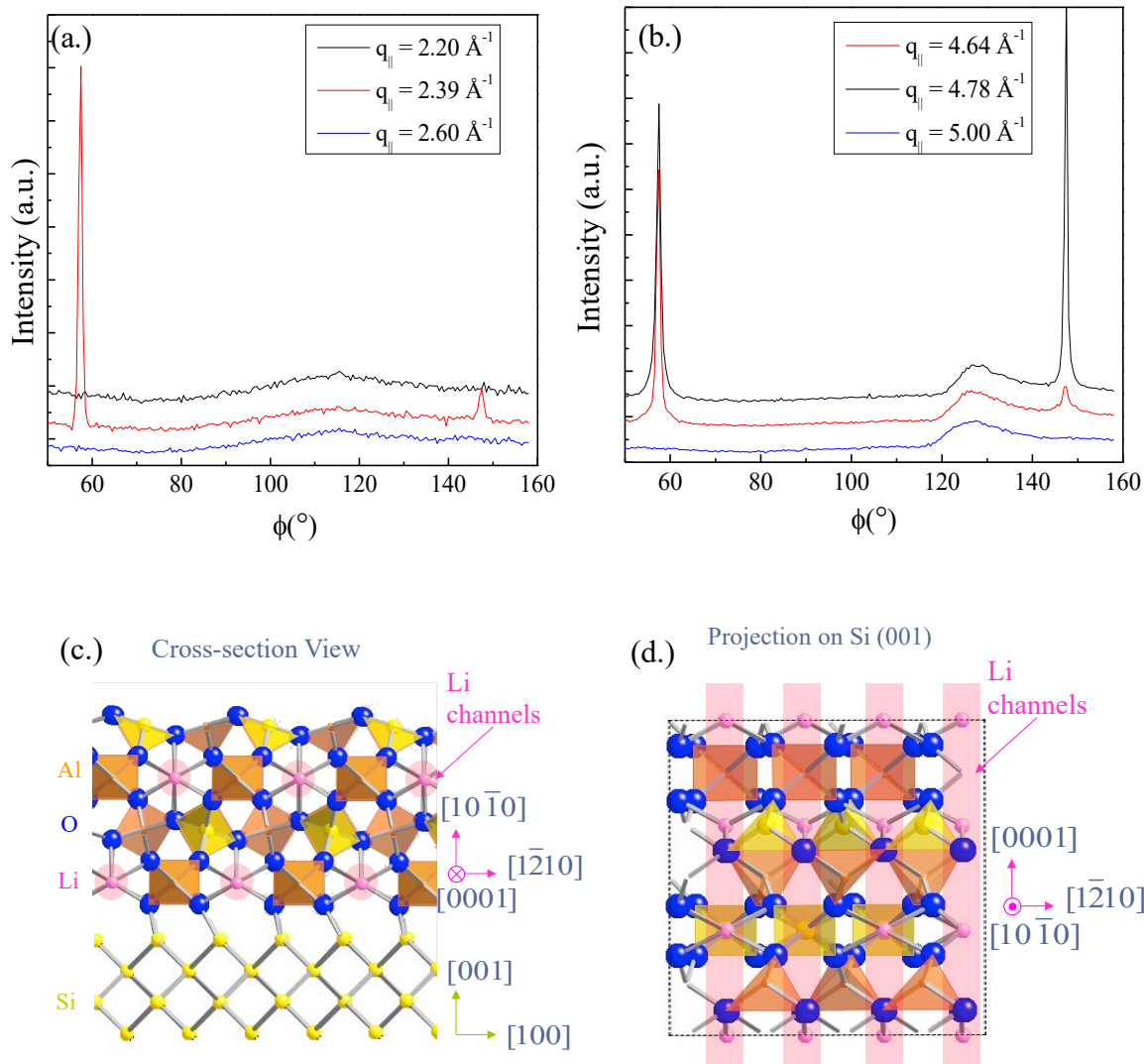
Figure 4-11. Phi scans of the β-LiAlSiO$_4$ ($1\bar{2}10$) peak (a) and of the Si(400) and LiAlSiO$_4$($2\bar{4}20$) (b) with q values of 4.74 Å^{-1} and 4.64 Å^{-1}, respectively, all demonstrating four-fold symmetry. Crystal models showing the interfacial epitaxial relationship of β-LiAlSiO$_4$ on a Si (001) substrate: (c) side-view and (d) top-view. The light pink circles and bars are visual guides to show the location and direction of the 1-D channels.

4.3   Electrochemical Characterization of LiAlSiO$_4$ Solid Electrolytes

Next the ionic conductivity of the β-LiAlSiO$_4$ solid electrolyte was characterized by electrochemical impedance spectroscopy (EIS). Since the silicon substrate was necessary for crystallization of the β-LiAlSiO$_4$ thin film, a p-doped Si(001) wafer with a resistivity of 0.003-

0.005 Ohm-cm was utilized as the substrate. Top electrodes consisting of 150 nm Cu/10 nm Ti were deposited via dc sputtering through a shadow mask to create circular metal pads with a diameter of 500 microns. The EIS spectra were collected with a HP4286 LCR meter utilizing a 13 mV AC voltage and a frequency range of 1MHz to 20 Hz. Contact to the underlying p-Si(001) substrate was made by scratching with a diamond scribe and then contacting with tungsten probes. The EIS spectra were taken in ambient, but with a resistive heated sample stage, where the temperature was monitored via a type-k thermocouple. Temperatures above 100°C were utilized in order to reduce residual surface H_2O. The resulting EIS spectra as shown in Figure 4-12, showed a semicircular behavior indicative of ion transport, modelled by a resistor and constant phase element in parallel. As the temperature was increased a smaller semicircle was observed at lower frequency, modelled again with a resistor and constant phase element in parallel, where the resistance increased with temperature. This signature may be due to an oxide layer on the Cu electrode forming at higher temperatures, or an increase in resistance at the Si/β-LiAlSiO$_4$ interface. Regardless, the larger semi-circle component characteristic of ionic transport in the β-LiAlSiO$_4$ layer, decreases in resistance with increased temperatures, where the Log(σ_{ionic}) vs. 1/T is shown in Figure 4-12 (b), which was roughly linear over the temperatures tested. A thicker film consisting of 12 supercycles of the 12(Al_2O_3)-4(LiOH)-4(SiO_2) deposited on p-Si was also characterized also by impedance spectroscopy. To avoid unwanted oxidation of the top Cu electrodes, the EIS spectra was characterized at 45°C. The EIS data is shown in Figure 4-14, where the data was fit with an equivalent circuit consisting of a resistor (R_1) in series with a resistor (R_2) and constant phase element (C_1) in parallel, where the impedance can be given by the expression shown in Eq. (2-22), where ω is the frequency. The fitted vales were found to be 54.4 Ohms (R_1), 2.34×10^{-9} Farads for the constant phase element with a n value of 0.90764, and finally R_2, the

resistance associated with the solid electrolyte was found to 18917 Ohms. The fitted values correspond to an ionic conductivity of 1.3×10^{-7} S/cm, similar to the extrapolated value for the thinner LiAlSiO$_4$ as shown in Figure 4-14.
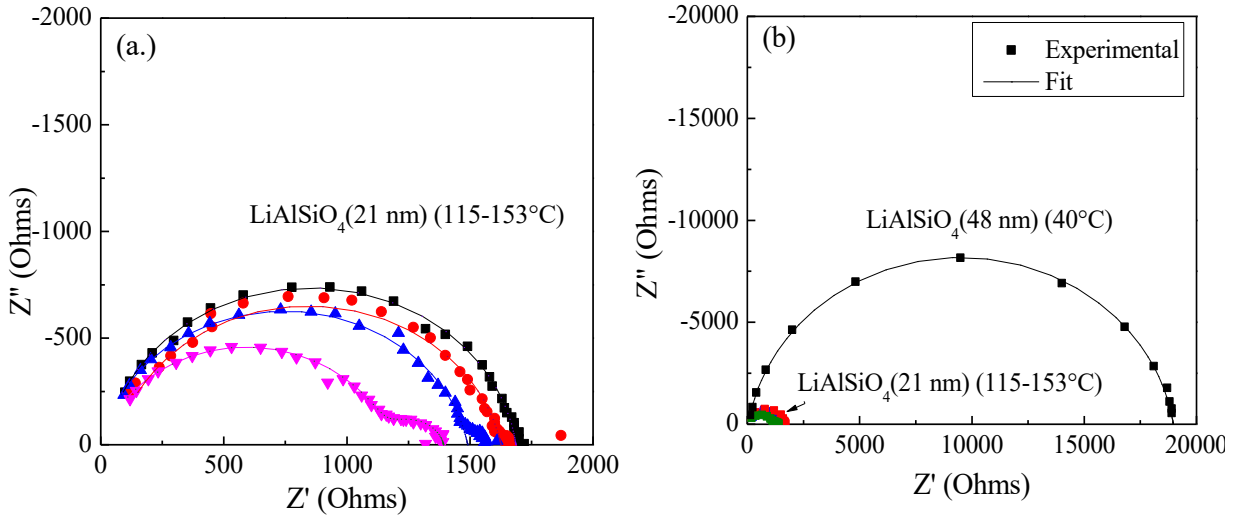
Figure 4-12. (a) EIS spectra of 21 nm LiAlSiO$_4$ thin film (b) EIS spectra taken of a 48 nm LiAlSiO$_4$ deposited with 12 cycles of 12(Al$_2$O$_3$)-4(LiOH)-4(SiO$_2$) at 40°C. Both of the spectra were fitted to an equivalent circuit model consisting of a resistor (R1) in series with a resistor (R2) and constant phase element (C1) in parallel.

In comparison EIS spectra of a Li$_x$Al$_y$Si$_z$O thin films consisting of the cycle sequence: 7(Al$_2$O$_3$)-11(LiOH)-2(SiO$_2$) also rapid thermal annealed at 900°C (1 minute), but that did not crystallize as shown previously in Figure 4-8, is shown below in Figure 4-13. The EIS spectra exhibited a tail-like feature at lower frequency modelled with a constant phase element representing most likely diffusion into the silicon substrate.
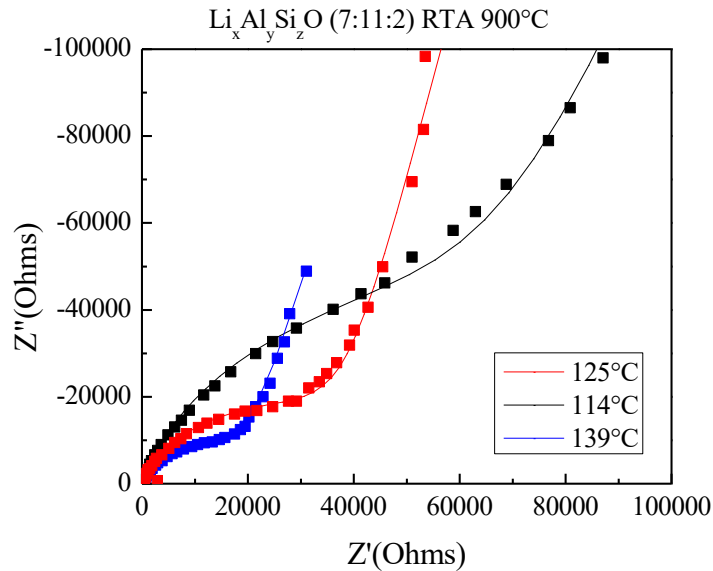
Figure 4-13(a) EIS spectra of ~20nm LiAlSiO$_4$ thin film deposited with a sequence of 7(Al$_2$O$_3$)-11(LiOH)-2(SiO$_2$) . The spectra were fitted to an equivalent circuit model consisting of a resistor (R1) in series with a resistor (R2) and constant phase element (C1) in parallel, as well as an additional constant phase element to model the Warburg-like diffusion behavior.

An Arrhenius plot (Log(σ_{ionic}) vs. 1000/T) is shown in Figure 4-14, which was roughly linear over the temperatures tested. The activation energy calculated from Equation (1-36) was 0.18 eV as compared to 0.69-0.84 eV as reported by (Shin-Ichi 2004) for thin films deposited by pulsed laser deposition and 0.7-0.84 eV reported for amorphous ALD Li$_x$Al$_y$SiO$_z$ thin films (Perng 2014) (Cho 2016). The markedly lower activation energy most likely is due to some more complex phenomenon due to interaction from the Si substrate and the LiAlSiO$_4$ thin film at elevated temperature. One potential cause could be the transition from an ordered to more disordered structure upon heating of the sample, causing a reduction in the ionic conductivity of the LiAlSiO$_4$ layer. Additionally, lithium can alloy with silicon having the potential for there to be an interfacial

reaction layer near the substrate and LiAlSiO₄ interface, that may be masking signature of the ionic transport of the LiAlSiO₄ layer at elevated temperatures. This could have the effect of increased resistance from the interfacial layer as well as a decrease of the ionic conductivity of the LiAlSiO₄ as it is delithiated. A more complex model with an additional constant phase element in parallel with a resistor can be fit to the data, where the capacitance of the two layers would be need to be on the same order of magnitude and the resistance of the interfacial layer would be expected to counteract the reduced resistance associated with the ion transport at higher temperatures in the LiAlSiO₄ layer.

(a) (∥ c-axis) Bulk β-LiAlSiO₄
E_A: 0.79eV
(b) (⊥ c-axis)Bulk β-LiAlSiO₄
E_A: 0.78eV
(c) ALD $Li_{0.4}Al_{0.32}Si_{0.28}O$
E_a:0.70 eV
(d) 21 nm ALD β-LiAlSiO₄ (Cu Electrodes)
E_A: 0.18eV
(e) ALD $LiAlO_X$
E_a:0.46 eV
(f) ALD $Li_xAl_ySi_zO$
E_a:0.65 eV
(g) 21 nm ALD β-LiAlSiO₄ (Pt Electrodes)
E_A: 0.22eV
(h) ALD $Li_xAl_ySi_zO$
Ea:0.84 eV
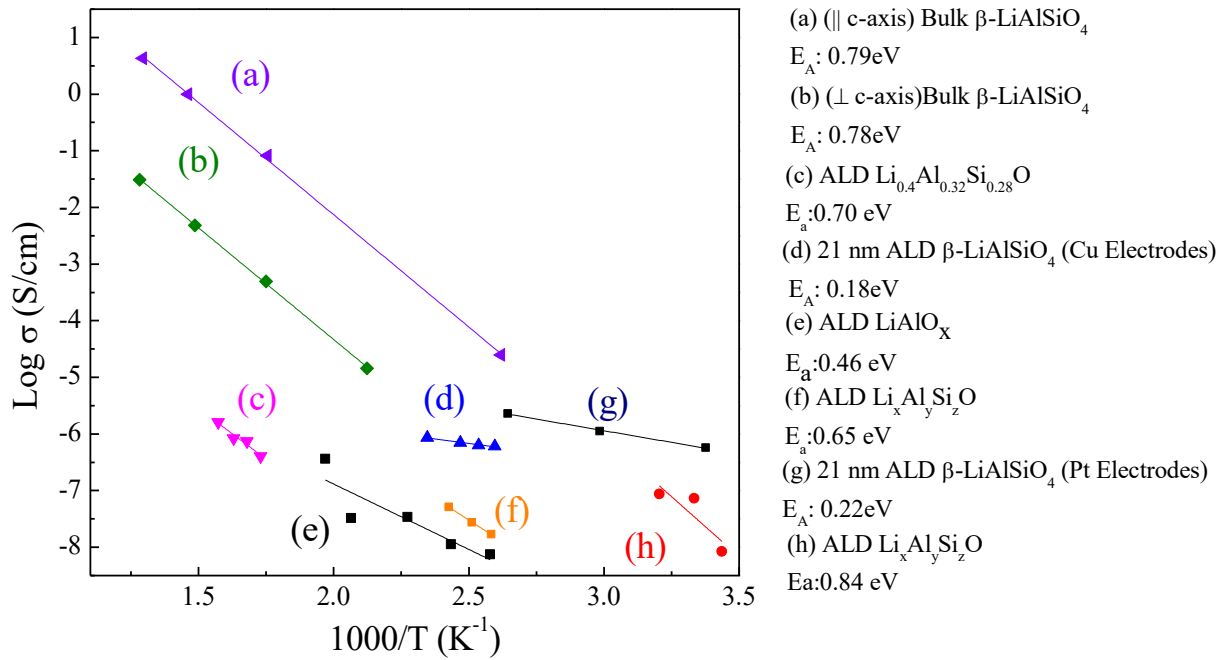
Figure 4-14. Ionic conductivity vs. 1/T plot where literature values for amorphous ALD LASO (Perng 2014, Cho 2016), amorphous ALD LAO(Perng 2014), and bulk values for crystalline LiAlSiO₄ (Nagel 1982).

The calculated ionic conductivity of the thicker 48 nm LiAlSiO$_4$ sample exhibited an ionic conductivity of 1.3 x 10^{-7} S/cm at 45°C, on the same order of magnitude of LIPON based solid electrolytes synthesized via ALD (Kozen 2015, Pearse 2017) and amorphous ALD LASO(Perng 2014), but nearly 2 order higher than an amorphous ALD Li$_{0.40}$Al$_{0.32}$Si$_{0.28}$O with similar composition(Cho 2016). The resistance increase associated with the thicker film as compared to the thinner 21 nm, gives evidence that the measured values are a function of the thin film, rather than surface effects. Ultimately, a conducting, Li-blocking bottom electrode would be more ideal for characterizing the activation energy and ionic conductivity of the LiAlSiO$_4$ thin films, but the c-Si substrate utilized here was needed to crystallize the ALD thin film. As the β-LiAlSiO$_4$ thin films tested here are oriented with c-axis perpendicular to the surface, a more ideal orientation may provide a pathway to further increases in the ionic conductivity, where β-LiAlSiO$_4$ is a known 1D ion-conductor with the highest ionic conductivity in the c-axis direction (Thangadurai 2002, Shin-Ichi 2004) .

4.4   Atomic Layer Deposition of LiSiPO(N) Solid Electrolytes

Although ALD of crystalline LiAlSiO$_4$ was demonstrated, further material development is required for enhanced ionic conductivities >1×10^{-7} S/cm. One potential promising material is LiSiPON, which offers better electrical properties and enhanced ionic conductivities (2×10^{-6} S/cm at room temperature) as compared to thin film LiPON. (Famprikis 2019). Building off the established process for ALD LiPON (Pearse 2017), initial characterization of the atomic layer deposition of LiSiPON based solid electrolytes was performed through a super cycle sequence consisting of $n[a$(LiO^{t}Bu-DEPA)-b(TEOS/H$_2$O)]. XPS was used to determine the surface composition of a LiSiPON thin film deposited with a ALD super cycle consisting of 1(LiO^{t}Bu-DEPA)-1(TEOS/H$_2$O) on Ge(001) at 280°C, in which the detailed scans for the Li 1s, Si 2p, P 1s,

and N1s orbitals are shown in Figure 4-15. The corresponding composition was determined to be $Li_{0.15}Si_{0.02}P_{0.14}O_{0.59}N_{0.02}C_{0.09}$, where some of the oxygen and carbon content is attributed to adventitious carbon. The C 1s peak is relatively and is aligned to 284.8 eV corresponding to sp^3 carbon. The combination of a lack of additional peaks at higher binding energy (>288 eV) indicated no significant lithium carbonate formation.
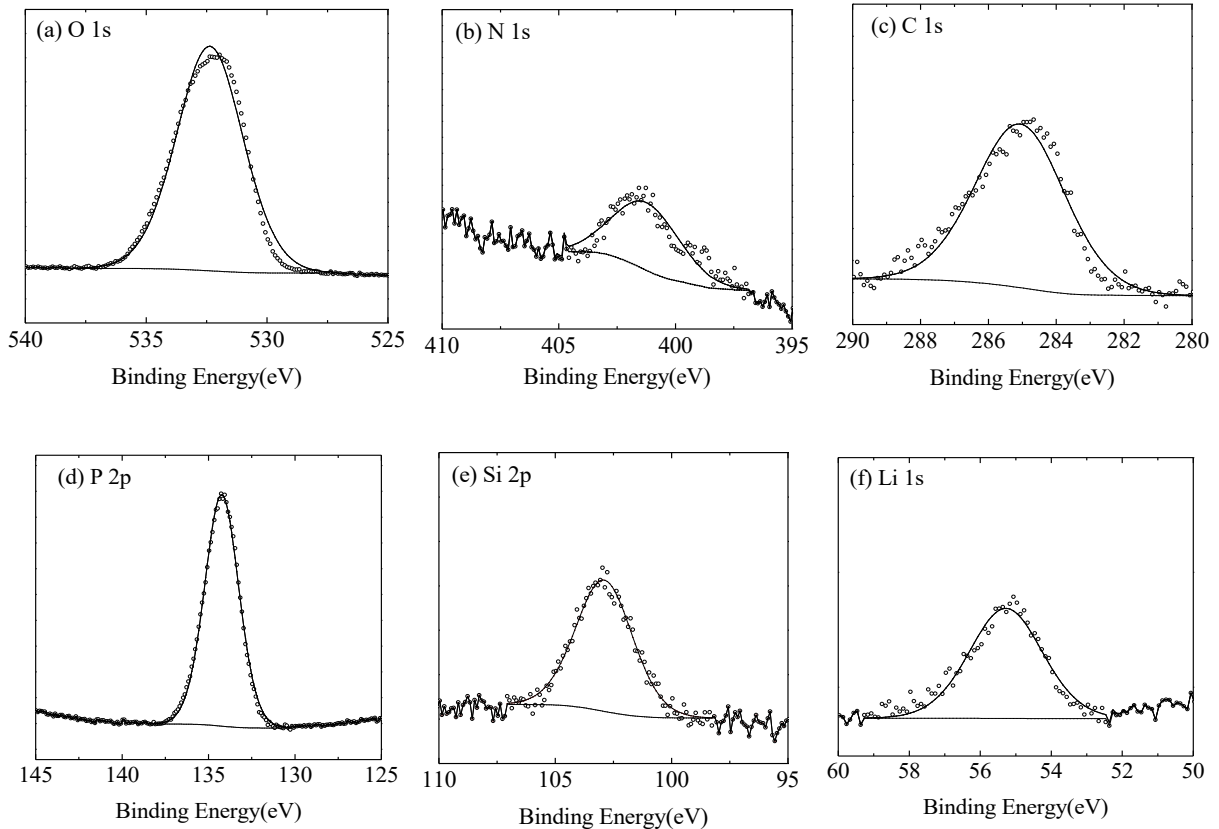
Figure 4-15. High Resolution XPS Detailed scans of the O 1s (a), N 1s (b), C 1s (c), P 2p (d), Si 2p (e), and Li 1s (f) regions of LiSiPO(N) sample deposited at 280°C on a Ge(001) wafer.

Next, the surface composition was quantified via XPS as a function of deposition temperature in the range of 230-290°C, the temperature range was selected to compare with that reported for LiPON (Pearse 2017). The measured relative compositions as a function of deposition temperature on Ge(001) substrates is shown in Figure 4-16(a). Nitrogen incorporation was

relatively low across all deposition temperatures tested, exhibiting the trend of decreased incorporation with increasing temperatures. The low nitrogen content as compared to the stoichiometry reported by (Pearse 2017) could be related to surface reaction of H_2O during the TEOS/H_2O cycle component or could be the effect of ambient reactivity as all the XPS was performed *ex-situ*. Due to lack of lithium carbonate signature in the XPS detailed scans it is hypothesized that the resulting film is closer to the stoichiometry of $LiPO_x$ with small amounts of nitrogen and silicon.

Ionic conductivity measurements were performed on a ~30 nm LiSiPON film as described above deposited an indium tin oxide/SiO_2 substrates. Top contact was made via a liquid mercury drop ranged from 0.177 to 0.0707 cm^2 in area with an assumed average area to be 0.0442 cm^2. The EIS spectra was measured at two places on the electrolyte surface, where the resistance decreased as function of continual measurement which most likely was due to increased wetting of the mercury on the electrolyte surface. Assuming the average area for mercury drop, then the resulting ionic conductivities would have an average ionic conductivity $8.6 \pm 6 \times 10^{-7}$ S/cm, similar or higher to those reported for LiPON (Kozen 2015, Pearse 2017, Put 2019). Although these are only initial results of the ALD process here, further process optimization may be fruitful for achieving higher ionic conductivities.
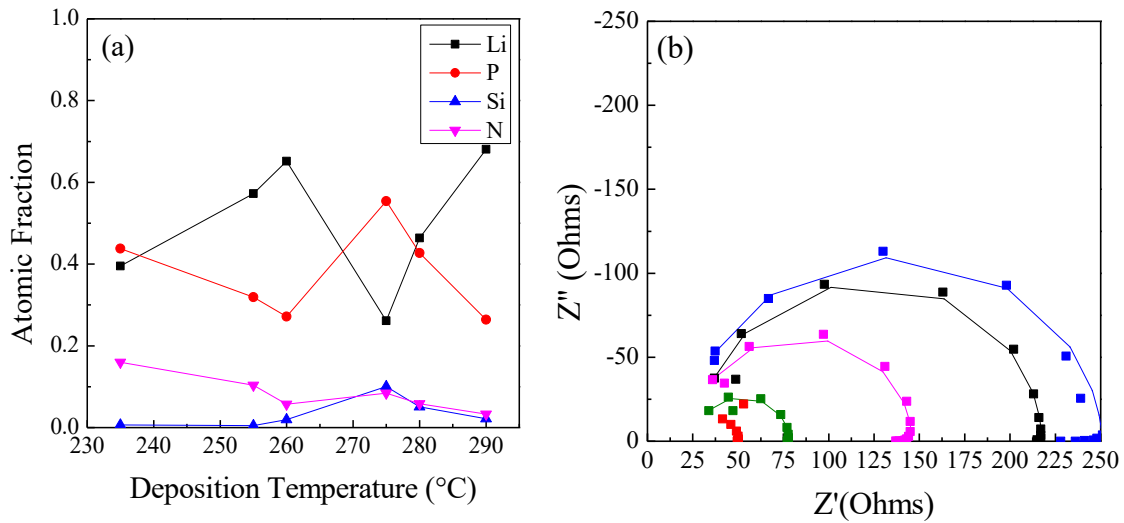
Figure 4-16. (a) Change in surface composition as a function of deposition temperature determined via XPS. Low nitrogen and silicon incorporation was observed with 275°C exhibiting the largest Si and N incorporation. (b) EIS spectra of a 30 nm LiSiPO(N) solid electrolyte deposited on indium tin oxide/SiO$_2$ substrates deposited with cycle sequence: (LiO^{t}Bu/DEPA)-(TEOS/H$_2$O). The solid electrolyte thin films were contacted with a "hanging" drop mercury set-up. The contact area of the mercury drops varied between measurements (hence the spectra above), but the contact area was estimated to be in the range of 0.177 to 0.0707 cm^2 in area. Assuming the average area to be 0.0442 cm^2, then the resulting ionic conductivities would have an average ionic conductivity $8.6 \pm 6 \times 10^{-7}$ S/cm.

In summary, ALD LiSiPON shows promise for as a solid electrolyte due to its high ionic conductivity ($8.6 \pm 6 \times 10^{-7}$ S/cm) in the as-deposited state, where further composition optimization could lead to further enhancement. The atomic layer deposition of thin film Li$_x$Al$_y$Si$_z$O solid electrolytes was demonstrated utilizing two silicon precursors and were amorphous as-deposited. The stoichiometry of the as-deposited Li$_x$Al$_y$Si$_z$O was tuned via the ALD super cycle consisting of a(Al$_2$O$_3$)-b(LiOH)-c(SiO$_2$), where a composition close to stoichiometric LiAlSiO$_4$ allowed for crystallization in the β-Eucryptite phase following rapid thermal annealing. The resulting thin film exhibited an epitaxial relationship with respect to the Si(001) substrate, with the relationship of β-LiAlSiO$_4$ ($1\bar{2}10$) ‖ Si (100) and β-LiAlSiO$_4$ ($10\bar{1}0$) ‖ Si (001). The 1-D

Li-ion channels along the c-axis of β-LiAlSiO$_4$ were parallel to the substrate, where further optimization presents the opportunity to achieve higher ionic conductivities. Since the epitaxial thin film has the potential to facilitate faster ion transport in the solid electrolyte, this work establishes the first attempt to control the orientation of these 1-D channels in solid-state thin films on silicon. With room temperature ionic conductivities on the order of 10^{-7} S/cm LiAlSiO$_4$ is in line with state-of-the-art ALD solid-state electrolytes where oxide-based electrolytes may have beneficial electrical and mechanical properties as compared to phosphate, sulfide, and fluoride based materials.

CHAPTER 5:   INTEGRATION OF THIN FILM SOLID-STATE ELECTROLYTES WITH NANOSTRUCTURED ANODES

Amorphous $Li_xAl_ySi_zO$ thin films show promise for direct integration with high capacity anodes for improved cycle life. Specifically, $Li_xAl_ySi_zO$ thin films (8 and 20 nm) were integrated on SiGe nanowires and remained intact during in-situ lithiation and delithiation, despite 30% radial expansion of the SiGe nanowire induced from lithium alloying. No significant differences were observed to the nanowire expansion between the two different electrolyte thicknesses. Additionally, the germanium component seemed to preferentially lithiathed over silicon producing a Si-rich crystalline core with a lowered lattice constant.

Furthermore, to improve upon the mechanical properties of $Li_xAl_ySi_zO$ for direct integration with high capacity anodes that undergo significant volume expansion, novel hybrid solid-state electrolytes consisting of sequential deposition of ALD $Li_xAl_ySi_zO$ and iCVD Poly(1,3,5,7-tetravinyl-1,3,5,7-tetramethylcyclotetrasiloxane (PV4D4) were demonstrated. The hybrid structure was able to be conformally coated on SiGe nanowires, exhibited a 4 MV/s breakdown voltage a 19 nA/cm^2 leakage current at 4V bias, and no significant interfacial resistance was introduced (measured ionic conductivity of 10^{-9} S/cm). The hybrid/Co_3O_4 thin film composited exhibited increased capacity with continuous cycling most likely due to uptake of lithium-ions in the PV4D4 layer making it more ionically conductivity allowing more Co3O4 to be lithiathed prior to the 0.2V cut-off. After 100 cycles at ~2C the hybrid and $Li_xAl_ySi_zO$ coated Co_3O_4 exhibited discharge capacities of 8.4% and 20.6% higher as compared to the uncoated Co_3O_4 anode, with the potential to offer further improvements to alloying anodes that undergo even larger volumetric changes during charge/discharge.

162

5.1 Lithiation of $Li_xAl_ySi_zO$ coated SiGe nanowires

Crystalline SiGe nanowires have gained interest for application as Li-ion battery anodes due to the high theoretical capacity (3579 mAh g^{-1} for Si and 1624 mAh g^{-1} for Ge) as well as the improved mechanical properties that can mitigate issues of the large lithiation induced volume expansion through heterostructuring (Kim 2018). Although the large surface area of nanostructured anodes can allow for high rate capability, SEI formation can be deleterious for cycle stability, especially on alloying electrodes with large volumetric changes upon lithiation/delithiation. A solid-state electrolyte coating that can be conformally coated on the nanowire structure could help improve capacity retention by acting as an "artificial" SEI layer, but the effects of such a coating on the lithiation behavior of the group IV nanowire-based anodes is unknown. SiGe nanowires with [112] axial growth direction were integrated with ALD $Li_xAl_ySi_zO$ thin film solid electrolytes and the lithiation behavior was characterized by *in-situ* TEM. Three experimental conditions are shown below: (1.) galvanostatic lithiation of an 8 nm $Li_xAl_ySiO_z$ coated SiGe nanowire, (2.) galvanostatic lithiation of a 20 nm $Li_xAl_ySi_zO$ coated SiGe nanowire, and (3.) potentiostatic lithiation of a 6 nm $Li_xAl_ySi_zO$ coated SiGe nanowire. General trends observed across the samples was the formation of a crystalline core with a smaller lattice constant upon lithiation—pointing to compression from the amorphous overlayer or preferential lithiation of Ge. Additionally, no significant breakdown of the electrolyte layer was observed as well as a core-shell like lithiation front with slow radial lithiation most likely limited by compressive stresses as observed by Liu et al (Liu 2013).

TEM images of the 20 nm $Li_xAl_ySi_zO$/SiGe nanowire before after lithiation at a constant current of 3 pA is shown in Figure 5-1 (a) and (b), respectively. The majority of the expansion was in the radial direction with slight expansion in the [112] axial direction. Areal mapping was utilized to

determine areal changes post lithiation utilizing imageJ software, indicating a 28% areal expansion. The lithiation of SiGe nanowire was not uniform across the wire, most likely due to slow radial diffusion of Li ions, but the change in diameter marked in Figure 5-1 was 26%, where the expansion is consistent with expansion associated with the observed amorphous $Li_xSi_yGe_z$ layer. The structure is presented in Figure 5-1 where (ii) marks the amorphous alloy region, (i) is the crystalline core (i), and (iii) marks the solid electrolyte layer (iii). In Figure 5-1 (d-e), TEM images showed a pristine 8 nm $Li_xAl_ySi_zO$/SiGe nanowire sample before and after lithiation galvanostatically at 1 pA. 2D areal mapping showed a 2D areal increase of 32% post lithiation and a measured radial change of nearly 39%, where again the change in diameter was not uniform across the nanowire due to incomplete lithiation. Comparatively, the 20 nm $Li_xAl_ySi_zO$/SiGe structure did not have a significant difference in the overall areal change, but did have less radial expansion near the lithium metal, this may be complicated due to differences in the dimension of the nanowire, but may be associated with decreased lithiation kinetics due to thicker electrolyte coating. The 8 nm $Li_xAl_ySi_zO$/SiGe was delithiated at the same applied current (1 pA), where a second layer formed uniformly across the surface nanowire (iv) as shown in Figure 5-1 (f) which is most likely Li metal from delithiation of the nanowire structure. The overall radius did not decrease significantly due to the overlayer formation (~1%), but there was slight axial contraction (~8.5 %).
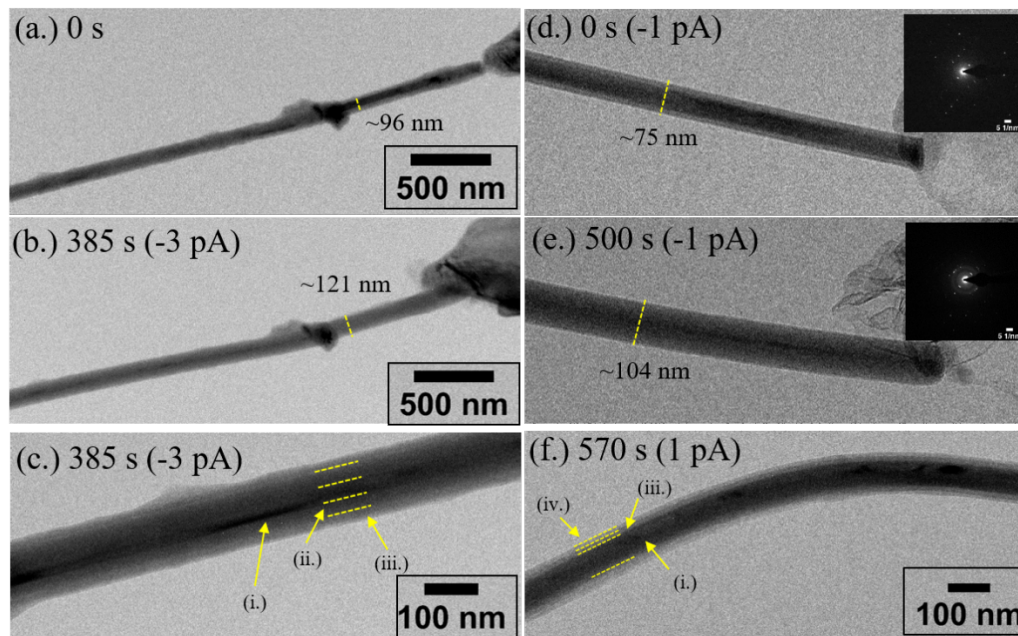
Figure 5-1. In-situ TEM of $Li_xAl_ySi_zO$ coated SiGe nanowires. (a) Pristine 20 nm $Li_xAl_ySi_zO$/SiGe in contact with Li metal (b) post lithiation at -3 pA. (c) 20 nm $Li_xAl_ySi_zO$/SiGe near substrate away from lithium metal shows distinct crystalline core (i) and amorphous alloy layer (ii.) as well as the intact $Li_xAl_ySi_zO$ layer (iii.). (d) is a pristine 8 nm $Li_xAl_ySi_zO$/SiGe nanowire in contact with lithium metal prior to lithiation (e) post lithiation at -1pA, (f) and post delithiation at (1 pA), where an overlayer formed on the surface (iv.), an intact electrolyte layer (iii.) and the SiGe nanowire (i). the inset of parts (d) and (e) are selected area electron diffraction, in which a single crystalline SiGe with lattice constant 5.55Å is observed in the pristine sample, and polycrystalline SiGe with amorphous rings most likely associated with the $Li_{15}Si_{4-x}Ge_x$ phase.

Selected area electron diffraction was performed before and after lithiation as shown in the inset of Figure 5-1 (d-e), where a decrease in measured lattice constant from 5.55Å to 5.51Å post lithiation, which would equate to a phase change from $Si_{0.44}Ge_{0.56}$ to $Si_{0.62}Ge_{0.38}$ utilization the relation described by (Dismukes 1964). Measured d values for several planes are shown in Table 5-1. Preferential lithiation of germanium has been observed previously in core-shell SiGe structures, where preferential lithiation of a Ge core in a Si/Ge core shell structure was observed (Liu 2013) nanowires as well as several core shell configurations (Liu 2015). The different lithiation behaviors between Si and Ge has been proposed to be due to difference in the chemical

potential barriers at each respective surface to diffuse (Tersoff 1990, Liu 2015) coupled with the fact that the Li-ion diffusivity is around 400 times higher in Ge as compared to Si (Fuller 1954, Chockla 2012, Li 2012). Both samples galvanostatically lithiathed showed a core-shell like lithiation behavior, where at the current density the nanowire should have completely lithiathed in a fraction of the time—indicating similar behavior that has been observed for silicon nanowires in which self-limiting lithiation was observed due to compressive stresses in the amorphous Li_xSi_y shell (Liu 2013). Furthermore, the lithiation behavior of the SiGe alloy is in contrast to isotropic lithiation observed in Ge nanowires (Liu 2011, Liu 2013).

Table 5-1. Measured d values for indexed lattice planes in SAED patterns of nanowire before and after lithiation

Sample	h	k	l	d(nm)
Pristine	2	2	0	0.197
	1	3	1	0.168
	1	1	1	0.319
	3	1	1	0.167
Post Lithiation	1	1	3	0.166
	1	3	5	0.093
	2	2	4	0.112
	1	1	1	0.317

Next the lithiation behavior of a SiGe nanowire coated with a 5 nm $Li_xAl_ySi_zO$ coating was characterized via potentiostatic lithiation at -2.5V. Significant carbon deposition occurred during imaging, most likely due to contamination on the TEM sample holder making resolving the $Li_xAl_ySi_zO$ electrolyte difficult as well as the ability to monitor volumetric changes upon lithiation. As shown in Figure 5-2, shrinking of the SiGe crystalline core was observed during lithiation to form an amorphous Li_xSi_yGe phase, in which the core's diameter changed ~29% post lithiation. Comparing changes in the SiGe nanowire near the lithium metal contact an observed radial expansion from 53 to 69 nm equating to a ~30% radial increase. The formation of the amorphous $Li_xSi_yGe_z$ phase was not uniform across the nanowire as can be seen in Figure 5-3 (b), but was

measured to be 15-19 nm, where the crystalline core near the lithium metal contact ranged from 29-37 nm. The thinnest region of the crystalline core was ~50 nm from the Au tip, most likely the site of slow radial lithiation, in which the front had not yet propagated down the length of the wire as shown in the STEM HAADF image shown in Figure 5-3 (b).
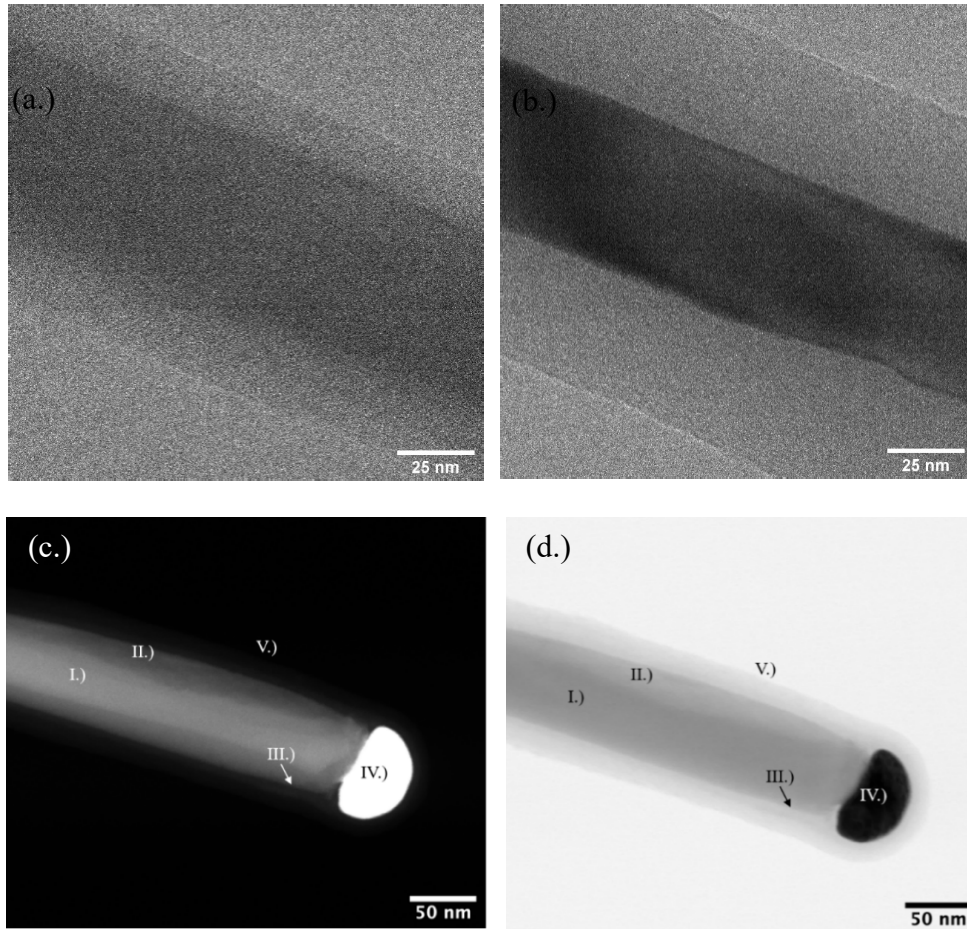
Figure 5-2. TEM image of pristine SiGe Nanowire with 5 nm LASO coating (a) and post lithiation at -2.5V (b). The top darker region is the silicon wedge substrate, the bottom lighter region is the Li_2O/Li metal contact, the dark tip of the nanowire is a gold nanoparticle utilized to catalyze the SiGe nanowire growth. The SiGe crystalline core reduces from a diameter of 68.1 to 48.5 nm a change of nearly 30%. HAADF(a) and BF(b) STEM of the LASO coated SiGe post lithiation at -2.5V. Region (i) is identified as crystalline core of the SiGe remaining post lithiation, (ii) is identified as an amorphous $Li_xSi_yGe_z$ phase, (iii) intact LASO electrolyte later, (v) carbon layer deposited during imaging from the electron beam.

Post-lithiation SAED and EDS were performed on the lithiated $Li_xAl_ySi_zO/SiGe$ nanowire as well as an adjacent pristine nanowire to assess changes in the composition and structure. SAED patterns of the pristine wire are shown in the inset of Figure 5-3, where the SiGe nanowire is single crystalline. The overlapping diffraction spots could be due to being off zone-axis or potentially twinning within the nanowire structure. A lattice constant of 5.54Å was calculated from the indexed diffraction spots, indicating a composition of roughly $Si_{0.51}Ge_{0.49}$, in comparison to the lithiathed structure (different nanowire) the lattice constant was calculated to be 5.48Å, indicating a composition of $Si_{0.73}Ge_{0.27}$ in line with compositional changes observed in the galvanostatically lithiathed nanowires. An EDS line-scan to quantify the concentration profile of Si and Ge was measured across the pristine and lithiathed nanowire as shown in (a) and (c) of Figure 5-3, respectively. All of the line-scans were post-processed utilizing a 5-point average, in order to reduce signal/noise for clearer interpretation. Direct comparison of the absolute intensity of the Si and Ge signal as a function of the distance is not applicable due to various atomic sensitivity factors of each. In the pristine nanowire sample, the silicon profile is slightly wider than the germanium profile, as expected due to the presence of the solid electrolyte layer. Across the nanowire, the profile for both Si and Ge were relatively flat as expected since the nanowire was single crystalline with some tapering in the profile due to the cylindrical nature of the nanowire. In comparison, the Ge and Si profiles varied significantly post lithiation. Assuming a uniform concentration for both Ge and Si across the nanowire, the expected profile post lithiation, would have a uniform maximum in the center of the nanowire corresponding to the crystalline core, where there should be lower intensity in the amorphous lithiathed regions due to the lower density of both Si and Ge as well as the 30% radial expansion. For Si the line plot exhibits a flat plateau of maximum intensity roughly 28 nm in width corresponding to the crystalline core, where the profile slopes

downwards corresponding to the amorphous alloy phase. The Ge profile exhibits a similar flat profile roughly 28 nm in width like the Si profile and a down sloping profile in the amorphous alloying region, but as a peak of larger intensity in the center. In the context of the electron diffraction results, the Ge profile is interpreted as follows: a crystalline core, of uniform Si composition, but a diminished Ge concentration moving in the radial direction, which would account for the contracted lattice constant observed via electron diffraction post lithiation.
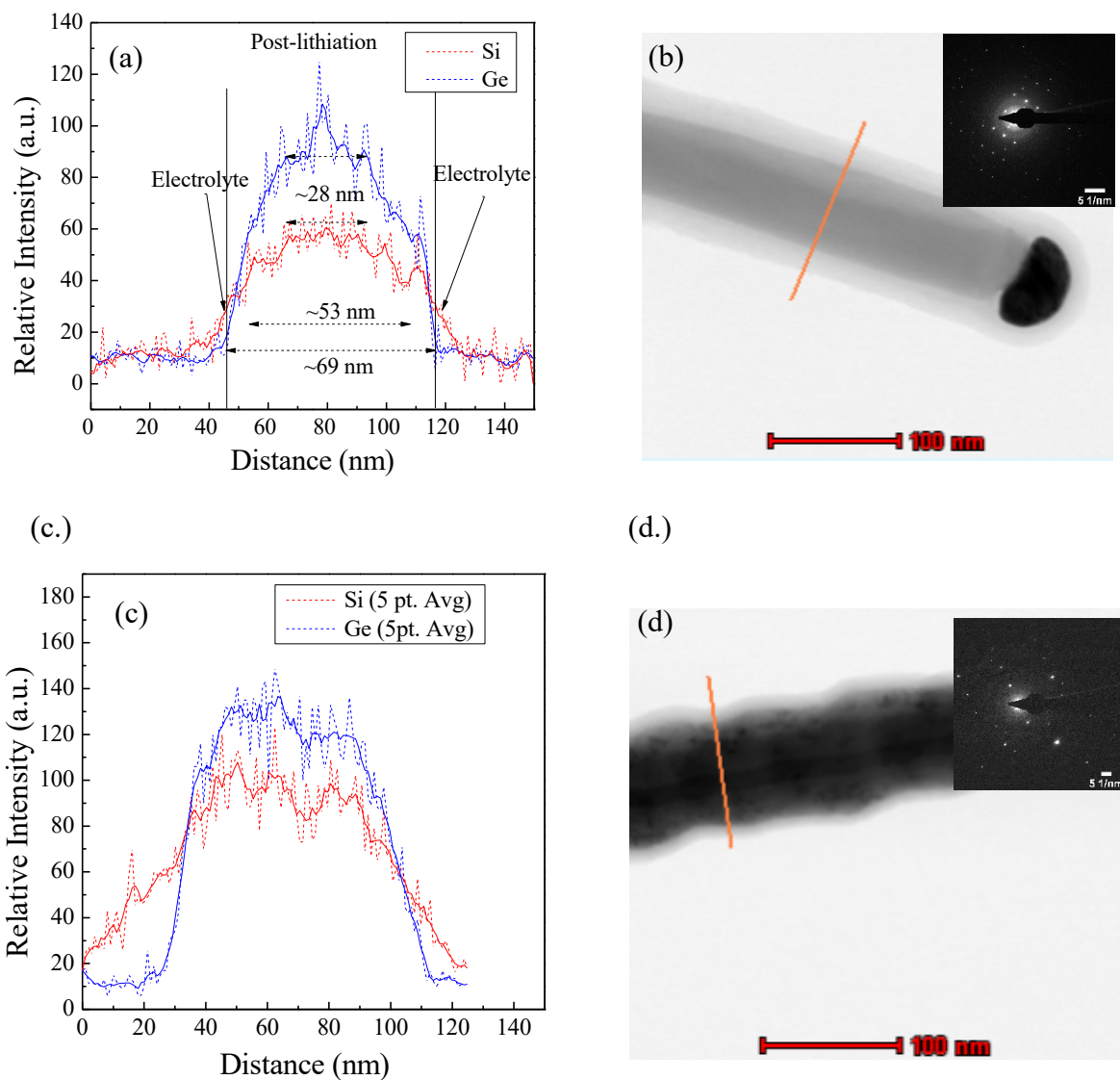
Figure 5-3. EDS line scans of the (a) nanowire tip post lithiation and (b) another pristine nanowire and the corresponding BF STEM images for the (c) nanowire tip post lithiation nad (d) another pristine nanowire. Selected Area Electron Diffraction of the pristine LASO/SiGe samples and post lithiation at -2.5V are shown as insets in (c,d). Indexing of the remaining crystalline component post lithiation demonstrates a lattice constant of 5.48 Å vs. 5.54 Å in the pristine sample. The alloy composition calculated from both lattice constants corresponds to $Si_{0.73}Ge_{0.27}$ (post-lithiation) and $Si_{0.51}Ge_{0.50}$ (pristine)

Overall, a few consistent phenomena were observed in the lithiation of $Li_xAl_ySiO_z$ coated

SiGe nanowires. Germanium seemed to be preferentially lithiathed over silicon in the SiGe

nanowires producing a Si-rich crystalline core with a lowered lattice constant. No obvious break in the electrolyte was observed during the lithiation of the nanowire, where similar radial expansion was observed for $Li_xAl_ySi_zO$ coatings of 8 and 20 nm. Utilizing a solid-state electrolyte coating as shown here that can be conformally coated on the nanowire structure could help improve capacity retention by acting as an "artificial" SEI layer for further improved capacity retention in SiGe nanowire-based anodes.

5.2   Structural Properties of ALD $LiMn_2O_4$/ALD LASO/SiGe Nanowire Structure

An all-solid-state nanowire battery was fabricated to assess the structure properties of the $Li_{1+x}Mn_{2-x}O_4$ films deposited on a 3D structure. A SiGe nanowire was utilized as a substrate/current collector/anode. Next an ALD $Li_xAl_ySi_zO$ layer was deposited on the SiGe nanowire to act as a solid electrolyte layer. The composition of the $Li_xAl_ySi_zO$ was quantified via XPS on a Pt-Si substrate processed during the same deposition on the SiGe nanowires. The composition was determined to be $Li_{0.16}Al_{0.2}Si_{0.64}O_{2.7}$, where the oxygen stoichiometry was calculated from the percentages of the metal cations. XPS spectra of a sample with sequential deposition of ALD $Li_{1+x}Mn_{2-x}O_4$ and ALD $Li_xAl_ySiO_z$ is shown in Figure 5-4.
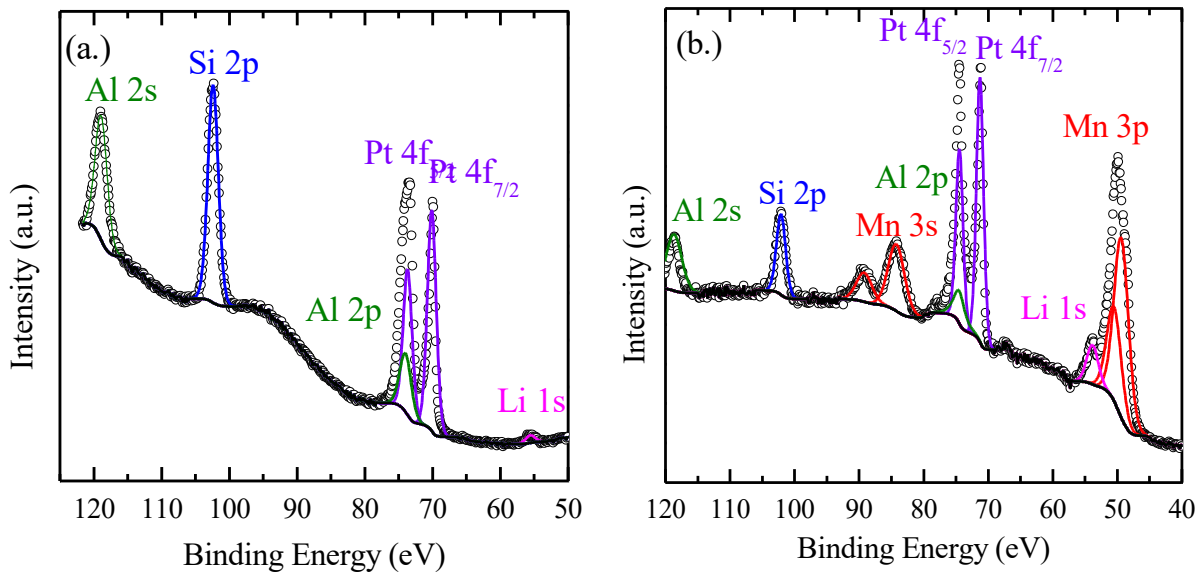
Figure 5-4. High Resolution XPS of $Li_{1+x}Mn_{2-x}O_4$/LASO on Pt-Si post rapid thermal annealing (b.). The 2D Pt-Si substrate was run during the deposition on the SiGe Nanowire substrates. The calculated composition of the as-deposited lithium aluminum silicate was $Li_{0.16}Al_{0.20}Si_{0.64}O_{2.7}$

A conformal thin $Li_xAl_ySi_zO$ film coated SiGe film is shown in the TEM image in Figure 5-5 (b), where the (i.) denotes carbon deposition (ii.) the SiGe nanowire, (iii.) the $Li_xAl_ySi_zO$ layer, and (iv.) the gold nanoparticle utilized for SiGe growth. The TEM holder was utilized without proper O_2 plasma cleaning, which led to significant carbon deposits throughout imaging. A lattice constant of 5.54Å was calculated from the average of several diffraction spots from the selected area electron diffraction shown in Figure 5-5(a), indicating a composition of roughly $Si_{0.51}Ge_{0.49}$ utilizing an empirical relation (Dismukes 1964). The $Li_xAl_ySi_zO$ deposition in the full-cell stack was twice the number of global cycles as shown in Figure 5-5, resulting in a thickness of ~12-16 nm.
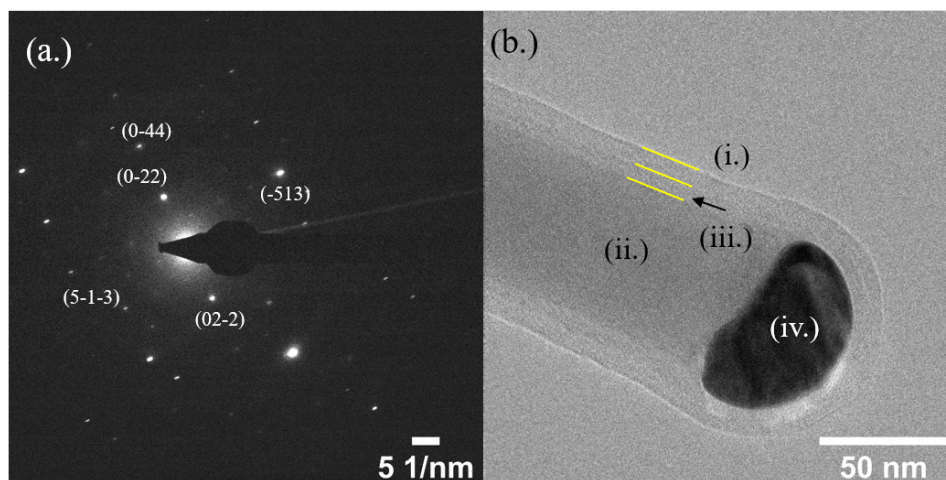
Figure 5-5. TEM Characterization of Nanobattery consisting of LiMn$_2$O$_4$/LASO/SiGe Nanowire. (a) Selected area electron diffraction (SAED) of ALD LASO coated SiGe nanowire. (b) TEM image of ALD LASO coated SiGe Nanowire, where (i) is carbon deposited in TEM, (ii) SiGe nanowire, (iii) amorphous ALD LASO layer, (iv) gold nanoparticle utilized in SiGe growth.

Next a ~20 nm LiMn$_2$O$_4$ films was deposited on the Li$_x$Al$_y$Si$_z$O coated SiGe nanowire to act as a cathode material. There was a vacuum break between the ALD deposition of Li$_x$Al$_y$Si$_z$O and LiMn$_2$O$_4$, which could potentially lead to lithium carbonate formation on the surface of the electrolyte layer. The nanostructure was then rapid thermally annealed for 1 minute at 750°C to crystallize the LiMn$_2$O$_4$ film into the electrochemically active spinel phase. A TEM image of the final structure is shown Figure 5-6(a) and dark field STEM of another nanowire is shown in Figure 5-6(b). Immediate observation is that the Au tip has broken and diffused down the length of the nanowire (dark regions in BF, light regions in DF) during the annealing process.
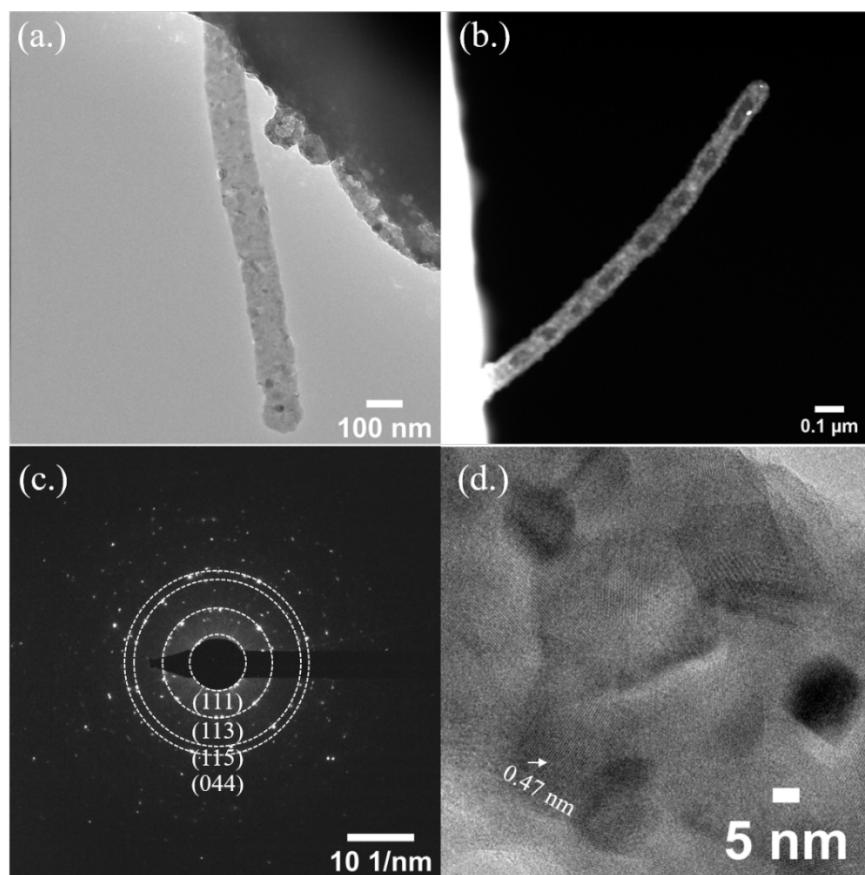
Figure 5-6. (a) TEM image (b) HAADF STEM of $LiMn_2O_4$/LASO(12nm)/SiGe nanowire post annealing at 750°C (1 minute, 50°C/s), (c) SAED pattern of $LiMn_2O_4$/LASO(12nm)/SiGe nanowire, and (d) HRTEM of $LiMn_2O_4$/LASO(12 nm)/SiGe nanowire.

The edges are rough due to $LiMn_2O_4$ crystallite formation along the surface of the nanowire. SAED is shown in Figure 8e, where polycrystalline rings are observed corresponding to the $LiMn_2O_4$ phase, where for instance the d spacing associated with the (113) set of planes was measured to be 0.247 nm as compared to the 0.249 nm value as measured in the literature (JCPDS reference pattern 00-035-0782). The calculated lattice constant form the average of the d-spacing measurements was 8.25 Å. Lastly, HRTEM of one of the nanowire samples is shown in Figure 5-6 (d), where 0.47-0.48 nm lattice spacing was observed associated with the (111) planes of $LiMn_2O_4$

as well as various regions exhibiting Moiré diffraction patterns most likely arising from overlap of rotated $LiMn_2O_4$ lattices.

Table 5-2. Measured D-spacings from SAED pattern of Nanowire Structure

Plane	Measured D-spacing (nm)	Theoretical D-spacing (nm)
(022)	0.293	0.291
(113)	0.249	0.248
(222)	0.239	0.238
(224)	0.168	0.168
(115)	0.159	0.159
(044)	0.146	0.146
(135)	0.139	0.140

Although the structure was not ideal to deploy as functioning solid-state battery it does present as interesting platform for future in-situ TEM characterization and highlights the challenges associated with device integration. Due to the inherent control over composition, atomic layer deposition is a unique tool to explore various compositions not accessible via other synthesis techniques that could provide insight into the development of high-performance materials.

5.3   Hybrid Inorganic/Organic Solid Electrolytes for Integration with Co_3O_4 Anodes

Composited solid electrolytes (or "Hybrid") consisting of a metal-oxide and polymeric component were fabricated and their properties explored. For fabrication of the hybrid electrolyte, a thin $Li_xAl_ySi_zO$ layer was deposited (~5 nm) by ALD at UCLA, and the iCVD pV4D4 deposition at MIT, where the deposited film thickness was on the order of 30 nm. Choice of the layer orientation (metal oxide) was chosen to ensure optimal interface with the anode material as well as potential electrochemical stability. This choice recently utilized in a similar coating scheme described by (Zhao 2019), mimics the solid electrolyte interphase observed in lithium-ion batteries, in which a thinner inorganic layer forms at the electrode surface followed by a thicker organic layer. The solid electrolyte interphase—although a product of the electrolyte breakdown, helps to form a stabilized interfacial layer for stabile charge/discharge allowing ion transport, but preventing further electrolyte breakdown. When moving towards next generation high capacity anodes such as with lithium metal or alloying anodes (Si, Ge, Al, Sn), ever critical becomes the mechanical stability of this solid electrolyte interphase layer due to the large volume expansion/contraction upon lithiation and delithiation. Utilization of these anode materials in all-solid-state thin film batteries also may lead to battery shorting, whether it be due mechanical fatigue from expansion/contraction of lithium metal dendrite formation in the case of lithium metal batteries.

The added advantage of utilizing ALD and iCVD as a deposition tool is electrolyte conformality, which allows for uniform coating on high-aspect ratio structures. High surface area electrode structures can allow for high areal energy density, but generally must be balanced against decreased coulombic efficiency due to increased electrolyte breakdown. Utilizing a "hybrid" solid electrolyte layer as an artificial SEI layer offers the potential to increase the cycle stability of these

high surface area electrodes. Although only a few processing conditions are presented here, the results are promising for further optimization for highly controlled artificial solid electrolyte interphase layers for improved cycle stability in high capacity anodes.

As more extensive materials characterization of ALD LASO and iCVD PV4D4 materials individually are presented in the previous section as well as elsewhere (Perng 2014, Chen 2015), focus was on their material properties as a couple. Figure 5-7 shows a high resolution TEM image of a conformal coating of the sequential ALD/iCVD layers on a SiGe nanowire.
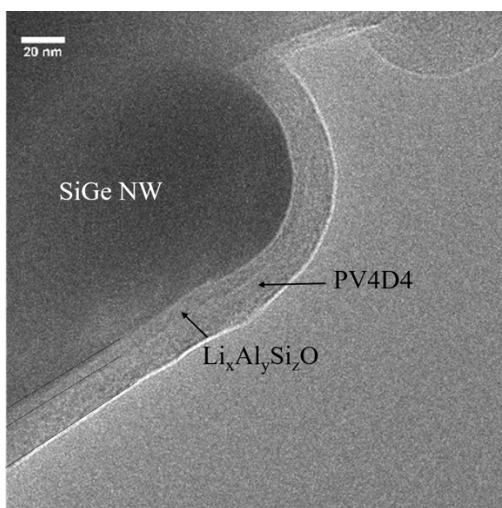
Figure 5-7. TEM image of SiGe nanowire coated with 5 nm LASO followed by 15 nm of PV4D4.

First, the electrical properties of the hybrid electrolyte were characterized, in which the lithium hydroxide component was removed from the ALD sequence to delineate effects of lithium transport (~3 nm AlSiO$_4$, 30 nm PV4D4). The electrical properties of the solid electrolyte become crucial when scaling down thickness in utilization as both a solid-state electrolyte in a thin film battery as well as use as an artificial SEI layer. In a solid-state battery, the electrolyte layer must prevent self-discharge between the electrodes (low leakage current, pinholes) as well as dielectric breakdown as the electrolyte thickness is order of tens of nanometers.

The sample structure for electrochemical testing consisted of a hybrid layer consisting of 3 nm AlSiO$_4$/30 nm PV4D4 deposited on indium tin oxide/SiO$_2$ substrates, where electrical contact was made circular top electrodes via 100 nm Pt/10 nm Ti electrodes fabricated via electron beam evaporation with use of a shadow mask. IV curves are presented in Figure 5-8(a) over a 50 ms period, in which box-like IV behavior was observed characteristic of a capacitor-like behavior, with a large increase in current observed at -14V bias—most likely indicative of partial breakdown. Leakage current measurements were taken from 1V to 4 V as shown in Figure 5-8 (b). The observed leakage current of 2×10^{-7} A/cm^2 at 4V (relevant to lithium-ion batteries), would cause complete discharge of a one-micron thick LiMn$_2$O$_4$ (606 mAh/cm^3) cathode in ~300 hours and a 100 nm LiMn$_2$O$_4$ in ~30 hours. The thickness of 5 nm Li$_x$Al$_y$Si$_z$O/30 nm PV4D4 should be suitable as a thin film solid electrolyte, but further confirmation of the pinhole density is needed. Ideally, thicker electrolytes layers would be ideal, but this must be weighed against increases in ionic resistance that could undermine battery performance.
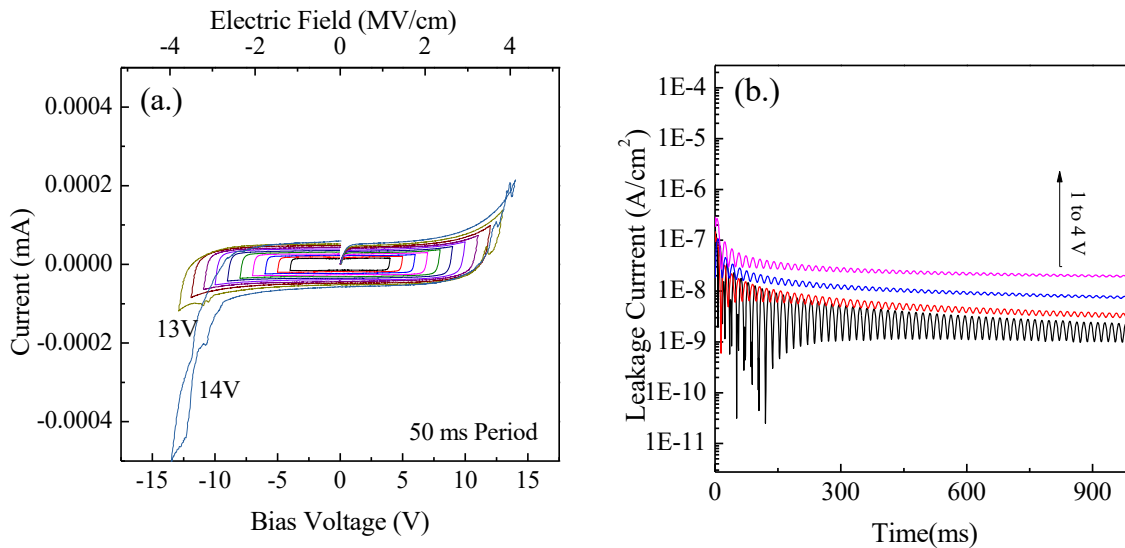
Figure 5-8. Electrical Characterization of AlSiO$_4$/PV4D4 thin films. (a) IV curves with a 50 ms period, where the current was measured as a function of sweeping the voltage. Partial breakdown was observed upon biasing at -14V. (b) Leakage current after applying a bias of 1 to 4V.

Co$_3$O$_4$ thin film anodes were integrated with various solid electrolyte coatings to determine the effect on the electrochemical performance. A hybrid electrolyte consisting of 5 nm Li$_x$Al$_y$Si$_z$O and 30 nm of PV4D4 was explored as well as 5 nm Li$_x$Al$_y$Si$_z$O. The ordering of the inorganic/polymeric layers was chosen to mimic "natural" SEI formation where a thin dense inorganic layer forms on the electrode surface followed by a larger organic based layer. Only the thicknesses of the coatings mentioned here were characterized, but further optimization of the both layer thicknesses may lead to more optimal electrode performance. iCVD PV4D4 thin films do not inherently contain lithium so they need to be either soaked in liquid electrolyte or electrochemically lithiathed by slow charge/discharge of the underlying electrode. To lithiate the PV4D4 layer, an initial conditioning step was performed at a specific current of 2.2µA cm^{-2} (C/10) for ten cycles (3 cycles for the uncoated Co$_3$O$_4$ and Li$_x$Al$_y$Si$_z$O/Co$_3$O$_4$), where the charge/discharge capacity is summarized in Figure 5-9(a) and several charge/discharge profiles are shown in Figure

179

5-9(b). A lower voltage cut-off of 0.2V vs. Li/Li$^+$ was employed to prevent lithiation of the underlying Pt-Si substrate. As can be seen in Figure 5-9(a), the uncoated Co$_3$O$_4$, there is very low columbic efficiency on the first cycle commonly observed in conversion type anodes that can be attributed to SEI formation as well as potential loss of Li$_2$O, due to preferential formation of CoO vs. Co$_3$O$_4$ upon delithiation (Li 2018). The Li$_x$Al$_y$Si$_z$O coated Co$_3$O$_4$ demonstrated lower capacity than the uncoated sample, but after the first cycle the coulombic efficiency was much improved. Part of the lowered capacity (as observed for the Hybrid coated samples) could be due partially to the increased ohmic resistance allowing less of the thin film electrode to be lithiathed at the lower voltage cut-off. Lastly, the hybrid coated Co$_3$O$_4$ lithiathed immediately demonstrating a capacity slightly lower than the Li$_x$Al$_y$Si$_z$O coated Co$_3$O$_4$, but interestingly, the capacity increased with continual cycling—hypothesized to be due to lithiation of the PV4D4 layer, where the coulombic efficiency steadily improved across the 10 conditioning cycles.
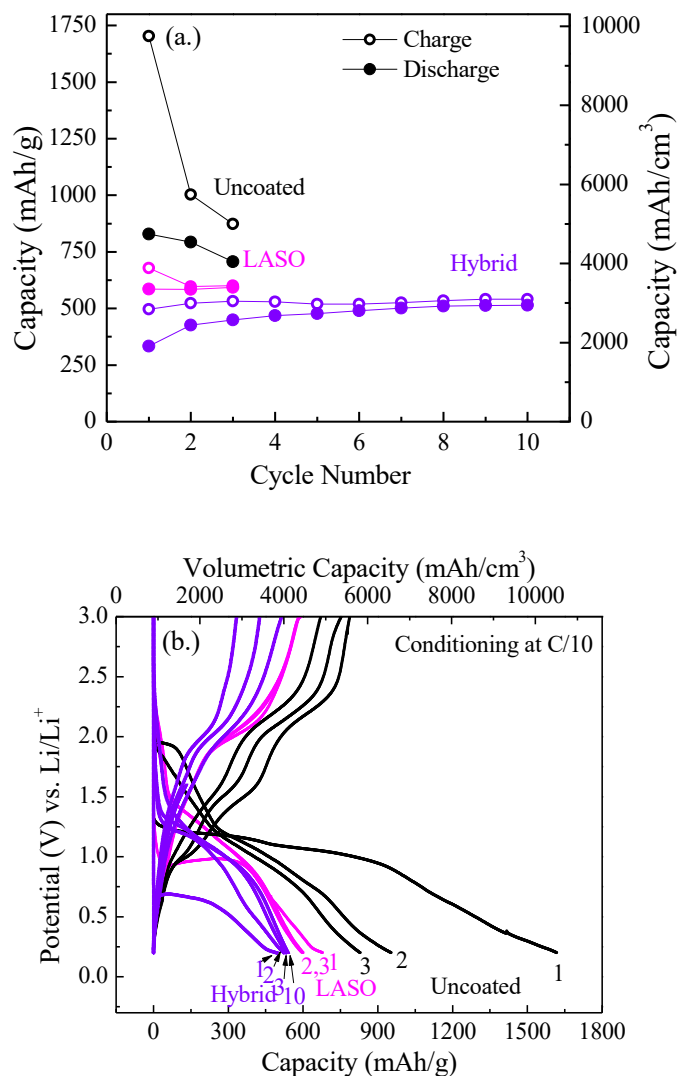
Figure 5-9 (a) Charge/discharge capacities of Co_3O_4 with various thin film coatings at a specific current of 2.2 μA cm^{-2} (~C/10). Uncoated ~40 nm Co_3O_4 is shown in black, 5 nm LASO/Co_3O_4 (pink), and 30 nm PV4D4/5 nm LASO/Co_3O_4 (purple). Cycling at 2.2 μA cm^{-2} was performed for 10 cycles on the hybrid sample to allow for lithiation of the PV4D4 layer. (b) Charge/Discharge profiles for first cycles at 2.2 μA cm^{-2}.

Next the capacity retention was assessed over 100 cycles at 43.7 μA cm^{-2} (~2C) for the various coated Co_3O_4 thin film anodes. At 43.7 μA cm^{-2} the uncoated Co_3O_4 thin film exhibited a relatively constant coulombic efficiency near 90% significantly dropping off during the first 50 cycles and ending at a discharge capacity of 2038 mAh cm^{-3}. The $Li_xAl_ySi_zO$/Co_3O_4 thin film

exhibited a gradual decrease in capacity with continual cycling exhibiting an ending 99.5% coulombic efficiency and a discharge capacity of 2458 mAh/cm^3. The hybrid/Co$_3$O$_4$ thin film exhibited increased capacity with continual cycling—33% increase over the 100 cycles as compared to a 12% and 40% decreased observed for the LASO/Co$_3$O$_4$ and Co$_3$O$_4$ thin films, respectively. The ending discharge capacity and coulombic efficiency of hybrid/Co$_3$O$_4$ was 2210 mAh cm^{-3} and 99.2%, slightly lower than the Li$_x$Al$_y$Si$_z$O/Co$_3$O$_4$, but higher than the uncoated Co$_3$O$_4$ thin film. This is expected to be due to increased ionic conductivity in the PV4D4 layer of the hybrid electrolyte with continual galvanostatic cycling allowing for increased utilization of the underlying Co$_3$O$_4$ anode.
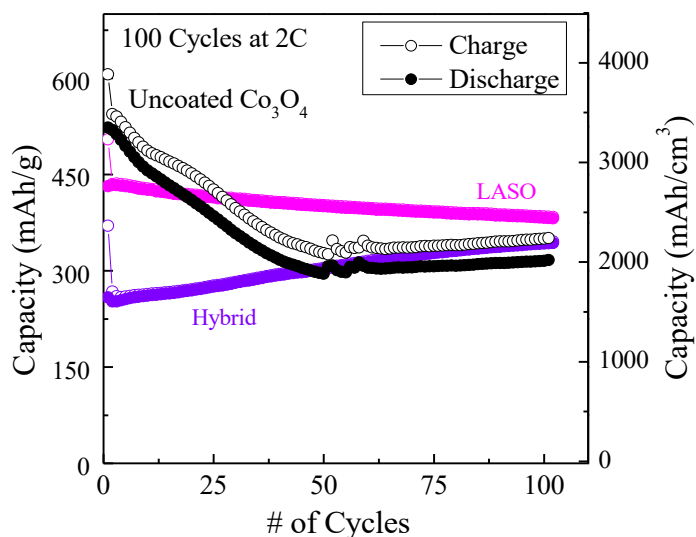
Figure 5-10. Galvanostatic cycling of thin film Co$_3$O$_4$ electrodes coated with various solid electrolytes at a specific current of 43.7 µA cm^{-2} (~2C) for 100 cycles post conditioning. The LASO coated sample ended with highest capacity and best capacity retention, but the hybrid structure continued to increase in capacity with increasing cycles, most likely indicative decreased resistance to ion transport.

EIS was taken of the hybrid/Co$_3$O$_4$ thin film before and after the galvanostatic cycling at 2.2 µA cm^{-2} (~C/10) and 43.7 µA cm^{-2} (~2C) and is shown in Figure 5-11. The EIS spectra were fit to an equivalent circuit, where the ones for before cycling and post cycling are shown in inset

of Figure 5-11 (a) and (b), respectively. Since the before cycling the hybrid electrolyte consists of an ionically conductivity $Li_xAl_ySi_zO$ layer as well as a weakly ionically conductive PV4D4 (some lithiation expected from soaking in liquid electrolyte) an equivalent circuit consisting of two resistor/constant phase elements in parallel were utilized to model ion transport. The small semi-circle was fit with an ionic resistance of 479 Ohms, which would equate to an ionic conductivity of 3.1×10^{-9} S/cm similar to what has been previously observed for amorphous thin film $Li_xAl_ySi_zO$ (Cho 2016) and a 1.1×10^{-10} S/cm associated with the PV4D4 layer. The EIS spectra of the hybrid/Co_3O_4 post galvanostatic cycling was fit to a simplified equivalent circuit, in which the $Li_xAl_ySi_zO$ and PV4D4 components are fit to a single resistor/constant phase element in parallel. The fitted spectra resulted in a calculated ionic conductivity of 2.54×10^{-9} S/cm for the hybrid film, but the effect of the SEI layer could not be delineated.
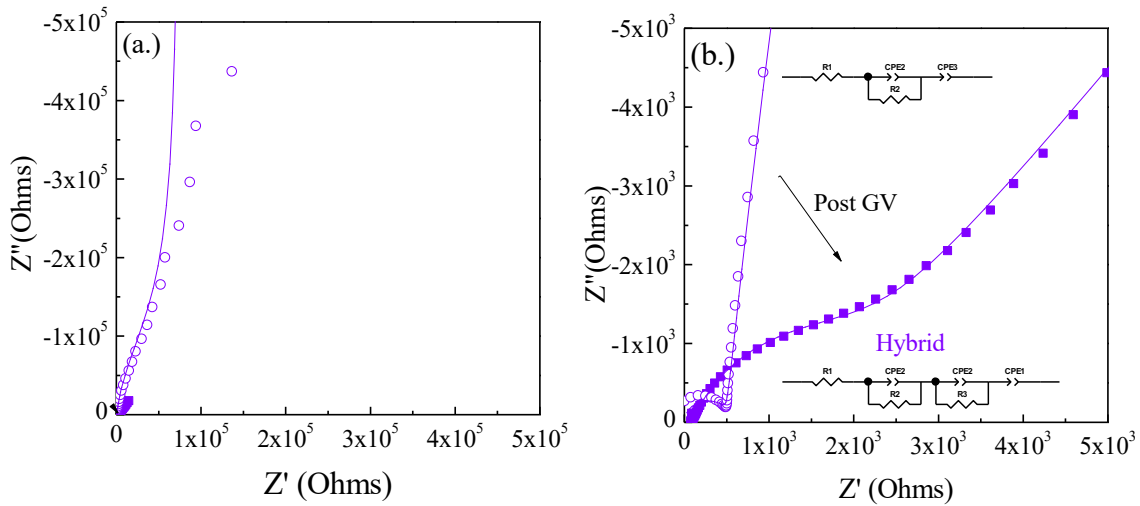
Figure 5-11. EIS spectra pre and post cycling of the hybrid/Co_3O_4 solid electrolyte/electrode couple. Semi-circle characteristic of Li-ion transport can be observed post galvanostatic cycling due to lithiation of the hybrid electrolyte as well as SEI formation, where the tail to lower frequency corresponds to the diffusion of Li^+ into the electrode.

In summary, several solid-state electrolytes were integrated with nanostructured anodes and their performance during charge/discharge was assessed. Two thicknesses of amorphous $Li_xAl_ySi_zO$ remained intact during lithiation induced volume expansion from underlying SiGe nanowire. This shows promise for the utilization of $Li_xAl_ySi_zO$ thin film coatings as "artificial SEI" coatings to stabilize nanostructured anodes as well as points to their mechanical feasibility in an all-solid-state-thin film battery. Next, amorphous $Li_xAl_ySi_zO$ was combined with polymeric iCVD PV4D4 thin films, exhibiting negligible interfacial resistance between the two solid-state electrolyte layers as well as conformal coatings consisting of sequential deposition of each of material components. Upon integration with Co_3O_4 thin film anodes both $Li_xAl_ySi_zO$ and the hybrid material improved capacity retention, where further integration with alloying type anodes may provide further improvements. One potential application is the coating of alloying type nanostructures (Si, Ge Al, Sn, etc.), where the ALD/iCVD layer can help stabilize the SEI layer on the high surface area structure as well as potentially reduce mechanical issues due the lithiation induced volume expansion such as delamination from the current collector, pulverization of the active material, and cracking in the SEI layer.

CHAPTER 6:   SUMMARY

This thesis demonstrated the synthesis of several material systems with direct applicability to realizing 3D lithium-ion microbatteries, where tuning of the stoichiometry was leveraged to control the structural, chemical, and electrochemical properties. ALD $LiCoO_2$ and $LiMn_2O_4$ thin films were synthesized via a solid solution of the constituent oxides Co_3O_4, MnO_2, and $LiOH$, where rapid thermal annealing was utilized for crystallization into the electrochemically active structure. The $LiMn_2O_4$ thin films exhibited great rate capability and capacity retention. 66% of the areal capacity was achieved upon increasing the specific current by a factor of a 100, indicating good rate capability. Furthermore, at a specific current of 35.91 μA cm^{-2} (5C) 97% of the capacity was achieved after 100 cycles. Further development of more complex stoichiometries to achieve higher operating voltages is the next step, where for instance synthesis of $LiMn_{1.5}M_{0.5}O_4$ (M: Ni, Co, Fe) is feasible utilizing the approach taken here with similar precursor chemistries. Furthermore adaption of precursors such as $LiMn_{1.5}Co_{0.5}(thd)_5$ utilized as single-source CVD-type precursors could be utilized for further control of thin film stoichiometry (Han 2019). Due to the fine thickness control of ALD, it gives a unique tool to further explore novel material heterostructures, where for instance layering of various materials in a laminate type structure is feasible. In the initial stages of thin film electrode materials via ALD, most electrochemical properties are assessed in a 2D thin film geometry, where further work is needed to assess changes when translating to 3D geometries. Ultimately, realization of 3D lithium-ion microbatteries via ALD may be through the development spatial ALD (sALD) processes to enable much faster processing times for depositing the thicknesses needed of the materials. Optimization of sALD to determine the balance between processing times vs. level of conformality will be important, where ALD electrode materials may be able to withstand a degree of non-conformality, where for ALD

solid-state electrolytes conformality may be more crucial. Furthermore, the integration of the various ALD components will most likely prove very important to device performance, where issues such as thermal budget need to be considered, especially if individual layers need to be annealed to be functional.

The synthesis and characterization of several solid-state electrolyte systems were demonstrated here, with specific focus on the integration with nanostructured anodes. An ALD solid-state electrolyte, $LiAlSiO_4$, was crystallized to form the β-Eucryptite phase upon rapid thermal annealing demonstrating a well-defined epitaxial relationship to the silicon substrate. Further development of crystalline metal oxide solid-state electrolytes offers great potential for improved ionic conductivities, but their realization is met with significant challenges: their stoichiometries are often complex requiring significantly more ALD process optimization, dependency on substrate choice which not only must be a close lattice match, but also a functioning anode or cathode, as well as thermal budget issues due to the high mobility of lithium. Future work on the down-scaling limit of the electrolyte thickness in 3D lithium-ion microbatteries is of interest as it is not considered in traditional battery fabrication. Scaling of the electrolyte to thicknesses on the order of 10 nm may produce issues such as limited Li^+ concentration as well as depending on the Debye length of the electrolyte electrostatic interactions between the two electrodes would be expected, which may have a significant effect on ion-transport. Future modelling work upon some of the effects of this kind of electrolyte/electrode scaling would be interesting to assess the feasibility of ultra-thin solid-state electrolyte

Beyond the ionic conductivity, secondary properties become important on integrating electrolytes with electrodes. For instance, results of integration of $Li_xAl_ySi_zO$ thin films with SiGe nanowire anodes were promising as they remained intact during the lithiation induced volume

expansion of the underlying alloying anode. To further improve upon the mechanical properties of $Li_xAl_ySi_zO$ for direct integration with high capacity anodes that undergo significant volume expansion, Novel hybrid solid-state electrolytes consisting of sequential deposition of ALD $Li_xAl_ySi_zO$ and iCVD Poly(1,3,5,7-tetravinyl-1,3,5,7-tetramethylcyclotetrasiloxane (PV4D4) were also demonstrated. No significant interfacial resistance was introduced via sequential ALD/iCVD depositions and the hybrid layer's ionic conductivity increased during galvanostatic cycling, where the pV4D4 is proposed to uptake lithium ions. The hybrid electrolyte was integrated on Co_3O_4 thin film anodes where improved cycle life was observed. Integration of $Li_xAl_ySi_zO$ and hybrid solid electrolyte coatings with thin film and nanostructured anodes shows promise for their applicability in 3D solid-state microbatteries. A more immediate application of hybrid electrolyte coatings could be to stabilize alloying type anodes nano and microstrucutres. An ion conducting artificial SEI layer improve the cycle-life through mitigation issues associated with loss of electrical contact of the active material, pulverization and cracking, and unstable SEI formation. Furthermore, this work is a starting point for further material optimization for hybrid-like thin film structures consisting of inorganic/polymeric components, where there exists a wide range of materials deposited via ALD, MLD, and iCVD with vast ranging properties

APPENDICES

A. Plasma Enhanced ALD System

    A.1 Schematics

    A.2 List of Parts

    A.3 Standard Operating Procedure

    A.4 Troubleshooting and Maintenance

B. Thermal ALD System

    B.1 Reactor Schematics

    B.2 List of Parts

    B.3. Standard Operating Procedure

    B.4. Troubleshooting and Maintenance

APPENDIX A: PLASMA ENHANCED ALD SYSTEM

A.1 REACTOR SCHEMATICS

RADICAL SOURCE

Full Assembly

(Side View 1)

(Side View 2)

ITEM NUMBER	DESCRIPTION.
1	FLANGE, 4-5/8" CF BLANK, MOD'ED
2	GAS LINE, INNER, 3mm DIA O.D. TUBING
3	GAS LINE, OUTER, 0.25in DIA O.D. TUBING
4	AMPOULE HOUSING
5	POWER FEEDTHROUGH, ISI P/N 9411018

University of California, Los Angeles, Department of Chemical and Biomolecular Engineering							
Part	Radical source	Material	Mixed (stainless steel, teflon)				
Filename	Radical source.pdf	Scale	No	Units	inch	Quantity	1
Designer	Angstron Systems	Date					
Revised by		Date					
Contractor		Date					
Comments	Adapted from Angstron Systems	Tolerance	+/- .0001				

RADICAL SOURCE (Continued)

Full Assembly
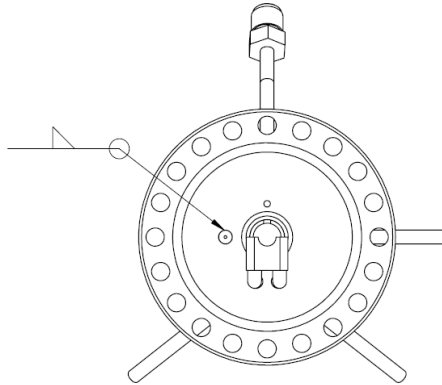
View from vacuum side

View from ambient side

Item 8 is welded to the outside part of item 1 and does not penetrate into item 1

8

7   6

2.8

2.5

2.4
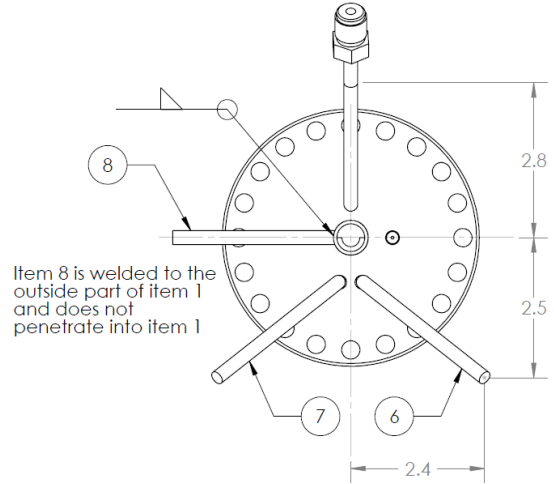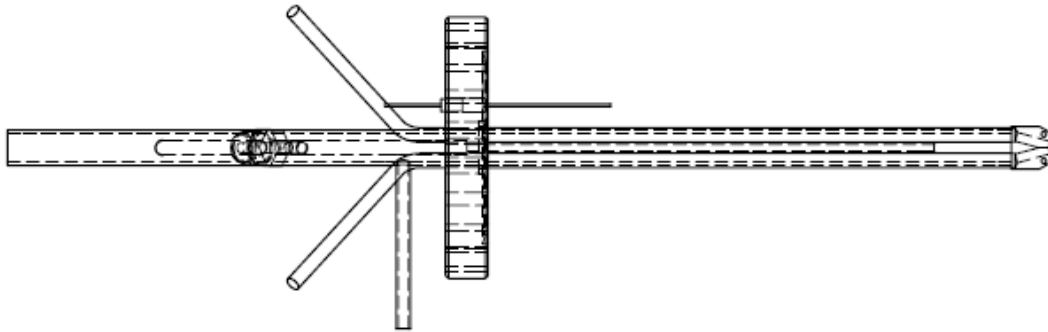
Full view

University of California, Los Angeles, Department of Chemical and Biomolecular Engineering							
Part	Radical source		Material	Aluminum Alloy (6082)			
Filename			Scale	No	Units	inch	Quantity	1
Designer	Angstron Systems		Date				
Revised by			Date				
Contractor			Date				
Comments	Adapted from Angstron Systems		Tolerance	+/- .0001			

RADICAL SOURCE (Continued)

Coaxial Waveguide

Thread ID 9/16-18.
Full threads engage ⟱ 2.25.

.25

2.75

Micorwave input

Ø .625

Ø .50

1.70

18.25

.125

.30

SECTION A-A

2.25

7.00

A

A

Port for item 8 welding

Micorwave input

Ø .20

.50

.31

.31

University of California, Los Angeles, Department of Chemical and Biomolecular Engineering							
Part	Radical source	Material	Stainless steel, OD 0.625, Wall 0.0625				
Filename	Radical source.pdf	Scale	No	Units	inch	Quantity	1
Designer	Angstron Systems	Date					
Revised by		Date					
Contractor		Date					
Comments	Adapted from Angstron Systems	Tolerance	+/- .0001				

RADICAL SOURCE (Continued)

Top Clamp for Quartz Ampoule
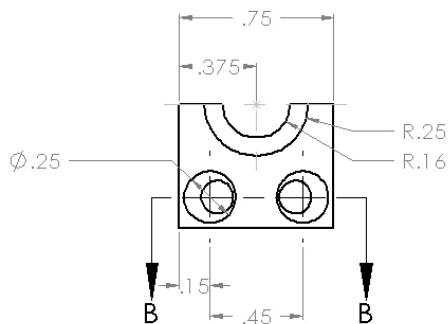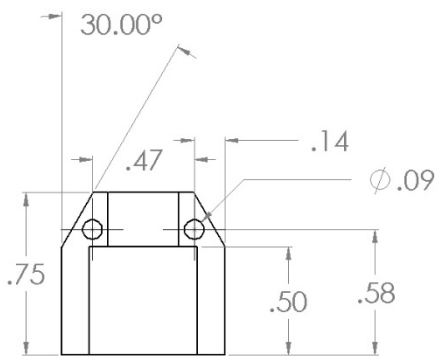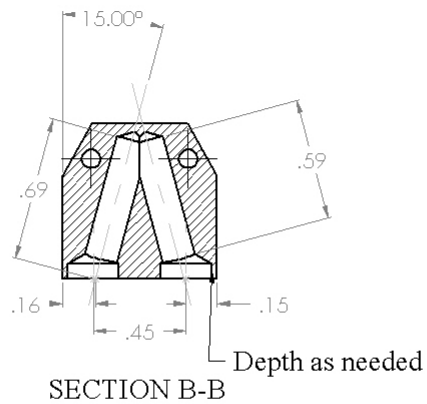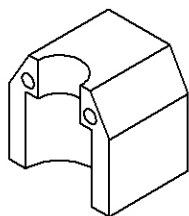
15.00°

.69

.59

.16

.45

.15

Depth as needed

SECTION B-B

30.00°

.47

.14

Ø.09

.75

.50

.58

.75

.375

R.25

R.16

Ø.25

.15

.45

B

B

University of California, Los Angeles, Department of Chemical and Biomolecular Engineering								
Part	Radical source	Material	Stainless steel (316)					
Filename		Scale	No	Units	inch	Quantity		1
Designer	Angstron Systems	Date						
Revised by		Date						
Contractor		Date						
Comments	Adapted from Angstron Systems			Tolerance	+/- .0001			

192

RADICAL SOURCE (Continued)

Bottom Clamp for Quartz Ampoule
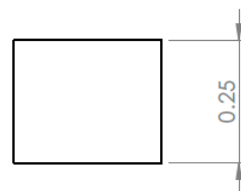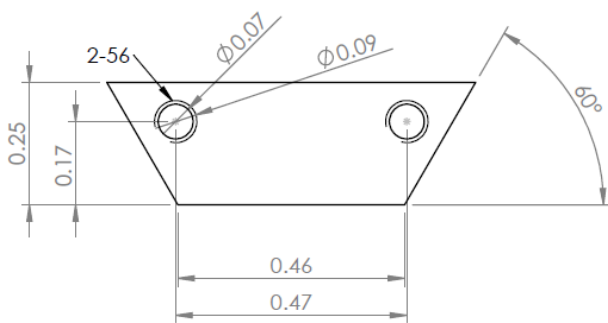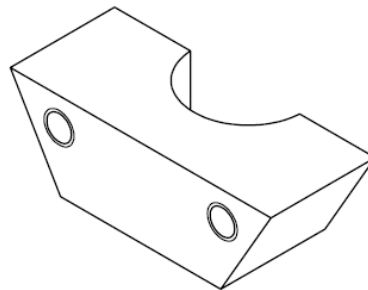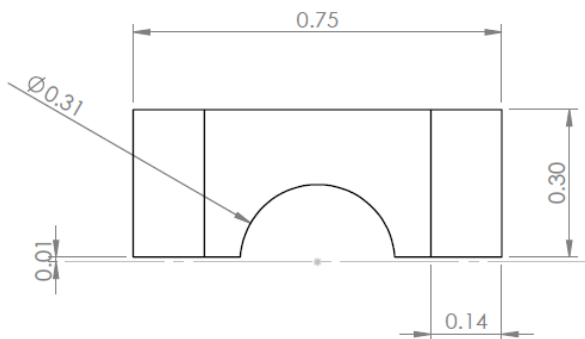
University of California, Los Angeles, Department of Chemical and Biomolecular Engineering							
Part	Radical source	Material	Stainless steel (516)				
Filename	quartz bottom	Scale	No	Units	inc	Quantity	1
Designer	Angstron Systems	Date					
Revised by		Date					
Contractor		Date					
Comments	Adapted from Angstron Systems			Tolerance	+/- .0001		

RADICAL SOURCE (Continued)

Modified 4-5/8" Conflat Flange
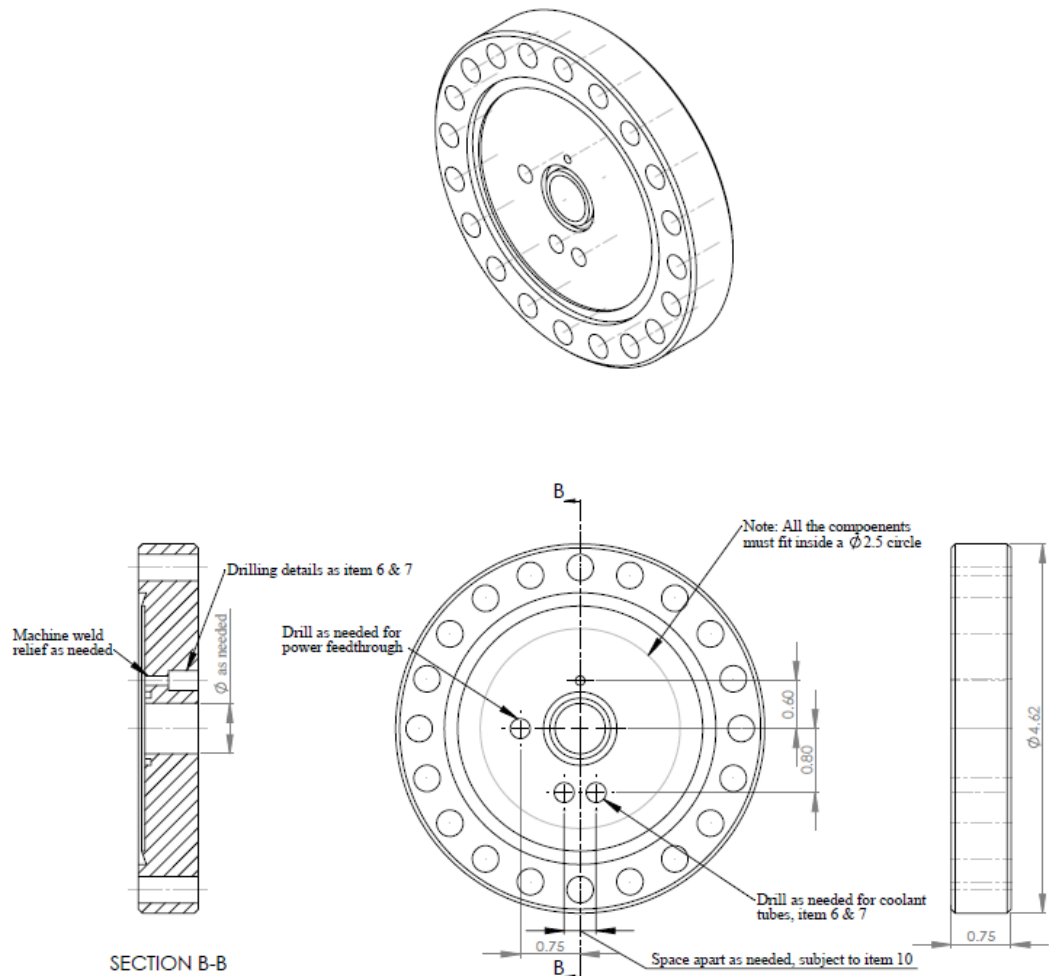
SECTION B-B

Machine weld relief as needed

Drilling details as item 6 & 7

Ø as needed

Drill as needed for power feedthrough

Note: All the compoenents must fit inside a Ø 2.5 circle

0.60

0.80

Ø 4.62

Drill as needed for coolant tubes, item 6 & 7

0.75

0.75

Space apart as needed, subject to item 10

University of California, Los Angeles, Department of Chemical and Biomolecular Engineering								
Part	Radical source		Material	4-5/8" Conflat flange (stainless steel)				
Filename			Scale	No	Units	inch	Quantity	1
Designer	Angstron Systems		Date					
Revised by			Date					
Contractor			Date					
Comments	Adapted from Angstron Systems		Tolerance	+/- .0001				

194

RADICAL SOURCE (Continued)

Tuning Slug
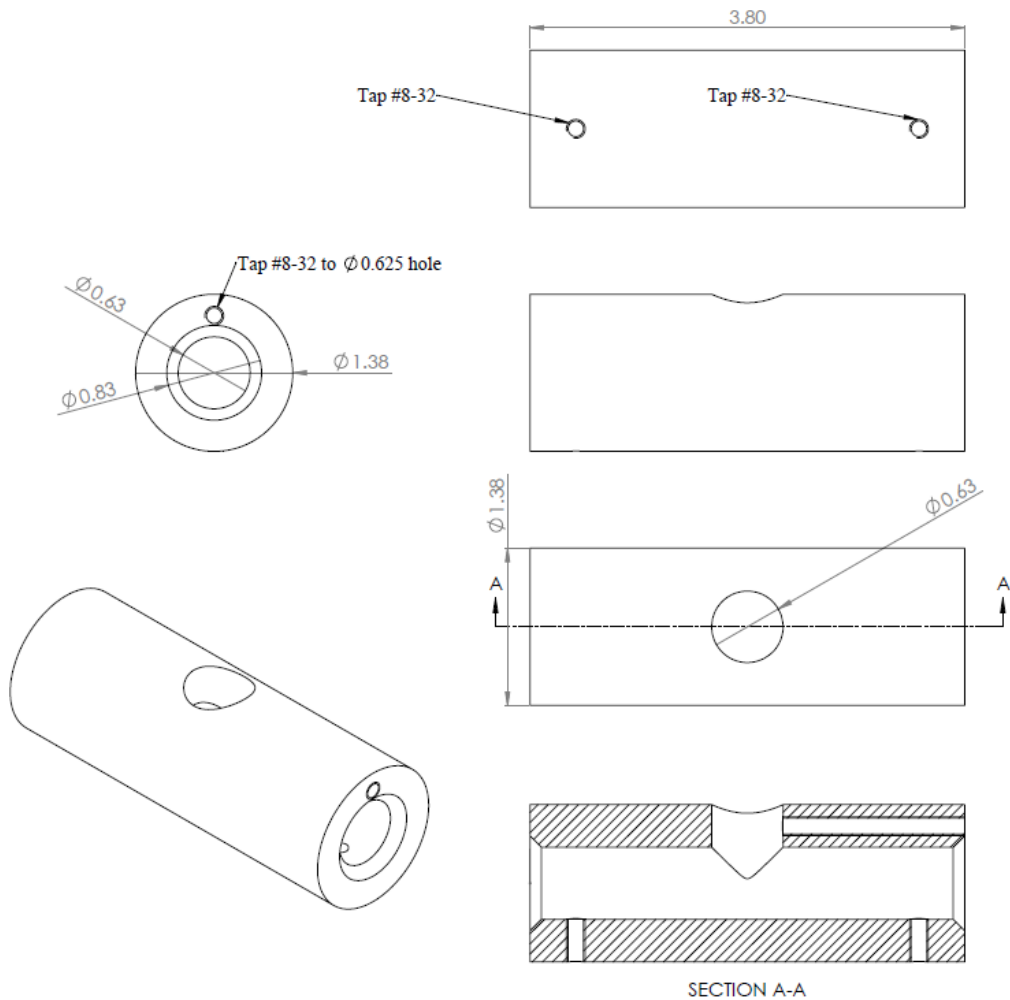
3.80

Tap #8-32

Tap #8-32

Tap #8-32 to $\varnothing$0.625 hole

$\varnothing$0.63

$\varnothing$1.38

$\varnothing$0.83

$\varnothing$1.38

$\varnothing$0.63

A

A

SECTION A-A

University of California, Los Angeles, Department of Chemical and Biomolecular Engineering								
Part	Radical source		Material	Stainless steel (516)				
Filename	TuningSlug.pdf		Scale	No	Units	inch	Quantity	1
Designer	Angstron Systems		Date					
Revised by			Date					
Contractor			Date					
Comments	Adapted from Angstron Systems		Tolerance	+/- .0001				

RADICAL SOURCE (Continued)

Teflon Bushing
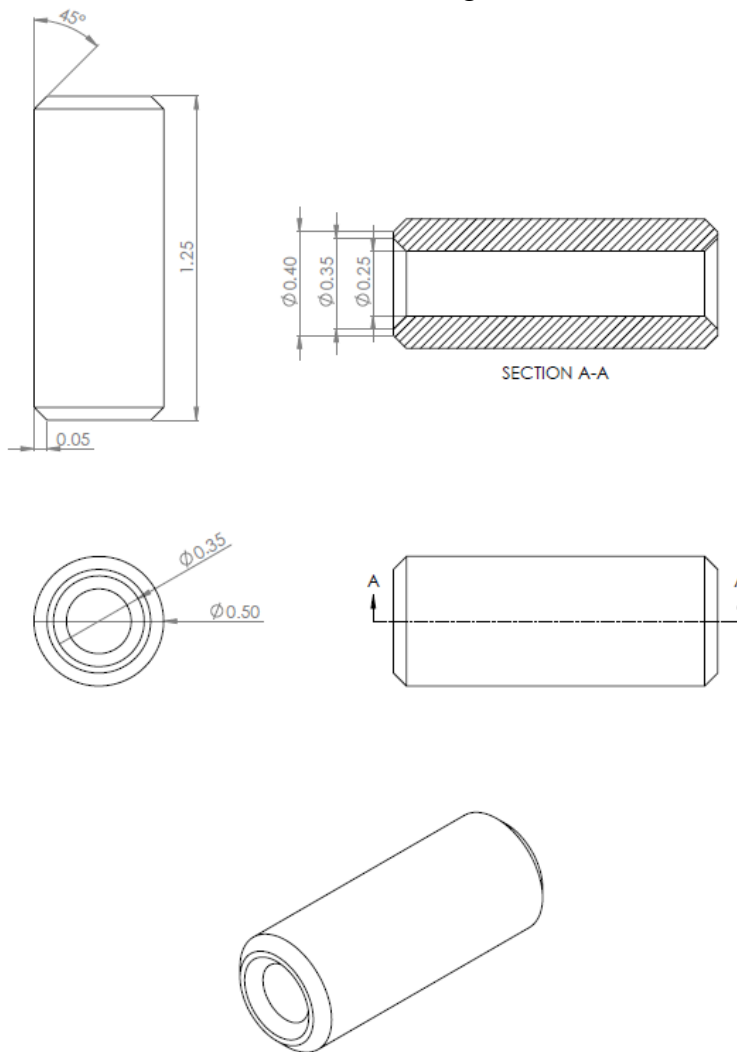
45°

1.25

0.05

Ø0.40
Ø0.35
Ø0.25

SECTION A-A

Ø0.35
Ø0.50

A

A

University of California, Los Angeles, Department of Chemical and Biomolecular Engineering								
Part	Radical source		Material	Teflon				
Filename	Teflon.pdf		Scale	No	Units	inch	Quantity	1
Designer	Angstron Systems		Date					
Revised by			Date					
Contractor			Date					
Comments	Adapted from Angstron Systems			Tolerance	+/- .0001			

RADICAL SOURCE (Continued)

Central Conductor

SECTION A-A

45.00°

118.00°

45.00°

Ø.25

Ø.12
Ø.16
Ø.18

.10
.09
.01
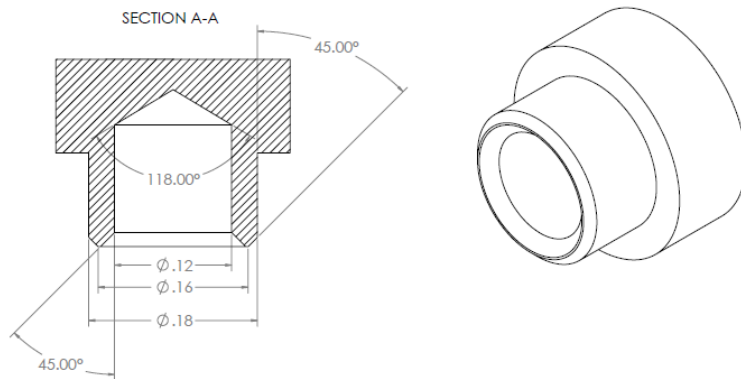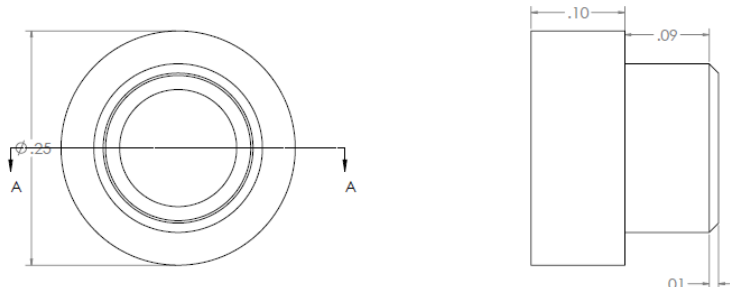
(Tip and Tube)

University of California, Los Angeles, Department of Chemical and Biomolecular Engineering							
Part	Radical source	Material	Stainless steel				
Filename	Central conductor.pdf	Scale	No	Units	inch	Quantity	1
Designer	Angstron Systems	Date					
Revised by		Date					
Contractor		Date					
Comments	Adapted from Angstron Systems	Tolerance	+/- .0001				

RADICAL SOURCE (Continued)

Quartz Ampoule
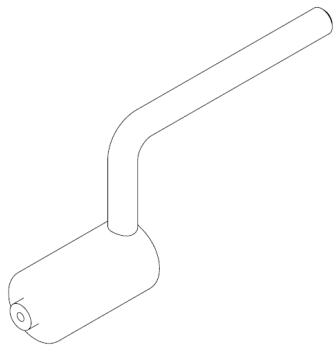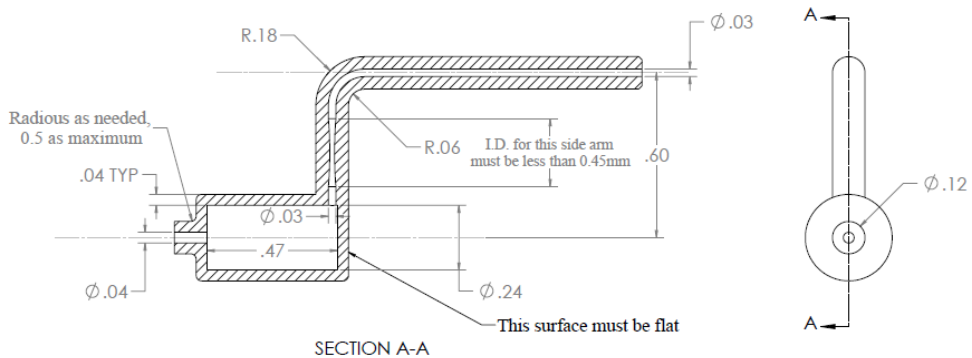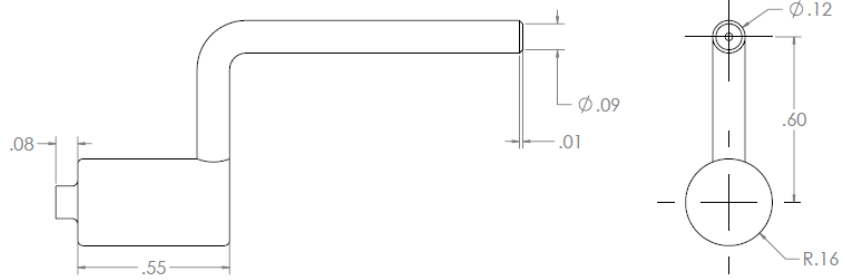
.08

.55

Ø.09
.01

Ø.12
.60
R.16

R.18
Ø.03
Radious as needed,
0.5 as maximum
R.06
I.D. for this side arm
must be less than 0.45mm
.60
.04 TYP
Ø.03
.47
Ø.04
Ø.24
This surface must be flat

SECTION A-A

A
A
Ø.12

University of California, Los Angeles, Department of Chemical and Biomolecular Engineering								
Part	Radical source	Material	Quartz					
Filename	Quartz Ampoule	Scale	No	Units	inch	Quantity		1
Designer	Angstron Systems	Date						
Revised by		Date						
Contractor		Date						
Comments	Adapted from Angstron Systems	Tolerance	+/- .0001					

A.2 LIST OF CHAMBER COMPONENTS

Electrical Equipment	Parameters
Mechanical Pump (Fomblin-prepped)	115 VAC, single phase
Microwave power supply	110 VAC, single phase
Temperature Controller	120 VAC, single phase
Sample Heater	Variable 0-30 VAC using transformer
Mass Flow Controllers	120VAC, single phase
Heating Wires	120 VAC
Kapton Heaters	120 VAC

Vendor	Catalog No.	Description
Alfa Aesar	11386	Indium foil, 0.1mm (0.004in) thick Puratronic, 99.9975%, 100mm x 100mm
Alfa Aesar	41359	Bis(2,2,6,6-tetramethyl-3,5-heptanedionato)Cobalt (II) 99.9%-Co
C.W. Swift	23N-50-0-30	Microwave connector, N type, article number 22642835
Duniway	DST-531	Thermocouple Sensor Tube, Nickel-plated, Mild Steel, 1/8 " NPT Port.
Duniway	TCG-531	Thermocouple Type 531 Gauge Controller
G. Finkenbeiner, Inc.	N/A	Quartz ampoule (custom-made)
Kurt J. Lesker	C6-0462	6-way Cross CF 4.63"
MDC	110000	Flange, 1.33", Blank
MDC	409004	MultiPort Flange 2.75"x5-1.33" Mini, T
MDC	310029	Angle Valve, 1.5" HV Manual, 2 3/4"CF
MDC	404002	Tee, 2.75"
MDC	414007	2.75'' CF to ¼'' MVCR Adapter
MDC	402000	Nipple, 1.33"
National Instruments	779453-01	USB-9481 4-ch SPST Relay Module
Nor-Cal Products	LFT-075-1-025	1.33" OD CF Single Liquid Feedthrough, 1/4" OD Tube
Omega	5TC-GG-K-30-36	316 SS VCR Face Seal Fitting, 1/4 in. Unplated Gasket, Non-Retained Style

Omega	CN1507TC	7 Channel Controller
Omega	NI80-012-200	80%Ni/20%Cr, 200' pool of 28 gauge bare resistance heating wire, diameter 0.0126"
Omega	SSR330DC25	Solid State Relay DC 25 Amp
Omega	CO1-K-72 INCH	Cement on T/C
Strem Chemicals	25-5000	Tris(2,2,6,6-tetramethyl-3,5-heptanedionato)manganese(III), 99%
Strem Chemicals	03-0780	Lithium t-butoxide, 98+%
Swagelok	SS-4-VCR-1	VCR Fitting, 1/4 in. Female Nut
Swagelok	SS-4MG-VCR-MH	VCR Fitting, 1/4 in. Female Nut, Gasket Face Seal Fitting, Vernier Handle
Swagelok	SS-HBVV51-C	Stainless Steel High-Pressure Bellows-Sealed Valve, 1/4 in. Female Swagelok VCR Face Seal Fitting, NC Actuator, Polyimide Stem Tip
Swagelok	SS-4-VCR-4	VCR Fitting, 1/4 in. Male Nut
Swagelok	SS-4MG-VCR-MH	SS Medium-Flow Metering Valve, Vernier Handle
Swagelok	SS-4BG-V51	SS Bellows-Sealed Valve, Spherical Stem Tip
Swagelok	316L-4-VCR-3AS	VCR Fitting, Short Automatic Tube Butt Weld Gland, 1/4 in. VCR

A.3 STANDARD OPERATING PROCEDURES

I. Loading and Unloading the Sample

Venting the system
1. Close roughing valve (**RV1**), **V2,** and **PV1** (turn off switch labeled roughing on pneumatic control box) as shown in Figure 1 (left.) and Figure 2.
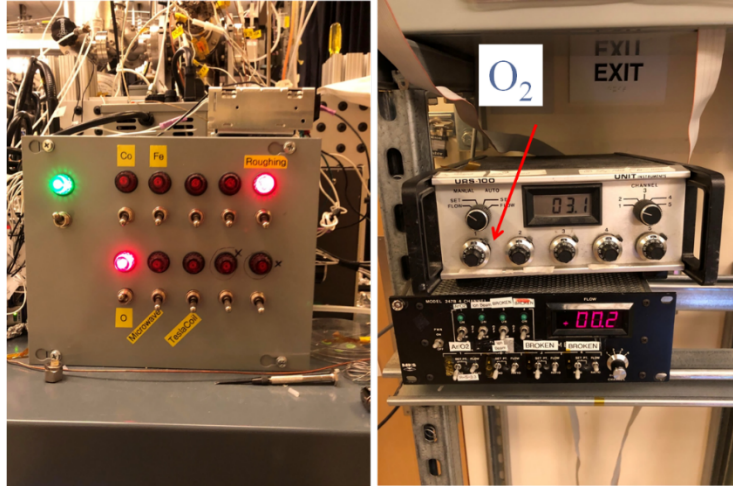
Figure A1. (a) Pneumatic Control Box (b.) MFC for O_2 and N_2
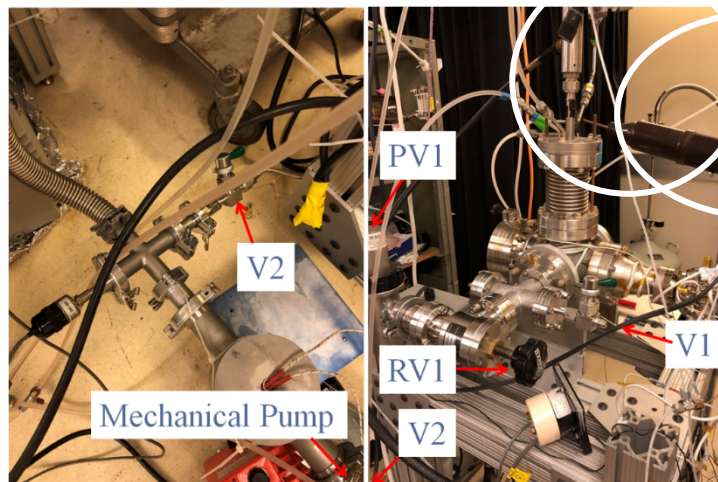
Figure A2. System with relevant valves marked. (a) V2 near mechanical pump below chamber (b) RV1 and V1 location on system.

2. Slowly open vent valve (**V1**) (Figure 2). Watch Thermocouple (TC) pressure gauge for large pressure increases to ascertain that mechanical pump is isolated from system. If pump is properly isolated, there should no pressure increase.
3. When system is vented to atmosphere, close vent valve (**V1**).
4. Loading/Sample door (Figure 3) can now be opened by twisting open latch.
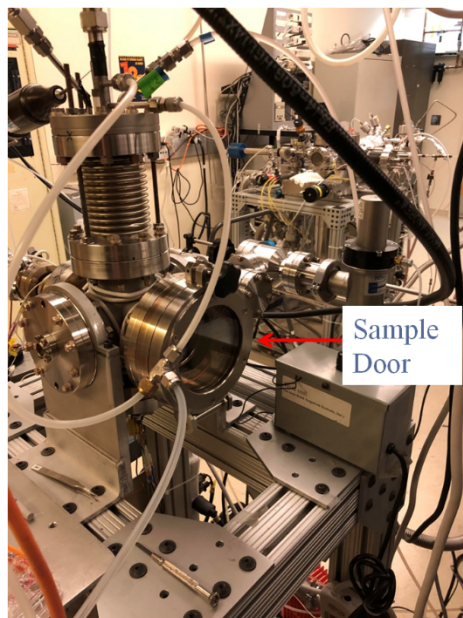
Figure A3. PEALD system loading door

Unloading a Sample
1. Before unloading the sample confirm that the **sample stage transformer is off** and un-plug power from back side.
2. Now **carefully** grab sample from the stainless steel sample stage (TC, Heating wires spot-welded so relatively fragile). Be careful not to damage the end of the radical source.

Loading a Sample
1. Before loading the sample confirm that the **sample stage transformer is off** and un-plug power from back side.
2. Carefully slide the sample onto the stainless steel sample stage (dish shape).
3. If necessary carefully align sample on stage to ensure uniform heating.
4. Close loading door and twist shut latch. (Note: once the system is pumped down you can loosen latch once again.)

Pumping the System
1. Check to make sure vent valve (**V1)** and loading door are closed.
2. Open (PV1) on the pneumatic control box labeled *Roughing.* There should be no pressure change observed on the TC gauge.
3. Slowly open roughing valve (**RV1)**. Once the system is almost pumped down open V2 V2 connected to mechanical pump while watching TC pressure gauge. Pressure should rapidly decrease if there are no leaks or openings to atmosphere (Figure 2).
4. Allow system to reach base pressure at approximately 25-35 mTorr.

II. Radical Source
1. Open gas line valve (**PV2)** by turning on the switch labeled *O* on the pneumatic control box (Figure 1) connected to radical source and allow time for line to be pumped to base pressure.
2. Make sure all valves for cooling water are opened.
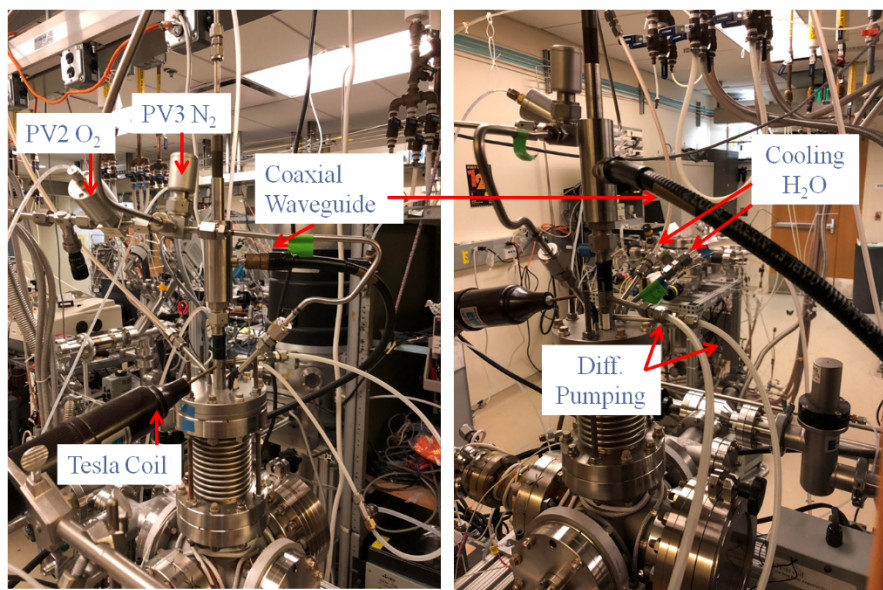
Figure A4. (a,b) Depiction of Radical source installed on the system at different angles. Labeled in the figure is the coaxial waveguide, differential pumping lines, O_2 and N_2 lines and valves as well as cooling lines.

3. Turn on microwave power source (farthest left switch, Figure 5) to allow electronic system to warm up (~30 min).

Figure A5. Microwave Power Source. Power switch (left), Operate/Standby switch (middle). Power control knob (right)

4. Open manual valve behind O_2 MFC (situated 5 inches behind MFC) to allow for O_2 flow from gasline to MFC.
5. Set flow rate (Ch. 1) to desired flow rate of O_2 (Ar MFC) (Shown in Figure A1(b)). UHP N_2 is connected to Ch. 5 on the MFC
6. If testing radical source turn the switch from remote to local, if running automated deposition turn switch from local to remote.

7. Turn the switch from standby to operate on located on the microwave power source (Figure 5).
8. Turn power control knob on microwave power source to intended power (25 W for O_2 & Ar, 30 W for N_2) and note reflected power (Typically ~4-5 W). If reflected power is too high (> 10 W), tuning of radical source may be required.
9. Quickly switch on and off Tesla coil to strike plasma using switch labeled tesla coil on the pneumatic control box (Figure 1) or the switch shown in (Figure 8).
<u>CAUTION: TESLA COIL OPERATES AT EXTREMELY HIGH VOLTAGE (~10000 V). TAKE EXTREME CAUTION TO MAKE SURE TESLA COIL TIP IS IN CONTACT WITH RADICAL SOURCE EXTERNAL ELECTRICAL TAIL</u>
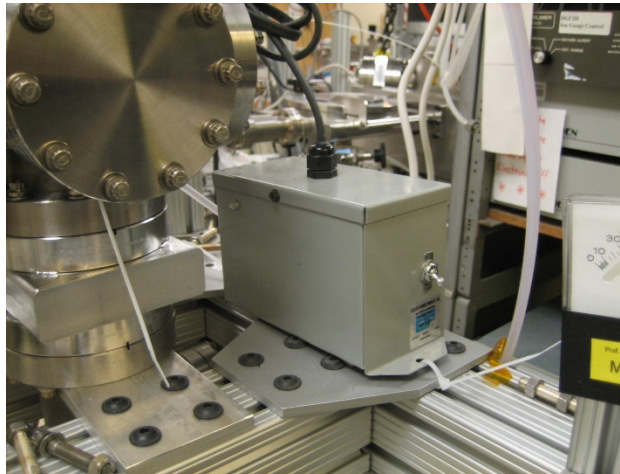
Figure A6. Tesla Coil switch

10. If the plasma did not strike, tune the radical source until resonant length is achieved by turning the tuning slug. Additionally, the waveguide can be adjusted to match the resistance through unscrewing the set screws and manually moving and up down the conductor. Confirm that the coaxial waveguide is contacting the inner conductor.
11. When running a deposition turn microwave source setting from local to remote to allow for controlled plasma strike during deposition

III. Running a deposition

1. Turn on heaters for doser and sample stage using temperature controller and allow time for heaters to reach intended temperatures* (Precursors: 130-150°C, Doser: 180-220ºC, Sample stage: up to 300°C) (Figure 9).
   * To turn on heater: press "CTR SEL 2" and select controller by repeatedly pressing it until intended controller is selected then press "RUNSTP 5" to turn on heater. Light underneath temperature read-out should turn on corresponding to heater. Heater is programmed to ramp up in temperature slowly for stability purposes. List of channels on controller: 1 (doser, wired in parallel for both dosers), 2 (gasline 1), 3(housing 1), 4(gasline 2), 5(housing 2), 6(sample stage), 7(chamber wall)
2. Turn on radical power supply to warm up electronics. Allow several minutes (~30 min).

Figure 7. Temperature controller

3. To test radical source, when operating temperatures have been reached, turn on radical source by switching "standby" to "operate" and slowly ramp up power, first stopping at 5 W for approximately 1 minute, and continuing to intended power. Strike plasma by switching on and off tesla coil and allow radicals to react for a short pulse (~30 seconds) to oxidize surface. Turn power supply to "standby" mode to stop pulse.
4. To pulse precursor, open precursor housing valve (**PV3 or PV4**) for the intended amount of time and then close valve. Generally, solid precursor pulse lasts 30 seconds. Gas precursor pulse lasts 2-5 seconds
5. Allow time to pump down (~30 seconds) following precursor pulse.
6. To pulse radical source, turn power source switch from standby to operate. Allow approximately 5 seconds for power source to reach target power.
7. Quickly switch on and off Tesla coil to strike plasma.
8. When plasma has been pulsed for intended time (typically ~30 seconds), turn off plasma by switching power source from operate to standby.
9. Allow time to pump down following radical pulse (typically ~15 seconds).
10. Repeat steps 4-9 until intended number of cycles has been reached.

IV. Normal Shutdown procedures

1. After final radical pulse cycle, turn off radical power supply by ramping power back down to 0 W, then flipping switch from operate to standby and then turning power switch to "OFF" position.

205

2. Turn off precursor heaters by pressing "CTR SEL 2" on temperature controller repeatedly until controller is selected and press RUN/STP 5. Light underneath temperature read-out should turn off corresponding to heater.
3. Close manual valve behind the O_2 MFC
4. Allow for the O_2 to be pumped out of the line, turn the MFC Ch.1 to 0, finally close the PV2 valve (labeled "O") on the pneumatic control box.
5. Allow substantial time for system to cool down (>60 minuntes)

A.4 MAINTENANCE

Replacing the quartz ampoule

- Vent the main chamber and then remove all fittings and connections, remove the radical source as well (note: be careful and do not bump the radical source assembly to the inner wall of the chamber)
- Remove the top clamp to reveal the quartz ampoule
- Remove Teflon heat-shrink tubing extending from gas-line feedthrough that is attached to the quartz ampoule
- When installing a new quartz ampoule, Indium foil must be wrapped around the cylindrical section to ensure enough heat conduction. Failure to do so might result in unstable plasma due to overheating and poor heat removal
- Replace Teflon heat-shrink tubing to connect the gas line to quartz ampoule
- Place quartz ampoule in the housing again to make sure that a proper thermal contact is achieved.
- Make sure that the end of the quartz ampoule is contacting the microwave waveguide 8. Secure the quartz ampoule to radical source by screwing down the top clamp
- Wrap wire extending from electrical feed through to allow tesla coil induced plasma generation if necessary

Replacing precursor in housing

- Turn-off all electrical connections (power strips)
- If replacing LiOtBu then vent system. If replacing other metalorganic precursors close the pneumatic valve associated with the precursor.
- Remove the aluminum foil wrapping from the precursor housing
- Disconnect the heating wires from the quick-snap electrical connections
- Unwrap heating wire, remove Kapton TC
- Take off housing, seal end vacuum side with male VCR gasket and fitting while the housing is removed.
- Triple rinse precursor housing a. First disassemble and dispose of leftover precursor b. Then sonicate in acetone/IPA/water (15 min each) c. Bake for 60 min at 120 C
- If loading LiOtBu: do so if possible, via arrange with the Dunn lab to use their glove box. If that is not possible use the home-made glove box in our lab. Once the housing is filled attach the pneumatic valve to seal in the precursor while still in the glove-box. Load LiOtBu on the LixAlySizO system, purge the system with all of the valves closed for 10 minutes with UHP N2. Open the LiOtBu to the system (now near atm of N2). Pump out entire system. Close the pneumatic valve for LiOtBu remove. Remove it from the system. Next vent, the PEALD chamber. Load the LiOtBu housing and valve. Then pump-down system.
- Once the precursor housing is reconnected, make sure that all valves are closed again

- You will need to vent the main chamber after reconnecting precursor housing before opening any of the valves a. After vented, open valve to precursor you replaced only. c. Pump down main chamber. (Base pressure will be higher)
- Reconnect all the heating coil and thermocouple lines as before
- Cover the housing with aluminum 16. Bake the precursor housing (at 100 C) if possible based on the vapor pressure.
- Run a dummy run to check for deposition.

A.4 TROUBLESHOOTING

Problem: Plasma will not strike/unstable/high reflected power

Solutions:

- First confirm that the O2 is flowing (noticeable change in base pressure) and the all of the cooling water lines are cold to the touch with all valves open (1 set of lines to the microwave power supply, 2 sets of lines to the radical source)
- If the quartz ampoule is not properly contacted to cooling block by Indium foil, the temperature of the ampoule could get too high. The indium foil can melt which will lead to the ampoule overheating.
- Next, check that the tesla coil is working by quickly switching it off and on while you look through the window of the door. Even with no gas flowing, the tesla coil will still ionize the gas in the system and should glow pinkish/orange. If you do not see this then check to see if the all metal near the electrical feedthrough in which the Tesla Coil is contact with is properly insulated. If the tesla coil does not turn on there could be an issue with power connection
- If the reflected power is high, turn the tuning slug and try to strike the plasma again. If the plasma strikes, but the power is high tune further with the tuning slug until the reflected power is lower. Confirm that the plasma strikes and the reflected power is low several time after tuning.
- If the plasma still will not strike, but the tesla coil is working the most likely issue is with the O_2 feedline. The heat-shrink tube connecting the stainless steel gasline and quartz ampoule degrades over time. If this is the issue, the region around the ampoule arm that the tesla coil is wrapped around will glow white when on due to the O_2 leak.
- Another common issue is the electrical feedthrough is not well insulated inside the chamber and the tesla coil is shorting between the electrical feedthrough and the radical source.
- It maybe also because of the bad contact between the N-1 cable and the inner conductor, check whether if there is greenish-blue oxidation of the inner conductor, which might influence the electric conduction. It can be fixed by using sandpaper to scrub the inner conductor surface and by tuning the location of contact

Problem: Doser not heating-up

Solutions:

- Make sure all electrical and TC connections are well connected and functioning. The most likely and simple solution is if one of the electrical connections is loose. Re-make any suspect connections and re-test. **BEFORE HANDLING ANY OF THE ELECTRICAL TURN OFF ALL POWERSTRIPS.**
- Turn on channel for Doser. Check to see if the temperature of any other channels rises due to heating of the doser. If this is the case, then the heating wires are working fine, but the TC has either come loose or is disconnected. This is rarely the issue, since generally if a TC fails when the doser heater is on it will most likely overheat.
- Check the fuse on the back of the transformer (it should read a resistance). If it reads overload, then replace the fuse.
- The next most likely issue is that the heating wire burnt out in the flexible Kapton heaters. Remove the doser and inspect the heating wire.

Problem: Sample Stage not working

Solutions:
- First unplug the transformer. Check the resistance of the fuse on the back of the transformer, if it reads overload then a new fuse is needed.
- Next Remove all electrical lines and measure the resistance across the electrical feedthroughs. If the reading is overload, then the electrical feedthrough has come detached to the stage and the stage will be fixed.
- If there is a resistance value on the electrical feedthrough (<10 Ohms) Then check the resistance across the TC as well as the TC to one of the feedthroughs. If the resistance across the TC reads overload, then the TC has broken. If it reads overload across the TC and electrical feedthrough it means the TC is no longer connected to the sample stage.
- If the sample stage is damaged, you can either repair or re-make one. The sample stage consists of stainless-steel shim foil, with NiCr wire spot welded across it in a ladder configuration. Next thicker stainless-steel wires are spot welded under the stage to the NiCr wire and fastened to the inside of electrical feedthrough via a brass coupling. The type-K thermocouple is spot-welded to the stainless-steel shim foil underneath the sample. If fixing an existing stage, all metal components that need to be spot welded, must be sanded down extensively. Test to make sure all components are electrically contacted with the multimeter before installing back on the chamber
- When repairing or utilizing a new sample stage lower the transformer setting. Ramp-up if the sample stage cannot reach the set-point.

Problem: No Deposition

Solutions:
- If there is no deposition and the radical source is working then either the precursor housing is empty or the doser/gas-line is clogged.

- If the gas-line is clogged, once removed from system clean with IPA, acetone, water in the fume hood. Thick stainless steel wire can be used to unclog regions.
- Dry out all the chemical solvents and water prior to placing the parts back on the chamber
- Dispose the chemical waste
- If the line is not clogged then most likely there is no longer precursor left in the housing.
- Follow the guidelines above for replacing precursor

APPENDIX B: THERMAL ALD SYSTEM

B1. Reactor Schematics
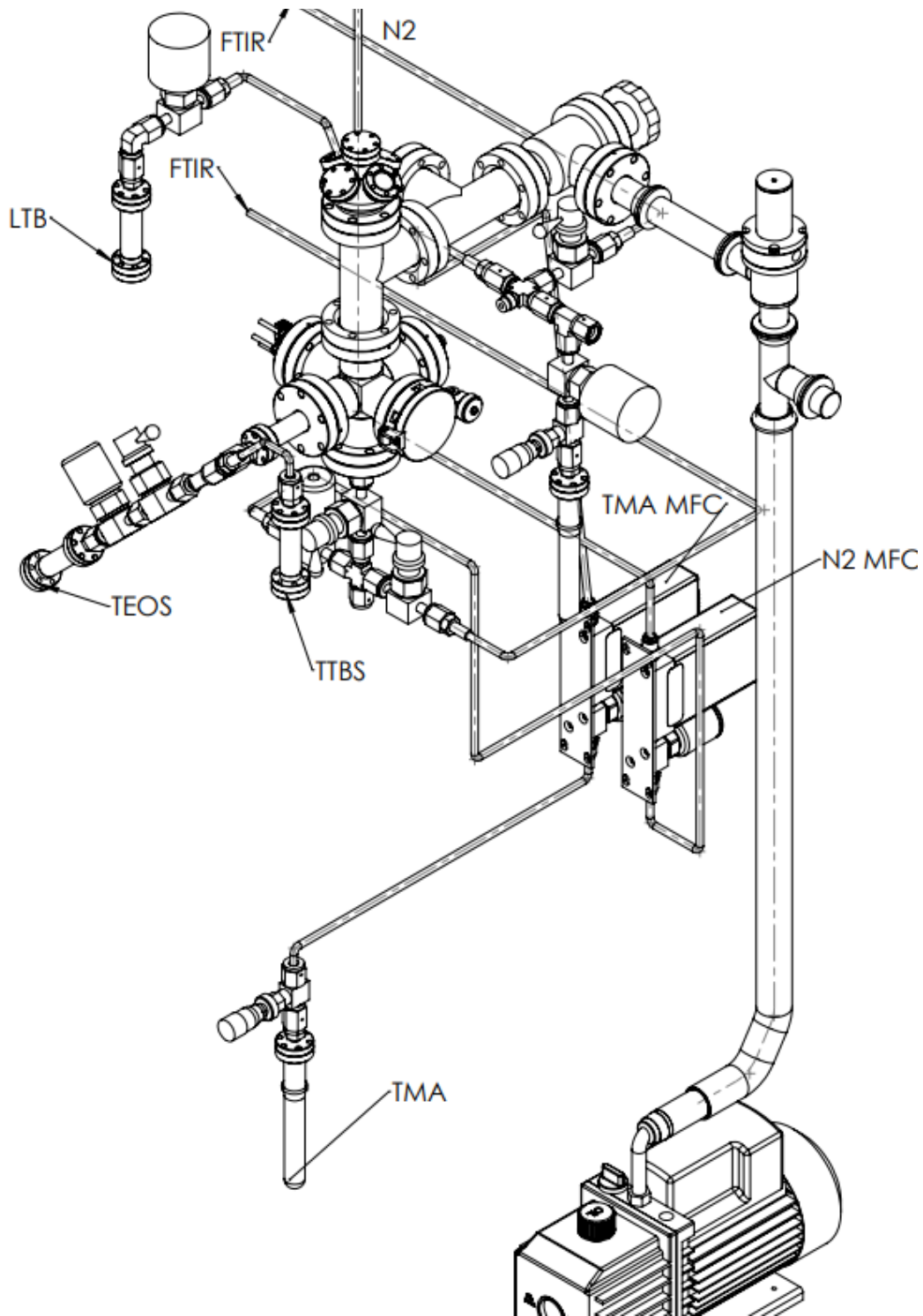
Figure B1. Thermal ALD reactor
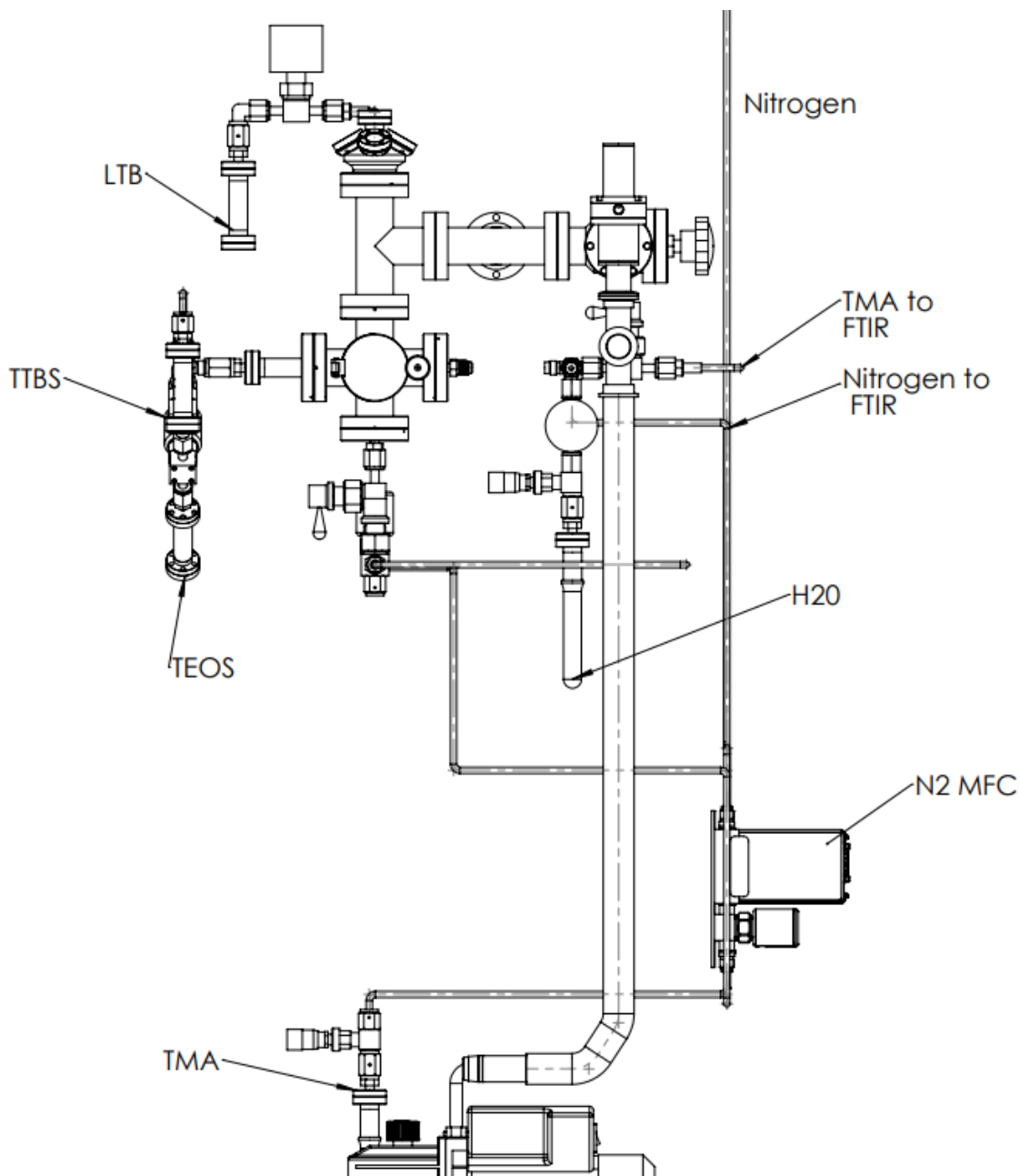
Figure B2. Thermal ALD reactor

B2. List of Components for Thermal ALD System

Company	Catalog Number	Description
Duniway	DST-531	Thermocouple Sensor Tube, Nickel-plated, Mild Steel, 1/8 " NPT Port.
	TCG-531	Thermocouple Type 531 Gauge Controller

	IFT-NW40-4	Molecular Sieve Trap, In-Line
	FT-4-MS	Molecular Sieve Replacement Material,, Zeolite 13-X
Nor-Cal Products	LFT-075-1-025	1.33" OD CF Single Liquid Feedthrough, 1/4" OD Tube
MDC	9392007	1.33'' Electrical/TC Feedthrough
	414007	2.75'' CF to ¼'' MVCR Adapter
	463000	1.33'' Glass-seal off
	402000	1.33'' Nipple
	150001	Zero LengthReducer: 2.75" to 1.33"
	404002	Tee, 2.75"
	407002	6-WayCross, 2.75"Tube
	665205	QuickDoor, 2.75"ViewPort
	110008	2.75'' Blank Flange
	110000	1.33'' Blank Flange
	731001	Adapter, NW25x.125"FPT
	414007	2.75" OD CF to 1/4" MVCR Adapter
	414006	1.33" OD CF to 1/4" MVCR Adapter
	310029	Angle Valve, 1.5" HV Manual, 2 3/4"CF
	409004	2-3/4'' Multiport
Swagelok	SS-4MG-VCR-MH	SS Medium-Flow Metering Valve, Vernier Handle
	SS-4BG-V51	SS Bellows-Sealed Valve, Spherical Stem Tip
	SS-DLV51	SS High-Purity High-Pressure Diaphragm-Sealed Valve
	SS-BNVCR4-P-C	16L SS High-Purity Bellows-Sealed Valve, 1/4 in.
	316L-4-VCR-3AS	316 SS VCR ¼ in Butt Weld Gland
	SS-4-VCR-1	316 SS VCR ¼ in. Female Nut
	SS-4-VCR-4	316 SS VCR ¼ in. Male Nut
	SS-4-HCG	¼ in. Stainless Steel Female NPT Hex Coupling

Kurt J. Lesker	TFT1KY2C302	1.33 inch TC/Power Feedthrough
Ari Industries Inc.	BXX09B88-4T	Inconel 600 Sheath Heater (Length: 88 inch Diameter: 0.09 inch)
Omega Engineering	CN1507TC	7 Channel Programmable Temperature Controller
	SSR330DC25	Solid State Relay (DC 25 Amp)
	CO1-K-72 INCH	Cement on Type K Thermocouple
	TT-K-24-100	PFA Insulated, 24 AWG, Type K Thermocouple
McMaster	69295K61	Compact Push-in Connector, Receptacle, 250V AC, for .093" Diameter Pin
	69295K81	Compact Push-in Connector, Plug, 250V AC, for .093" Diameter Pin
	69295K23	.093" Diameter Pin, 22-18 AWG, for 250V AC Compact Push-in Connector
	69295K33	.093" Diameter Socket, 22-18 AWG, for 250V AC Compact Push-in Connector
	7587K941	Stranded Single-Conductor Wire, UL 1007/1569, 20 AWG, 300 VAC, Black
	3641K26	High-Temperature Heat Cable, 96" Length, 400 Watts
	3641K23	High-Temperature Heat Cable, 24" Length, 100 Watts
	3641K24	High-Temperature Heat Cable, 36" Length, 125 Watts
	69145K68	Spade Terminal, Block, Vinyl Insulated, 22-18 AWG, #8 Screw/Stud
	7227K84	Butt Splice, Nylon-Insulated Double-Crimp, 22-18 AWG
	3869K34	Type K Thermocouple Connector, Female
	3869K35	Type K Thermocouple Connector, Male
	6994K24	Variable Voltage Output Transformer, Bench Top, 1440 VA, 120 VAC Input, 60 Hz

Controlled Motion Solutions, Inc.	PS2932BP	Solenoid: 3 Pin Connector Kit-Series
	PS2982B53P	Solenoid: 120/60 Coil Sol Kit
	PSTFTN0N10NP	10 STATE Manifold
Laminar Technologies	UFC-1100A	Mass Flow Rate controller
National Instruments	NI USB-9481	USB-Based High-Voltage Relay Output
MDC	9924004	Inline Electrical Connections (Diameter: 0.059 inch)
McMaster	9548K23	Type 316 Stainless Steel Shim Stock Roll, .004" Thick, 6" Width x 100" Length
	75065K14	Indoor Steel Enclosure with Knockouts (NEMA 1), 10" Height x 8" Width x 4" Depth
	9317T67	Corrosion-Resistant 304 Stainless Steel Wire Cloth Disc, 200 x 200 Mesh, 5/8" Diameter, .0021" Wire Diameter
	5272K292	Brass Yor-Lok Tube Fitting, Straight Adapter for 1/8" Tube OD x 1/8 NPT Male
	5384K51	Moisture-Resistant Polyethylene Vacuum Tubing, 1/16" ID, 1/8" OD, 1/32" Wall Thickness, Semi-Clear White, 50 ft. Length
	5454K61	Miniature Brass Fitting, Straight for 1/16" Tube ID x 10-32 Male Pipe Size
	9162K191	Chrome-Plated Brass Thread Pipe Fitting, 1/8 Pipe Size, Square Head Solid Plug
	5454K81	Miniature Brass Fitting, 10-32 Thread, Slotted Head Plug
	51875K61	Brass Compression Tube Fitting with Tube Support, Straight Adapter for 1/4" Tube OD x 1/8 Male Pipe
	5272K101	Front Sleeve for 1/4" Tube OD Brass Yor-Lok Tube Fitting
	5272K111	Back Sleeve for 1/4" Tube OD Brass Yor-Lok Tube Fitting

	5272K121	Nut for 1/4" Tube OD Brass Yor-Lok Tube Fitting
	7343K711	Toggle Switch, SPST, Off-On, 15 Amps, Quick-Disconnect
	5339T24	LED Panel Mount Indicating Light, 13 mm, Conical Shaped Lens, 120V AC/DC
	7060K63	Insulated Barrel Quick-Disconnect Terminal, Double-Crimp Female, 22-18 AWG, .25" Width x .032" Thickness Tab
	7087K15	Panel-Mount Glass/Ceramic Fuse Holder for 3AG/3AB Fuse, .25" Straight Angle Terminal
	7527K51	300 VAC/VDC Terminal Block, 10 Circuits, 3/8" Centerto-Center, 20 Amps
National Instruments	779453-01	NI USB-9481 USB-Based High-Voltage Relay Output
Omega Engineering	NI80-020-200	Resistance Heating Wire, Nickel-Chromium Alloy, 80% Nickel/ 20% Chromium, AWG 24
	NI80-012-200	Resistance Heating Wire, Nickel-Chromium Alloy, 80% Nickel/ 20% Chromium, AWG 28

B.2 LabVIEW and Automation

A NI-USB 9162 module (which is referred to as DAQ in the program) is used to translate USB signals from LabVIEW to a switch for automation purposes. LabVIEW and the drivers for the DAQ need to be installed before plugging the device into the computer. The DAQ can have up to 4 channels (or switches) active for automating selected pneumatic valves on the chamber.

In LabVIEW programming, the DAQ operates on Boolean (true or false for each channel) within a while loop to activate and deactivate the switch for pneumatic valves on the chamber. Selecting the DAQ wizard in LabVIEW will help set up the module to connect with the program. To verify the DAQ in the program represents the connected controller, right-click the DAQ wizard, select "Properties". A loading bar will appear to verify that the drivers were installed correctly.

There are two interface screens in LabVIEW that are primarily used to set up an automation program: the Front Panel, and the Block Diagram. The Block Diagram is used to assemble segments of the program to layout the pattern for a precursor deposition. For every precursor, there should be one "For" loop inside a larger "While" loop. For the

Lithium Aluminum Silicate (LASO) chamber, each precursor is followed by a nitrogen purge pulse, as well as an oxidizing pulse, followed by another nitrogen purge. The graphic programming schematic of one aluminum precursor cycle is shown in Figure 1.
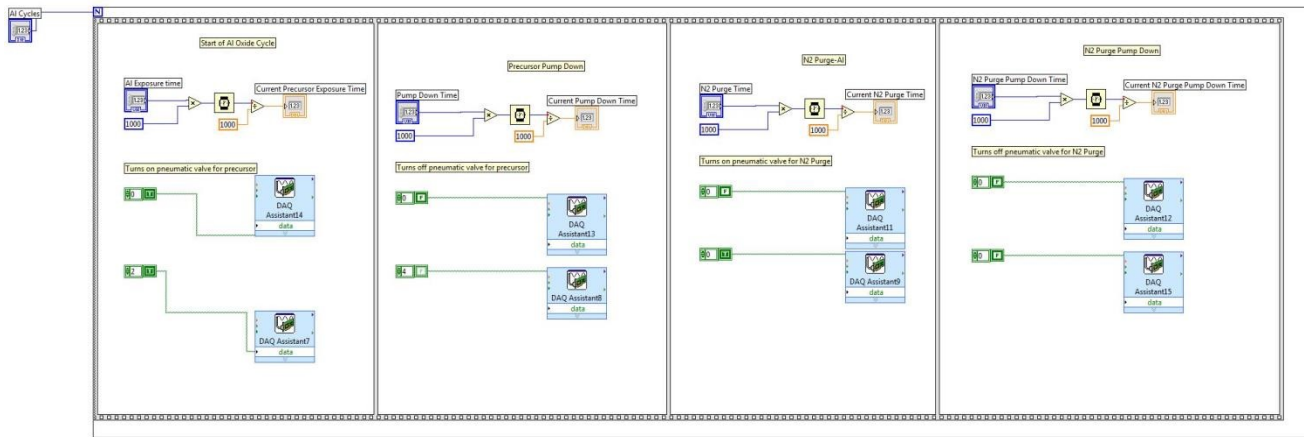
Figure B3 - Block Diagram of Aluminum Precursor Pulse.
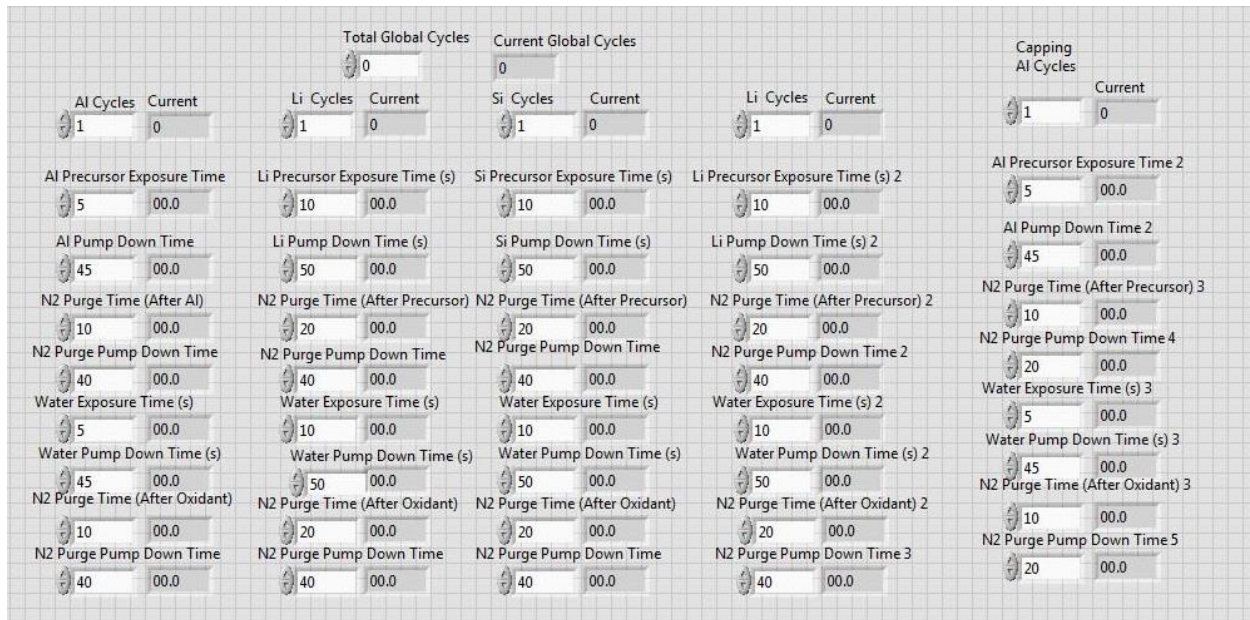
Figure B4 - Front Panel of LabVIEW Program

Each cycle for the precursor includes the precursor exposure and the oxidant exposure in atomic layer deposition. The number of repeats for each precursor cycle is indicated at the top of each column. There are four columns of precursors that can be used: aluminum (using trimethyl aluminum, or TMA), silicon (tris(tert-butoxy)silanol or TTBS, tetraethylorthosilicate (TEOS)), or lithium (lithium tert-butoxide or LTB). The columns are arranged in the following order: aluminum, lithium, silicon, lithium. This designates a global cycle.

Electrical Wiring for Temperature Control Heaters

The heaters on the lithium aluminosilicate (LASO) atomic layer deposition (ALD) chamber rely on high-temperature heat cables controlled by an Omega 7 Channel Temperature Controller (7CC). The Controller has a thermocouple connected to the LASO chamber which monitors the temperature of certain portions of the chamber. The Controller uses standard PID controls to ramp and maintain temperature on the LASO ALD chamber.

The output of the controller is intended to apply the necessary power to heating elements. Unfortunately, because the voltage is 5Vdc, the controller circuit is fed to solid state relays. When the temperature controller activates the circuit, the relay activates the 120Vac circuit containing the heating elements on the chamber.
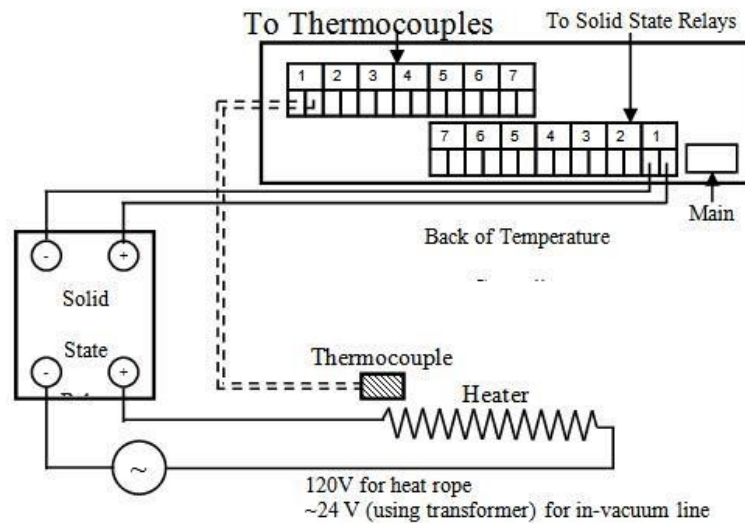
Figure B5 - Schematic of electrical wiring for temperature controlled heaters

Programming the Temperature Controller

Note: Before programming or checking a programmed profile, the Controller must be in *"stopped"* mode.

1) Enter programming mode of the Temperature Controller by first selecting the channel that needs to be programmed (by pressing CTR SEL on the controller panel).

2) Press and hold the CTR SEL key until the display states —ENTER PASSCODE.

3) The front keys are marked with a small digit in the lower right corner. Enter the pass-code combination: 3254.

4) Use the ▲▼ key until —PROFILE is displayed.

5) Push the PROG key.

6) The unit will display one of the channels with each push on the ▲▼ key. Select the desired controller, then push PROG to select it.

   a) The display display will briefly read "Strt SP" for "Start Setpoint" then the current value of the starting setpoint. Use and <DIG>keys to enter a desired value. The ▲▼ key increases and decreases the flashing digit, where the <DIG>key selects the next digit.

   b) Press SETUP to go to next function.

   c) The display will briefly read **SetPt 1** and then the current value of Setpoint #1. Use ▲▼ and <DIG> to enter the desired value, then press PROG to go to the following function.

   d) The display will read "Enter Time" and show the current time value. Time entered is the ramping time, or the time that it takes to ramp up to the set point (or soak time, if the previous and current setpoints are the same). The value shown for time is in minutes. Use ▲▼ and <DIG> to enter the desired value, then press PROG to go to the next function.
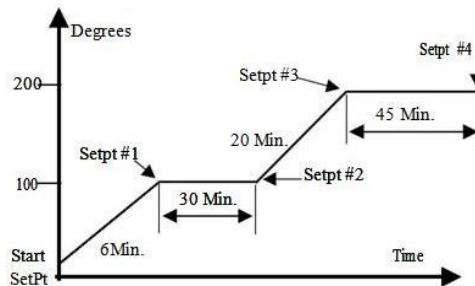
Figure B6 - Example Ramp Profile

   e) Repeat a-d to program setpoints #2 through #7. Once all 7 segments have been programmed, the display will revert back to the beginning of Programming mode selection. If all the seven segments are not used, the program can be aborted at any segment by pushing the EXT key. The segment in which EXT is pushed will be considered the end of the program. During Verify Program mode, the segment and all following segments are labeled as "PrG End" <u>Note:</u> After entering the time for the last segment, go to the next segment and then hit EXT.

A2.1.3 Verify Mode

1) Verify mode is used to check previously programmed ramp/soak profile, or making small changes to a program. Enter programming mode, and press ▲▼ until "VErIFY" is displayed.
2) Press PROG.
3) Select the desired controller to verify by pressing ▲▼, then press PROG to step through the profile.
4) Use the ▲▼ and <DIR> as in steps 6a-e of the programming section to edit a program.
5) At any time, pressing EXT to exit Verify mode. Unlike other programming modes, exiting Verify does not mark the end of a profile program.

A2.1.4 Run Mode

1) To run a controller, select the controller by pushing CTR SEL key, followed by a push on RUN/STP.
2) Pushing CTR SEL will display "CntrL 1" .
3) To select another controller, toggle CTR SEL until the desired controller is displayed.
4) To run a controller's profile, push the RUN STP key until the unit displays "Ctr. rUn". At this point the desired controller will run its programmed profile.
5) Once running, the controller can be put into an indefinite hold, or stopped.
6) To indefinitely hold a controller at any setpoint, press and hold the CTR SEL key at the desired controller, and *simultaneously* press SCN/HLD.
7) The controller will display "C# HOLd".
8) The controller will hold this point until the unit is placed back in Run mode.
9) To stop a controller after it has been put in run mode, select the controller that needs to be stopped using the CTR SEL key to select the controller. Press RUN/STP once.
10) To stop all controllers at the same time, push CTR SEL and RUN/STP keys simultaneously.

   The LASO ALD chamber automated deposition is possible through a LabVIEW program on a computer, and a set of circuits to activate a pneumatic valve on the chamber. A solenoid is used to convert electrical impulses to pressurized air flow. In the LASO ALD chamber, electrical impulses come from an NI-USB-9481 (DAQ) interfaced with the LabVIEW automatic deposition computer program. The pressurized air operates the pneumatic valves on the chamber. When the circuit is closed (by the manual switch on the solenoid box or the DAQ via LabVIEW), the solenoid valve is opened. Pressurized air then flows to the pneumatic valve by plastic tubing. The pneumatic valve opens when pressurized air is available. There are ten solenoid circuits (channels) in the solenoid box that can activate up to ten valves. Each DAQ can operate only four electrical channels. Two DAQ modules are used to operate the LASO ALD chamber.
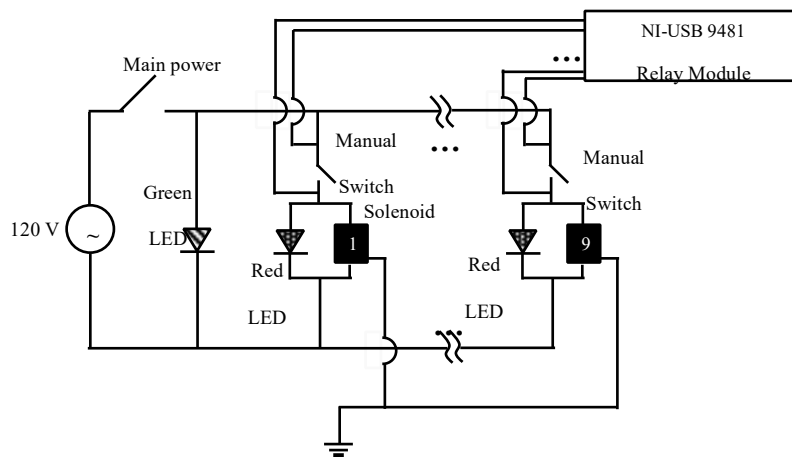
Figure B7- Schematic of Electrical Wiring for Automated Pneumatic Valve Control

B3. STANDARD OPERATING PROCEDURE

LASO ALD Hot Wall Reactor Chamber Operational Procedures
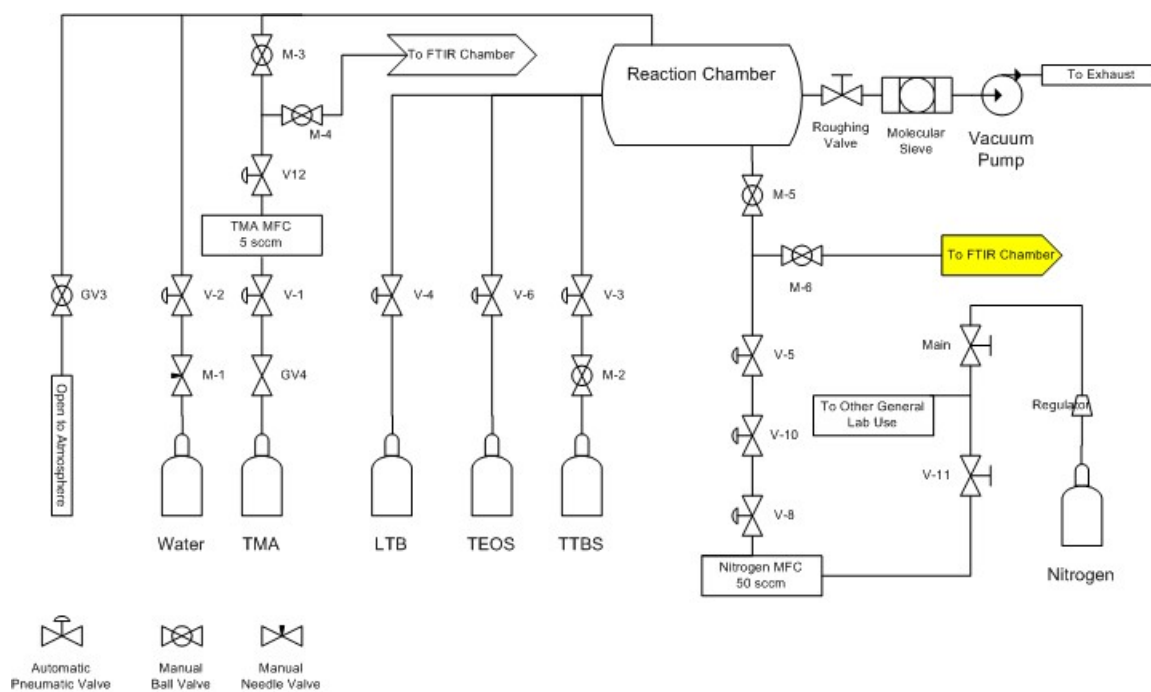
Figure B8 - LASO Chamber Gas Line Schematic

Chemicals Used:
1. Trimethyl Aluminum (TMA)
2. Tetraethyl Orthosilicate (TEOS)
3. Lithium tert-butoxide (LTB)

4. Tris(tert-butoxy)silanol (TTBS)
5. Diethyl phospharamide (DEPA)

EMERGENCY SHUTDOWN:
1. Close all the precursor/reactant valves: LTB (Li) , TEOS (Si) , TMA (Al), Water, DEPA, TTBS
2. Stop LabVIEW program on the computer
3. Reset any valves from LABVIEW
4. Close the valves to the chamber (GV1,2,3)
5. Shut down all the electronics: Transformers, Mass Flow Controller control panel
6. Proceed to emergency exit locations

OPERATING PROCEDURE:
Gas Line Schematic:
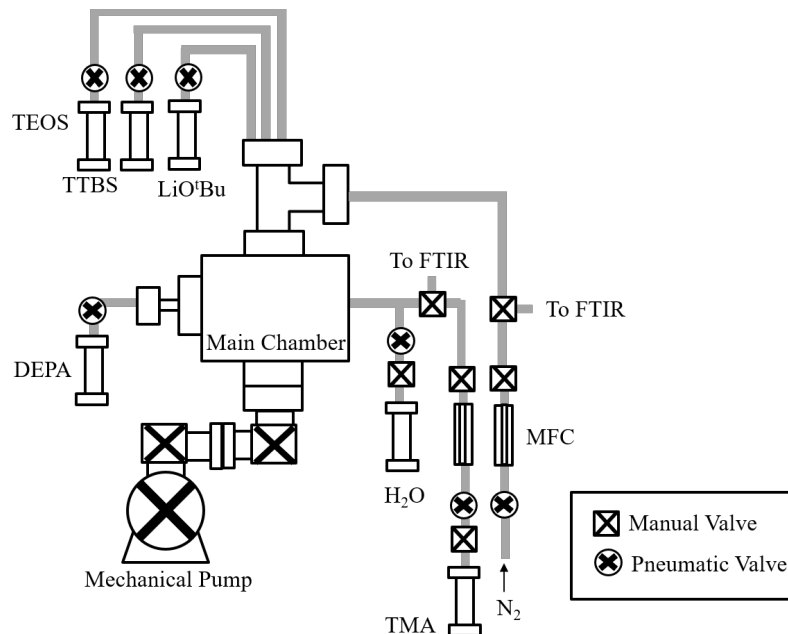
Figure B9. Thermal ALD reactor for deposition of $Li_xAl_ySi_zO$ and LiSiPON. The main component of the reactor consisted of a CF 6-way cross with OD 2.75", where the walls were heated to 150°C to prevent precursor adsorption. The pressure was maintained in the mTorr regime through use of a mechanical pump. Precursors were stored in 1.33" conflat housings, heated to provide adequate vapor flux to the sample surface.

- Ch5 and V8 – Valves controlling TMA flowrate, MFC channel 2
- Ch4, V5, V6, and V10 –Valves controlling N_2 flow rates, MFC channel 4
- V4 – Valve controlling LTB
- M1 and V1 – Valves controlling water flowrate

1. *Initial Check:* Make sure all the valves are closed.

2. *Venting the reactor:*
   a. Isolate the chamber: Turn off V9 of Solenoid box, and close manual roughing valve. Untighten door so it can be opened.
   b. Flow nitrogen by setting N2 MFC Channel 4 to 10-15%.
   c. Open V10 and V6 on the Solenoid box (Should be always open). Open V5 to vent the chamber.
   d. Purge chamber with nitrogen for 10 minutes, or until the door can open without resistance.
   e. After venting, close V5 on Solenoid Box to the chamber.

3. *Sample loading:*
   a. Once the chamber is door keep V5 on to remain flowing nitrogen throughout the chamber
   b. Make sure the Variable Transformer 1 for the sample stage is off and unplugged.
   c. Load sample onto stainless steel dish sample stage inside chamber through the door
   d. Once sample is secured close chamber door.
   e. Turn off V5 (nitrogen) and turn V9 (pneumatic roughing valve) back on.
   f. Slowly open manual roughing valve to slowly pump down the chamber
   g. Check the connections on the heating wires/ thermocouple of the sample stage to check for any shorts and then reconnect with temperature controller

Note: After loading, be sure to nitrogen purge (3x) before starting experiment (Leave V9 on for nitrogen purge). This removes water in the chamber that would interfere with water-sensitive precursors.

4. *Base pressure:* Slowly open the roughing valve, and allow the chamber pressure return to a base pressure around 75 mTorr.

5. *Nitrogen Purge:* (*)
   a. Set channel 4 of MFC controller to 10-15%.
   b. Open V10 and V6 (Should always be on) on the Solenoid box.
   c. Open V5 for 5 seconds, then close V5.
   d. Pressure will go up to 500 mTorr, then wait ~45 seconds until pressure returns to base pressure.
   e. Once base pressure is reached, repeat the procedure (* b-d) at least 2 more times (for a total of 3 times).
   f. Close V5, V6 and V10. Set N2 MFC to 0%

6. Heating: *(Note: Heat chamber, gas lines, and precursor housings concurrently)*
   a. Chamber: Heat the chamber wall to 150ºC by activating Ch 5,7 of 7Channel Controller-1 (Denoted as 7CC-1 from now on). Also, activate Ch6 (Chamber nipple

heater) and Ch7 (Chamber pumpline heater) on 7Channel Controller-2 (denoted as 7CC-2 henceforth).

Figure B10. Temperature Controller

b. Gas Line heating: Heat the gas lines by activating the following channels:
   i. 7CC-1:Ch4: TMA/Water Gas line
   ii. 7CC-2:Ch2: LTB Gas line
   iii. 7CC-2:Ch3: TTBS Gas line
c. Sample stage heating: Heat the sample stage by turning Variable Transformer-1 (Denoted as VT-1 from now on) (~28%), followed by activating Ch3 of 7CC-1

Figure B11. Transformers for the sample stage heater and dosers

d. Precursor heating: Heat the precursors by activating corresponding channels of 7CC-1 listed below:
   i. Lithium Tert-butoxide (LTB): Ch1 of 7CC-6
   ii. Tris(tert-butoxy)silanol (TTBS): Ch4 of 7CC-2
   iii.
   Note: TMA and TEOS is maintained at room temperature

e. Doser heating: Heat the doser by turning Variable Transformer-2 (Denoted as VT-2 from now on)(~20%), followed by activating corresponding channel of interest on 7-Channel Controller-2 (7CC-2)
   Ch1: LTB Doser

Figure B12. Temperature Controller 2 and Solid-state Relays

   f. In summary, the following channels need to be activated for LASO deposition:
       i.   7CC-1: 3, 4, 5,6,7
       ii. 7CC-2: 1, 2, 3, 4, 6, 7

Setpoint/ramping info of both 7CC-1 and 7CC-2 are listed below:

7CC-1 (As of 08/01/2014)

Channel	Description	Start Pt	SP1	t1	SP2	t2	SP3	t3	SP4	t4	SP5
08/01/2014 - 7 Channel Controller Setup for LASO Chamber										
1		25	80	20	80	15	160	20	160	2500	Pg End
2											
3	Sample Heater	25	75	20	75	15	225	20	225	2500	Pg End
4	Additional Ch. (Gasline)	25	45	20	45	15	60	20	60	2500	Pg End
5	Chamber Wall	25	50	20	50	15	100	20	100	2500	Pg End
6	Lithium tert-butoxide (LTB)	25	45	20	89	15	135	20	135	2500	Pg End
7	Chamber	25	150	20	150	15	150	20	150	2500	Pg End

7CC-2 (As of 08/01/2014)

Channel	Description	Start Pt	SP1	t1	SP2	t2	SP3	t3	SP4	t4	SP5
10/12/2013 - 7 Channel Controller 2 Setup for LASO Chamber										
1	Lithium tert-butoxide (LTB) Doser	25	80	15	80	10	160	20	160	2500	Pg End
2	Lithium tert-butoxide (LTB) Gasline	25	80	15	80	10	160	20	160	2500	Pg End
3	Tris(tert-butoxy)Silanol Gasline	25	50	15	50	10	75	20	75	2500	Pg End
4	Tris(tert-butoxy)Silanol Housing	25	30	15	30	10	45	20	45	2500	Pg End
5	Glycerol	25	50	15	50	10	120	20	120	2500	Pg End
6	Chamber Nipple Heater	25	100	20	100	15	150	20	150	2500	Pg End

226

7	Chamber Pumpline Heater	25	100	20	100	15	150	20	200	150	Pg End

7. *Manual Deposition:*

For LiAlSiO$_4$, alternate cycles of Al oxide (b cycles for each global cycle), Li oxide (a cycles for each global cycle), and Si oxide (c cycles for each global cycle). Deposit total of # global cycles. (Note: Aluminum deposit first because have good surface adhesion.)

The procedures listed below are only for one cycle each! (Note: pump down time can be extended if need be, but cannot extend pulse time.)

    a. Li$_2$O Deposition
        i. Slightly open 45 of lithium precursor Li-t-butoxide, LTB, for 10 seconds. Pressure will increase by 5-10 mTorr.
        ii. Close valve V4 for 50 seconds for pump down time. Make sure chamber goes back to base pressure.
        iii. Before the pump down time of 60 seconds are up, open water valve M1 to setting of 10.
        iv. After the pump down time of 60 seconds, open valve V2 for 10 seconds. Watch the pressure, should increase to 100-200 mTorr, but make sure it does not go above 200 mTorr. (Note: water does not have MFC so vapor pressure can be high.)
        v. Close V2, then close M1 for water.
        vi. Pump down for 60 seconds till base pressure has been reached. (Note: if chamber has not reached the base pressure after pump down time of 60 seconds, then do a Nitrogen Purge Step by pulsing nitrogen in for 10 seconds.)

    b. Al$_2$O$_3$ Deposition
        i. Open the valve V1 of Grey Solenoid Box for 5 seconds.
        ii. Close V1. Pump down for 45 seconds. Make sure chamber goes back to base pressure.
        iii. Before the pump down time of 45 seconds are up, open water valve M1 to setting of 10.
        iv. After the pump down time of 45 seconds, open valve V2 for 5 seconds. Watch the pressure, should increase to 100-200 mTorr, but make sure it does not go above 200 mTorr. (Note: water does not have MFC so vapor pressure can be high.)
        v. Close V2, then close M1 for water.
        vi. Pump down for 45 seconds till base pressure has been reached. (Note: if chamber has not reached the base pressure after pump down time of 60 seconds, then do a Nitrogen Purge Step by pulsing nitrogen in for 10 seconds.)

    c. SiO$_2$ Deposition

(Note: if nitrogen purge was used in previous deposition, need to reset the MFC channel 4 to 3% before beginning deposition.)

     i. Open V3

    ii. Half way open the valve GV2 for 20 seconds. Pressure will increase to 200 mTorr.

   iii. Close GV2, then close V3. Pump down for 60 seconds. Make sure chamber goes back to base pressure.

   iv. Before the pump down time of 60 seconds are up, open water valve M1 to setting of 10.

    v. After the pump down time of 60 seconds, open valve V2 for 15 seconds. Watch the pressure, should increase to 100-200 mTorr, but make sure it does not go above 200 mTorr. (Note: water does not have MFC so vapor pressure can be high.)

   vi. Close V2, then close M1 for water.

  vii. Pump down for 60 seconds till base pressure has been reached. (Note: if chamber has not reached the base pressure after pump down time of 60 seconds, then do a Nitrogen Purge Step by pulsing nitrogen in for 10 seconds.)

8. Automated Deposition

   a. Load LabVIEW program on the computer

       i. Open file "072913 – LASO and Al Capping Layer.vi"

      ii. Set number of cycles for the appropriate element.

          1. Each cycle includes a precursor pulse, nitrogen purge, water pulse, and another nitrogen purge.

          2. Times listed on each pulse step are not normally changed.

      iii. Set number of global cycles on the top of the worksheet. This loops the precursor pulses.

      iv. Check the temperatures on the Channel Controllers.

       v. Check sample in the sample holder.

      vi. Turn V9 on the Solenoid Box to "off", and open V6 and V10 on the Solenoid box.

     vii. On the computer, press the white arrow on the toolbar to begin the programmed deposition.
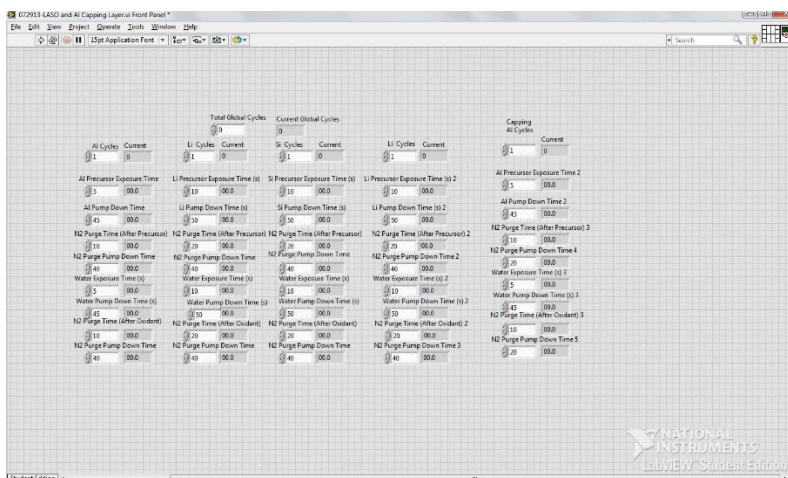
Figure B13. Labview Front Panel

9. *Finishing the deposition:*
    a. Close all MFC and valves.
    b. Turn off all the heating for chamber and precursor containers.
    c. Wait for the chamber to cool down to at least 50ºC. (This will take about ~1.0 hours)
    d. Nitrogen Purge 3 times (See Step 5).

10. *Sample unloading:*
    a. Perform Steps 1 and 2.
    b. Open the chamber to unload the sample.
    c. If not loading sample in soon, then pump down the chamber.

BIBLIOGRAPHY

Aaltonen, T., M. Alnes, O. Nilsen, L. Costelle and H. Fjellvåg (2010). "Lanthanum titanate and lithium lanthanum titanate thin films grown by atomic layer deposition." Journal of Materials Chemistry **20**(14): 2877-2881.

Aaltonen, T., O. Nilsen, A. Magrasó and H. Fjellvåg (2011). "Atomic Layer Deposition of Li2O–Al2O3 Thin Films." Chemistry of Materials **23**(21): 4669-4675.

Ahmed, B., D. H. Anjum, Y. Gogotsi and H. N. Alshareef (2017). "Atomic layer deposition of SnO2 on MXene for Li-ion battery anodes." Nano Energy **34**(Supplement C): 249-256.

Akkerman, A., T. Boutboul, A. Breskin, R. Chechik, A. Gibrekhterman and Y. Lifshitz (1996). "Inelastic Electron Interactions in the Energy Range 50 eV to 10 keV in Insulators: Alkali Halides and Metal Oxides." physica status solidi (b) **198**(2): 769-784.

Alford, T., L. Feldman and J. Mayer (2007). Fundamentals of Nanoscale Film Analysis, Springer.

Allen, J. L., J. Wolfenstine, E. Rangasamy and J. Sakamoto (2012). "Effect of substitution (Ta, Al, Ga) on the conductivity of Li7La3Zr2O12." Journal of Power Sources **206**: 315-319.

Alpen, U. V., E. Schönherr, H. Schulz and G. H. Talat (1977). "β-eucryptite—a one-dimensional Li-ionic conductor." Electrochimica Acta **22**(7): 805-807.

An, S. J., J. Li, C. Daniel, D. Mohanty, S. Nagpure and D. L. Wood (2016). "The state of understanding of the lithium-ion-battery graphite solid electrolyte interphase (SEI) and its relationship to formation cycling." Carbon **105**(Supplement C): 52-76.

Aono, H., E. Sugimoto, Y. Sadaoka, N. Imanaka and G. y. Adachi (1990). "Ionic Conductivity of Solid Electrolytes Based on Lithium Titanium Phosphate." Journal of The Electrochemical Society **137**(4): 1023-1027.

Aotani, N., K. Iwamoto, K. Takada and S. Kondo (1994). "Synthesis and electrochemical properties of lithium ion conductive glass, Li3PO4Li2SSiS2." Solid State Ionics **68**(1): 35-39.

Arbi, K., W. Bucheli, R. Jiménez and J. Sanz (2015). "High lithium ion conducting solid electrolytes based on NASICON Li1+xAlxM2−x(PO4)3 materials (M=Ti, Ge and 0≤x≤0.5)." Journal of the European Ceramic Society **35**(5): 1477-1484.

Armand, M. (1994). The history of polymer electrolytes.

Arthur, T. S., D. J. Bates, N. Cirigliano, D. C. Johnson, P. Malati, J. M. Mosby, E. Perre, M. T. Rawls, A. L. Prieto and B. Dunn (2011). "Three-dimensional electrodes and battery architectures." MRS Bulletin **36**(7): 523-531.

Ashuri, M., Q. He and L. L. Shaw (2016). "Silicon as a potential anode material for Li-ion batteries: where size, geometry and structure matter." Nanoscale **8**(1): 74-103.

Atosuo, E., M. Mäntymäki, K. Mizohata, M. J. Heikkilä, J. Räisänen, M. Ritala and M. Leskelä (2017). "Preparation of Lithium Containing Oxides by the Solid State Reaction of Atomic Layer Deposited Thin Films." Chemistry of Materials **29**(3): 998-1005.

Bachman, J. C., S. Muy, A. Grimaud, H.-H. Chang, N. Pour, S. F. Lux, O. Paschos, F. Maglia, S. Lupart, P. Lamp, L. Giordano and Y. Shao-Horn (2016). "Inorganic Solid-State Electrolytes for Lithium Batteries: Mechanisms and Properties Governing Ion Conduction." Chemical Reviews **116**(1): 140-162.

Bates, J. B., N. J. Dudney, G. R. Gruzalski, R. A. Zuhr, A. Choudhury, C. F. Luck and J. D. Robertson (1992). "Electrical properties of amorphous lithium electrolyte thin films." Solid State Ionics **53-56**: 647-654.

Bates, J. B., N. J. Dudney, G. R. Gruzalski, R. A. Zuhr, A. Choudhury, C. F. Luck and J. D. Robertson (1993). "Fabrication and characterization of amorphous lithium electrolyte thin films and rechargeable thin-film batteries." Journal of Power Sources **43**(1): 103-110.

Boulineau, S., M. Courty, J.-M. Tarascon and V. Viallet (2012). "Mechanochemical synthesis of Li-argyrodite Li6PS5X (X=Cl, Br, I) as sulfur-based solid electrolytes for all solid state batteries application." Solid State Ionics **221**: 1-5.

Briggs, D. (1981). "Handbook of X-ray Photoelectron Spectroscopy C. D. Wanger, W. M. Riggs, L. E. Davis, J. F. Moulder and G. E.Muilenberg Perkin-Elmer Corp., Physical Electronics Division, Eden Prairie, Minnesota, USA, 1979. 190 pp. $195." Surface and Interface Analysis **3**(4): v-v.

Cao, K., T. Jin, L. Yang and L. Jiao (2017). "Recent progress in conversion reaction metal oxide anodes for Li-ion batteries." Materials Chemistry Frontiers **1**(11): 2213-2242.

Cao, Y.-Q., S.-S. Wang, C. Liu, D. Wu and A.-D. Li (2019). "Atomic layer deposition of ZnO/TiO2 nanolaminates as ultra-long life anode material for lithium-ion batteries." Scientific Reports **9**(1): 11526.

Cao, Y., X. Meng and J. W. Elam (2016). "Atomic Layer Deposition of LixAlyS Solid-State Electrolytes for Stabilizing Lithium-Metal Anodes." ChemElectroChem **3**(6): 858-863.

Chamran, F., Y. Yeh, H. Min, B. Dunn and C. Kim (2007). "Fabrication of High-Aspect-Ratio Electrode Arrays for Three-Dimensional Microbatteries." Journal of Microelectromechanical Systems **16**(4): 844-852.

Chang, B., P. Leussink, F. Jensen, J. Hübner and H. Jansen (2018). "DREM: Infinite etch selectivity and optimized scallop size distribution with conventional photoresists in an adapted multiplexed Bosch DRIE process." Microelectronic Engineering **191**: 77-83.

Chang, J. and J. P. Chang (2017). "Achieving atomistic control in materials processing by plasma–surface interactions." Journal of Physics D: Applied Physics **50**(25): 253001.

Chang, J. P., J. C. Arnold, G. C. H. Zau, H.-S. Shin and H. H. Sawin (1997). "Kinetic study of low energy argon ion-enhanced plasma etching of polysilicon with atomic/molecular chlorine." Journal of Vacuum Science & Technology A **15**(4): 1853-1863.

Chen, L., K.-S. Chen, X. Chen, G. Ramirez, Z. Huang, N. R. Geise, H.-G. Steinrück, B. L. Fisher, R. Shahbazian-Yassar, M. F. Toney, M. C. Hersam and J. W. Elam (2018). "Novel ALD Chemistry Enabled Low-Temperature Synthesis of Lithium Fluoride Coatings for Durable Lithium Anodes." ACS Applied Materials & Interfaces **10**(32): 26972-26981.

Chen, N., B. Reeja-Jayan, J. Lau, P. Moni, A. Liu, B. Dunn and K. K. Gleason (2015). "Nanoscale, conformal polysiloxane thin film electrolytes for three-dimensional battery architectures." Materials Horizons **2**(3): 309-314.

Chen, R., W. Qu, X. Guo, L. Li and F. Wu (2016). "The pursuit of solid-state electrolytes for lithium batteries: from comprehensive insight to emerging horizons." Materials Horizons **3**(6): 487-516.

Chen, S., Y. Zhao, B. Sun, Z. Ao, X. Xie, Y. Wei and G. Wang (2015). "Microwave-assisted Synthesis of Mesoporous Co3O4 Nanoflakes for Applications in Lithium Ion Batteries and Oxygen Evolution Reactions." ACS Applied Materials & Interfaces **7**(5): 3306-3313.

Chen, X., E. Pomerantseva, P. Banerjee, K. Gregorczyk, R. Ghodssi and G. Rubloff (2012). "Ozone-Based Atomic Layer Deposition of Crystalline V2O5 Films for High Performance Electrochemical Energy Storage." Chemistry of Materials **24**(7): 1255-1261.

Cheng, F., Z. Tao, J. Liang and J. Chen (2008). "Template-Directed Materials for Rechargeable Lithium-Ion Batteries." Chemistry of Materials **20**(3): 667-681.

Cheng, F., H. Wang, Z. Zhu, Y. Wang, T. Zhang, Z. Tao and J. Chen (2011). "Porous LiMn2O4 nanorods with durable high-rate capability for rechargeable Li-ion batteries." Energy & Environmental Science **4**(9): 3668-3675.

Cho, J.-H. and S. T. Picraux (2013). "Enhanced Lithium Ion Battery Cycling of Silicon Nanowire Anodes by Template Growth to Eliminate Silicon Underlayer Islands." Nano Letters **13**(11): 5740-5747.

Cho, J., T. Kim, T. Seegmiller and J. P. Chang (2015). "Mechanistic study of atomic layer deposition of AlxSiyO thin film via in-situ FTIR spectroscopy." Journal of Vacuum Science & Technology A **33**(5): 05E130.

Cho, J., T. Kim, T. Seegmiller and J. P. Chang (2016). "Elucidating the Surface Reaction Mechanisms During Atomic Layer Deposition of LixAlySizO by in Situ Fourier Transform Infrared Spectroscopy." The Journal of Physical Chemistry C **120**(22): 11837-11846.

Chockla, A. M., K. C. Klavetter, C. B. Mullins and B. A. Korgel (2012). "Solution-Grown Germanium Nanowire Anodes for Lithium-Ion Batteries." ACS Applied Materials & Interfaces **4**(9): 4658-4664.

Choi, J. W. and D. Aurbach (2016). "Promise and reality of post-lithium-ion batteries with high energy densities." <u>Nature Reviews Materials</u> **1**: 16013.

Chourasia, A. R. and D. R. Chopra (1994). "Elemental Manganese Studied by X-ray Photoemission Spectroscopy Using Mg and Zr Radiations." <u>Surface Science Spectra</u> **3**(1): 74-81.

Christie, A. M., S. J. Lilley, E. Staunton, Y. G. Andreev and P. G. Bruce (2005). "Increasing the conductivity of crystalline polymer electrolytes." <u>Nature</u> **433**(7021): 50-53.

Chu, I.-H., H. Nguyen, S. Hy, Y.-C. Lin, Z. Wang, Z. Xu, Z. Deng, Y. S. Meng and S. P. Ong (2016). "Insights into the Performance Limits of the Li7P3S11 Superionic Conductor: A Combined First-Principles and Experimental Study." <u>ACS Applied Materials & Interfaces</u> **8**(12): 7843-7853.

Chuang, T. J., C. R. Brundle and D. W. Rice (1976). "Interpretation of the x-ray photoemission spectra of cobalt oxides and cobalt oxide surfaces." <u>Surface Science</u> **59**(2): 413-429.

Chunyan, D., Z. Weiwei, W. Bin, L. Xin, W. Dong, Z. Yong and W. Guangwu (2017). "A general strategy toward graphitized carbon coating on iron oxides as advanced anodes for lithium-ion batteries." <u>Nanotechnology</u> **28**(34): 345404.

Coclite, A. M., R. M. Howden, D. C. Borrelli, C. D. Petruczok, R. Yang, J. L. Yagüe, A. Ugur, N. Chen, S. Lee, W. J. Jo, A. Liu, X. Wang and K. K. Gleason (2013). "25th Anniversary Article: CVD Polymers: A New Paradigm for Surface Modifi cation and Device Fabrication." <u>Advanced Materials</u> **25**(38): 5392-5423.

Comstock, D. J. and J. W. Elam (2013). "Mechanistic Study of Lithium Aluminum Oxide Atomic Layer Deposition." <u>The Journal of Physical Chemistry C</u> **117**(4): 1677-1683.

Cremers, V., R. L. Puurunen and J. Dendooven (2019). "Conformality in atomic layer deposition: Current status overview of analysis and modelling." <u>Applied Physics Reviews</u> **6**(2): 021302.

D. Shannon, R., R. C. Shannon, O. Medenbach and R. X. Fischer (2002). "Refractive Index and Dispersion of Fluorides and Oxides." <u>Journal of Physical and Chemical Reference Data</u> **31**(4): 931-970.

Dasgupta, N. P., J. F. Mack, M. C. Langston, A. Bousetta and F. B. Prinz (2010). "Design of an atomic layer deposition reactor for hydrogen sulfide compatibility." <u>Review of Scientific Instruments</u> **81**(4): 044102.

Dasgupta, N. P., X. Meng, J. W. Elam and A. B. F. Martinson (2015). "Atomic Layer Deposition of Metal Sulfide Materials." <u>Accounts of Chemical Research</u> **48**(2): 341-348.

Delft, J. A. v., D. Garcia-Alonso and W. M. M. Kessels (2012). "Atomic layer deposition for photovoltaics: applications and prospects for solar cell manufacturing." <u>Semiconductor Science and Technology</u> **27**(7): 074002.

Deng, Y., C. Eames, B. Fleutot, R. David, J.-N. Chotard, E. Suard, C. Masquelier and M. S. Islam (2017). "Enhancing the Lithium Ion Conductivity in Lithium Superionic Conductor (LISICON) Solid Electrolytes through a Mixed Polyanion Effect." ACS Applied Materials & Interfaces **9**(8): 7050-7058.

Dhivya, L., N. Janani, B. Palanivel and R. Murugan (2013). "Li+ transport properties of W substituted Li7La3Zr2O12 cubic lithium garnets." AIP Advances **3**(8): 082115.

Di Castro, V. and G. Polzonetti (1989). "XPS study of MnO oxidation." Journal of Electron Spectroscopy and Related Phenomena **48**(1): 117-123.

Diddens, D., A. Heuer and O. Borodin (2010). "Understanding the Lithium Transport within a Rouse-Based Model for a PEO/LiTFSI Polymer Electrolyte." Macromolecules **43**(4): 2028-2036.

Dismukes, J. P., L. Ekstrom and R. J. Paff (1964). "Lattice Parameter and Density in Germanium-Silicon Alloys1." The Journal of Physical Chemistry **68**(10): 3021-3027.

Dissanayake, M. A. K. L., W. N. S. Rupasinghe, J. M. N. I. Jayasundara, P. Ekanayake, T. M. W. J. Bandara, S. N. Thalawala and V. A. Seneviratne (2013). "Ionic conductivity enhancement in the solid polymer electrolyte PEO9LiTf by nanosilica filler from rice husk ash." Journal of Solid State Electrochemistry **17**(6): 1775-1783.

Dobbelaere, T., F. Mattelaer, J. Dendooven, P. Vereecken and C. Detavernier (2016). "Plasma-Enhanced Atomic Layer Deposition of Iron Phosphate as a Positive Electrode for 3D Lithium-Ion Microbatteries." Chemistry of Materials **28**(10): 3435-3445.

Donders, M. E., W. M. Arnoldbik, H. C. M. Knoops, W. M. M. Kessels and P. H. L. Notten (2013). "Atomic Layer Deposition of LiCoO2 Thin-Film Electrodes for All-Solid-State Li-Ion Micro-Batteries." Journal of The Electrochemical Society **160**(5): A3066-A3071.

Dong, L., K. Shou, D. R. Frutiger, A. Subramanian, L. Zhang, B. J. Nelson, X. Tao and X. Zhang (2008). "Engineering Multiwalled Carbon Nanotubes Inside a Transmission Electron Microscope Using Nanorobotic Manipulation." IEEE Transactions on Nanotechnology **7**(4): 508-517.

Dudney, N. J. (2008). "Thin Film Microbatteries." Interface(IssueNv2008): 44-48.

Dudney, N. J. and Y.-I. Jang (2003). "Analysis of thin-film lithium batteries with cathodes of 50 nm to 4 μm thick LiCoO2." Journal of Power Sources **119-121**(Supplement C): 300-304.

Durgapal, P., J. R. Ehrstein and N. V. Nguyen (1998). "Thin film ellipsometry metrology." AIP Conference Proceedings **449**(1): 121-131.

Ebin, B., V. Battaglia and S. Gürmen (2014). "Comparison of 4V and 3V electrochemical properties of nanocrystalline LiMn2O4 cathode particles in lithium ion batteries prepared by ultrasonic spray pyrolysis." Ceramics International **40**(5): 7029-7035.

Elam, J. W., M. Schuisky, J. D. Ferguson and S. M. George (2003). "Surface chemistry and film growth during TiN atomic layer deposition using TDMAT and NH3." Thin Solid Films **436**(2): 145-156.

Elam, J. W., G. Xiong, C. Y. Han, H. H. Wang, J. P. Birrell, U. Welp, J. N. Hryn, M. J. Pellin, T. F. Baumann, J. F. Poco and J. H. Satcher (2006). "Atomic Layer Deposition for the Conformal Coating of Nanoporous Materials." Journal of Nanomaterials **2006**: 5.

Famprikis, T., J. Galipaud, O. Clemens, B. Pecquenard and F. Le Cras (2019). "Composition Dependence of Ionic Conductivity in LiSiPO(N) Thin-Film Electrolytes for Solid-State Batteries." ACS Applied Energy Materials **2**(7): 4782-4791.

Ferrari, S., M. Loveridge, S. D. Beattie, M. Jahn, R. J. Dashwood and R. Bhagat (2015). "Latest advances in the manufacturing of 3D rechargeable lithium microbatteries." Journal of Power Sources **286**: 25-46.

Fives, K., R. McGrath, C. Stephens, I. T. McGovern, R. Cimino, D. S. L. Law, A. L. Johnson and G. Thornton (1989). "ARUPS of water adsorption on Si(100) and Si(111) surfaces." Journal of Physics: Condensed Matter **1**(SB): SB105-SB109.

Fojtik, M., D. Kim, G. Chen, Y. Lin, D. Fick, J. Park, M. Seok, M. Chen, Z. Foo, D. Blaauw and D. Sylvester (2013). "A Millimeter-Scale Energy-Autonomous Sensor System With Stacked Battery and Solar Cells." IEEE Journal of Solid-State Circuits **48**(3): 801-813.

Fu, X., D. Yu, J. Zhou, S. Li, X. Gao, Y. Han, P. Qi, X. Feng and B. Wang (2016). "Inorganic and organic hybrid solid electrolytes for lithium-ion batteries." CrystEngComm **18**(23): 4236-4258.

Fuller, C. S. and J. C. Severiens (1954). "Mobility of Impurity Ions in Germanium and Silicon." Physical Review **96**(1): 21-24.

Fuller, E. J., F. E. Gabaly, F. Léonard, S. Agarwal, S. J. Plimpton, R. B. Jacobs-Gedrim, C. D. James, M. J. Marinella and A. A. Talin (2017). "Li-Ion Synaptic Transistor for Low Power Analog Computing." Advanced Materials **29**(4): 1604310.

Furusawa, S.-i., H. Tabuchi and T. Tsurui (2007). "Ionic conductivity of lithium alumino-silicate thin films on SiO2 glass and Al2O3 substrates." Solid State Ionics **178**(15): 1033-1038.

Gao, Z., H. Sun, L. Fu, F. Ye, Y. Zhang, W. Luo and Y. Huang (2018). "Promises, Challenges, and Recent Progress of Inorganic Solid-State Electrolytes for All-Solid-State Lithium Batteries." Advanced Materials **30**(17): 1705702.

Goriparti, S., E. Miele, F. De Angelis, E. Di Fabrizio, R. Proietti Zaccaria and C. Capiglia (2014). "Review on recent progress of nanostructured anode materials for Li-ion batteries." Journal of Power Sources **257**(Supplement C): 421-443.

Grünebaum, M., M. M. Hiller, S. Jankowsky, S. Jeschke, B. Pohl, T. Schürmann, P. Vettikuzha, A.-C. Gentschev, R. Stolina, R. Müller and H.-D. Wiemhöfer (2014). "Synthesis and

electrochemistry of polymer based electrolytes for lithium batteries." Progress in Solid State Chemistry **42**(4): 85-105.

Gummow, R. J., A. de Kock and M. M. Thackeray (1994). "Improved capacity retention in rechargeable 4 V lithium/lithium-manganese oxide (spinel) cells." Solid State Ionics **69**(1): 59-67.

Haag, J. M., G. Pattanaik and M. F. Durstock (2013). "Nanostructured 3D Electrode Architectures for High-Rate Li-Ion Batteries." Advanced Materials **25**(23): 3238-3243.

Hagström, S. B. M., R. Z. Bachrach, R. S. Bauer and S. A. Flodström (1977). "Oxidation of Aluminum Surfaces Studied by Synchrotron Radiation Photoelectron Spectroscopy." Physica Scripta **16**(5-6): 414-419.

Hallinan, D. T. and N. P. Balsara (2013). "Polymer Electrolytes." Annual Review of Materials Research **43**(1): 503-525.

Hämäläinen, J., J. Holopainen, F. Munnik, T. Hatanpää, M. Heikkilä, M. Ritala and M. Leskelä (2012). "Lithium Phosphate Thin Films Grown by Atomic Layer Deposition." Journal of The Electrochemical Society **159**(3): A259-A263.

Hämäläinen, J., F. Munnik, T. Hatanpää, J. Holopainen, M. Ritala and M. Leskelä (2011). "Study of amorphous lithium silicate thin films grown by atomic layer deposition." Journal of Vacuum Science & Technology A **30**(1): 01A106.

Han, H., Z. Wei, A. S. Filatov, J. C. Carozza, M. Alkan, A. Y. Rogachev, A. Shevtsov, Artem M. Abakumov, C. Pak, M. Shatruk, Y.-S. Chen and E. V. Dikarev (2019). "Three to tango requires a site-specific substitution: heterotrimetallic molecular precursors for high-voltage rechargeable batteries." Chemical Science **10**(2): 524-534.

Han, X., Y. Gong, K. Fu, X. He, G. T. Hitz, J. Dai, A. Pearse, B. Liu, H. Wang, G. Rubloff, Y. Mo, V. Thangadurai, E. D. Wachsman and L. Hu (2017). "Negating interfacial impedance in garnet-based solid-state Li metal batteries." Nature Materials **16**(5): 572-579.

Hausmann, D., J. Becker, S. Wang and R. G. Gordon (2002). "Rapid Vapor Deposition of Highly Conformal Silica Nanolaminates." Science **298**(5592): 402.

Hendriks, R., D. M. Cunha, D. P. Singh and M. Huijben (2018). "Enhanced Lithium Transport by Control of Crystal Orientation in Spinel LiMn(2)O(4) Thin Film Cathodes." ACS Applied Energy Materials **1**(12): 7046-7051.

Hill, J. M., D. G. Royce, C. S. Fadley, L. F. Wagner and F. J. Grunthaner (1976). "Properties of oxidized silicon as determined by angular-dependent X-ray photoelectron spectroscopy." Chemical Physics Letters **44**(2): 225-231.

Hornsveld, N., B. Put, W. M. M. Kessels, P. M. Vereecken and M. Creatore (2017). "Plasma-assisted and thermal atomic layer deposition of electrochemically active Li2CO3." RSC Advances **7**(66): 41359-41368.

Hsin-Kuei, H. and J. W. Rabalais (1981). "Chemisorption and the initial stage of oxidation on Mn." Surface Science **107**(2): 376-390.

Hu, Y., A. Ruud, V. Miikkulainen, T. Norby, O. Nilsen and H. Fjellvåg (2016). "Electrical characterization of amorphous LiAlO2 thin films deposited by atomic layer deposition." RSC Advances **6**(65): 60479-60486.

Hu, Y. W. (1977). "Ionic Conductivity of Lithium Orthosilicate—Lithium Phosphate Solid Solutions." Journal of The Electrochemical Society **124**(8): 1240.

Ikonen, T., T. Nissinen, E. Pohjalainen, O. Sorsa, T. Kallio and V. P. Lehto (2017). "Electrochemically anodized porous silicon: Towards simple and affordable anode material for Li-ion batteries." Scientific Reports **7**(1): 7880.

Ilton, E. S., J. E. Post, P. J. Heaney, F. T. Ling and S. N. Kerisit (2016). "XPS determination of Mn oxidation states in Mn (hydr)oxides." Applied Surface Science **366**: 475-485.

Jalili, N. and K. Laxminarayana (2004). "A review of atomic force microscopy imaging systems: application to molecular metrology and biological sciences." Mechatronics **14**(8): 907-945.

Jarnestad, J. (2019). Goodenough's Battery, The Royal Swedish Academy of Sciences.

Jen, S.-H., J. A. Bertrand and S. M. George (2011). "Critical tensile and compressive strains for cracking of Al2O3 films grown by atomic layer deposition." Journal of Applied Physics **109**(8): 084305.

Jian, Z., Y.-S. Hu, X. Ji and W. Chen (2017). "NASICON-Structured Materials for Energy Storage." Advanced Materials **29**(20): 1601925.

Jin, Y., L. Wang, Y. Shang, J. Gao, J. Li and X. He (2015). "Facile synthesis of monodisperse Co3O4 mesoporous microdisks as an anode material for lithium ion batteries." Electrochimica Acta **151**(Supplement C): 109-117.

Johnson, R. W., A. Hultqvist and S. F. Bent (2014). "A brief review of atomic layer deposition: from fundamentals to applications." Materials Today **17**(5): 236-246.

Julien, C., E. Haro-Poniatowski, M. A. Camacho-Lopez, L. Escobar-Alarcon and J. Jimenez-Jarquin (2000). "Growth of LiMn2O4 thin films by pulsed-laser deposition and their electrochemical properties in lithium microbatteries." Materials Science and Engineering: B **72**(1): 36-46.

Kahlaoui, R., K. Arbi, I. Sobrados, R. Jimenez, J. Sanz and R. Ternane (2017). "Cation Miscibility and Lithium Mobility in NASICON Li1+xTi2–xScx(PO4)3 (0 ≤ x ≤ 0.5) Series: A Combined NMR and Impedance Study." Inorganic Chemistry **56**(3): 1216-1224.

Kamaya, N., K. Homma, Y. Yamakawa, M. Hirayama, R. Kanno, M. Yonemura, T. Kamiyama, Y. Kato, S. Hama, K. Kawamoto and A. Mitsui (2011). "A lithium superionic conductor." Nature Materials **10**(9): 682-686.

Kazyak, E., K.-H. Chen, A. L. Davis, S. Yu, A. J. Sanchez, J. Lasso, A. R. Bielinski, T. Thompson, J. Sakamoto, D. J. Siegel and N. P. Dasgupta (2018). "Atomic layer deposition and first principles modeling of glassy Li3BO3–Li2CO3 electrolytes for solid-state Li metal batteries." Journal of Materials Chemistry A **6**(40): 19425-19437.

Kazyak, E., K.-H. Chen, K. N. Wood, A. L. Davis, T. Thompson, A. R. Bielinski, A. J. Sanchez, X. Wang, C. Wang, J. Sakamoto and N. P. Dasgupta (2017). "Atomic Layer Deposition of the Solid Electrolyte Garnet Li7La3Zr2O12." Chemistry of Materials **29**(8): 3785-3792.

Kazyak, E., K. N. Wood and N. P. Dasgupta (2015). "Improved Cycle Life and Stability of Lithium Metal Anodes through Ultrathin Atomic Layer Deposition Surface Treatments." Chemistry of Materials **27**(18): 6457-6462.

Kganyago, K. R. and P. E. Ngoepe (2003). "Structural and electronic properties of lithium intercalated graphite ${\mathrm{LiC}}_{6}$." Physical Review B **68**(20): 205111.

Khan, Y., A. E. Ostfeld, C. M. Lochner, A. Pierre and A. C. Arias (2016). "Monitoring of Vital Signs with Flexible and Wearable Medical Devices." Advanced Materials **28**(22): 4373-4395.

Kim, D., N. Li, C. J. Sheehan and J. Yoo (2018). "Degradation of Si/Ge core/shell nanowire heterostructures during lithiation and delithiation at 0.8 and 20 A g−1." Nanoscale **10**(16): 7343-7351.

Kim, H., H.-B.-R. Lee and W. J. Maeng (2009). "Applications of atomic layer deposition to nanofabrication and emerging nanodevices." Thin Solid Films **517**(8): 2563-2580.

Kim, S. Y., J. Lee, B.-H. Kim, Y.-J. Kim, K. S. Yang and M.-S. Park (2016). "Facile Synthesis of Carbon-Coated Silicon/Graphite Spherical Composites for High-Performance Lithium-Ion Batteries." ACS Applied Materials & Interfaces **8**(19): 12109-12117.

Klinger, M. and A. Jäger (2015). "Crystallographic Tool Box (CrysTBox): automated tools for transmission electron microscopists and crystallographers." Journal of applied crystallography **48**(Pt 6): 2012-2018.

Klug, J. A., T. Proslier, J. W. Elam, R. E. Cook, J. M. Hiller, H. Claus, N. G. Becker and M. J. Pellin (2011). "Atomic Layer Deposition of Amorphous Niobium Carbide-Based Thin Film Superconductors." The Journal of Physical Chemistry C **115**(50): 25063-25071.

Kozen, A. C., A. J. Pearse, C.-F. Lin, M. Noked and G. W. Rubloff (2015). "Atomic Layer Deposition of the Solid Electrolyte LiPON." Chemistry of Materials **27**(15): 5324-5331.

Kozen, A. C., A. J. Pearse, C.-F. Lin, M. A. Schroeder, M. Noked, S. B. Lee and G. W. Rubloff (2014). "Atomic Layer Deposition and in Situ Characterization of Ultraclean Lithium Oxide and Lithium Hydroxide." The Journal of Physical Chemistry C **118**(48): 27749-27753.

Kuwano, J. and A. R. West (1980). "New Li+ ion conductors in the system, Li4GeO4-Li3VO4." Materials Research Bulletin **15**(11): 1661-1667.

Kuwata, N., M. Nakane, T. Miyazaki, K. Mitsuishi and J. Kawamura (2018). "Lithium diffusion coefficient in LiMn2O4 thin films measured by secondary ion mass spectrometry with ion-exchange method." Solid State Ionics **320**: 266-271.

Labyedh, N., F. Mattelaer, C. Detavernier and P. M. Vereecken (2019). "3D LiMn2O4 thin-film electrodes for high rate all solid-state lithium and Li-ion microbatteries." Journal of Materials Chemistry A **7**(32): 18996-19007.

Lau, J., R. H. DeBlock, D. M. Butts, D. S. Ashby, C. S. Choi and B. S. Dunn (2018). "Sulfide Solid Electrolytes for Lithium Battery Applications." Advanced Energy Materials **8**(27): 1800933.

Lau, K. K. S. and K. K. Gleason (2006). "Initiated Chemical Vapor Deposition (iCVD) of Poly(alkyl acrylates): An Experimental Study." Macromolecules **39**(10): 3688-3694.

Lebugle, A., U. Axelsson, R. Nyholm and N. Mårtensson (1981). "ExperimentalLandMCore Level Binding Energies for the Metals22Ti to30Zn." Physica Scripta **23**(5A): 825-827.

Lee, S.-J., J.-H. Bae, H.-W. Lee, H.-K. Baik and S.-M. Lee (2003). "Electrical conductivity in Li–Si–P–O–N oxynitride thin-films." Journal of Power Sources **123**(1): 61-64.

Lee, S. W., I. Ryu, W. D. Nix and Y. Cui (2015). "Fracture of crystalline germanium during electrochemical lithium insertion." Extreme Mechanics Letters **2**(Supplement C): 15-19.

Leick, N., J. W. Weber, A. J. M. Mackus, M. J. Weber, M. C. M. v. d. Sanden and W. M. M. Kessels (2016). "In situ spectroscopic ellipsometry during atomic layer deposition of Pt, Ru and Pd." Journal of Physics D: Applied Physics **49**(11): 115504.

Leite, M. S., D. Ruzmetov, Z. Li, L. A. Bendersky, N. C. Bartelt, A. Kolmakov and A. A. Talin (2014). "Insights into capacity loss mechanisms of all-solid-state Li-ion batteries with Al anodes." Journal of Materials Chemistry A **2**(48): 20552-20559.

Lesel, B. K., J. S. Ko, B. Dunn and S. H. Tolbert (2016). "Mesoporous LixMn2O4 Thin Film Cathodes for Lithium-Ion Pseudocapacitors." ACS Nano **10**(8): 7572-7581.

Létiche, M., E. Eustache, J. Freixas, A. Demortière, V. De Andrade, L. Morgenroth, P. Tilmant, F. Vaurette, D. Troadec, P. Roussel, T. Brousse and C. Lethien (2017). "Atomic Layer Deposition of Functional Layers for on Chip 3D Li-Ion All Solid State Microbattery." Advanced Energy Materials **7**(2): 1601402.

Li, C. C., X. M. Yin, Q. H. Li, L. B. Chen and T. H. Wang (2011). "Topochemical Synthesis of Cobalt Oxide-Based Porous Nanostructures for High-Performance Lithium-Ion Batteries." Chemistry – A European Journal **17**(5): 1596-1604.

Li, J., X. Xiao, F. Yang, M. W. Verbrugge and Y.-T. Cheng (2012). "Potentiostatic Intermittent Titration Technique for Electrodes Governed by Diffusion and Interfacial Reaction." The Journal of Physical Chemistry C **116**(1): 1472-1478.

Li, Q., J. Wu, Z. Yao, Y. Xu, M. M. Thackeray, C. Wolverton and V. P. Dravid (2018). "Dynamic imaging of metastable reaction pathways in lithiated cobalt oxide electrodes." Nano Energy **44**: 15-22.

Lian, P.-J., B.-S. Zhao, L.-Q. Zhang, N. Xu, M.-T. Wu and X.-P. Gao (2019). "Inorganic sulfide solid electrolytes for all-solid-state lithium secondary batteries." Journal of Materials Chemistry A **7**(36): 20540-20557.

Lim, B. S., A. Rahtu and R. G. Gordon (2003). "Atomic layer deposition of transition metals." Nature Materials **2**(11): 749-754.

Liu, C., E. I. Gillette, X. Chen, A. J. Pearse, A. C. Kozen, M. A. Schroeder, K. E. Gregorczyk, S. B. Lee and G. W. Rubloff (2014). "An all-in-one nanopore battery array." Nat Nano **9**(12): 1031-1039.

Liu, C., Z. G. Neale and G. Cao (2016). "Understanding electrochemical potentials of cathode materials in rechargeable batteries." Materials Today **19**(2): 109-123.

Liu, H., Z. Zheng, B. Chen, L. Liao and X. Wang (2017). "Cobalt Oxide Porous Nanofibers Directly Grown on Conductive Substrate as a Binder/Additive-Free Lithium-Ion Battery Anode with High Capacity." Nanoscale Research Letters **12**: 302.

Liu, J., M. N. Banis, X. Li, A. Lushington, M. Cai, R. Li, T.-K. Sham and X. Sun (2013). "Atomic Layer Deposition of Lithium Tantalate Solid-State Electrolytes." The Journal of Physical Chemistry C **117**(39): 20260-20267.

Liu, J., M. N. Banis, Q. Sun, A. Lushington, R. Li, T.-K. Sham and X. Sun (2014). "Rational Design of Atomic-Layer-Deposited LiFePO4 as a High-Performance Cathode for Lithium-Ion Batteries." Advanced Materials **26**(37): 6472-6477.

Liu, Q., Z. Geng, C. Han, Y. Fu, S. Li, Y.-b. He, F. Kang and B. Li (2018). "Challenges and perspectives of garnet solid electrolytes for all solid-state lithium batteries." Journal of Power Sources **389**: 120-134.

Liu, X. H., F. Fan, H. Yang, S. Zhang, J. Y. Huang and T. Zhu (2013). "Self-Limiting Lithiation in Silicon Nanowires." ACS Nano **7**(2): 1495-1503.

Liu, X. H., S. Huang, S. T. Picraux, J. Li, T. Zhu and J. Y. Huang (2011). "Reversible Nanopore Formation in Ge Nanowires during Lithiation–Delithiation Cycling: An In Situ Transmission Electron Microscopy Study." Nano Letters **11**(9): 3991-3997.

Liu, X. H., Y. Liu, A. Kushima, S. Zhang, T. Zhu, J. Li and J. Y. Huang (2012). "In Situ TEM Experiments of Electrochemical Lithiation and Delithiation of Individual Nanostructures." Advanced Energy Materials **2**(7): 722-741.

Liu, Y., X. H. Liu, B.-M. Nguyen, J. Yoo, J. P. Sullivan, S. T. Picraux, J. Y. Huang and S. A. Dayeh (2013). "Tailoring Lithiation Behavior by Interface and Bandgap Engineering at the Nanoscale." Nano Letters **13**(10): 4876-4883.

Liu, Y., Q. Sun, Y. Zhao, B. Wang, P. Kaghazchi, K. R. Adair, R. Li, C. Zhang, J. Liu, L.-Y. Kuo, Y. Hu, T.-K. Sham, L. Zhang, R. Yang, S. Lu, X. Song and X. Sun (2018). "Stabilizing the Interface of NASICON Solid Electrolyte against Li Metal with Atomic Layer Deposition." <u>ACS Applied Materials & Interfaces</u> **10**(37): 31240-31248.

Liu, Y., S. Vishniakou, J. Yoo and S. A. Dayeh (2015). "Engineering Heteromaterials to Control Lithium Ion Transport Pathways." <u>Scientific Reports</u> **5**(1): 18482.

Liu, Z., F. Huang, J. Yang, B. Wang and J. Sun (2008). "New lithium ion conductor, thio-LISICON lithium zirconium sulfide system." <u>Solid State Ionics</u> **179**(27): 1714-1716.

Loho, C., R. Djenadic, M. Bruns, O. Clemens and H. Hahn (2017). "Garnet-Type Li7La3Zr2O12 Solid Electrolyte Thin Films Grown by CO2-Laser Assisted CVD for All-Solid-State Batteries." <u>Journal of The Electrochemical Society</u> **164**(1): A6131-A6139.

Long, J. W., B. Dunn, D. R. Rolison and H. S. White (2004). "Three-Dimensional Battery Architectures." <u>Chemical Reviews</u> **104**(10): 4463-4492.

Lu, J., C. Zhan, T. Wu, J. Wen, Y. Lei, A. J. Kropf, H. Wu, D. J. Miller, J. W. Elam, Y.-K. Sun, X. Qiu and K. Amine (2014). "Effectively suppressing dissolution of manganese from spinel lithium manganate via a nanoscale surface-doping approach." <u>Nature Communications</u> **5**(1): 5693.

Maier, J. (2014). "Pushing Nanoionics to the Limits: Charge Carrier Chemistry in Extremely Small Systems." <u>Chemistry of Materials</u> **26**(1): 348-360.

Mallick, B. C., C.-T. Hsieh, K.-M. Yin, Y. A. Gandomi and K.-T. Huang (2019). "Review—On Atomic Layer Deposition: Current Progress and Future Challenges." <u>ECS Journal of Solid State Science and Technology</u> **8**(4): N55-N78.

Mäntymäki, M., E. Atosuo, M. J. Heikkilä, M. Vehkamäki, M. Mattinen, K. Mizohata, J. Räisänen, M. Ritala and M. Leskelä (2019). "Studies on solid state reactions of atomic layer deposited thin films of lithium carbonate with hafnia and zirconia." <u>Journal of Vacuum Science & Technology A</u> **37**(2): 020929.

Mäntymäki, M., J. Hämäläinen, E. Puukilainen, T. Sajavaara, M. Ritala and M. Leskelä (2013). "Atomic Layer Deposition of LiF Thin Films from Lithd, Mg(thd)2, and TiF4 Precursors." <u>Chemistry of Materials</u> **25**(9): 1656-1663.

Marichy, C., M. Bechelany and N. Pinna (2012). "Atomic Layer Deposition of Nanostructured Materials for Energy and Environmental Applications." <u>Advanced Materials</u> **24**(8): 1017-1032.

Masoud, E. M., A. A. El-Bellihi, W. A. Bayoumy and M. A. Mousa (2013). "Organic–inorganic composite polymer electrolyte based on PEO–LiClO4 and nano-Al2O3 filler for lithium polymer batteries: Dielectric and transport properties." <u>Journal of Alloys and Compounds</u> **575**: 223-228.

Mattelaer, F., K. Geryl, G. Rampelberg, J. Dendooven and C. Detavernier (2017). "Amorphous and Crystalline Vanadium Oxides as High-Energy and High-Power Cathodes for Three-

Dimensional Thin-Film Lithium Ion Batteries." ACS Applied Materials & Interfaces **9**(15): 13121-13131.

Mattelaer, F., K. Geryl, G. Rampelberg, T. Dobbelaere, J. Dendooven and C. Detavernier (2016). "Atomic layer deposition of vanadium oxides for thin-film lithium-ion battery applications." RSC Advances **6**(115): 114658-114665.

Mattelaer, F., P. M. Vereecken, J. Dendooven and C. Detavernier (2015). "Deposition of MnO Anode and MnO2 Cathode Thin Films by Plasma Enhanced Atomic Layer Deposition Using the Mn(thd)3 Precursor." Chemistry of Materials **27**(10): 3628-3635.

McDowell, M. T., S. W. Lee, W. D. Nix and Y. Cui (2013). "25th Anniversary Article: Understanding the Lithiation of Silicon and Other Alloying Anodes for Lithium-Ion Batteries." Advanced Materials **25**(36): 4966-4985.

Mehrer, H. (2007). Diffusion in Solids. Berlin, Germany, Springer. **155:** 95-104.

Meng, X., D. J. Comstock, T. T. Fister and J. W. Elam (2014). "Vapor-Phase Atomic-Controllable Growth of Amorphous Li2S for High-Performance Lithium–Sulfur Batteries." ACS Nano **8**(10): 10963-10972.

Miikkulainen, V., O. Nilsen, M. Laitinen, T. Sajavaara and H. Fjellvåg (2013). "Atomic layer deposition of LixTiyOz thin films." RSC Advances **3**(20): 7537-7542.

Miikkulainen, V., O. Nilsen, H. Li, S. W. King, M. Laitinen, T. Sajavaara and H. Fjellvåg (2014). "Atomic layer deposited lithium aluminum oxide: (In)dependency of film properties from pulsing sequence." Journal of Vacuum Science & Technology A **33**(1): 01A101.

Miikkulainen, V., A. Ruud, E. Østreng, O. Nilsen, M. Laitinen, T. Sajavaara and H. Fjellvåg (2014). "Atomic Layer Deposition of Spinel Lithium Manganese Oxide by Film-Body-Controlled Lithium Incorporation for Thin-Film Lithium-Ion Batteries." The Journal of Physical Chemistry C **118**(2): 1258-1268.

Minami, T., A. Hayashi and M. Tatsumisago (2006). "Recent progress of glass and glass-ceramics as solid electrolytes for lithium secondary batteries." Solid State Ionics **177**(26): 2715-2720.

Miyazaki, R. and H. Maekawa (2012). "Li+-Ion Conduction of Li3AlF6 Mechanically Milled with LiCl." ECS Electrochemistry Letters **1**(6): A87-A89.

Mizuno, F., A. Hayashi, K. Tadanaga and M. Tatsumisago (2005). "New, Highly Ion-Conductive Crystals Precipitated from Li2S–P2S5 Glasses." Advanced Materials **17**(7): 918-921.

Mizushima, K., P. C. Jones, P. J. Wiseman and J. B. Goodenough (1980). "LixCoO2 (0<x<-1): A new cathode material for batteries of high energy density." Materials Research Bulletin **15**(6): 783-789.

Moitzheim, S., J. E. Balder, R. Ritasalo, S. Ek, P. Poodt, S. Unnikrishnan, S. De Gendt and P. M. Vereecken (2019). "Toward 3D Thin-Film Batteries: Optimal Current-Collector Design and Scalable Fabrication of TiO2 Thin-Film Electrodes." ACS Applied Energy Materials **2**(3): 1774-1783.

Moitzheim, S., B. Put and P. M. Vereecken (2019). "Advances in 3D Thin-Film Li-Ion Batteries." Advanced Materials Interfaces **6**(15): 1900805.

Moni, P., A. Al-Obeidi and K. K. Gleason (2017). "Vapor deposition routes to conformal polymer thin films." Beilstein journal of nanotechnology **8**: 723-735.

Morimoto, H., H. Yamashita, M. Tatsumisago and T. Minami (1999). "Mechanochemical Synthesis of New Amorphous Materials of 60Li2S·40SiS2 with High Lithium Ion Conductivity." Journal of the American Ceramic Society **82**(5): 1352-1354.

Mukai, K. and T. Uyama (2017). "Toward Positive Electrode Materials with High-Energy Density: Electrochemical and Structural Studies on LiCoxMn2–xO4 with $0 \leq x \leq 1$." ACS Omega **2**(8): 5142-5149.

Murayama, M., R. Kanno, M. Irie, S. Ito, T. Hata, N. Sonoyama and Y. Kawamoto (2002). "Synthesis of New Lithium Ionic Conductor Thio-LISICON—Lithium Silicon Sulfides System." Journal of Solid State Chemistry **168**(1): 140-148.

Nagel, W. and H. Böhm (1982). "Ionic conductivity studies on LiAlSiO4   SiO2 solid solutions of the high quartz type." Solid State Communications **42**(9): 625-631.

Nelson, A. J., J. G. Reynolds and J. W. Roos (2000). "Core-level satellites and outer core-level multiplet splitting in Mn model compounds." Journal of Vacuum Science & Technology A **18**(4): 1072-1076.

Nilsen, O., V. Miikkulainen, K. B. Gandrud, E. Østreng, A. Ruud and H. Fjellvåg (2014). "Atomic layer deposition of functional films for Li-ion microbatteries." physica status solidi (a) **211**(2): 357-367.

Nisula, M. and M. Karppinen (2016). "Atomic/Molecular Layer Deposition of Lithium Terephthalate Thin Films as High Rate Capability Li-Ion Battery Anodes." Nano Letters **16**(2): 1276-1281.

Nisula, M., Y. Shindo, H. Koga and M. Karppinen (2015). "Atomic Layer Deposition of Lithium Phosphorus Oxynitride." Chemistry of Materials **27**(20): 6987-6993.

Nitta, N., F. Wu, J. T. Lee and G. Yushin (2015). "Li-ion battery materials: present and future." Materials Today **18**(5): 252-264.

Ohta, S., T. Kobayashi and T. Asaoka (2011). "High lithium ionic conductivity in the garnet-type oxide Li7−X La3(Zr2−X, NbX)O12 (X=0–2)." Journal of Power Sources **196**(6): 3342-3345.

Oleshko, V. P., T. Lam, D. Ruzmetov, P. Haney, H. J. Lezec, A. V. Davydov, S. Krylyuk, J. Cumings and A. A. Talin (2014). "Miniature all-solid-state heterostructure nanowire Li-ion batteries as a tool for engineering and structural diagnostics of nanoscale electrochemical processes." Nanoscale **6**(20): 11756-11768.

Ostfeld, A. E., A. M. Gaikwad, Y. Khan and A. C. Arias (2016). "High-performance flexible energy storage and harvesting system for wearable electronics." Scientific Reports **6**(1): 26122.

Østreng, E., K. B. Gandrud, Y. Hu, O. Nilsen and H. Fjellvåg (2014). "High power nano-structured V2O5 thin film cathodes by atomic layer deposition." Journal of Materials Chemistry A **2**(36): 15044-15051.

Østreng, E., P. Vajeeston, O. Nilsen and H. Fjellvåg (2012). "Atomic layer deposition of lithium nitride and carbonate using lithium silylamide." RSC Advances **2**(15): 6315-6322.

Park, J. S., X. Meng, J. W. Elam, S. Hao, C. Wolverton, C. Kim and J. Cabana (2014). "Ultrathin Lithium-Ion Conducting Coatings for Increased Interfacial Stability in High Voltage Lithium-Ion Batteries." Chemistry of Materials **26**(10): 3128-3134.

Pearse, A., T. Schmitt, E. Sahadeo, D. M. Stewart, A. Kozen, K. Gerasopoulos, A. A. Talin, S. B. Lee, G. W. Rubloff and K. E. Gregorczyk (2018). "Three-Dimensional Solid-State Lithium-Ion Batteries Fabricated by Conformal Vapor-Phase Chemistry." ACS Nano **12**(5): 4286-4294.

Pearse, A. J., T. E. Schmitt, E. J. Fuller, F. El-Gabaly, C.-F. Lin, K. Gerasopoulos, A. C. Kozen, A. A. Talin, G. Rubloff and K. E. Gregorczyk (2017). "Nanoscale Solid State Batteries Enabled by Thermal Atomic Layer Deposition of a Lithium Polyphosphazene Solid State Electrolyte." Chemistry of Materials **29**(8): 3740-3753.

Peled, E. and S. Menkin (2017). "Review—SEI: Past, Present and Future." Journal of The Electrochemical Society **164**(7): A1703-A1719.

Perng, Y.-C., J. Cho, S. Y. Sun, D. Membreno, N. Cirigliano, B. Dunn and J. P. Chang (2014). "Synthesis of ion conducting LixAlySizO thin films by atomic layer deposition." Journal of Materials Chemistry A **2**(25): 9566-9573.

Petitto, S. C. and M. A. Langell (2004). "Surface composition and structure of Co3O4(110) and the effect of impurity segregation." Journal of Vacuum Science & Technology A **22**(4): 1690-1696.

Pham, C. D., J. Chang, M. A. Zurbuchen and J. P. Chang (2017). "Magnetic Properties of CoFe2O4 Thin Films Synthesized by Radical-Enhanced Atomic Layer Deposition." ACS Applied Materials & Interfaces **9**(42): 36980-36988.

Pitawala, H. M. J. C., M. A. K. L. Dissanayake, V. A. Seneviratne, B.-E. Mellander and I. Albinson (2008). "Effect of plasticizers (EC or PC) on the ionic conductivity and thermal properties of the (PEO)9LiTf: Al2O3 nanocomposite polymer electrolyte system." Journal of Solid State Electrochemistry **12**(7): 783-789.

Poizot, P., S. Laruelle, S. Grugeon, L. Dupont and J. M. Tarascon (2000). "Nano-sized transition-metal oxides as negative-electrode materials for lithium-ion batteries." Nature **407**(6803): 496-499.

Popov, G., M. Mattinen, T. Hatanpää, M. Vehkamäki, M. Kemell, K. Mizohata, J. Räisänen, M. Ritala and M. Leskelä (2019). "Atomic Layer Deposition of PbI2 Thin Films." Chemistry of Materials **31**(3): 1101-1109.

Put, B., M. J. Mees, N. Hornsveld, S. Hollevoet, A. Sepúlveda, P. M. Vereecken, W. M. M. Kessels and M. Creatore (2019). "Plasma-Assisted ALD of LiPO(N) for Solid State Batteries." Journal of The Electrochemical Society **166**(6): A1239-A1242.

Put, B., P. M. Vereecken, N. Labyedh, A. Sepulveda, C. Huyghebaert, I. P. Radu and A. Stesmans (2015). "High Cycling Stability and Extreme Rate Performance in Nanoscaled LiMn2O4 Thin Films." ACS Applied Materials & Interfaces **7**(40): 22413-22420.

Putkonen, M., T. Aaltonen, M. Alnes, T. Sajavaara, O. Nilsen and H. Fjellvåg (2009). "Atomic layer deposition of lithium containing thin films." Journal of Materials Chemistry **19**(46): 8767-8771.

Rao, R. P. and S. Adams (2011). "Studies of lithium argyrodite solid electrolytes for all-solid-state batteries." physica status solidi (a) **208**(8): 1804-1807.

Reeja-Jayan, B., N. Chen, J. Lau, J. A. Kattirtzi, P. Moni, A. Liu, I. G. Miller, R. Kayser, A. P. Willard, B. Dunn and K. K. Gleason (2015). "A Group of Cyclic Siloxane and Silazane Polymer Films as Nanoscale Electrolytes for Microbattery Architectures." Macromolecules **48**(15): 5222-5229.

Ren, Y., K. Chen, R. Chen, T. Liu, Y. Zhang and C.-W. Nan (2015). "Oxide Electrolytes for Lithium Batteries." Journal of the American Ceramic Society **98**(12): 3603-3623.

Ruud, A., V. Miikkulainen, K. Mizohata, H. Fjellvåg and O. Nilsen (2017). "Enhanced process and composition control for atomic layer deposition with lithium trimethylsilanolate." Journal of Vacuum Science & Technology A **35**(1): 01B133.

Ruzmetov, D., V. P. Oleshko, P. M. Haney, H. J. Lezec, K. Karki, K. H. Baloch, A. K. Agrawal, A. V. Davydov, S. Krylyuk, Y. Liu, J. Huang, M. Tanase, J. Cumings and A. A. Talin (2012). "Electrolyte Stability Determines Scaling Limits for Solid-State 3D Li Ion Batteries." Nano Letters **12**(1): 505-511.

Sakuda, A., A. Hayashi and M. Tatsumisago (2013). "Sulfide Solid Electrolyte with Favorable Mechanical Property for All-Solid-State Lithium Battery." Scientific Reports **3**(1): 2261.

Santhanagopalan, D., D. Qian, T. McGilvray, Z. Wang, F. Wang, F. Camino, J. Graetz, N. Dudney and Y. S. Meng (2014). "Interface Limited Lithium Transport in Solid-State Batteries." The Journal of Physical Chemistry Letters **5**(2): 298-303.

Schindler, P., Y. Kim, D. Thian, J. An and F. B. Prinz (2016). "Plasma-enhanced atomic layer deposition of BaTiO3." Scripta Materialia **111**: 106-109.

Schneider, T., K. Artyushkova, J. E. Fulghum, L. Broadwater, A. Smith and O. D. Lavrentovich (2005). "Oriented Monolayers Prepared from Lyotropic Chromonic Liquid Crystal." Langmuir **21**(6): 2300-2307.

Seong, H., J. Choi, B. J. Kim, H. Park and S. G. Im (2017). "Vapor-phase synthesis of sub-15 nm hybrid gate dielectrics for organic thin film transistors." Journal of Materials Chemistry C **5**(18): 4463-4470.

Shao, C., Z. Yu, H. Liu, Z. Zheng, N. Sun and C. Diao (2017). "Enhanced ionic conductivity of titanium doped Li7La3Zr2O12 solid electrolyte." Electrochimica Acta **225**: 345-349.

Sharon, D., P. Bennington, C. Liu, Y. Kambe, B. X. Dong, V. F. Burnett, M. Dolejsi, G. Grocke, S. N. Patel and P. F. Nealey (2018). "Interrogation of Electrochemical Properties of Polymer Electrolyte Thin Films with Interdigitated Electrodes." Journal of The Electrochemical Society **165**(16): H1028-H1039.

Sheil, R. and J. P. Chang (2020). "Synthesis and integration of thin film solid state electrolytes for 3D Li-ion microbatteries." Journal of Vacuum Science & Technology A **38**(3): 032411.

Shen, B. H., S. Wang and W. E. Tenhaeff (2019). "Ultrathin conformal polycyclosiloxane films to improve silicon cycling stability." Science Advances **5**(7): eaaw4856.

Shen, Z. X., J. W. Allen, P. A. P. Lindberg, D. S. Dessau, B. O. Wells, A. Borg, W. Ellis, J. S. Kang, S. J. Oh, I. Lindau and W. E. Spicer (1990). "Photoemission study of CoO." Physical Review B **42**(3): 1817-1828.

Shibata, S. (2016). "Thermal Atomic Layer Deposition of Lithium Phosphorus Oxynitride as a Thin-Film Solid Electrolyte." Journal of The Electrochemical Society **163**(13): A2555-A2562.

Shin-ichi, F., S. Satoshi, S. Kaduhiro and T. Hitoshi (2004). "Preparation and ionic conductivity of β-LiAlSiO4 thin film." Solid State Ionics **167**(3): 325-329.

Shit, R. C., S. Sharma, D. Puthal and A. Y. Zomaya (2018). "Location of Things (LoT): A Review and Taxonomy of Sensors Localization in IoT Infrastructure." IEEE Communications Surveys & Tutorials **20**(3): 2028-2061.

Smith, R. I. and A. R. West (1991). "Crystal structure of α-Li2.5Al0.5SiO4." Journal of Solid State Chemistry **93**(2): 436-442.

Song, S., J. Lu, F. Zheng, H. M. Duong and L. Lu (2015). "A facile strategy to achieve high conduction and excellent chemical stability of lithium solid electrolytes." RSC Advances **5**(9): 6588-6594.

Soni, S. K., B. W. Sheldon, X. Xiao, A. F. Bower and M. W. Verbrugge (2012). "Diffusion Mediated Lithiation Stresses in Si Thin Film Electrodes." Journal of The Electrochemical Society **159**(9): A1520-A1527.

Souquet, J. L. (1981). "Ionic Transport in Amorphous Solid Electrolytes." Annual Review of Materials Science **11**(1): 211-231.

Su, Q., J. Zhang, Y. Wu and G. Du (2014). "Revealing the electrochemical conversion mechanism of porous Co3O4 nanoplates in lithium ion battery by in situ transmission electron microscopy." Nano Energy **9**(Supplement C): 264-272.

Su, Y., J. Falgenhauer, T. Leichtweiß, M. Geiß, C. Lupó, A. Polity, S. Zhou, J. Obel, D. Schlettwein, J. Janek and B. K. Meyer (2017). "Electrochemical properties and optical transmission of high Li+ conducting LiSiPON electrolyte films." physica status solidi (b) **254**(2): 1600088.

Talin, A. A., D. Ruzmetov, A. Kolmakov, K. McKelvey, N. Ware, F. El Gabaly, B. Dunn and H. S. White (2016). "Fabrication, Testing, and Simulation of All-Solid-State Three-Dimensional Li-Ion Batteries." ACS Applied Materials & Interfaces **8**(47): 32385-32391.

Tan, B. J., K. J. Klabunde and P. M. A. Sherwood (1991). "XPS studies of solvated metal atom dispersed (SMAD) catalysts. Evidence for layered cobalt-manganese particles on alumina and silica." Journal of the American Chemical Society **113**(3): 855-861.

Tang, J., D. Bishop, S. Kim, M. Copel, T. Gokmen, T. Todorov, S. Shin, K. Lee, P. Solomon, K. Chan, W. Haensch and J. Rozen (2018). ECRAM as Scalable Synaptic Cell for High-Speed, Low-Power Neuromorphic Computing. 2018 IEEE International Electron Devices Meeting (IEDM).

Tang, S. B., M. O. Lai and L. Lu (2007). "Characterization of crystallized LiMn2O4 thin films grown by pulsed laser deposition." Philosophical Magazine **87**(22): 3249-3258.

Tatsumisago, M. and A. Hayashi (2012). "Superionic glasses and glass–ceramics in the Li2S–P2S5 system for all-solid-state lithium secondary batteries." Solid State Ionics **225**: 342-345.

Tersoff, J. (1990). "Forces on charged defects in semiconductor heterostructures." Physical Review Letters **65**(7): 887-890.

Thackeray, M. M. (1997). "Manganese oxides for lithium batteries." Progress in Solid State Chemistry **25**(1): 1-71.

Thackeray, M. M., J. R. Croy, E. Lee, A. Gutierrez, M. He, J. S. Park, B. T. Yonemoto, B. R. Long, J. D. Blauwkamp, C. S. Johnson, Y. Shin and W. I. F. David (2018). "The quest for manganese-rich electrodes for lithium batteries: strategic design and electrochemical behavior." Sustainable Energy & Fuels **2**(7): 1375-1397.

Thangadurai, V. and W. Weppner (2002). "Solid state lithium ion conductors: Design considerations by thermodynamic approach." Ionics **8**(3): 281-292.

Thangadurai, V. and W. Weppner (2006). "Recent progress in solid oxide and lithium ion conducting electrolytes research." Ionics **12**(1): 81-92.

Thokchom, J. S., N. Gupta and B. Kumar (2008). "Superionic Conductivity in a Lithium Aluminum Germanium Phosphate Glass–Ceramic." Journal of The Electrochemical Society **155**(12): A915.

Tian, H., F. Xin, X. Wang, W. He and W. Han (2015). "High capacity group-IV elements (Si, Ge, Sn) based anodes for lithium-ion batteries." Journal of Materiomics **1**(3): 153-169.

Tuller, H. (2007). Ion Conduction and Applications. Springer Handbook of Electronic and Photonic Materials. P. C. Safa Kasap, Springer International**:** 247-266.

Van der Heide, P. (2011). Data Collection and Quantification X-ray Photoelectron Spectroscopy: An Introduction to Principles and Practices, Wiley**:** 61-99.

Vinado, C., S. Wang, Y. He, X. Xiao, Y. Li, C. Wang and J. Yang (2018). "Electrochemical and interfacial behavior of all solid state batteries using Li10SnP2S12 solid electrolyte." Journal of Power Sources **396**: 824-830.

Wagner, R., G. J. Redhammer, D. Rettenwander, A. Senyshyn, W. Schmidt, M. Wilkening and G. Amthauer (2016). "Crystal Structure of Garnet-Related Li-Ion Conductor Li7–3xGaxLa3Zr2O12: Fast Li-Ion Conduction Caused by a Different Cubic Modification?" Chemistry of Materials **28**(6): 1861-1871.

Wang, B., B. C. Chakoumakos, B. C. Sales, B. S. Kwak and J. B. Bates (1995). "Synthesis, Crystal Structure, and Ionic Conductivity of a Polycrystalline Lithium Phosphorus Oxynitride with the γ-Li3PO4 Structure." Journal of Solid State Chemistry **115**(2): 313-323.

Wang, B., J. Liu, Q. Sun, R. Li, T.-K. Sham and X. Sun (2014). "Atomic layer deposition of lithium phosphates as solid-state electrolytes for all-solid-state microbatteries." Nanotechnology **25**(50): 504007.

Wang, B., Y. Zhao, M. N. Banis, Q. Sun, K. R. Adair, R. Li, T.-K. Sham and X. Sun (2018). "Atomic Layer Deposition of Lithium Niobium Oxides as Potential Solid-State Electrolytes for Lithium-Ion Batteries." ACS Applied Materials & Interfaces **10**(2): 1654-1661.

Wang, G., C. Lu, X. Zhang, B. Wan, H. Liu, M. Xia, H. Gou, G. Xin, J. Lian and Y. Zhang (2017). "Toward ultrafast lithium ion capacitors: A novel atomic layer deposition seeded preparation of Li4Ti5O12/graphene anode." Nano Energy **36**: 46-57.

Wang, G. X., Y. Chen, K. Konstantinov, M. Lindsay, H. K. Liu and S. X. Dou (2002). "Investigation of cobalt oxides as anode materials for Li-ion batteries." Journal of Power Sources **109**(1): 142-147.

Wang, J., F. Fan, Y. Liu, K. L. Jungjohann, S. W. Lee, S. X. Mao, X. Liu and T. Zhu (2014). "Structural Evolution and Pulverization of Tin Nanoparticles during Lithiation-Delithiation Cycling." Journal of The Electrochemical Society **161**(11): F3019-F3024.

Wang, X., X. Li, X. Sun, F. Li, Q. Liu, Q. Wang and D. He (2011). "Nanostructured NiO electrode for high rate Li-ion batteries." Journal of Materials Chemistry **21**(11): 3571-3573.

Wang, X. H., C. Guan, L. M. Sun, R. A. Susantyoko, H. J. Fan and Q. Zhang (2015). "Highly stable and flexible Li-ion battery anodes based on TiO2 coated 3D carbon nanostructures." Journal of Materials Chemistry A **3**(30): 15394-15398.

Whittingham, M. S. (2004). "Lithium Batteries and Cathode Materials." Chemical Reviews **104**(10): 4271-4302.

Winter, M. and R. J. Brodd (2004). "What Are Batteries, Fuel Cells, and Supercapacitors?" Chemical Reviews **104**(10): 4245-4270.

Wright, P. V. (2002). "Developments in Polymer Electrolytes for Lithium Batteries." MRS Bulletin **27**(8): 597-602.

Xie, J., A. D. Sendek, E. D. Cubuk, X. Zhang, Z. Lu, Y. Gong, T. Wu, F. Shi, W. Liu, E. J. Reed and Y. Cui (2017). "Atomic Layer Deposition of Stable LiAlF4 Lithium Ion Conductive Interfacial Layer for Stable Cathode Cycling." ACS Nano **11**(7): 7019-7027.

Xie, M., X. Sun, S. M. George, C. Zhou, J. Lian and Y. Zhou (2015). "Amorphous Ultrathin SnO2 Films by Atomic Layer Deposition on Graphene Network as Highly Stable Anodes for Lithium-Ion Batteries." ACS Applied Materials & Interfaces **7**(50): 27735-27742.

Xu, J.-S. and Y.-J. Zhu (2012). "Monodisperse Fe3O4 and γ-Fe2O3 Magnetic Mesoporous Microspheres as Anode Materials for Lithium-Ion Batteries." ACS Applied Materials & Interfaces **4**(9): 4752-4757.

Xu, J., S. Dou, H. Liu and L. Dai (2013). "Cathode materials for next generation lithium ion batteries." Nano Energy **2**(4): 439-442.

Xu, X., Z. Wen, X. Wu, X. Yang and Z. Gu (2007). "Lithium Ion-Conducting Glass–Ceramics of Li1.5Al0.5Ge1.5(PO4)3–xLi2O (x=0.0–0.20) with Good Electrical and Electrochemical Properties." Journal of the American Ceramic Society **90**(9): 2802-2806.

Yang, L., T. Wang, Y. Zou and H.-L. Lu (2017). "Band Offsets and Interfacial Properties of HfAlO Gate Dielectric Grown on InP by Atomic Layer Deposition." Nanoscale Research Letters **12**(1): 339.

Yao, F., D. T. Pham and Y. H. Lee (2015). "Carbon-Based Materials for Lithium-Ion Batteries, Electrochemical Capacitors, and Their Hybrid Devices." ChemSusChem **8**(14): 2284-2311.

Yin, L., H. Yuan, L. Kong, Z. Lu and Y. Zhao (2020). "Engineering Frenkel defects of anti-perovskite solid-state electrolytes and their applications in all-solid-state lithium-ion batteries." Chemical Communications **56**(8): 1251-1254.

Young, M. J., S. Letourneau, R. E. Warburton, W. M. Dose, C. Johnson, J. Greeley and J. W. Elam (2019). "High-Rate Spinel LiMn2O4 (LMO) Following Carbonate Removal and Formation

of Li-Rich Interface by ALD Treatment." The Journal of Physical Chemistry C **123**(39): 23783-23790.

Yu, C., S. Ganapathy, E. R. H. v. Eck, H. Wang, S. Basak, Z. Li and M. Wagemaker (2017). "Accessing the bottleneck in all-solid state batteries, lithium-ion transport over the solid-electrolyte-electrode interface." Nature Communications **8**(1): 1086.

Yu, C., L. van Eijck, S. Ganapathy and M. Wagemaker (2016). "Synthesis, structure and electrochemical performance of the argyrodite Li6PS5Cl solid electrolyte for Li-ion solid state batteries." Electrochimica Acta **215**: 93-99.

Yu, X., J. B. Bates, G. E. Jellison and F. X. Hart (1997). "A Stable Thin-Film Lithium Electrolyte: Lithium Phosphorus Oxynitride." Journal of The Electrochemical Society **144**(2): 524-532.

Zaera, F. (2012). "The Surface Chemistry of Atomic Layer Depositions of Solid Thin Films." The Journal of Physical Chemistry Letters **3**(10): 1301-1309.

Zardetto, V., B. L. Williams, A. Perrotta, F. Di Giacomo, M. A. Verheijen, R. Andriessen, W. M. M. Kessels and M. Creatore (2017). "Atomic layer deposition for perovskite solar cells: research status, opportunities and challenges." Sustainable Energy & Fuels **1**(1): 30-55.

Zewde, B. W., S. Admassie, J. Zimmermann, C. S. Isfort, B. Scrosati and J. Hassoun (2013). "Enhanced Lithium Battery with Polyethylene Oxide-Based Electrolyte Containing Silane–Al2O3 Ceramic Filler." ChemSusChem **6**(8): 1400-1405.

Zhang, L. Q., X. H. Liu, Y.-C. Perng, J. Cho, J. P. Chang, S. X. Mao, Z. Z. Ye and J. Y. Huang (2012). "Direct observation of Sn crystal growth during the lithiation and delithiation processes of SnO2 nanowires." Micron **43**(11): 1127-1133.

Zhang, M., K. Yin, Z. D. Hood, Z. Bi, C. A. Bridges, S. Dai, Y. S. Meng, M. P. Paranthaman and M. Chi (2017). "In situ TEM observation of the electrochemical lithiation of N-doped anatase TiO2 nanotubes as anodes for lithium-ion batteries." Journal of Materials Chemistry A **5**(39): 20651-20657.

Zhang, W.-J. (2011). "A review of the electrochemical performance of alloy anodes for lithium-ion batteries." Journal of Power Sources **196**(1): 13-24.

Zhao, J., M. Wang and K. K. Gleason (2017). "Stabilizing the Wettability of Initiated Chemical Vapor Deposited (iCVD) Polydivinylbenzene Thin Films by Thermal Annealing." Advanced Materials Interfaces **4**(18): 1700270.

Zhao, Y., M. Amirmaleki, Q. Sun, C. Zhao, A. Codirenzi, L. V. Goncharova, C. Wang, K. Adair, X. Li, X. Yang, F. Zhao, R. Li, T. Filleter, M. Cai and X. Sun (2019). "Natural SEI-Inspired Dual-Protective Layers via Atomic/Molecular Layer Deposition for Long-Life Metallic Lithium Anode." Matter **1**(5): 1215-1231.

Zhao, Y. and L. L. Daemen (2012). "Superionic Conductivity in Lithium-Rich Anti-Perovskites." Journal of the American Chemical Society **134**(36): 15042-15047.

Zhao, Y., K. Zheng and X. Sun (2018). "Addressing Interfacial Issues in Liquid-Based and Solid-State Batteries by Atomic and Molecular Layer Deposition." Joule **2**(12): 2583-2604.

Zheng, F., M. Kotobuki, S. Song, M. O. Lai and L. Lu (2018). "Review on solid electrolytes for all-solid-state lithium-ion batteries." Journal of Power Sources **389**: 198-213.

Zhu, G.-N., L. Chen, Y.-G. Wang, C.-X. Wang, R.-C. Che and Y.-Y. Xia (2013). "Binary Li4Ti5O12-Li2Ti3O7 Nanocomposite as an Anode Material for Li-Ion Batteries." Advanced Functional Materials **23**(5): 640-647.

Zuo, X., J. Zhu, P. Müller-Buschbaum and Y.-J. Cheng (2017). "Silicon based lithium-ion battery anodes: A chronicle perspective review." Nano Energy **31**(Supplement C): 113-143.